

On the application of Large-Eddy simulations in engine-related problems

Citation for published version (APA):

Huijnen, V. (2007). *On the application of Large-Eddy simulations in engine-related problems*. [Phd Thesis 1 (Research TU/e / Graduation TU/e), Mechanical Engineering]. Technische Universiteit Eindhoven.
<https://doi.org/10.6100/IR628798>

DOI:

[10.6100/IR628798](https://doi.org/10.6100/IR628798)

Document status and date:

Published: 01/01/2007

Document Version:

Publisher's PDF, also known as Version of Record (includes final page, issue and volume numbers)

Please check the document version of this publication:

- A submitted manuscript is the version of the article upon submission and before peer-review. There can be important differences between the submitted version and the official published version of record. People interested in the research are advised to contact the author for the final version of the publication, or visit the DOI to the publisher's website.
- The final author version and the galley proof are versions of the publication after peer review.
- The final published version features the final layout of the paper including the volume, issue and page numbers.

[Link to publication](#)

General rights

Copyright and moral rights for the publications made accessible in the public portal are retained by the authors and/or other copyright owners and it is a condition of accessing publications that users recognise and abide by the legal requirements associated with these rights.

- Users may download and print one copy of any publication from the public portal for the purpose of private study or research.
- You may not further distribute the material or use it for any profit-making activity or commercial gain
- You may freely distribute the URL identifying the publication in the public portal.

If the publication is distributed under the terms of Article 25fa of the Dutch Copyright Act, indicated by the "Taverne" license above, please follow below link for the End User Agreement:

www.tue.nl/taverne

Take down policy

If you believe that this document breaches copyright please contact us at:

openaccess@tue.nl

providing details and we will investigate your claim.

On the Application of Large-Eddy Simulations in Engine-related Problems

PROEFSCHRIFT

ter verkrijging van de graad van doctor aan de
Technische Universiteit Eindhoven, op gezag van de
Rector Magnificus, prof.dr.ir. C.J. van Duijn, voor een
commissie aangewezen door het College voor
Promoties in het openbaar te verdedigen
op dinsdag 4 september 2007 om 16.00 uur

door

Vincent Huijnen

geboren te Enschede

Dit proefschrift is goedgekeurd door de promotoren:

prof.dr.ir. R.S.G. Baert
en
prof.dr. L.P.H. de Goey

Copromotor:
dr.ir. L.M.T. Somers

Copyright © 2007 by V. Huijnen

All rights reserved. No part of this publication may be reproduced, stored in a retrieval system, or transmitted, in any form, or by any means, electronic, mechanical, photocopying, recording, or otherwise, without the prior permission of the author.

Cover design: Bregje Schoffelen, Oranje Vormgevers

A catalogue record is available from the Eindhoven University of Technology Library

ISBN: 978-90-386-1078-8

Contents

1	Introduction	1
1.1	Background	1
1.2	Turbulence	3
1.3	This thesis	4
2	Theoretical background	7
2.1	Governing equations	7
2.1.1	Direct numerical simulations	8
2.2	The phenomenology of Turbulence	9
2.2.1	RANS: Averaging the turbulence	11
2.2.2	LES: Filtering the turbulence	13
2.3	LES turbulence modeling	13
2.3.1	Introduction to subgrid modeling	14
2.3.2	Subgrid-scale models	16
2.3.3	Near-wall modeling	20
2.3.4	Inflow conditions	21
2.4	Turbulence modeling for engine applications.	22
2.4.1	The phenomenology of engine turbulence	22
2.4.2	Choice of the solver	23
3	LES in confined flow geometries	25
3.1	Introduction	25
3.2	The numerical methods	29
3.2.1	Kiva-3V	29
3.2.2	The convective scheme	30
3.2.3	FASTEST-3D	32
3.3	Square duct simulations	33
3.3.1	The numerical setup	34
3.3.2	Results	36
3.3.3	Discussion	40
3.4	A practical engine head simulation	41
3.4.1	The numerical setup	42
3.4.2	Results and discussions	45
3.4.3	Discussion	47
3.5	Conclusions	49

4	Modeling the turbulent mixing of a gas jet	51
4.1	Introduction	51
4.2	Phenomenology of liquid and gaseous fuel jets	53
4.2.1	Liquid fuel jets	53
4.2.2	Gaseous fuel jets	55
4.2.3	Modeling Diesel sprays using a gas jet	58
4.3	The mixing model	58
4.3.1	The mixture fraction	59
4.3.2	The numerical setup	60
4.4	Results	62
4.4.1	Steady state behaviour	63
4.4.2	The unsteady behaviour of the turbulent gas jet	68
4.4.3	Comparison to a liquid jet model	77
4.4.4	Global mixture composition	79
4.5	Conclusions	81
5	Modeling finite-rate chemistry in turbulent diffusion flames	83
5.1	Introduction	83
5.1.1	Combustion regimes encountered in engine flows	83
5.1.2	Objectives	85
5.1.3	Chapter layout	86
5.2	Non-premixed combustion modeling	86
5.2.1	Diffusion flamelet modeling	86
5.2.2	A progress variable method for non-premixed systems	88
5.3	Effects of turbulence	90
5.3.1	The LES filtered governing equations	91
5.3.2	The PDF Method	92
5.3.3	The numerical methodology	93
5.4	LES of a piloted diffusion flame	93
5.4.1	The setup of the Sandia flame D	94
5.4.2	Results	98
5.4.3	Analysis of the chemistry models	106
5.4.4	Concluding remarks	111
5.5	A sooting benzene diffusion flame	111
5.5.1	The process of soot formation	112
5.5.2	Modeling soot in diffusion flames	114
5.5.3	The setup for the Large-Eddy simulation	119
5.5.4	Results	121
5.6	Conclusions	127
6	General conclusions	129
A	The numerical scheme of FASTEST-3D	133
A.1	Discretization	133
A.2	The solution algorithm	136
	Bibliography	139

Contents	vii
Abstract	151
Samenvatting	153
Curriculum Vitae	155
Dankwoord	157

Introduction

The work which is described in this thesis is a contribution to the development of the modeling of turbulent flows for engine-related problems. The motivation to work on this problem lies in the demands from the community on an increased fuel efficiency and a reduction of pollutants formation in internal combustion engines. The subject of this thesis is a combination of the validation of numerical methods and turbulence as well as turbulent combustion modeling. In this chapter the proposed modeling methodology is briefly introduced. Also an outline of this thesis is presented.

1.1 Background

Free to move

A main driving force for many developments in the human world is the need for freedom, in the sense that one can decide personally what actions one is going to take and where one is heading for. An underlying aspect here is a freedom in the sense of thought and speech: one should decide personally what is best for him/her. This will generally result in a movement of thought: people will not stick to a single way of thinking. Similarly, there is a freedom to move, to get in contact with other people's opinions, other habits, other atmospheres. However, this freedom in the more philosophical sense is not sufficient. It always needs to be realized by the movement of products and of the people themselves, in cars, ships, airplanes. The need for transportation will remain necessary and will be growing in the next decades, notwithstanding that a growth in virtual transportation and communication via modern electronic tools can be observed as well.

An increase in freedom will go in hand with an increase in mobility. The power source and mechanical heart of this mobility is nowadays the Internal-Combustion (IC) engine. The IC engine is popular simply because this type of engine has been proven to be the cheapest, most efficient and practical tool for energy conversion into transportation. Moreover, this will remain to be true in the coming decades as can be concluded from any of the main energy studies, for instance the WETO study [164]. But along with the benefits of free movement there will be a trend towards higher fuel needs, more noise production, traffic accidents, queueing, and pollutant formation, which, in turn, will limit our freedom.

A need to improve engines

Above limitations call for an improvement, mainly by means of engineering solutions. We do not necessarily need to live with the negative aspects of an internal combustion engine. We are free to make developments. As a matter of fact, we are *forced* to develop our engines further, simply because in the aforementioned sense engines limit the total level of freedom. From a customer's standpoint one of the main arguments is an increase in energy output for the lowest amount of fuel consumption, which calls for efficient combustion techniques. From a society point of view reduced levels of soot and NO_x exhaust are demanded, as pollutants reduce the health and vitality of a community, see, e.g., Avakian *et al.* [7].

Car manufacturers are forced to develop their engines to meet the regulation from the European government on the one hand and the local customer's needs, in terms of fuel efficiency and traveling comfort on the other hand. Along with the industrial drive, naturally there is an academic ambition to develop new engine concepts, on a more fundamental basis. Here, new insights in the underlying processes with respect to the combustion inside an IC engine are expected to lead to improvements in engine design.

The role of CFD

One type of engine, the Diesel engine, is efficient in terms of fuel consumption. Therefore this type of engine is mainly used for heavy duty transport purposes. At the same time these engines are more and more used in the personal car industry. However, the non-homogeneous fuel distribution during the combustion process in the engine leads to relatively high levels of soot formation.

Diesel engine combustion is an extremely complex problem to model, Reitz and Rutland [132]. When going through a typical combustion cycle of a Diesel engine we start at the intake stroke. Fast valve and piston movement take place and subsequently large inflow velocities are present. As the valves are closed, the turbulent swirling air is compressed. Then fuel is injected as a spray. Droplets break up and vaporize and combustion starts at some critical location. The chemical energy is released and the gas expands, forcing the piston to move downwards. This is the power stroke. Typical combustion products such as CO_2 and H_2O are produced, along with pollutants. During the exhaust phase most of the combustion products leave the cylinder. In the next cycle a new air intake starts. Due to turbulence variations, cycle to cycle variations occur, which may lead to different engine cycle characteristics for different cycles.

From the above it is clear that in modern Diesel engines both heat release rate and emissions formation are strongly influenced by the fuel-air mixing process which in turn is the outcome of the interaction between the injected fuel spray, the combustion and the in-cylinder flow field.

Through numerical modeling a better understanding can be gained of the details of in-cylinder combustion processes. This can lead to a design optimization in an early stage of the development process. Therefore in the long term such a method of investigation can be shorter and less expensive than is typically encountered in experimental methods. This drives the development towards new modeling tools.

With the increase of computational power, the development of sophisticated numerical schemes and an increase in multi-disciplinary cooperation, new theoretical modeling approaches and modeling software become available. One aspect concerns a novel modeling of the turbulent fluid flow. Within this area of research the current thesis is intended to give a new contribution.

1.2 Turbulence

The fluid flow inside cylinder geometries in actual engines is fully turbulent. The main properties of the turbulence for any particular application depend basically on two aspects: the geometry and the mass flow. The Reynolds number is used to specify the turbulence. It describes the ratio of the inertial forces compared to the friction forces,

$$\text{Re} = \frac{\mathcal{U}\mathcal{L}}{\nu}. \quad (1.1)$$

Here, \mathcal{U} is a typical velocity scale, generally related to the global mass flow, \mathcal{L} a typical length scale of the geometry and ν a property of the fluid: the viscosity. With increasing Reynolds number, the flow becomes more turbulent. The modeling of turbulent flows, which are inherently unsteady, fluctuating flows, is classically tackled using an averaging technique. In this method all turbulent scales are modeled while only the mean flow is resolved. This is the Reynolds Averaged Navier Stokes (RANS) modeling technique.

RANS turbulence modeling

In RANS all turbulent properties are modeled using a limited number of turbulent quantities. In most industrial RANS codes, these are the turbulent kinetic energy k and the turbulent dissipation rate ε . For a critical discussion the reader is referred to Hanjalić [58]. Focus of the RANS modeling is on predicting mean flow properties. Effects that take place on the smallest turbulent scales are not considered important as they have little direct impact on the mean fluid dynamics. Therefore, for processes that are dominated by an interplay with turbulence (such as mixing and combustion) that mainly take place far from walls and that depend on relatively small scale vortical structures, a RANS approach will be less appropriate. RANS will only reveal global information of the mixing.

LES turbulence modeling

In a Large Eddy Simulation (LES) more details of the flow are taken into account, compared to RANS. The turbulent flow is filtered in space, rather than averaged, as in RANS. Therefore all turbulent scales, up to a cutoff length are explicitly evaluated. It can be argued that by performing a more detailed simulation a more accurate description of the processes can be expected. However, there are modelling issues related to this approach, which need to be accounted for. This makes the use of LES models not straightforward. Therefore an investigation with respect to the applicability of this type of models for engine studies needs to be performed.

1.3 This thesis

This thesis addresses the application of the LES technique to Diesel engines. The reasons for applying LES are multiple. For future engine modeling and design it is important not only to consider the flow to be time-dependent, but also to explicitly resolve the turbulence structures temporally as well as spatially. Time dependent, because the engine flow is highly unsteady, due to the movements of the valves, the injection and subsequent combustion. This can in principle be performed using an Unsteady RANS formulation. However, in that case the turbulent structures are not resolved. An accurate description of the interplay of turbulence with combustion processes is important, especially to account properly for chemical species that are not in their equilibrium values. In particular, for the prediction of pollutants a correct modeling of non-equilibrium effects is crucial, Navarro-Martinez and Kronenburg [101]. This means that not only the mean flow field needs to be described accurately, also the turbulence statistics is essential. In RANS the turbulence is typically assumed to be homogeneous and global estimates for the mixing rates and reaction rates are based on this assumption. Therefore RANS models are less appropriate for the modeling of pollutant formation in engines. Instead, the LES approach is designed to give more detailed information on the turbulence statistics, which makes it a more suitable modeling tool in this sense.

As simple as the LES method seems, its application is not straightforward. Both the numerical method and the applied turbulence models can be a source of error, Meyers *et al.* [94]. First of all, any model implementation should be validated in sufficient detail. Also, problems on the use of LES for practical applications need investigation. Additionally, any interaction with other physical effects, with special attention to the combustion process should be considered. But analysis of LES modeling where the complete Diesel combustion process is modeled directly is very difficult and will be obscured by the complexity of the system. Such an approach will not reveal any of the issues that are related to separate aspects. Therefore a representative selection of key Diesel engine flow processes has been studied in this thesis.

The outline of this thesis

As a start, the application of LES for a generic wall bounded shear flow is considered, which is an important aspect in any turbulence model that is applied. Also the impact of the shear flow modeling on the modeling of the complex flow structures as occurring in a typical engine geometry is studied. It is found that shear flows can not appropriately be modeled in the current formulation of the LES method. Therefore in the remainder no turbulence-wall interactions are considered. Another aspect that is examined is the mixing process of the fuel and air, which is a necessary tool for turbulent combustion modeling. Finally, the application of LES to the prediction of non-premixed combustion was studied, in particular considering finite-rate chemistry effects and the potential for the prediction of soot in such flames.

The results are presented in six chapters. Apart from this introduction and the final conclusions, the contents of this thesis can be described as follows. First of

all, non-reactive turbulent flows are considered. The underlying physical laws are explained in chapter 2. In chapter 3 it is shown how such a model can be translated into a working simulation code. The different turbulence LES sub-grid models are analyzed and validated, as well as the impact of the numerical method on the flow simulation. This is shown for a generic flow geometry: a square duct flow. Also a series of Large-Eddy simulations of the turbulent flow in an engine geometry is presented: the flow in a steady engine head setup attached to a cylinder. This setup is representative to study typical flow properties of such a complex geometry, such as wall shear, swirl and tumble. This chapter illustrates the difficulties of the LES approach when simulating practical engine-related flow problems. It is shown that a poor resolution near the walls and numerical discretization errors will severely influence the mean and turbulent flow properties in such a situation.

In chapter 4 LES is used to calculate a developing turbulent gaseous fuel jet. This type of flow is similar to the fuel/air mixing as takes place in direct injection (Diesel) engines. Here an LES modeling approach for turbulent mixing is introduced and validated. It is shown that the gaseous fuel jet follows well the similarity theory developed for axisymmetrical turbulent jets. The gaseous fuel jet modeled using LES is compared to a phenomenological liquid spray jet model. When corrected for the difference in cone angle between the fuel spray and the gas jet it is shown that these models are exchangeable.

Combustion in Diesel engines can be considered mainly as non-premixed. This type of combustion problems is often tackled by so-called laminar flamelet methods. Here the main parameter that defines the mixing state is the mixture fraction. But the effect of turbulence on the chemistry cannot simply be accounted for with this single parameter. Other, more detailed methods are necessary. In chapter 5 models are presented that couple chemistry models to the turbulent flow field. The classical method that uses a mixing-time scale (i.e., the scalar dissipation rate) is compared to a newly developed method where reaction progress is tracked explicitly. The applicability of the different methods is validated using the well documented Sandia flame D. In the final sections of chapter 5 a sooting turbulent diffusion flame is modeled, where a crucial impact of non-equilibrium effects of the soot formation chemistry on the predicted soot production is illustrated. The methodology to account for these effects is presented, as well as its application on a sooting turbulent benzene flame.

Theoretical background

In this chapter the theoretical background for the modeling of the fluid dynamics is introduced. The general conservation equations for turbulent transport of mass, momentum, energy and species, as used throughout this thesis, are given. The LES filtering operation is presented, leading to the filtered transport equations. In the second part of this chapter the focus is on models that describe the subgrid scale turbulence. This will serve as a basis for the simulations as presented in chapter 3. Finally, a brief classification is given of the approaches to solve fluid dynamical problems related to engine cases.

2.1 Governing equations

Modeling fluid dynamics starts with the definition of the underlying physical laws. The choice which models are used here defines the physical limitations of the problems that can be solved. Here the laws of conservation of mass and momentum, known as the Navier-Stokes equations are introduced. These equations can be written as

$$\frac{\partial \rho}{\partial t} + \frac{\partial \rho u_j}{\partial x_j} = 0, \quad (2.1)$$

$$\frac{\partial \rho u_i}{\partial t} + \frac{\partial \rho u_j u_i}{\partial x_j} = \frac{\partial}{\partial x_j} (\rho \sigma_{ij}) + \rho g_i - \frac{\partial p}{\partial x_i}. \quad (2.2)$$

Here ρ is the density of the fluid, u_i the velocity in x_i -direction, p the pressure, σ_{ij} the stress tensor and g_i the acceleration by gravity. For Newtonian fluids the stress tensor reads

$$\sigma_{ij} = \nu \left[\left(\frac{\partial u_i}{\partial x_j} + \frac{\partial u_j}{\partial x_i} \right) - \frac{2}{3} \frac{\partial u_k}{\partial x_k} \delta_{ij} \right], \quad (2.3)$$

with ν the kinematic molecular viscosity. These equations are the main conservation equations that are required for fluid dynamics and turbulence modeling, and are therefore the heart of any fluid-dynamical solver. For the conservation of total energy an independent equation needs to be addressed. This equation is given here, in terms of temperature (see, e.g., Moin *et al.* [96]):

$$\frac{\partial \rho c_v T}{\partial t} + \frac{\partial \rho u_j c_v T}{\partial x_j} = \frac{\partial}{\partial x_i} \left(\lambda \frac{\partial T}{\partial x_i} \right) + \omega_T. \quad (2.4)$$

Here λ and c_v denote the thermal conductivity and specific heat at constant volume respectively. ω_T describes the total heat release rate, e.g., by chemical reactions, using an Arrhenius-like expression, see, e.g., Warnatz *et al.* [162]. In equation 2.4 the heating term due to internal friction has been neglected, as well as a term accounting for acoustic interactions and pressure waves. This approximation is valid for low Mach number flows. Moreover, there is no $\frac{\partial p}{\partial t}$ term in the above equation. This is valid for constant pressure problems, such as in case of steady, open systems. Note that this term should be retained in applications for reciprocating engines where the piston movement induces a pressure rise.

When chemistry starts to play a role the modeling of additional quantities will become necessary. The conservation equations for the species mass fraction are given by

$$\frac{\partial \rho Y_i}{\partial t} + \frac{\partial \rho u_j Y_i}{\partial x_j} = \frac{\partial}{\partial x_j} \left(\rho D_i \frac{\partial Y_i}{\partial x_j} \right) + \omega_i. \quad (2.5)$$

Here, Y_i denotes the mass fraction of species i , and D_i its diffusion coefficient. ω_i is the chemical source term. For species diffusion the diffusivity is often related to the thermal diffusivity $\frac{\lambda}{\rho c_p}$, given by the Lewis number

$$\text{Le}_i = \frac{\lambda}{\rho D_i c_p}. \quad (2.6)$$

To close the above system of equations, a coupling between the pressure, density and temperature needs to be provided. In the remainder of this work we will adopt the ideal gas law

$$\rho = \frac{pM}{RT}, \quad (2.7)$$

where R is the universal gas constant. This assumption is well-applicable for IC engine modeling, see Evlampiev [44]. This equation relates the local density ρ to the molar mass M and the temperature T at a specific working pressure.

2.1.1 Direct numerical simulations

When solving equations 2.1, 2.2, 2.4, 2.5 and 2.7 directly in some numerical method one is applying the Direct Numerical Simulation (DNS) approach: all turbulent scales are resolved up to the Kolmogorov scale η , which is the smallest scale of the continuum. When only considering fluid dynamical scales, it can be shown that the number of required grid points for such a simulation scales as $N_t \sim \text{Re}^{9/4}$, Sagaut [139]. This is untractable for typical practical simulations, where Re can easily reach values of about 50.000, based on the cylinder diameter and the mass flow rates. Additionally the chemical length scales that should be accounted for are typically of the size of 0.1 mm, for atmospheric flames, and decreasing with increasing pressure. Therefore the DNS approach cannot be used in practical applications. This implies that modelling of the fluid dynamics as well as the chemistry is inevitable. In order to understand how the turbulence can be modelled it is necessary to understand some of its nature.

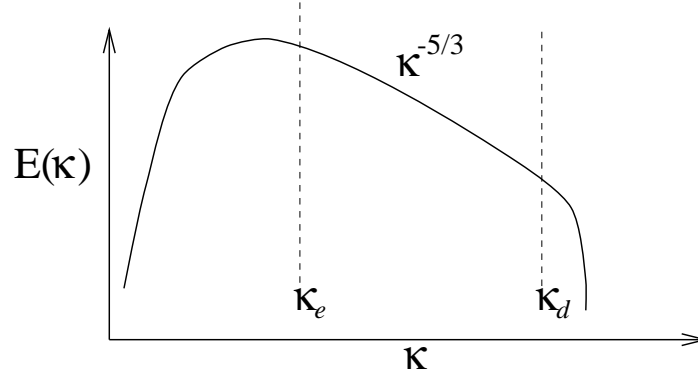


Figure 2.1 : A typical energy spectrum of turbulence as a function of the wave number. Both scales are logarithmic

2.2 The phenomenology of Turbulence

Turbulence can be defined as the interplay of ordered, coherent structures. In general terms, these coherent structures can emerge from chaos at the smallest scales under the action of an external constraint. In these circumstances small perturbations have a chance to grow and become significant, Lesieur [85]. This is due to the non-linear form of the system, as described by the Navier-Stokes equations. The turbulent vortical structures range in size from the very small ones, defined by the Kolmogorov scale η containing only a marginal amount of kinetic energy, up to the large-scale coherent structures. These large structures are responsible for a large fraction, up to 90 %, of the transport of the conserved properties such as species, mass, momentum and energy, Ferziger [45]. However, the appearance and evolution of these coherent structures is difficult to predict. It is instructive to introduce the spectrum of the turbulent kinetic energy. In figure 2.1 the energy of the turbulence as a function of its wave number κ is presented, with κ the inverse of wave length, $\kappa = 2\pi/l$. The turbulence spectrum can be divided into a macro-structure (small κ) and a micro-structure (large κ). In between a cascade process takes place. The macro-structure is dominated by the non-linear processes; viscous effects are negligible. The kinetic energy of the turbulence scales with \mathcal{U}^2 , with \mathcal{U} the velocity scale of the macro-structure. These structures are the most dominant in the energy-domain. Here the turbulence is in general non-homogeneous and is strongly influenced by the boundary conditions of the geometry. Its typical wave number is: $\kappa \approx \kappa_e = 2\pi/\mathcal{L}$ with \mathcal{L} the largest scale, a typical length scale of the geometry.

At the opposite side of the spectrum the small scale turbulence velocity and length scale are defined by the Kolmogorov scales v (velocity scale) and η (length scale). Then $\kappa \approx \kappa_d = 2\pi/\eta$. These are the smallest turbulent scales in the domain. These scales are assumed to depend only on local processes: viscosity (ν) and dissipation (ε). By dimensional analysis it can be derived that, Kolmogorov [76],

$$\eta = \left(\frac{\nu^3}{\varepsilon} \right)^{1/4}. \quad (2.8)$$

This is the micro structure where the turbulence is dissipated by molecular viscosity effects. The viscous term is now important, as the velocity gradients are large. In

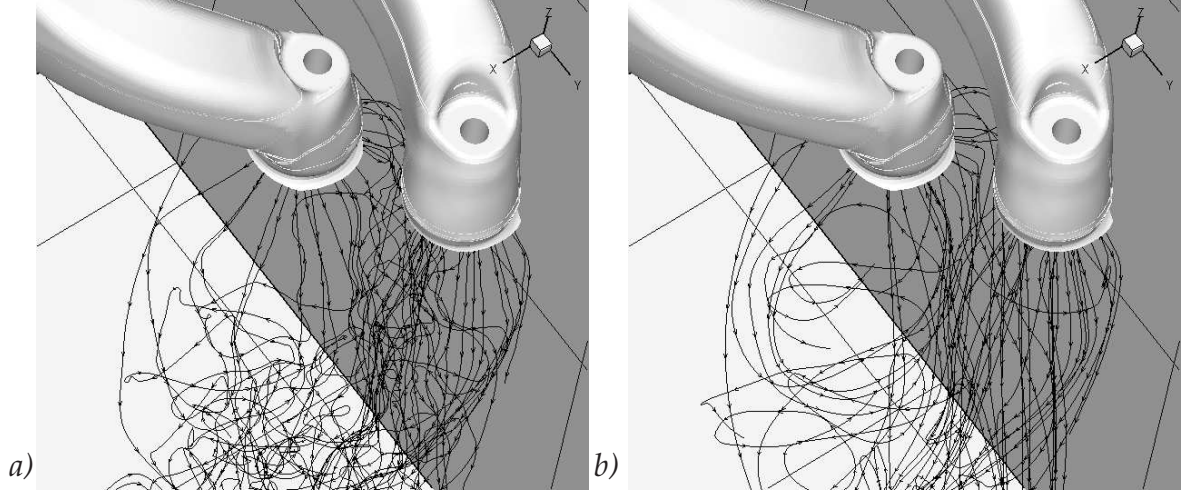


Figure 2.2 : An illustration of the turbulent flow in a Diesel engine. (a) instantaneous, turbulent streamlines, (b) some streamlines of the average flow field.

case of a scale separation between the macro scales and the micro scales, the macro-scales \mathcal{U} and \mathcal{L} are not of direct importance in this regime: its non-homogeneous information is lost during the three-dimensional cascade process. This means that the structure of the microscale is universal, the turbulence is only indirectly coupled to the large scales. This universal behavior is valid for large Reynolds numbers, i.e. when the large scales and the small scales are completely separated: $\kappa_d/\kappa_e \gg 1$. Consequently, close to the walls this universal behavior shifts to the smaller scales. The relation that connects the small scales to the large scales, in the case of homogeneous isotropic turbulence is given by:

$$\frac{\mathcal{L}}{\eta} = \text{Re}^{3/4} \quad (2.9)$$

with Re the bulk Reynolds number, based on the characteristic velocity scale \mathcal{U} and length scale \mathcal{L} , see equation 1.1. The coupling of the large and the small scales is dominated by the processes in the so-called inertial subrange. In this regime, the spectrum is independent of the macro scale because $\kappa \gg \kappa_e$. On the other hand the spectrum is independent of viscosity as well as $\kappa \ll \kappa_d$. The only parameter left responsible for the energy cascade process, is the dissipation ε which is in equilibrium with the injection of kinetic energy at the large scales. Based on dimensional analysis the shape of the spectrum in the inertial subrange can be found:

$$E(\kappa) = C_k \varepsilon^{2/3} \kappa^{-5/3} \quad (2.10)$$

with C_k the Kolmogorov constant: $C_k \approx 1.6$, as shown by Kolmogorov [76].

The above considerations illustrate that it is artificial to make a strict distinction between the different turbulent scales that are studied. Turbulence is an effect of the sum of all scales that appear in a system.

However, sometimes one is only interested in the mean flow properties, omitting turbulent statistics as unnecessary information. In terms of engine flows one can be interested in the large-scale tumbling and swirling motions, which show a very regular flow pattern on an average picture, see figure 2.2. In an instantaneous snapshot

these flow patterns are very irregular and hard to recognize. This illustrates that all instant turbulent eddies build up the mean picture, where only the largest-scale flow patterns are retained. However, this also shows that just the knowledge of a mean flow picture masks a lot of information of the actual fluid flow. Therefore, in fluid flow modeling not only the mean flow features are considered but also the turbulent statistics. Apart from the DNS method this modeling can be achieved by the RANS and the LES approach.

2.2.1 RANS: Averaging the turbulence

In RANS, the full equations for any quantity ϕ are decomposed into a mean $\bar{\phi}$ and a fluctuating ϕ' part:

$$\bar{\phi} = \phi - \phi', \quad (2.11)$$

$$\bar{\phi} = \lim_{n \rightarrow \infty} \frac{1}{n} \sum_{i=1}^n \phi_i. \quad (2.12)$$

This procedure is known as Reynolds ensemble averaging, over realizations i , and provides equations for all mean quantities as a function of space and time. With respect to engines, the ensemble averaging procedure refers to averaging over cycles. For steady state problems, the ensemble averaging corresponds simply to time-averaging of the turbulence. In the frequency domain, only the lowest turbulent frequencies, corresponding to wave numbers up to κ_e , are explicitly calculated, the rest is modelled. If density varies generally the Favre-averaging procedure will be adopted. This is defined as

$$\tilde{\phi} = \bar{\rho\phi} / \bar{\rho}. \quad (2.13)$$

This substitution greatly simplifies all averaging and filtering procedures where variable density effects play a role. By applying above procedures to the Navier-Stokes equations and the energy equation the following set of equations can be found:

$$\frac{\partial \bar{\rho}}{\partial t} + \frac{\partial \bar{\rho} \tilde{u}_j}{\partial x_j} = 0, \quad (2.14)$$

$$\frac{\partial \bar{\rho} \tilde{u}_i}{\partial t} + \frac{\partial \bar{\rho} \tilde{u}_j \tilde{u}_i}{\partial x_j} = \frac{\partial}{\partial x_j} (\bar{\rho} \tilde{\sigma}_{ij} - \bar{\rho} \tau_{ij}) + \bar{\rho} g_i - \frac{\partial \bar{p}}{\partial x_i}, \quad (2.15)$$

$$\frac{\partial \bar{\rho} c_v \tilde{T}}{\partial t} + \frac{\partial \bar{\rho} \tilde{u}_j c_v \tilde{T}}{\partial x_j} = \frac{\partial}{\partial x_j} \left(\tilde{\lambda} \frac{\partial \tilde{T}}{\partial x_j} - c_v \bar{\rho} q_j \right) + \bar{\omega}_T, \quad (2.16)$$

$$\frac{\partial \bar{\rho} \tilde{Y}_i}{\partial t} + \frac{\partial \bar{\rho} \tilde{u}_j \tilde{Y}_i}{\partial x_j} = \frac{\partial}{\partial x_j} \left(\bar{\rho} \tilde{D}_i \frac{\partial \tilde{Y}_i}{\partial x_j} - \bar{\rho} J_{ij} \right) + \bar{\omega}_i. \quad (2.17)$$

In above equations the turbulent contribution in the diffusive terms of the energy and species concentration due to the averaging is neglected, as is generally accepted, Poinot and Veynante [124]. Note that equations 2.14-2.17 closely resemble the original equations; only extra terms are found that are given in the diffusion part of the

Table 2.1 : Modeling constants for the $k - \varepsilon$ model

C_μ	$C_{\varepsilon 1}$	$C_{\varepsilon 2}$	$C_{\varepsilon 3}$	σ_k	σ_ε
0.09	1.44	1.92	1.44	1.0	1.3

transport equations. These represent the influence of turbulent fluctuations from all frequencies on the mean flow. These terms can be represented as:

$$\tau_{ij} = \widetilde{u_i u_j} - \tilde{u}_i \tilde{u}_j, \quad (2.18)$$

$$q_j = \widetilde{u_j T} - \tilde{u}_j \tilde{T}, \quad (2.19)$$

$$J_{ij} = \widetilde{u_j Y_i} - \tilde{u}_j \tilde{Y}_i. \quad (2.20)$$

The turbulent stress τ_{ij} , the turbulent energy and species transport q_j and J_{ij} can be interpreted as resulting mean rates of transport of momentum, energy and species due to the turbulent movements of the fluid. The main contribution will come from the large scale fluctuations, as these are the most energetic. These additional terms (in the momentum equation it is the Reynolds stress and in the energy equation the turbulent heat flux) have to be modelled. In one of the simplest, and most widely used models the Boussinesq hypothesis [20], assuming homogeneity of the turbulence, is adopted:

$$\tau_{ij} = \frac{2}{3} k \delta_{ij} - \nu_t \left(\frac{\partial \tilde{u}_i}{\partial x_j} + \frac{\partial \tilde{u}_j}{\partial x_i} \right) \quad (2.21)$$

where ν_t denotes the turbulent viscosity, modeled as (e.g. Launder and Spalding [81])

$$\nu_t = C_\mu \frac{k^2}{\varepsilon}, \quad (2.22)$$

with C_μ a modeling parameter. Here, transport equations for the total turbulent kinetic energy $k = \widetilde{u_i u_i} / 2$ and dissipation ε come into play. The transport equation for k is given by

$$\bar{\rho} \frac{\partial k}{\partial t} + \bar{\rho} \tilde{u}_j \frac{\partial k}{\partial x_j} = \bar{\rho} P + \frac{\partial}{\partial x_j} \left(\frac{\nu_t}{\sigma_k} \frac{\partial k}{\partial x_j} \right) - \bar{\rho} \varepsilon, \quad (2.23)$$

where $P = -\widetilde{u'_i u'_j} \frac{\partial \tilde{u}_i}{\partial x_j}$ denotes the production term of turbulent kinetic energy. Under the assumption of local isotropy the transport equation for the dissipation rate

$\varepsilon = \nu \widetilde{\left(\frac{\partial u_i}{\partial x_j} \right)^2}$ is written as

$$\begin{aligned} \bar{\rho} \frac{\partial \varepsilon}{\partial t} + \bar{\rho} \tilde{u}_j \frac{\partial \varepsilon}{\partial x_j} = & - \left(\frac{2}{3} C_{\varepsilon 1} - C_{\varepsilon 3} \right) \bar{\rho} \varepsilon \frac{\partial \tilde{u}_i}{\partial x_i} + \frac{\partial}{\partial x_j} \left(\frac{\nu_t}{\sigma_\varepsilon} \frac{\partial \varepsilon}{\partial x_j} \right), \\ & - \bar{\rho} \frac{\varepsilon}{k} (C_{\varepsilon 1} P + C_{\varepsilon 2} \varepsilon). \end{aligned} \quad (2.24)$$

The modeling constants are given in table 2.1.

Most industrial computational codes still rely on this type of $k - \varepsilon$ models. Advantages are the robustness, the relative simplicity, and the relatively low computational costs. However, since long this model has been denounced in the academic world for its failure in the modeling of anisotropic turbulence, which is occurring in practically all industrial applications where complex geometries are present.

The RANS approach has been extended to Unsteady-RANS and models have been developed with second moment Reynolds Stress closures (RSM) and near-wall treatment, see, e.g., Pope [128] and references therein. Notwithstanding many reported successes on generic anisotropic turbulence cases (see e.g. Yang *et al.* [166, 167]) these models have never become standard in industrial codes, see e.g. Hanjalić [58] and Laurence [82]. One reason is that the coupling of these turbulence models is less robust than in the case of an eddy viscosity closure. This implies a firm knowledge on turbulence theory and a large experience to handle simulations where these models are incorporated. Simplifications, by replacing the second moment closure, where six transport equations for the Reynolds stress terms are solved, with Algebraic Stress Models (ASM) improve the stability and numerical efficiency of the model. But this inherently decreases the modeling accuracy, as all ASM models are based on simplifications of the full Reynolds Stress equations, as pointed out by Hanjalić [58].

2.2.2 LES: Filtering the turbulence

In the LES approach a spatial filtering procedure is applied to the governing equations. All quantities are resolved up to some level of detail, at some location in the inertial subrange: $\kappa_e < \kappa_C < \kappa_d$ with κ_C a cutoff frequency. This scales typically to the mesh size. The details are filtered out spatially over a domain D :

$$\bar{\Phi} = \int_D G(\mathbf{x} - \mathbf{x}') \Phi(\mathbf{x}') d\mathbf{x}'. \quad (2.25)$$

Here, G is the convolution kernel, the definition of the adopted filter. Turbulence with length scales larger than the filter size should be explicitly resolved. The structures smaller than this size are in principle unknown. Therefore a *subgrid scale* (SGS) model has to be defined.

An argument for LES seems the clearness of the method: only the smallest scales of the turbulence are modeled, whereas the rest is fully resolved. This is in contrast to the RANS approach, where all turbulent scales are modeled, which may require many scaling parameters. However, numerical accuracy as well as computational demands of the LES models pose limitations to the applicability. Therefore still the RANS approach remains most suitable for practical, industrial flow problems (Laurence [82]), whereas the LES approach still needs development on many aspects to become fully applicable for a wide range of problems.

2.3 LES turbulence modeling

Applying the spatial filter to the governing equations and adopting the Favre averaging procedure leads to the following set of equations, which are essentially iden-

tical as the RANS averaged equations:

$$\frac{\partial \bar{\rho}}{\partial t} + \frac{\partial \bar{\rho} \tilde{u}_j}{\partial x_j} = 0, \quad (2.26)$$

$$\frac{\partial \bar{\rho} \tilde{u}_i}{\partial t} + \frac{\partial (\bar{\rho} \tilde{u}_j \tilde{u}_i)}{\partial x_j} = \frac{\partial \bar{\rho} \tilde{\sigma}_{ij}}{\partial x_j} - \frac{\partial \bar{\rho} \tau_{ij}}{\partial x_j} + \bar{\rho} g_i - \frac{\partial \bar{p}}{\partial x_i}, \quad (2.27)$$

$$\frac{\partial \bar{\rho} c_v \tilde{T}}{\partial t} + \frac{\partial \bar{\rho} \tilde{u}_j c_v \tilde{T}}{\partial x_j} = \frac{\partial}{\partial x_j} \left(\tilde{\lambda} \frac{\partial \tilde{T}}{\partial x_j} - c_v \bar{\rho} q_j \right) + \bar{\omega}_T, \quad (2.28)$$

$$\frac{\partial \bar{\rho} \tilde{Y}_i}{\partial t} + \frac{\partial \bar{\rho} \tilde{u}_j \tilde{Y}_i}{\partial x_j} = \frac{\partial}{\partial x_j} \left(\bar{\rho} \tilde{D}_i \frac{\partial \tilde{Y}_i}{\partial x_j} - \bar{\rho} J_{ij} \right) + \bar{\omega}_i. \quad (2.29)$$

The difference with the RANS counterpart is that in the above equation, τ_{ij} , the turbulent stress, is responsible for the subgrid-scale velocity fluctuations instead of the total turbulent stress. Similarly, q_j is responsible for subgrid-scale energy fluctuations and J_{ij} for the subgrid-scale fluctuations in species concentration Y_i . In above equations the subscale contribution of the diffusive terms of the energy and species concentration due to the filtering is neglected, as is standard practise, Piomelli [119]. For the following discussion we will focus only on the modeling of τ_{ij} . It is standard practise to model q_j and J_{ij} analogous to τ_{ij} . Some of these details will be discussed in chapter 4. Here, and for the following two chapters, predicting the velocity field is of interest.

2.3.1 Introduction to subgrid modeling

Using a triple decomposition the subgrid stress tensor can be rewritten as, Sagaut [139],

$$\tau_{ij} = L_{ij} + C_{ij} + R_{ij}, \quad (2.30)$$

with $L_{ij} = \left(\widetilde{\tilde{u}_i \tilde{u}_j} - \tilde{u}_i \tilde{u}_j \right)$ the Leonard stresses accounting for the interaction of two resolved eddies on the resolved scale, $C_{ij} = \left(\widetilde{\tilde{u}_i u'_j} + \widetilde{\tilde{u}_j u'_i} \right)$ the cross terms, and $R_{ij} = \widetilde{u'_i u'_j}$ the subgrid scale Reynolds stresses. The Leonard tensor represents the SGS contribution from the resolved scales and can be computed explicitly; the cross terms represent the interactions of the resolved with the unresolved scales while the Reynolds stresses represent the interaction of the unresolved scales, acting on the resolved scales.

With the velocity field divided into a resolved field and a subgrid scale field, also analogous to the RANS approach transport equations can be constructed for the resolved kinetic energy $q_r^2 = \tilde{u}_i \tilde{u}_i / 2$ as well as for the subgrid scale kinetic energy $q_{sgs}^2 = \widetilde{u'_i u'_i} / 2$, see, e.g., Sagaut [139]. This will be helpful to understand the

mechanisms of energy transfer:

$$\begin{aligned}
 \bar{\rho} \frac{\partial q_r^2}{\partial t} + \bar{\rho} \tilde{u}_j \frac{\partial q_r^2}{\partial x_j} &= \underbrace{\bar{\rho} \tau_{ij} \frac{\partial \tilde{u}_i}{\partial x_j}}_I - \underbrace{\bar{\rho} \nu \frac{\partial \tilde{u}_i}{\partial x_j} \frac{\partial \tilde{u}_i}{\partial x_j}}_{II} \\
 &\quad - \underbrace{\bar{\rho} \frac{\partial \tilde{u}_i \bar{p}}{\partial x_i}}_{III} + \underbrace{\bar{\rho} \frac{\partial}{\partial x_i} \left(\nu \frac{\partial q_r^2}{\partial x_i} \right)}_{IV} \\
 &\quad + \underbrace{\bar{\rho} \tilde{u}_i \tilde{u}_j \frac{\partial \tilde{u}_i}{\partial x_j}}_V - \underbrace{\bar{\rho} \frac{\partial \tilde{u}_i \tau_{ij}}{\partial x_j}}_{VI}
 \end{aligned} \tag{2.31}$$

Here, term I is the subgrid dissipation, II the dissipation by viscous effects, III the diffusion by pressure effects, IV the diffusion by viscous effects, V the production term and VI the diffusion by interaction with subgrid modes. The transport equation for the subgrid kinetic energy $q_{sgs}^2 = \tilde{u}_i' u_i' / 2$ reads

$$\begin{aligned}
 \bar{\rho} \frac{\partial q_{sgs}^2}{\partial t} + \bar{\rho} \tilde{u}_j \frac{\partial q_{sgs}^2}{\partial x_j} &= \underbrace{-\bar{\rho} \tau_{ij} \tilde{S}_{ij}}_I - \underbrace{\bar{\rho} \frac{\nu}{2} \frac{\partial \tilde{u}_i'}{\partial x_j} \frac{\partial \tilde{u}_i'}{\partial x_j}}_{II} \\
 &\quad + \underbrace{\bar{\rho} \frac{\partial}{\partial x_j} \left(\tilde{u}_j' \bar{p} + \frac{1}{2} \tilde{u}_i' u_i' u_j' \right)}_{III} + \underbrace{\bar{\rho} \frac{\partial}{\partial x_j} \left(\nu \frac{\partial q_{sgs}^2}{\partial x_j} \right)}_{IV},
 \end{aligned} \tag{2.32}$$

where $\tilde{S}_{ij} = \frac{1}{2} \left(\frac{\partial \tilde{u}_i}{\partial x_j} + \frac{\partial \tilde{u}_j}{\partial x_i} \right)$. In the above equation, term I denotes the production from the resolved scales, II is the turbulent dissipation. Term III consists of two parts: the diffusion by pressure effects and the turbulent transport, and term IV is the viscous diffusion term. For a subgrid scale model that is based on the transport equation of the subgrid scale energy it is necessary to solve above equation. Then terms II and III need to be closed. The dissipation term ε is generally modeled using dimensional reasoning, see Horiuti [51], leading to:

$$\varepsilon = \frac{\nu}{2} \frac{\partial \tilde{u}_i'}{\partial x_j} \frac{\partial \tilde{u}_i'}{\partial x_j} = C_d \frac{(q_{sgs}^2)^{3/2}}{\Delta}, \quad C_d = \pi \left(\frac{2}{3C_k} \right)^{3/2}, \tag{2.33}$$

with C_k the Kolmogorov constant, usually set to $C_k = 1.6$. For term III the gradient hypothesis can be assumed, i.e. the non-linear term is proportional to the gradient of q_{sgs}^2 . This is referred to as the Kolmogorov-Prandtl relation:

$$\bar{\rho} \frac{\partial}{\partial x_j} \left(\tilde{u}_j' \bar{p} + \frac{1}{2} \tilde{u}_i' u_i' u_j' \right) = \bar{\rho} C_2 \frac{\partial}{\partial x_j} \left(\Delta \sqrt{q_{sgs}^2} \frac{\partial q_{sgs}^2}{\partial x_j} \right). \tag{2.34}$$

For the factor C_2 generally the value of 0.1 is used. From equation 2.32 an estimate for q_{sgs}^2 can be constructed, by relating this term to τ_{ij} . This can be done by assuming

a local equilibrium. Then, all terms in equation 2.32 vanish, except for the production and destruction term, terms I and II , which balance each other. This leads to the expression

$$-\tau_{ij}\tilde{S}_{ij} = C_d \frac{(q_{sgs}^2)^{3/2}}{\Delta}. \quad (2.35)$$

The next step will be to find a way to treat the SGS stresses.

2.3.2 Subgrid-scale models

The first step towards the subgrid-scale modelling is in general to make the eddy viscosity assumption, Sagaut [139], which is known as the Boussinesq hypothesis. Here it is assumed that the energy transfer from the resolved to the subgrid scales is analogous to molecular mechanisms. Then the stress term is written as:

$$\tau_{ij} = 2\nu_t \tilde{S}_{ij}. \quad (2.36)$$

Now an expression for the turbulent viscosity has to be provided. Such a model can either be based on the resolved scales or on the subgrid scales. These models will be presented in the following subsections. Additionally, the models can be improved by evaluating the model constants dynamically. This procedure will be discussed in the last part of this section.

The Smagorinsky model

The classical eddy-viscosity model was proposed by Smagorinsky [144]. It assumes an equilibrium between turbulence production and its dissipation. Then, the turbulent viscosity is proportional to the subgrid-scale characteristic length scale Δ and to a characteristic subgrid-scale turbulent velocity $v_\Delta = \Delta|\tilde{S}|$ with $|\tilde{S}| = \sqrt{2\tilde{S}_{ij}\tilde{S}_{ij}}$, leading to:

$$\nu_t = (C_S \Delta)^2 |\tilde{S}| \quad (2.37)$$

with $C_S \approx 0.18$, Lilly [88]. However, in practice this constant is often adjusted to improve results, and thereby reducing the dissipation. This model is based on turbulence on the large scales. The advantage of this model is its simplicity. The Smagorinsky model is suitable for isotropic homogeneous turbulence. In case of a channel flow the model constant is generally adapted, e.g. to $C_S = 0.1$ in Deardorff [35]. However, due to the assumption of homogeneous turbulence the model fails close to the wall as it is too dissipative. The model clearly does not work for transitional flows in a boundary layer on a flat plate, starting with a laminar profile to which a small perturbation is added: the flow remains laminar, due to an excessive eddy viscosity coming from the mean shear, Germano *et al.* [53]. The turbulent viscosity is nonzero as soon as the velocity field exhibits spatial variations, even if it is laminar and all scales are resolved.

When a small value for C_S is introduced, this will result into a proper dissipation in the laminar regime, allowing turbulence to grow. But in the turbulent regimes the dissipation now turns out to be too low, as C_S is fixed to this low value, Vreman *et al.* [159].

The WALE model

The so-called Wall Adapting Local Eddy-viscosity (WALE) model as proposed by Nicoud and Ducros [103] is based on γ_{ij} , the traceless symmetric part of the square of the velocity gradient tensor. It is constructed such that it will detect turbulent structures with (large) strain rate, and/or rotation rate. When writing

$$a_{ij} = \frac{\partial \tilde{u}_i}{\partial x_j} \quad (2.38)$$

this tensor can be written as:

$$\gamma_{ij} = \frac{1}{2}a_{im}a_{mj} - \frac{1}{3}\delta_{ij}a_{kl}a_{kl}. \quad (2.39)$$

From this tensor the function G can be constructed:

$$G = \gamma_{ij}\gamma_{ij}. \quad (2.40)$$

This function, which is based on the second invariant of the gradient tensor, vanishes for pure shear flows, for instance close to walls. In this limiting case, where the distance to the wall $y \simeq 0$, G behaves like $O(y^2)$. However, a turbulent viscosity that would be based on this function directly does not show the correct behavior close to the walls, which should be $\nu_t = O(y^3)$. In order to let the function follow this behavior, the turbulent diffusion should be proportional to $G^{3/2}$. To match the dimensions $G^{3/2}$ is scaled to $(\tilde{S}_{ij}\tilde{S}_{ij})^{5/2}$. Notice that $(\tilde{S}_{ij}\tilde{S}_{ij})$ is $O(1)$ close to the walls. However, this ratio is not well conditioned numerically. Therefore, in the denominator the term $G^{5/4}$ is added. This term is negligible in the near-wall region. Concluding, the resulting model for the eddy-viscosity reads:

$$\nu_t = (C_w \Delta)^2 \frac{G^{3/2}}{(\tilde{S}_{ij}\tilde{S}_{ij})^{5/2} + G^{5/4}}. \quad (2.41)$$

The constant C_w is set to 0.5, based on results from homogeneous isotropic turbulence, Nicoud and Ducros [103].

A generalized analytical subgrid-scale model

Another version of this approach for a SGS model is proposed by Vreman [160]. Just like the WALE model this model needs only local filter information and first-order velocity derivatives. The eddy viscosity is based on the flow functional B :

$$B = b_{11}b_{22} - b_{12}^2 + b_{11}b_{33} - b_{13}^2 + b_{22}b_{33} - b_{23}^2, \quad (2.42)$$

$$b_{ij} = \Delta_m^2 a_{mi}a_{mj}. \quad (2.43)$$

Then, the subgrid dissipation reads

$$\nu_t = C_V \sqrt{\frac{B}{a_{ij}a_{ij}}}. \quad (2.44)$$

The subgrid dissipation is based on the flow functional B because this functional B vanishes for the same (inhomogeneous) flow types as the theoretical subgrid dissipation, like in transitional flow and laminar shear flow at near-wall regions. The tensor b is positive semidefinite, which implies $B \geq 0$. B is an invariant of the matrix b while $a_{ij}a_{ij}$ is an invariant of $a^T a$. Notice that $b = \Delta^2 \alpha^T \alpha$ in the case of identical filter width Δ_m in any direction. Thus, ν_t will reduce to zero in case of vanishing $a_{ij}a_{ij}$.

The constant is chosen $C_V = 0.081$, corresponding to $C_V \approx 2.5C_S^2$, with C_S its theoretical value of 0.18 for homogeneous isotropic turbulence. A lower value for this constant would represent a smaller filter size.

Subgrid kinetic energy models

Different models have been developed based on the application of a transport equation for the subgrid scale kinetic energy, e.g., Horiuti [51]. These are all of the form

$$\nu_t = C_m \Delta \sqrt{q_{sgs}^2}. \quad (2.45)$$

Assumptions have to be made when modeling of the subgrid scale kinetic energy equation, equation 2.32. The structure of this model is similar to RANS modeling, which makes it easy to incorporate these models into an existing RANS code. This model has been used by Sone and Menon [147] in the Kiva-3V code. The drawback of this model is that an extra transport equation needs to be solved, requiring additional computational efforts.

Dynamic subgrid-models

The Smagorinsky eddy viscosity model is able to represent the global, dissipative effects of the small scales in a satisfactory way in cases of homogeneous isotropic turbulence. However, in other cases of transitional flows, highly anisotropic flows and under-resolved flows this SGS model will behave far less than appropriate. Also any transfer to and from the small scales cannot be represented.

In order to overcome these problems without modifying the structure of the subgrid models strongly, dynamic models have been developed, Germano *et al.* [53]. In this approach the model coefficient is determined dynamically, and reacts locally on the flow, based on the energy content of the smallest resolved scale, rather than a priori input as in the standard Smagorinsky model. The coefficient is determined locally in space and time, depending on the local flow characteristics. The main notion of a dynamic adjustment of the model is the use of a test filter $\hat{\Delta}$ which is twice the grid filter width Δ . The total stress tensor \mathcal{T}_{ij} at the test filter $\hat{\Delta}$ can be written as:

$$\mathcal{T}_{ij} = \widehat{u_i u_j} - \hat{u}_i \hat{u}_j \quad (2.46)$$

and the subgrid-scale stresses τ_{ij} defined as in equation 2.18:

$$\tau_{ij} = \widetilde{u_i u_j} - \tilde{u}_i \tilde{u}_j. \quad (2.47)$$

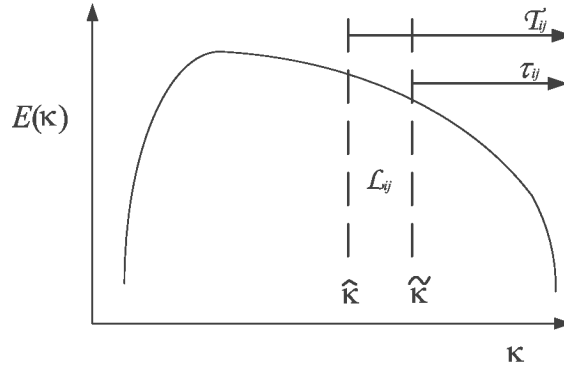


Figure 2.3 : A sketch of the dynamic procedure, showing the physical interpretation and relation of the filtered turbulent stress \mathcal{T}_{ij} , describing the $\hat{\kappa}$ test filtered scale turbulent stresses, to the subgrid-scale stresses τ_{ij} , describing the $\tilde{\kappa}$ subgrid scale turbulent stresses, and the resolved stress tensor \mathcal{L}_{ij}

Now, when subtracting both terms it follows that [53]

$$\mathcal{L}_{ij} = \mathcal{T}_{ij} - \hat{\tau}_{ij}, \quad (2.48)$$

where the resolved turbulent stress tensor \mathcal{L}_{ij} for the test filter $\hat{\Delta}$ can be written as:

$$\mathcal{L}_{ij} = \widehat{\tilde{u}_i \tilde{u}_j} - \hat{\tilde{u}}_i \hat{\tilde{u}}_j. \quad (2.49)$$

This is a remarkable result, which relates the resolved stresses to the filtered unresolved stresses. From equation 2.49 it can be seen that \mathcal{L}_{ij} is known. The subtraction in equation 2.48 can be interpreted as a kind of band-pass filter, see also figure 2.3. Physically this can be interpreted as follows: The tensor \mathcal{T}_{ij} that describes all stress terms at the filtered $\hat{\Delta}$ level is equal to the sum of the resolved turbulent stresses \mathcal{L}_{ij} and the subgrid tensor τ_{ij} , that is filtered at the $\hat{\Delta}$ level.

Now subgrid models for both stresses are introduced. The simplest approach is to apply the Smagorinsky model for both τ_{ij} and \mathcal{T}_{ij} :

$$\tau_{ij} - \frac{1}{3}\tau_{kk}\delta_{ij} = 2C\Delta^2|\tilde{S}|(\tilde{S}_{ij} - \frac{1}{3}\tilde{S}_{kk}\delta_{ij}) = 2Cm_{ij}^{sgs}, \quad (2.50)$$

$$\mathcal{T}_{ij} - \frac{1}{3}\mathcal{T}_{kk}\delta_{ij} = 2C\hat{\Delta}^2|\hat{\tilde{S}}|(\hat{\tilde{S}}_{ij} - \frac{1}{3}\hat{\tilde{S}}_{kk}\delta_{ij}) = 2Cm_{ij}^{test}. \quad (2.51)$$

From these equations a local, dynamic equation for C can be constructed, using equality 2.48. This system is overdetermined, as five independent equations are available for one model parameter C . Lilly [89] proposed to perform a minimization procedure in the least-squares sense. Then, writing

$$M_{ij} = \widehat{m_{ij}^{sgs}} - m_{ij}^{test} \quad (2.52)$$

it follows for the dynamic model coefficient:

$$C = \frac{M_{ij}\mathcal{L}_{ij}}{2M_{ij}M_{ij}}. \quad (2.53)$$

This parameter can show strong spatial and temporal variations. Some kind of averaging is necessary, otherwise unphysical fluctuations may occur that can lead to instability problems. Germano *et al.* [53] proposed an averaging procedure of the nominator and denominator over homogeneous directions. However, this method is clearly not applicable for flows in complex-geometries. It has been shown that by means of a temporal relaxation of the model parameter the stability is conserved, Wegner [163]. Also negative values of the model parameter can be encountered, which results in energy-backscattering. However, a physical argument that this effect is correctly accounted for in this way is questionable, as the model is in principle based on information on the resolved scales only. No information on the amount of kinetic energy in the subgrid scales is available.

Discussion: Which model to choose

In the previous section a short overview of available LES subgrid scale models was presented. By giving this overview it is not clear which model is preferred. The most complicated model is not automatically the best performing one. Some considerations may be helpful in order to make a sound decision. The Smagorinsky model is well known for its over-prediction of the turbulent stresses in regions where the turbulence is not homogeneous. Thus only for cases where the walls do not play any role this simple model may be sufficient. The problem of inhomogeneous turbulence is solved by applying a dynamic procedure. This method has been applied on relatively simple geometries, Germano *et al.* [53], as well as complex geometries, e.g. Wegner [163]. However, the filtering approach leads to difficulties in practical simulations, especially on (coarse) unstructured meshes, Nicoud and Ducros [103]. Moreover, one has to assure stability by an averaging procedure in space and/or time. These issues have driven the search for easier to implement, more stable, local SGS models, such as presented by Nicoud and Ducros [103] and Vreman [160].

In chapter 3 the proposed subgrid-scale models will be compared to each other for the applied solver. Then the choice of the subgrid-scale model to be used in the remaining simulations in this thesis will be motivated in more detail.

2.3.3 Near-wall modeling

LES is well applicable for flows that are far away from walls. The small scales are modelled, while the important, large scale energy-containing eddies are explicitly evaluated.

However, the length scale of the energy-carrying, large structures depends on the Reynolds number near the wall. As the energy-producing events, which scale with the Reynolds number, should be captured, the resolution of the boundary layer should be increased considerably. This means that the grid spacing Δ should be some fraction of the local inertial length scale, $\mathcal{L} = k^{3/2}/\varepsilon$. Normally, $\Delta/\mathcal{L} \approx 1/10$ is required for a good channel flow resolution, Bagget *et al.* [9]. Close to the wall, growth of the small scales is inhibited by the presence of the wall. Therefore \mathcal{L} scales directly with the distance from the wall. Secondly, the exchange mechanisms between the resolved and the unresolved scales are altered: in the near-wall re-

gion the subgrid scales may contain some significant Reynolds-stress producing events, which in general the standard subgrid-scale stresses cannot account for: the Reynolds stresses are interactions on the subgrid scales, which produce stress effects on the resolved scale. The mesh requirements to resolve these effects are computationally prohibitive. The ability of the previously presented subgrid scale models to properly account for the important physical effects near the walls is different. Piomelli [118] showed that the dynamic Smagorinsky model is in principle able to model the shear stresses, turbulence intensities and mean velocity profiles properly for high Reynolds number channel flow calculations. On the other hand, the Smagorinsky model was shown to fail dramatically due to its overprediction of the wall shear. The application of the WALE model on a coarse mesh was shown to over-predict the streamwise velocity magnitude, Temmerman *et al.* [153]. Improvements can be made by the application of a wall modeling method. This can be achieved by the application of a hybrid RANS-LES method. The general idea is to apply RANS methods for turbulence modeling at the near-wall regime, while the unsteady LES method is used inside the domain, where the inertial subrange is sufficiently resolved by the applied mesh, see e.g., Tessicini *et al.* [154] and de Langhe *et al.* [79, 80].

An alternative solution lies in the application of dedicated wall models. Overviews have been given by Cabot and Moin [27] and Schmidt *et al.* [141]. In wall models the first grid point is typically located in the logarithmic layer. Then the wall model should provide information on the wall stresses and the wall-normal velocity component at the first grid point.

2.3.4 Inflow conditions

In LES the presence of the large scale turbulent structures is of vital importance, as all statistics is based on these structures. A realistic time series of the velocity field at the inlet should be provided.

These inflow data should satisfy the Navier-Stokes equations, which in turn implies a separate simulation to produce this data. Effectively this means that the inflow boundary is shifted further upstream, and let all relevant fluctuations develop inside the computational domain. This is a good method in the case that uncertainties exist on the exact flow conditions at the inlet boundary, as will be discussed in chapter 3. However, this is a costly operation, which should be avoided if possible. Methods to solve this problem have been discussed by Lund *et al.* [90]. The first approximation would be to use a laminar profile with some random disturbances added. The natural transition to turbulence is then evaluated explicitly. However, simulating the transition in itself remains relatively costly. The amplitude of the random fluctuations can easily be set to satisfy the size of the velocity field variance. The problem lies in the mimicking of the phase relationships between the three-dimensional velocity fluctuations, Klein [73]. This is important for simulating a realistic turbulent structure.

Another approach is to extract the inflow boundary conditions from a dedicated auxiliary simulation. Even the crudest of these kind of simulations will in general be more accurate than the random fluctuation method. The advantage lies in the fact

that no costly development section is obligatory in the main simulation. The simplest auxiliary simulation approach is simulating a parallel flow in which periodic boundary conditions are imposed in both the streamwise and spanwise directions, while extracting some velocity field from it. Still, a complete separate flow simulations needs to be performed.

Another method, as adopted in this work, is to create artificial turbulence that is based on a prescribed mean flow as well as the Reynolds stress tensor. This turbulence is created by an appropriate filtering of random fluctuations using a Gaussian two-point correlation function. In this way instantaneous velocity fields that contain proper length scales can be reconstructed, see Klein [73]. This method will be adopted in some of the simulations.

2.4 Turbulence modeling for engine applications.

With the available models described globally, we need to focus on our particular application, i.e., turbulence and combustion modeling of in-cylinder engine flows. It is clear that direct injection (DI) Diesel and gasoline engines fluid dynamics play an important role in the process of fuel-air mixing and subsequent combustion.

It can be helpful, although artificial, to make a distinction between all processes that take place in the engine, and to study these processes separately. When doing so these aspects can then be analyzed in more detail. In the following subsection these processes are briefly introduced. After that, one can decide which solver is adequate to use.

2.4.1 The phenomenology of engine turbulence

Typical flow features in an engine cylinder are the swirling and tumbling motions, arising from the jet-like flow due to the intake ports. A schematic representation of a typical Diesel engine setup is given in figure 2.4. The valve movement (the opening of the valve, and the subsequent downward/upward movement) defines the timing of the air intake, the piston movement has a decompressing and compressing effect on the flow. A typical phenomenon as taking place in in-cylinder engine flows is referred to as squish, i.e. the final part of compression of the fluid flow, where the compressed gasses are strongly forced to move into the piston bowl.

Turbulent structures arise from the jet-like flow at the intake ports. The size of typical eddies will initially scale to the valve lift, about 0.01 m. After compression the length scale of the largest eddies relax to 0.1 m, proportional to the cylinder diameter. The velocity scale \mathcal{U} is about the velocity at the intake ports: up to 100 m/s.

Near top dead center, where the piston is close to its maximum height, the injected fuel sprays induce new turbulence in the cylinder. The fuel will mix with the air, and soon the combustion processes start. For Diesel engines this process can be considered globally as non-premixed combustion, but details like soot and NO_x production will strongly depend on local species concentrations, as well as local turbulence intensity. These engine processes can all be characterized in terms of

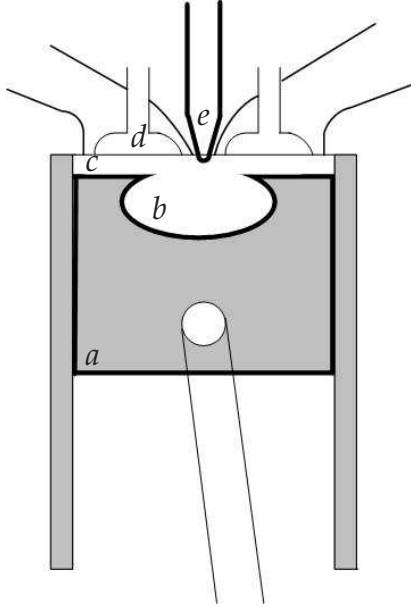


Figure 2.4 : Geometry of a direct injection combustion engine. (a) piston, (b) bowl, (c) region where squish takes place, (d) valves, (e) fuel injector.

average flow fields, turbulent structures, free shear turbulence, turbulence-wall interactions and additionally mixing and combustion processes that strongly interact with the turbulence.

2.4.2 Choice of the solver

In the previous section the most commonly used LES turbulence models have been described, which can be used for studying in-cylinder flow aspects. Also the typical features of in-cylinder flows that should be modelled are outlined. Now the question can be reformulated at another, higher level, namely in terms of CFD codes: which code is best fitted to solve this problem? The main issue concerns the complexity of the physical processes that one wishes to study. Generally there is a trade-off in complexity of the code and its accuracy and computational efficiency. For simplicity computational codes can be divided into three groups. The first kind are accurate solvers, dedicated to a special sub-process. This kind of solvers is generally maintained and developed mainly by single research departments. Dedicated LES solvers can be developed for simple geometries, for instance to test subgrid-scale models [92] or designed to model turbulent jet flames [121]. Results achieved with these types of codes are in this work used as a reference. The codes are generally fully open source and can be adapted completely on the source code level, to investigate the (detailed) process of study.

The second kind of solvers are the complex CFD solvers that are available on open source basis, mainly maintained by a larger scientific community. Examples of these kind of solvers are the Kiva family [5], [157], the FASTEST code [93], [163], and the AVBP code [8].

Thirdly, there are several general purpose commercial solvers usable for a relatively wide range of applications. In this case many physical models can be in-

cluded; the interaction of models can be studied in 'real' situations. However, the accuracy of all models is generally limited. Moreover, these commercial packages usually use a closed source code. Also the computational efficiency may be reduced in complex solvers, due to inefficient, but stable coding, for the sake of user-friendliness. Examples of this kind of solvers are Fluent/CFX [47], STAR-CD [148] and Fire [46]. The applicability of this type of codes has been investigated for engine simulations by Smits [146], where RANS type simulations have been presented using the Fluent code. Promising results have been presented on flow simulations using complex, moving geometries. This type of simulation can in the near future be extended towards a more complete simulation, by including the modeling of more processes that take place in an engine, and can be regarded optimal for parametric type of studies.

Based on above considerations two different computational codes have been selected throughout this thesis, which were best suited for the chosen object of study, namely the Kiva-3V code and the FASTEST code. In the next chapter the Kiva-code is used for the testing of the LES implementation in this type of codes. Also a comparison on the applicability of the solver with respect to realistic engine geometries will be presented for the Kiva-3V code and the FASTEST code. In the remaining chapters, the FASTEST code has been chosen, because of its favorable numerical and meshing features, as will be explained in the next chapter.

LES in confined flow geometries

In this chapter the application of the LES approach to the flow in a square duct and the flow in a realistic engine geometry is considered. Also the numerical method used in Kiva-3V is described with focus on the convection scheme. It is shown that the accuracy of the numerical scheme as well as the resolution have a crucial impact on the LES prediction of the flow in a square duct. Next, one URANS simulation and four Large-Eddy simulations of the turbulent flow in a cylinder, attached to a production-type heavy-duty Diesel engine head have been performed, with two different flow solvers. The results elucidate the multiple sensitivities of the turbulence prediction on the subgrid-scale model and the numerics.

3.1 Introduction

In internal-combustion engines the level of turbulence plays an important role in the optimization of the efficiency. Turbulence will be highly anisotropic, due to swirling and tumbling motions. Recently, several approaches and many different turbulence models have been developed to account for the turbulence effects in practical flows. The starting point in the numerical turbulence modeling originates from the classical RANS $k - \epsilon$ model, as has been discussed in section 2.2.1.

Stimulated by the large increase in computational resources and the development of new CFD codes, the Large-Eddy Simulation (LES) has come within reach for the use of more practical applications. As has been discussed in section 2.2.2 only turbulence on the smallest scales is modeled. Especially for the modeling of combustion the application of an LES approach in the inner part of the cylinder is preferable. The formation of pollutants like soot takes place under globally inhomogeneous conditions. Additionally, the instantaneous chemical source terms are very sensitive to the local concentrations. RANS type of methods, where the turbulence is averaged out are not suitable to give this type of information. LES can be more preferable in this sense. The LES approach has been shown to be successful on a broad range of generic cases. An early overview of an LES approach for engine applications has been given by Celik *et al.* [29], whereas Haworth and Jansen [60]

presented computations on a simplified piston-cylinder assembly. However, theoretical considerations make the use of the LES approach in practical applications questionable.

Therefore in this chapter two types of simulations are performed. The first series concerns a square duct flow, using the engine code Kiva-3V. This code has been adapted in this thesis project for Large-Eddy simulations. Despite of the simple geometry of the duct, the fluid dynamics already shows some complex features. Moreover, contrary to typical engine geometries for such a geometry a well established amount of numerical and experimental data exists, so that a detailed comparison, analysis and validation is possible.

In the second part of this chapter a complex swirling and tumbling flow in a production-type heavy-duty Diesel engine head is simulated. The predictive quality of two CFD codes is compared to each other and to experimental data for this flow setup.

Kiva-3V

The Kiva code series is developed at the Los Alamos National Laboratory. It is primarily written for simulating flows in reciprocating internal-combustion engines. From a relatively simple two dimensional compressible flow simulator with fuel sprays and combustion, it has been developed in the last twenty years to a three-dimensional, time-dependent solver, including the modeling of chemically reactive flows, Reitz and Rutland [132].

In the latest version released in 2006, Torres and Trujillo [157], Kiva-4 can handle unstructured, body fitted grids. The Kiva-family has long been available for use in the engine community, which resulted in many engine studies (e.g. Barths *et al.* [16], Celik *et al.* [28]), and the testing and development of new models, applicable for engine simulations (e.g. Tao *et al.* [152]).

Concerning the turbulence modeling, Kiva-3V has been developed for RANS simulations of in-cylinder engine flow and combustion problems. However, as has been described in the previous chapter, RANS turbulence modeling often leads to an over-simplification of the fluid flow in internal combustion engines. The assumption of isotropy, as is used in the two-equation $k - \varepsilon$ model, does not generally hold. Therefore in this work the code is extended for the use of Large-Eddy simulations of the turbulent flow. Previous studies on LES with Kiva-3V have been reported in literature. Sone *et al.* [147] presented results using a subgrid-scale turbulent kinetic energy model. However, the filter size remains relatively large. Celik *et al.* [28] has presented LES results in the Kiva-3V environment, using a Smagorinsky type of model. The fluid flow in a compressed cylinder has been computed. However, some effects have not been fully cleared by the previously mentioned authors.

The modeling of the fluid dynamics in Kiva that needs investigation concerns the influence of the accuracy of the applied numerical scheme, the influence of the resolution and the impact of the subgrid-scale (SGS) model.

Problems of LES in Kiva-3V

The issue of the accuracy arises from the fact that engine codes like Kiva-3V, that are primarily written for modeling multiphase reacting flows in complex geometries, generally use lower order finite volume schemes. When applying directly the LES approach, by replacing the RANS turbulent viscosity with the LES counterpart, the numerical diffusion caused by the truncation error can be of the same order of magnitude as the turbulent viscosity, especially in the case of upwind-biased schemes, Mittal and Moin [95]. Therefore the numerical scheme influences the effective filter size, Geurts [54]. Moreover, in the inertial subrange the turbulent kinetic energy cascades within scales that are of the same order of magnitude. Thus, the subgrid model should be based on the lowest resolved turbulent scales. For any correct turbulence model this implies that these scales need to be evaluated correctly, i.e. the numerical dissipation should be much smaller than the modelled subgrid-scale dissipation, such that the modeling part is dominant, see e.g. Piomelli [119].

The question regarding the resolution is posed because for any quantitative LES care needs to be taken that all scales up to the inertial subrange are sufficiently resolved. But the isotropic turbulence in the near-wall region is restricted to very small scales. This requires a very fine mesh with adapted meshing strategies, and additionally large computational resources, see e.g. Sagaut [139] or Pope [128]. Yet, for practical applications this is not achievable, the computational demands are simply not affordable. The question that remains here is which impact an under-resolved boundary layer will have on the overall flow structure.

Also the impact of the SGS model is critical in regions close to walls where turbulence is inhomogeneous and shear plays a dominant role. In transition regions the flow is very sensitive to the presence of SGS dissipation. In this work the Smagorinsky model, that is based on the assumption of homogeneous turbulence at the subgrid-scales, is compared to the WALE and Vreman models, which take inhomogeneous SGS turbulence into account. Also a dynamic model is tested. Finally, the turbulence model is switched off, to assess the impact of the applied numerical scheme.

LES for engine simulations

An additional problem related to engine simulations concerns the inflow boundary condition. As mentioned in section 2.3.4 Lund *et al.* [90] showed that in case of using non-physical inflow boundary conditions, such as a constant velocity inflow or random fluctuations, a long development region is required to reproduce the correct mean and turbulence statistics. Also the initial conditions for LES in more engine-like simulations are shown to significantly influence the flow characteristics, Devesa [39].

In figure 2.4 a schematic picture of a typical Diesel engine near top dead center has been illustrated. In a running engine with a moving piston the fluid flow is compressed at the intake stroke. In the final phase, the squish, the fluid flow is strongly forced to move towards the center of the cylinder, into the piston bowl. RANS results presented by Payri *et al.* [112] indicate a very strong impact of the squish on the turbulence intensity of the flow field. The squish produces twice as

much energy as remained from the tumble breakdown during compression. This indicates that not much of the preceding flow statistics remains after the squish. The average flow patterns in these RANS simulations close to the injection phase differ from one another, mainly due to different piston bowl geometries. But the resulting flow from the squish is not generally circle-symmetrical in all cases, especially not in cases of larger bowls. Then it is remarked that some of the initial flow features survive, Payri [112] *et al.* In an LES setting Toledo *et al.* [156] shows fairly different flow statistics of a tumbling flow after compression due to differences in the initial conditions. This can be associated to a precessing vortex core, which is one of the origins of cycle-to-cycle variations. This gives arguments that the impact of the inlet stroke on the compression and ensuing combustion process cannot fully be neglected. The squish will strongly interfere with the remaining global swirling flow, and also with the remaining turbulence. But while this generated turbulence intensity itself will be very high on a global level, its character can be fairly different from one case to the next, due to the initial conditions at the intake stroke.

The questions that are raised by the considerations mentioned above can now be formulated: What is the impact of the applied resolution, the accuracy of the scheme and the subgrid scale model, as investigated in detail on the square duct geometry, on the predictiveness of the LES method in a practical engine geometry? What is the impact of the inflow conditions in the LES approach on the resulting flow phenomena? Also the differences between the RANS and LES methods will be elucidated. The location and magnitude of the global swirling and tumbling motions as well as the modelled turbulence intensities are considered for both turbulence approaches.

This chapter

To cover all these issues from going from theory to a practical simulation, this chapter has the following structure. In the next section the numerical procedure as employed in the Kiva-3V code will be outlined briefly. Special emphasis is put on the convection scheme as this is of key importance when performing Large-Eddy simulations.

In section 3.3 square duct simulations are presented on two mesh types, to investigate the impact of the resolution on the results. This information is necessary, as for typical engine calculations relatively coarse meshes are used. The different turbulence models are also compared to each other on this setup.

In order to investigate the questions concerning a practical engine simulation the flow in a steady state engine geometry is studied subsequently. For the numerical part two CFD codes have been used: Kiva-3V, and FASTEST-3D, see, e.g., Mergler [93]. With Kiva-3V a URANS $k-\varepsilon$ simulation and two coarse Large-Eddy simulations have been performed. With FASTEST two Large-Eddy simulations, with different grid resolutions have been conducted, one on a relatively coarse mesh, comparable to the mesh in Kiva-3V, and one where the resolution has been approximately doubled. Results are compared to PIV experiments performed by de Leeuw [83]. In section 3.4 the modeling and the numerical procedures for the engine flow simulations are briefly described, followed by a discussion of the results. Finally conclusions are drawn in section 3.5.

3.2 The numerical methods

In this section first the numerical algorithm of Kiva-3V with respect to the fluid flow is briefly described. For a complete overview of all models available in Kiva-3V and for its conversion into the numerical schemes, the reader is referred to Amsden [5]. In the final part the FASTEST-3D code is briefly introduced.

3.2.1 Kiva-3V

The governing equations for the fluid dynamics are as listed in section 2.1. In the standard version of Kiva-3V the Reynolds averaging procedure is applied to these equations, leading to the RANS set of equations 2.14-2.16. Also the transport of chemical species as well as separate transport equations for droplets can be solved. The governing equations in Kiva3-V are adapted to include these effects. For instance, the conservation of mass in the Kiva-3V environment is given by

$$\frac{\partial \bar{\rho}}{\partial t} + \frac{\partial (\bar{\rho} \tilde{u}_j)}{\partial x_j} = \dot{\bar{\rho}}^s \quad (3.1)$$

where $\dot{\bar{\rho}}^s = \sum_m \dot{\bar{\rho}}_m^s$ denotes the total mass source due to spray evaporation, where the summation runs over all species concentrations. In this chapter the internal energy remains constant as no chemical reactions, compression or expansion have been simulated. Therefore its description is omitted here. In the original version of Kiva-3V equations for the turbulent kinetic energy and the turbulent dissipation are solved, according to equations 2.23 and 2.24.

The Kiva-3V code has been adapted for the LES approach. One major change concerns the implementation of different LES subgrid-scale models: the Smagorinsky, WALE, Vreman and dynamic Smagorinsky SGS models, equations 2.37, 2.41, 2.44 and 2.50, respectively. Thus, the equations that describe the average flow properties in Kiva-3V are now used to evaluate the filtered quantities. But an important difference is that the LES filtering requires a higher accuracy of the numerical implementation of these equations. The numerical scheme will be described below, with special attention to the adaptations that have been developed in this thesis.

The equations that describe the fluid dynamics are discretised and implemented into a Fortran 77 code. In Kiva-3V the finite-volume concept is adopted. This means that the flow domain is divided into sub-domains; these are the computational cells, also referred to as finite volumes. These volumes are arbitrary hexahedrons, such that curved geometries can be meshed. For every computational cell in the domain the conservation equations are solved.

Kiva-3V is based on the so-called *Arbitrary Lagrangian-Eulerian* (ALE) method. This method is chosen because the computational cells can move in an arbitrarily prescribed manner, thereby in principle allowing a Lagrangian, Eulerian or mixed evolution of the mesh. In this method the mesh is in principle able to move and follow the changes in the combustion chamber geometry, due to the movement of the valves and the piston.

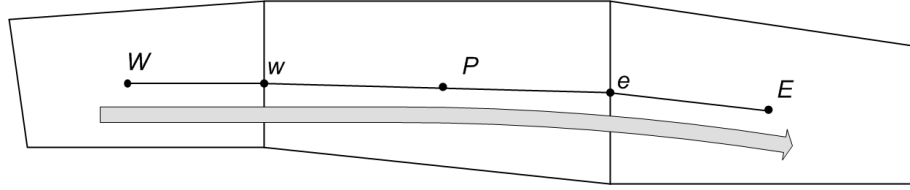


Figure 3.1 : Two dimensional representation of the grid arrangement for the convective scheme in the Kiva-3V code. The arrow denotes the local flow direction.

Temporal discretization

In the ALE method of Kiva-3V three phases can be distinguished. In the first phase, *Phase A*, the new properties with respect to the spray are evaluated. Also the source terms of mass and energy due to the chemistry and the spray are updated. In the second phase, *Phase B*, the Lagrangian evaluation of all conservation equations is performed. With respect to the momentum equation the new velocity field due to viscous, pressure and external forcing effects is computed. The solution for the velocity field at the end of Phase B is found by performing a predictor-corrector procedure which is based on the method described by the Semi-Implicit Pressure Linked Equations, or SIMPLE method, Patankar [111]. This phase can be performed implicit, semi-implicit or explicit, based on considerations of both stability and efficiency. The solution of the implicit conservation equations is obtained using a Conjugate Residual Method. Also the new Lagrangian locations of the computational cells are evaluated. The temporal discretization of all governing equations is written in terms of first order accuracy.

In the last phase, *Phase C*, convection is evaluated. Here all cells are mapped back onto a predefined Eulerian grid arrangement. This phase is evaluated explicitly and can be divided in sub-cycles. In this thesis only geometrically stationary problems have been considered, which means that the new mesh locations coincide with the old ones. This stage is evaluated explicitly, using a convective time step Δt_c that is the same or smaller than the total time step of the complete cycle, based on the Courant criterion $u_r \Delta t_c / \Delta x$ with u_r the fluid velocity relative to the grid and Δx the grid size. In the original Kiva-3V description the so-called Quasi Second Order Upwind Scheme (QSOU) is provided, which is formally first order, but second order in cases of smooth scalar fields.

In Kiva-3V the global error of the spatial discretization ranges from first to second order, depending on the grid used and the smoothness of the fields to be transported. It is worth to spend extra attention on the convection step in the numerical scheme, as this part is vital for any proper LES.

3.2.2 The convective scheme

In the convective step, contrary to the diffusion step, the transported scalar fields are not smoothed out. Therefore any errors due to the discretization will either result in smoothing (mixing) or in some kind of un-mixing. The smoothing is favorable for the stability of the code, but it will mask details of the fluid flow at the resolved level. On the other hand the un-mixing will cause a destabilization of the code. In

the convective phase the values of the scalar quantities ϕ (mass, momentum, species concentrations) at the cell boundaries are essentially required, Amsden [5]. These values are interpolated in the following way:

$$\phi_e = \phi_P + \frac{x_e - x_P}{x_P - x_W} \Psi(r) (\phi_P - \phi_W). \quad (3.2)$$

Here the subscripts e , E and W denote the cells relative to the center cell P , see figure 3.1. Cell P is always located in the upwind direction of the local flow. In this equation the limiter function Ψ is introduced. This function comes from a Total Variation Diminishing (TVD) procedure, that is introduced in the search for stable, but at the same time higher order schemes, see e.g. Hirsch [62]. For a first order upwind scheme it can easily be seen that $\Psi(r) = 1$.

The motivation for using TVD schemes lies in their stability, which is important for simulations where destabilizing effects, such as highly curved meshes in combination with high velocity gradients may appear. Standard second order schemes, such as the second order upwind or central scheme may cause serious stability problems. The use of upwind schemes is necessary to keep the algorithm stable. However, lower order upwind schemes decrease the accuracy of the solver, and are thereby directly adding a numerical filter over the turbulent fluctuations. Thus it is of importance to reduce the level of upwinding as much as possible, but at the same time keeping the algorithm bounded. For this goal TVD schemes are designed. In Kiva-3V a so called Quasi Second Order Upwind (QSOU) differencing scheme is used. This can be qualified with the limiter function

$$\Psi(r) = \max(0, \min(r, 1)), \quad (3.3)$$

where r is the ratio of the central- and the upwind gradient:

$$r = \left(\frac{\phi_E - \phi_P}{x_E - x_P} \right) / \left(\frac{\phi_P - \phi_W}{x_P - x_W} \right). \quad (3.4)$$

Notice, that for $\Psi(r) = r$ the interpolation scheme would be a second order accurate central scheme. The QSOU scheme can also be referred to as the minmod scheme, which is second order at locations where gradients remain small. The flux limiter function Ψ for the minmod scheme is the lower line in figure 3.2a: For $r < 1$ the fully second order central scheme is used, whereas for $r > 1$, i.e. large gradients of $\Phi_E - \Phi_P$, the first order upwind scheme is fully retained.

By replacing the limiter function with a less dissipative scheme we can reduce the impact of the algorithm on the numerical filtering. In this work with the Kiva-3V code the MUSCL scheme is applied. This limiter can be written as

$$\Psi(r) = \max(0, \min(2, \frac{3}{4}r + \frac{1}{4}, 2r)) \quad (3.5)$$

and follows a more curved line in the $\Psi(r)$ space. In the flame simulations in the FASTEST-3D code, as will be presented in chapter 5, it appeared the most useful to apply the so called Charm limiter function [163]. This is a smooth limiter function:

$$\Psi(r) = \max \left(0, r \frac{3r + 1}{(r + 1)^2} \right). \quad (3.6)$$

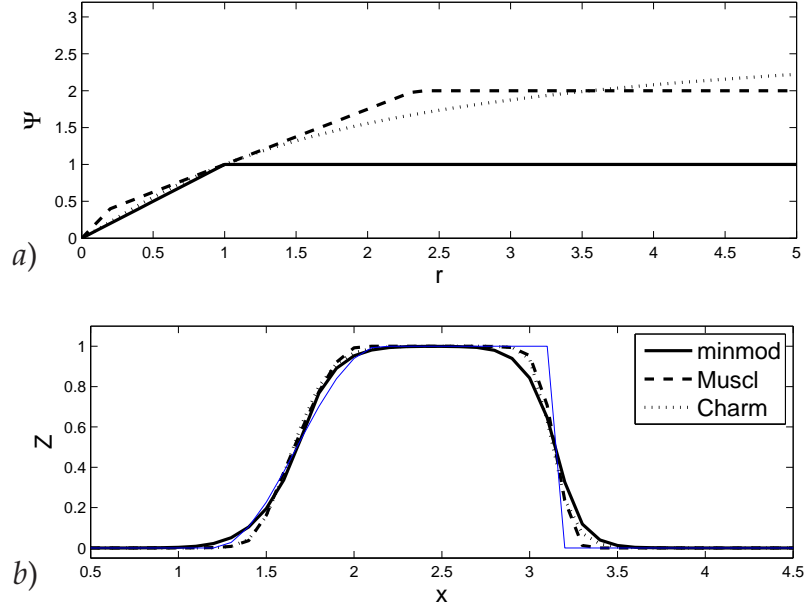


Figure 3.2 : (a) different flux limiter functions Ψ as a function of gradient ratio r . Thick solid lines: the Minmod scheme. (---): MUSCL scheme. (···): Charm scheme. (b) Convection of a one-dimensional sine wave (left-side) and step function (right-side). cfl: 0.2, 60 timesteps. Thin solid line: the analytical solution.

With the MUSCL and Charm limiter functions some contributions to the value of ϕ_e are enhanced, for locations in the flow where the gradients are relatively weak. At the same time the local maxima will be slightly flattened, while the gradients are made more steep. This effect can be seen in figure 3.2b. Here the convection of a one-dimensional sine-wave (at the left side) and a step function (at the right side) is evaluated using three different schemes. This is compared to the analytical solution of the convected shape, that is denoted by the thin solid line. Both the MUSCL and Charm limiters are better capable to track the step function, at the right side of the figure, whereas they tend to steepen the gradients in the smoother region, at the left side.

This indicates that the diffusive components of the MUSCL and Charm convective schemes are reduced compared to the QSOU scheme. Notwithstanding this improvement, numerical dissipation cannot fully be neglected, as has been discussed by Garnier *et al.* [50].

3.2.3 FASTEST-3D

In FASTEST-3D the governing equations are discretized using the finite-volume method. The code features block-structured, boundary-fitted grids. Second-order central schemes taking into account the grid non-orthogonality by means of multilinear interpolation (Lehnhäuser and M. Schäfer [84]) are used for spatial discretization. Pressure-velocity coupling is achieved via a SIMPLE procedure. As time integration scheme the second-order implicit Crank-Nicolson method is used. The code is parallelized based on domain decomposition using the *MPI* message passing li-

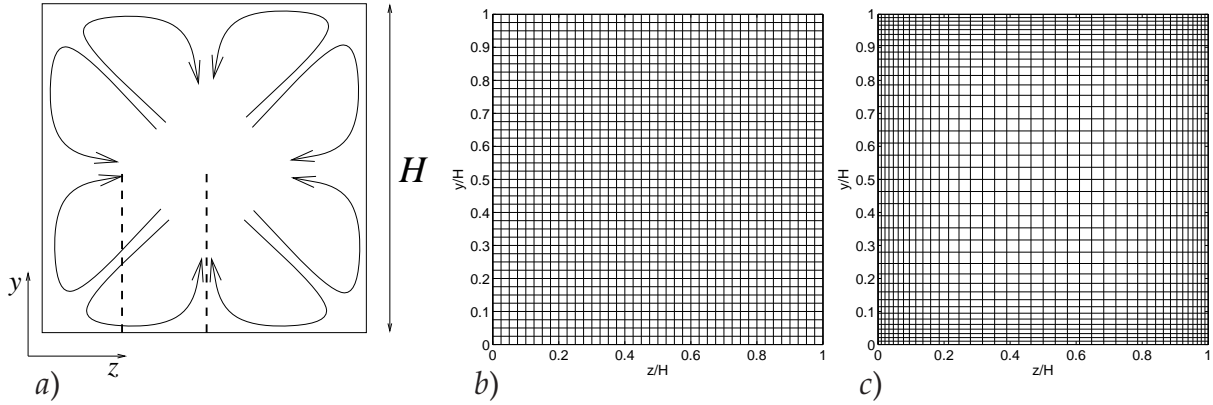


Figure 3.3 : Geometry and orientation of the square duct. y and z denote the spanwise flow directions. The dashed lines denote the locations where statistics is presented: $z = 0.25H$ and $z = 0.5H$, the arrows show the average, spanwise flow direction. (b) Illustration of the coarse mesh (c) refined mesh.

brary. For details on the method we refer to Mengler [93], Durst and Schäfer [42] or Wegner [163]. More details on the numerical method as used in FASTEST are outlined in appendix A.

The dynamic formulation is employed for the subgrid scale stress-tensor τ_{ij} , with Lilly's formulation of Germano's dynamic procedure for the determination of the model coefficient, Lilly [89]. No special wall treatment is used. Instead, the boundary layer is resolved and the dynamic procedure should be able to capture the correct asymptotic behavior of the SGS model when approaching the wall, Lesieur and Metais [86].

3.3 Square duct simulations

For validation of the LES turbulence models numerical simulations of a turbulent flow in a square duct geometry with periodic boundary conditions for the streamwise direction have been performed. This geometry is chosen for its simplicity. Yet, the fluid dynamics shows complex structures. This is a reflection of the anisotropy of the shear stress tensor. A characteristic of flow in square ducts is that it is accompanied by turbulence driven secondary motions perpendicular to the streamwise direction, figure 3.3. Although the magnitude of these motions may be as little as 2% of the bulk velocity, they have an important effect on the overall flow structure. It is well known that simple RANS models such as the available $k - \varepsilon$ model do not reveal any secondary flow.

Prediction of turbulence properties in regions of the flow domain where these secondary fluid motions occur are a test case for the LES method, as implemented in the Kiva-code. Furthermore, this geometry is well suited to study the turbulence behavior and the predicted shear of the different models close to walls, which is of basic importance for confined situations, like internal combustion engines. Finally, for this situation well established literature results are available: numerical as well as experimental [30, 37, 52, 57, 66, 92, 108]. Boundary layer flows are typically classified using the friction velocity u_τ . This velocity scale results from an applied force,

counteracting the shear at the walls. For square ducts this friction velocity scale reads

$$u_\tau^2 = -\frac{1}{4} \frac{1}{\rho} \frac{\partial p}{\partial x} = \frac{1}{4} H g_x, \quad (3.7)$$

with H the hydraulic diameter of the duct. As can be seen from this equation the forcing of the flow can be of the form of a pressure gradient $\frac{\partial p}{\partial x}$ or a body force (i.e. gravity g_x) in streamwise direction. In this work a body force is applied.

To assess our LES implementation in the Kiva-3V code, results are compared to numerical solutions that have been achieved in a DNS study performed by Gavrilakis [52] and an LES study by Madabhushi [92]. In the work of Gavrilakis a detailed DNS study at $\text{Re}_\tau = 300$ is presented, with $\text{Re}_\tau = \frac{u_\tau H}{\nu}$. The grid resolution in the DNS ranges from $\Delta y^+ = 0.45$ close to the walls towards $\Delta y^+ = 4.6$ at the center, and in streamwise direction a distance of $\Delta x^+ = 9.4$, with $1000 \times 127 \times 127$ cells in the three directions, with $\Delta x^+ = \Delta x \frac{u_*}{\nu}$. Now, u_* is defined as the actual shear stress velocity at the walls, which is defined as

$$u_*^2 = \nu \left. \frac{\partial u}{\partial y} \right|_{y=0}. \quad (3.8)$$

Madabhushi performed an LES study at $\text{Re}_\tau = 360$, with 64 cells in both spanwise directions and 32 cells in streamwise direction. This was performed with a code that was second order accurate in space and time. The streamwise direction has been evaluated in spectral space. The first grid point in spanwise direction was located at $\Delta y^+ = 2.0$.

In the present work four subgrid-scale models have been tested: the Smagorinsky, WALE, Vreman and dynamic Smagorinsky models. Simulations with these models are compared to each other and to a reference case without a subgrid-scale model, the so-called 'no-model' case. Additionally one simulation is performed using the QSOU limiter function to test the improvements using the MUSCL scheme. This scheme has been used in all remaining simulations.

3.3.1 The numerical setup

To test the impact of the grid resolution the simulations are performed on two different meshes, both consisting of $x, y, z = 60 \times 40 \times 40$, figure 3.3b,c. In the first mesh the computational cells are equally distributed, and the first gridpoint from the wall is located at $\Delta y^+ = 8.8$ in wall units, which is relatively coarse. Here the spanwise gridspacing in wall units was equal: $\Delta z^+ = 8.8$, while in the streamwise direction this is $\Delta x^+ = 36$. In the second mesh the grid is refined towards the walls. Here the first gridpoint is at $\Delta y^+ = 3.5$. The two meshes are referred to as 'C' and 'F' respectively.

The aspect ratio is taken $L/H = 6.2$, with H the height and L the length of the domain. This is identical to the geometry used in studies by e.g. Madabhushi *et al.* [92] and Huser *et al.* [66]. These dimensions were found to be sufficient, as can be verified by the correlation lengths, as shown in figure 3.4. This figure displays the

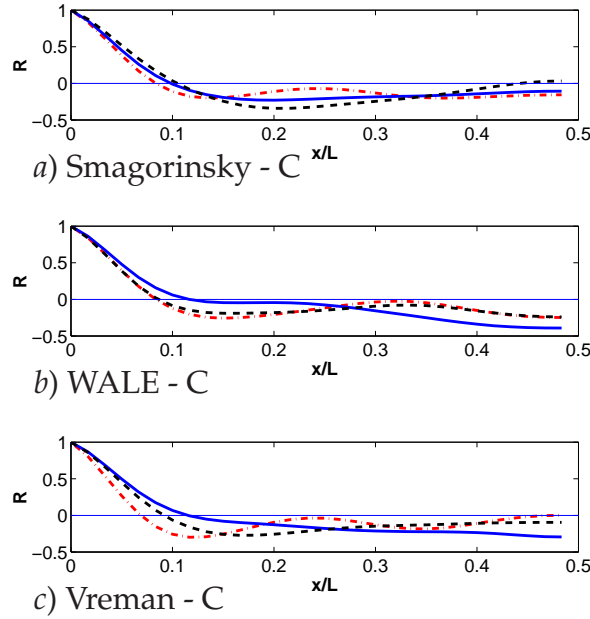


Figure 3.4 : (a,b,c) Correlations of the three components of the velocity field at the centerline of the duct. (—) : R_{uu} , (---) : R_{vv} , (- · -) : R_{ww} .

correlation R_{uu} , R_{vv} and R_{ww} of the three velocity components along the duct centerline, representing the distance at which turbulent structures remain correlated:

$$R_{uu}(x) = \langle \tilde{u}''(x') \tilde{u}''(x' - x) \rangle, \quad (3.9)$$

where $\tilde{u}''(x) = \langle \tilde{u}(x) \rangle - \tilde{u}(x)$, and the brackets denoting the averaging procedure over space and time. The correlation in the velocity field decreases well in the first region, $x/L \leq 0.1$. At larger distances the correlation remains non-zero in all simulation cases. To reduce the correlation a longer duct length is necessary. However, due to computational costs this was not feasible. Moreover, it is assumed that the correlation is sufficiently low for the study that is performed here, as other effects will have a larger impact on the flow statistics. The Mach number was set to $Ma = 0.05$, so compressibility effects can be neglected.

In all three simulations the flow was driven by an identical, constant body force g . This replaces the pressure gradient (see equation 3.7). The forcing was set to match to a Reynolds number of $Re_\tau = 360$. For this Reynolds number Madabhushi [92] found a bulk Reynolds number $Re_b = \frac{U_b H}{\nu} = 5810$, where the bulk velocity scale U_b is the mean streamwise velocity, based on the total flow area. The initial conditions of the flow field are defined as a parabolic streamwise velocity profile with random, divergence free velocity fluctuations added. These fluctuations are of the order of 5 % of the local streamwise velocity, the spatial size of the fluctuations is correlated to the grid size: the smallest structures are of the order of five computational cells.

Convergence is defined as the steady state where the mean velocity and amplitude and frequency of the fluctuating field do not change. This is reached when the flow has passed approximately 10 duct lengths. This took approximately 200 hours on a 2 GHz single CPU computing facility for both meshes. Another 200 hours of computational time was required to achieve converged statistics. The statistics are

Table 3.1 : Mean flow quantities Re_* and Re_b , based on the effective shear velocity u_* and bulk velocity U_b respectively, and the ratio of the centerline velocity U_c over the bulk velocity. 'C' refers to the coarse resolution, 'F' to the refined mesh.

Case	Re_*	Re_b	U_c/U_b
Smagorinsky - C	244	6080	1.35
WALE - C	317	7880	1.21
Vreman - C	332	7725	1.22
Vreman - C - QSOU	330	8995	1.25
dynamic - C	311	7813	1.22
<i>no model</i> - C	339	7665	1.20
Smagorinsky - F	257	5800	1.43
WALE - F	318	7550	1.28
Vreman - F	324	7220	1.29
<i>no model</i> - F	347	7490	1.29
Gavrilakis [52]	300	4410	1.33
Madabhushi [92]	360	5810	1.28

evaluated based on two data planes perpendicular to the streamwise velocity field, $0.5L$ apart from each other. The data was collected from $t = 110 t_*$ to $180 t_*$, with $t_* = L/U_b$. The data is averaged over the four corners, as they are statistically identical.

3.3.2 Results

The results of the simulations are analyzed on three different levels: the bulk flow quantities, the mean flow characteristics and the turbulent statistics.

Bulk flow quantities

In Table 3.1 the results of the bulk quantities for the different simulations are presented. For every simulation a new Re_b and Re_* was evaluated, defined using the local shear stress velocity u_* at the mid-wall location ($z = 0.5H$) of the duct. The results all show a discrepancy with the work of Madabhushi and Gavrilakis: whereas Re_* is relatively low, Re_b exceeds the values found in literature. This indicates that u_* is underestimated in all simulations. Also notice that the simulations performed with the Smagorinsky model show substantially smaller Reynolds numbers than all other models, including the *no model* variant. The Vreman-QSOU model results in a larger bulk Reynolds number than the MUSCL variant. When comparing the coarse mesh simulations with the simulations with refinement, Re_τ increases, while Re_b decreases.

A reason for the high values of Re_b is the low resolution. This results in an inability to resolve steep mean gradients, which are encountered close to the walls. Moreover, the turbulent structures cannot properly be resolved. Then the flow will laminarize and the bulk throughput increases, leading to an increase of Re_b . It can

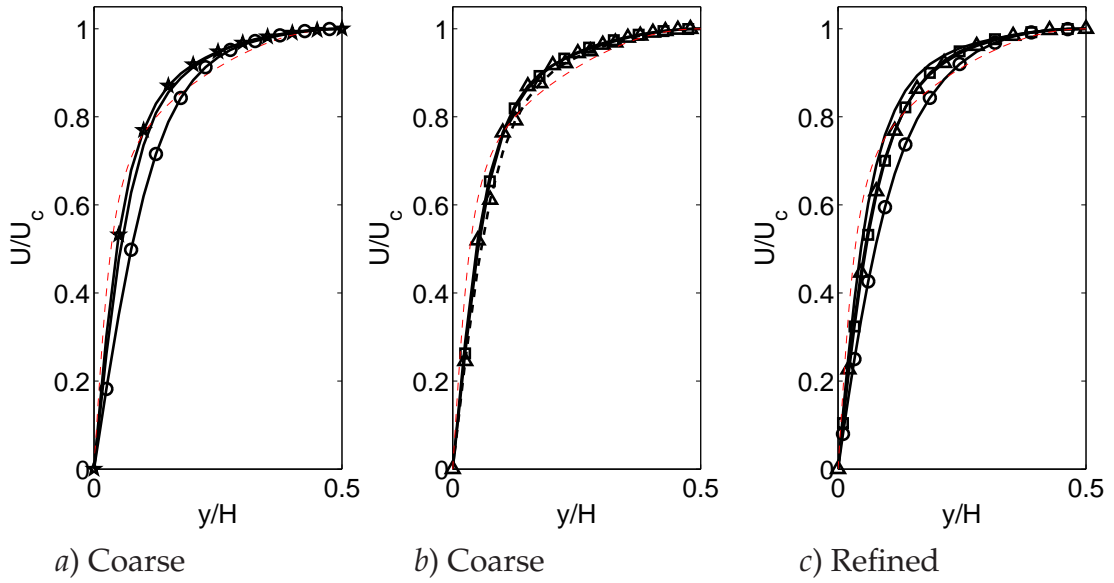


Figure 3.5 : Streamwise velocity field at $z = 0.5H$ for the coarse and refined mesh simulations. Reference data: Gavrilakis [52] (---). For clearness the coarse mesh results are presented in two figures. (a) The models are \circ Smagorinsky; \star dynamic model; (—) no model; (b) \square WALE; \triangle Vreman model; (- - \triangle - -) Vreman - QSOU.

be seen that with increasing wall resolution these effects decrease. The steep gradients are better resolved and additionally more turbulent structures can grow in the boundary layer. For the remainder of this study the velocity-scale U_b is considered more appropriate for scaling the velocity, instead of the shear velocity u_τ , as the wall layer is not fully resolved. Also notice that the simulations including a subgrid scale model and the no-model variants lead to very similar results (except for the Smagorinsky model), indicating that the subgrid scale model is not very active. Other effects, as described above, are more crucial.

The ratio of the centerline velocity to the bulk velocity U_c/U_b is clearly the largest for the Smagorinsky model, while all other models give similar low values around 1.21 for the coarse mesh simulations and about 1.3 for the mesh with refinement. The Smagorinsky model is known to over-predict the turbulent dissipation in the shear flow close to the walls. With increasing Reynolds number the profiles of the streamwise velocity should become flatter and gradients in the wall region steeper, which leads to a decrease in the ratio U_c/U_b . In case of the Smagorinsky model both Reynolds numbers decrease, due its large dissipation near the walls. This effect is well visible in figure 3.5a,c.

Mean flow profiles

The mean streamwise profiles are shown in figure 3.5. The velocities are in this case scaled to the centerline velocity U_c , to focus on the shape of the profiles. All models follow the reference profile reasonably accurately, except for the Smagorinsky model, as discussed above.

The spanwise flow field is compared to the results obtained by Gavrilakis [52], as shown in figure 3.6a. Three representative cases are shown in figure 3.6: Smagorin-

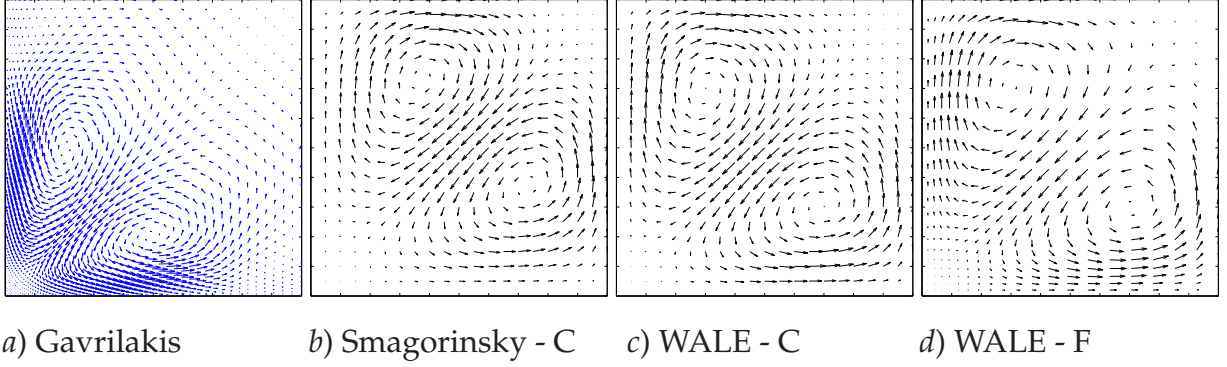


Figure 3.6 : Spanwise velocity fields from the reference simulation Gavrilakis [52] and three representative simulations. The figure of the quadrant is constructed by mirroring the diagonal.

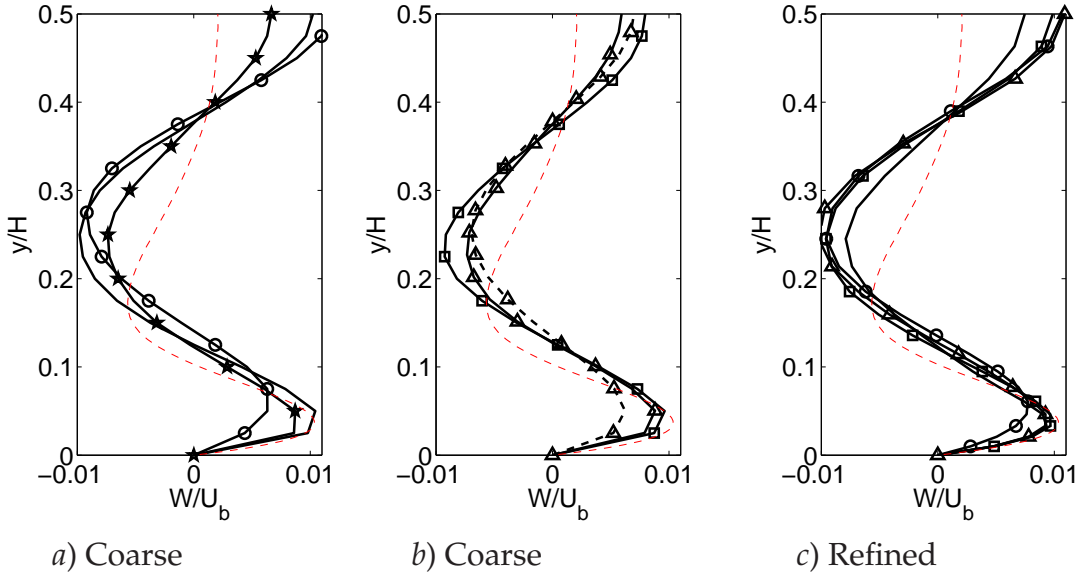


Figure 3.7 : Spanwise velocity profiles at $z = 0.25H$ for the coarse and refined mesh simulations. Reference data: Gavrilakis [52] (---). (a) The models are \circ Smagorinsky; \star dynamic model; (—) no model; (b) \square WALE; \triangle Vreman model; (- - \triangle - -) Vreman - QSOU.

sky - C, WALE - C and WALE - F. These simulations all show clearly the secondary flow. The simulation results show qualitatively the same features, relatively independent of the model. On the other hand, the DNS results [52] shows a recirculation area that is located more towards the corner, compared to our simulations.

Figure 3.7 shows the strength of the secondary flow at $z = 0.25H$, see figure 3.3. For the coarse mesh simulations the WALE, Vreman and the dynamic model, as well as the *no model* variant are the most capable of representing the secondary flow close to the wall, contrary to the Smagorinsky model. The Vreman-QSOU simulation shows a smaller contribution to the secondary flow than the MUSCL variant, but is in the same order of magnitude as the Smagorinsky model. At the refined mesh the WALE - F, Vreman - F and no model follow the DNS values properly close to the wall, while the Smagorinsky - F still under-predicts the magnitude of the spanwise velocity. The profiles at locations further away from the wall differ more

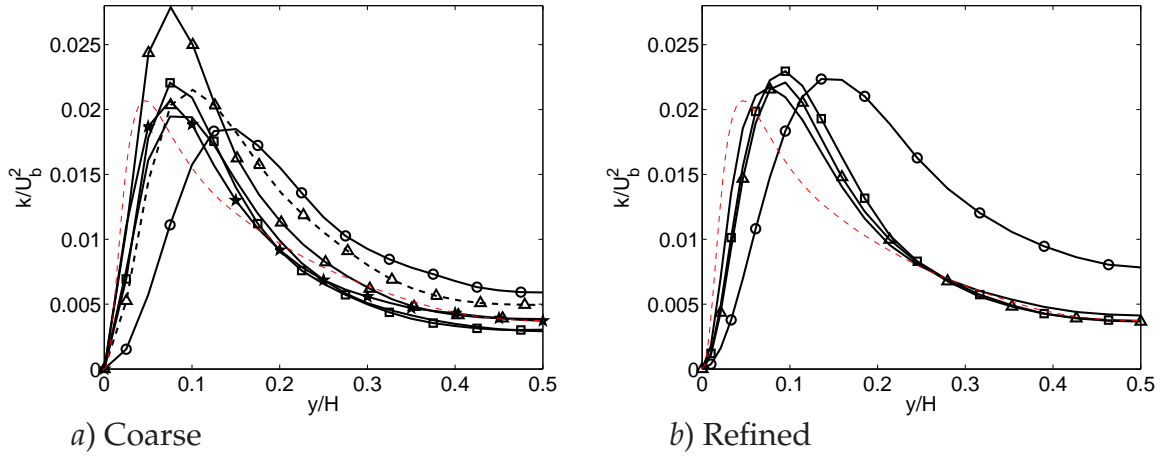


Figure 3.8 : Total resolved kinetic energy at $z = 0.5H$, compared to Gavrilakis [52] (- - -). (a) Coarse mesh, (b) Refined mesh. The models are \circ Smagorinsky; \square WALE; \triangle Vreman model; (- - \triangle - -) Vreman - QSOU; \star dynamic model, (—): no-model.

substantially from the DNS results, corresponding to the shift of the recirculation area, visible from figure 3.6. An explanation for the observations can be provided by the impact of the numerical scheme, the subgrid model and the resolution. The Smagorinsky model will dampen the secondary flow motion. The other subgrid scale models will account better for anisotropic turbulence near the walls, and filter out the shear component. The subgrid scale models are now less active and lead to similar results as the no-model variant. Still the effect of the numerical scheme is important, notwithstanding that the MUSCL variant leads to more appropriate results as the QSOU method. The refinement leads to a slight improvement, in particular for the Smagorinsky model.

Turbulence statistics

The total resolved turbulent kinetic energy (k) at half the duct cross section ($z = 0.5H$), from the wall up to the duct centerline ($y = 0.5H$), is shown in figure 3.8. These profiles are scaled to the bulk velocity. For the coarse mesh simulations the WALE, dynamic and no model variants show a similar level of turbulent kinetic energy as reported by Gavrilakis. The Vreman model overpredicts this value, whereas the Vreman-QSOU model prediction for k is again reduced compared to the MUSCL variant, but shows a broader profile. This can be attributed to the larger numerical diffusion that is inherent to this numerical scheme, and can explain the poor prediction of the secondary flow pattern close to the wall. The Smagorinsky model shows a shift in its maximum value more towards the center of the domain. For the refined mesh simulations the Vreman model now shows a more accurate prediction of the turbulence intensity, which makes it more comparable with the other models (WALE, no model) and the DNS. Still the Smagorinsky model remains shifted. When considering the different contributions to the turbulent kinetic energy it was observed that the streamwise turbulence profiles lead to similar behavior as k in figure 3.8. The simulations have more difficulties representing the smaller terms

$(\langle \tilde{v}''\tilde{v}'' \rangle)$ and $(\langle \tilde{w}''\tilde{w}'' \rangle)$ correctly. In all cases these normal and spanwise directions are under-predicted.

Also when considering the shear stress profiles τ_{xy} , it has been observed that the subgrid-scale contribution $\langle \nu_t(\partial \tilde{u}/\partial y + \partial \tilde{v}/\partial x) \rangle$ was marginal in all cases, except for the Smagorinsky variant, which explains the reduced value for Re_τ .

The dynamic, WALE, Vreman and Vreman - QSOU model show a reduced contribution from the subgrid-scale model compared to the Smagorinsky model. There are only minor differences between these models and the simulations where the subgrid-scale model has been switched off. This indicates that the impact of the subgrid scale model is only very small. Therefore, even using the MUSCL scheme for the convection still much of the turbulence dissipation is performed by the numerical scheme.

3.3.3 Discussion

In the presented simulations it is shown that the effective Reynolds number was substantially different compared to the Large-Eddy simulation from Madabhushi [92]. This indicates that the accuracy of the numerical scheme has a large impact on the effective shear. By using a less dissipative TVD scheme this effect diminished, but remains the most crucial. Also the choice of the SGS model can have impact on the flow statistics. Especially the Smagorinsky model showed a reduced mass flow compared to the other models. With increasing wall resolution these effects diminished. These observations indicate that for achieving fair results on global flow quantities it is essential in Kiva-3V to apply boundary conditions based on fixed mass flow rather than a force, such as a pressure gradient.

When corrected for the shear, reasonable agreement is achieved with respect to the mean profiles. On the coarse mesh all models are capable to represent the mean secondary flow field. These models turn out to be only marginally dissipative, therefore these results are comparable to the *no model* variant. This shows that in this study the numerical scheme masks much of the effects of the SGS models.

By increasing the wall resolution, the results showed a slight improvement. This is the most clearly visible from the effective shear Reynolds number Re_{*} . In these cases the shear layer was better resolved, resulting in a less pronounced contribution from the numerical scheme to the turbulence statistics. This indicates that the code does converge to the correct solution with increasing mesh size.

The results show that one should be very careful in predicting the correct shear if the wall region is not well resolved. Based on the considerations given above, in the remainder of this chapter a fixed mass flow boundary condition has been applied, in conjunction with the WALE model for the Kiva-3V simulations.

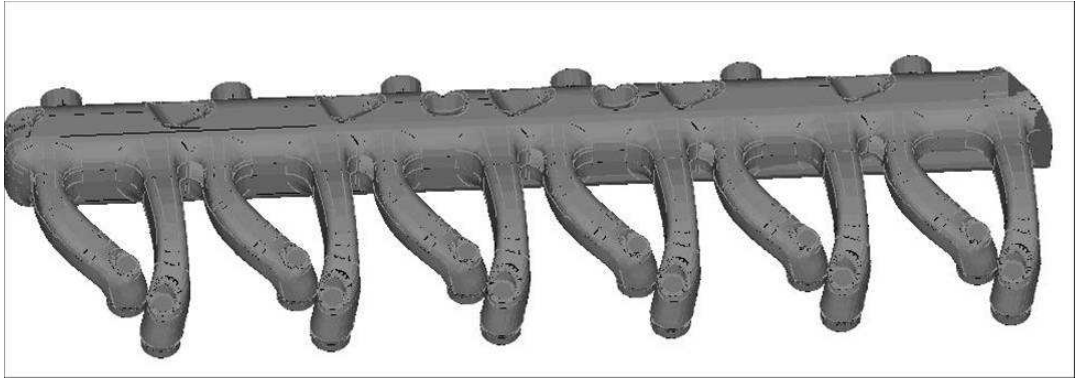


Figure 3.9 : Inflow manifold of a low-swirl heavy duty Diesel engine. The fresh air enters the manifold from the right side, and flows through the twelve runners, connected to six cylinders. At the end of the runners the valves are located to admit the fresh air into the cylinders.

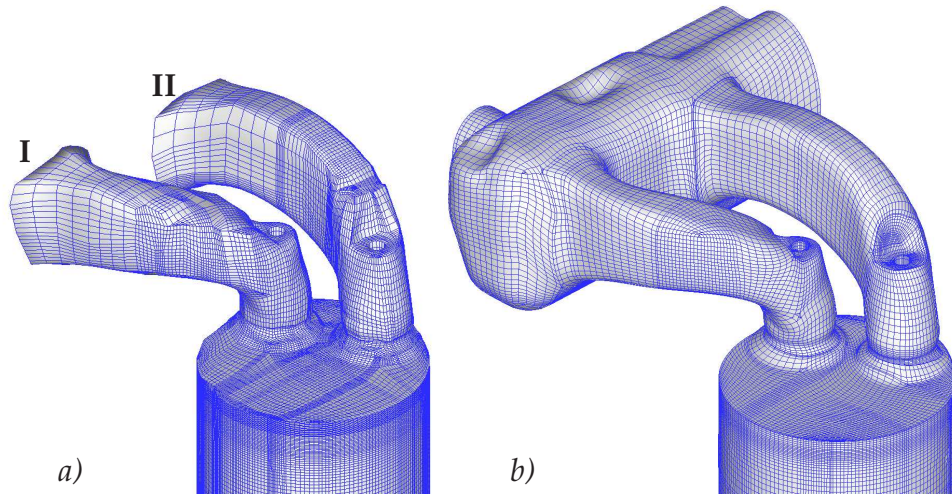


Figure 3.10 :Geometry of a cylinder with inflow manifold. (a) Kiva simulations, (b) FASTEST simulations. I and II denote the two runners.

3.4 A practical engine head simulation

In the previous sections a simple duct geometry has been simulated, testing the impact of the numerical scheme, the subgrid scale models and the resolution. However, we are more concerned with practical problems related to turbulence modeling in engines. One is then more concerned with typical engine flow problems, such as the impact of turbulence on the combustion process, the cycle-to-cycle variations, and the presence and magnitude of swirling and tumbling motions, than in a correct prediction of the secondary flow profiles and turbulence intensities in a square duct simulation. One leading question is: What do the simulations, performed in the previous section, mean for the modeling of a complex, engine-like geometry when applying an LES approach? Are the detailed problems of LES, enlightened in the square duct simulations, equally decisive in such a complex geometry? Therefore in this section the flow in a cylinder, induced by the inflow manifold of a heavy duty Diesel engine, is investigated.

In figure 3.9 a typical inflow manifold of a heavy duty Diesel engine is presented.

The runners connect the inflow manifold with the cylinders. In this case there are six cylinders connected to the runners. At the end of the runners the valves can be opened to control the flow of fresh gasses into the cylinder. The shape of the runners will have a large impact on the resulting flow dynamics down in the cylinder. In this work a so-called low swirl cylinder head is investigated.

Figure 3.10 shows in more detail the connection of the inlet runners to the cylinder. In reality the cylinder head incorporates four valves: two inlet and two exhaust valves. In the experiments as well as the simulations a steady state investigation of the flow is performed: only the flow due to the inlet runners is modeled. Therefore a constant valve lift of the inlet valves of 9 mm is applied, while the exhaust valves are closed. This means that the piston at the bottom of the cylinder is removed, such that the fluid can flow steadily through the complete domain.

Such a steady flow setup is often used to characterize a production type cylinder head experimentally. The bore diameter D is 130 mm. For the current simulation study a constant mass flow of 204 gr/s is applied through the cylinder. This corresponds approximately to the maximum flow rate occurring during the intake stroke of an engine running at full load. The corresponding Reynolds number Re_{inlet} based on the port diameter and the flow rate is around $2.2 \cdot 10^5$.

The numerical results are compared to particle image velocimetry (PIV) data, performed by de Leeuw [83]. Therefore the cylinder has been removed and replaced with a dummy perspex cylinder, such that it is optically accessible.

3.4.1 The numerical setup

Kiva-3V simulations

Three simulations have been performed with Kiva-3V, see table 3.2. All simulations used the same mesh, shown in figure 3.10a. This mesh consists of approximately 400,000 cells, refined at the top of the cylinder. In the first simulation *Kiva A* the classical URANS $k - \varepsilon$ model is adopted. The other simulations are performed in the LES mode. In the second simulation referred to as *Kiva B* the inflow boundary condition is set based on simple considerations of equal mass flow through the two runners. In the third simulation, simulation *Kiva C*, the actual space-dependent flow profiles through the two runners is controlled in two inlet planes such that it equals the mean velocity profiles at these planes as found in the FASTEST results. In the Kiva simulations a smaller domain is modelled than in the FASTEST simulations. This was because of the computational expenses: not only the computational time was a limiting factor, also the available memory limited the size of the computation. Therefore, to keep sufficient resolution inside the cylinder, only a small upstream region was simulated additionally. This is standard practise in this type of simulations, e.g., Payri *et al.* [112], but the validity of this choice is unclear beforehand. It is not obvious how the flow conditions in the two runners are related to each other.

In all simulations a zero-gradient outflow boundary is defined at the bottom, at $z/D = 3$. The influence of this downstream boundary is assumed to be sufficiently reduced as the depth of the cylinder has been set to $3D$, while performing the main analysis up to $z = 1.75D$.

Table 3.2 : List of performed simulations

Simulation	number of cells [millions]	turbulence model	Mass flow (I - II) [kg/s]
<i>Kiva A</i>	0.4	URANS $k-\varepsilon$	0.102 - 0.102
<i>Kiva B</i>	0.4	LES WALE	0.102 - 0.102
<i>Kiva C</i>	0.4	LES WALE	0.110 - 0.094
<i>FASTEST A</i>	0.5	LES dynamic	turbulent, 0.204
<i>FASTEST B</i>	2.5	LES dynamic	turbulent, 0.204

FASTEST-3D simulations

Two calculations have been carried out using the FASTEST code, see table 3.2. The first computation had a relatively coarse resolution, this simulation is referred to as *FASTEST A*. The number of cells reaches 0.5 million cells. In the second simulation the grid-cell size is reduced in every direction, which results in a total of 2.5 million cells, referred to as simulation *FASTEST B*. As the FASTEST code applies a multi-block strategy, this implies that so-called O-grids can be used which will improve the quality of the mesh, especially at all curved areas near the walls. In the current simulations the convective scheme has been blended with a first order upwind scheme, at a level of 10%, in order for the solver to remain stable at locations of very skewed cells, especially near the valves. In the FASTEST simulations a larger part of the inflow manifold is simulated, compared to the Kiva simulations, see figure 3.10b. Therefore the fluid is naturally distributed over the two inflow runners. The mass flow rates at the two runners, at the locations where the Kiva simulations start, has been evaluated. For both the coarse and the fine mesh simulations these values were 0.11 kg/s for runner I and 0.094 kg/s for runner II.

Moreover, at the inflow plane turbulent inflow conditions are provided consisting of a correlated inflow field with turbulent statistics based on pipe flow measurements, Eggels [43]. This procedure is based on the inflow generator developed by Klein *et al.* [73], and is adapted for arbitrary surfaces. At the bottom a zero-gradient outflow boundary condition is defined.

Computational requirements

The computational time for both the Kiva-3V and FASTEST simulations was approximately 2 months on different high-performance computing facilities. The *FASTEST A* simulation is parallelized on two CPU's where *FASTEST B* has used eight CPU's. All Kiva-3V simulations ran on a single CPU. The simulated physical time equals 0.15 sec, which is estimated to be sufficient to capture approximately 100 large-scale turbulent time-scales in the upper part of the domain, where the fluctuations have a relatively short time scale.

For all simulations the y^+ value is evaluated for the first grid point normal to the wall, as an indication of the resolution of the boundary layer by the applied grid, see table 3.3. For the Large-Eddy simulations with the FASTEST code y^+ reaches values up to 6000 close to the valves, where instantaneous velocity magnitudes are extreme. Downward in the cylinder the average values decrease to 1000. Close

Table 3.3 : Evaluation of y^+ for the different simulations

Simulation	max. y^+ at $Z/D = 0.25$	average y^+ at $Z/D=0.25$	max. y^+ at $Z/D = 1.75$	average y^+ at $Z/D=1.75$
<i>Kiva A</i>	11000	2900	2150	410
<i>Kiva B</i>	21500	4480	1950	530
<i>FASTEST A</i>	6330	2900	4300	1750
<i>FASTEST B</i>	5850	1890	2700	960

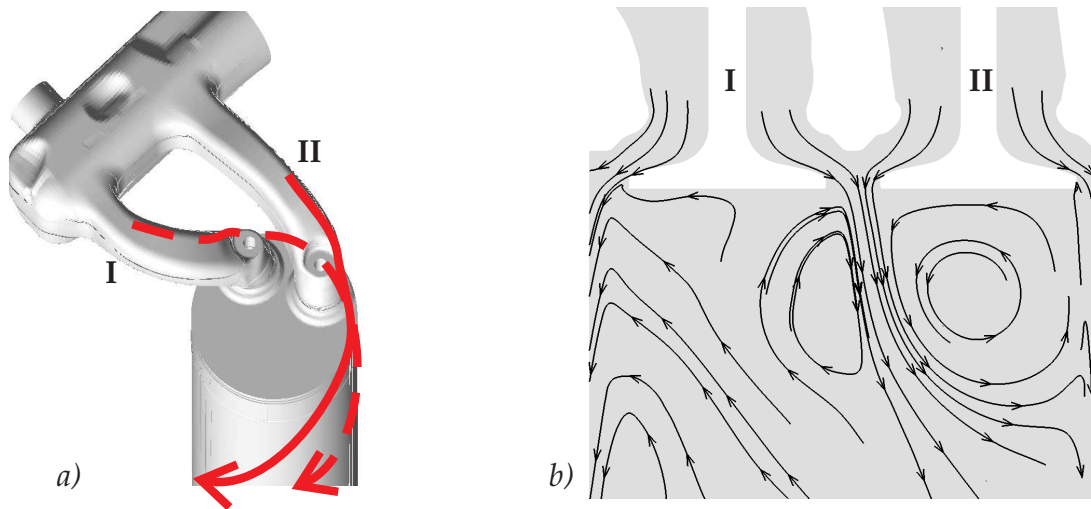


Figure 3.11 : (a) Illustration of the two main vertical jets, arising from the two runners. These jets drive the mean swirling motion. (b) Streamlines illustrating the mean tumbling flow by the recirculation areas below the valves. Simulation *FASTEST B*.

to the valves the y^+ values for the Kiva-simulations exceed the levels from both *FASTEST* simulations, due to the relatively coarse mesh. However, at the bottom of the cylinder the y^+ values are much reduced compared to the *FASTEST* simulations, reflecting moderate velocities close to the walls.

It is acknowledged that these values indicate that the turbulent wall shear flow is completely not resolved in any case. For a good resolution of the shear flow at the wall in a pure LES, the value of y^+ should be of the order unity. While a fixed mass flow has been applied, the simulated Reynolds number was appropriate, but the local shear can have an important impact on the local flow behavior. This can have consequences on the average, global flow patterns that are induced by the shape of the valves and cylinder wall, as well as the balancing of the imposed mass flow through the runners.

A more appropriate wall modeling method can be achieved by introducing a hybrid scheme, where the wall region is modeled using a RANS approach, and the region far away with the LES approach. Recent efforts in this direction are reported by Tessicini *et al.* [154], Temmerman *et al.* [153] and de Langhe *et al.* [79,80].

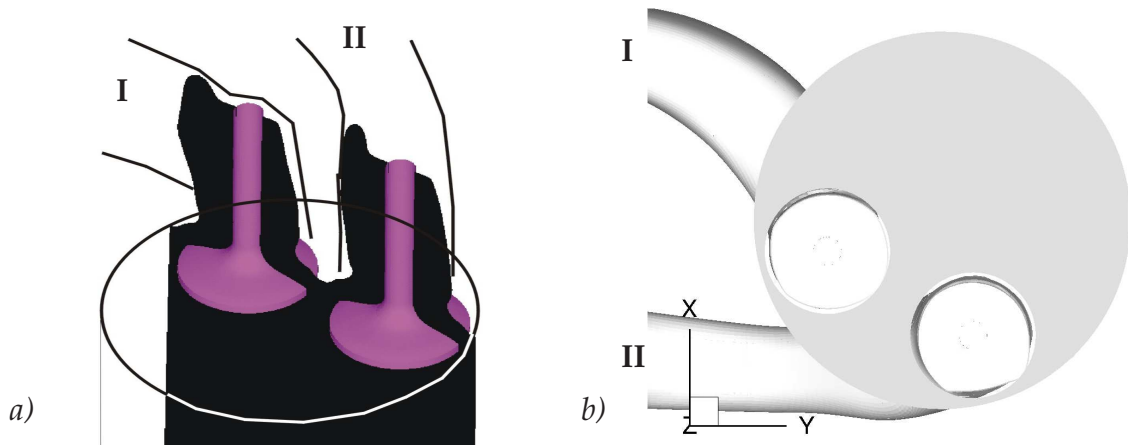


Figure 3.12 : (a) Location of the plane where the data is evaluated, indicated by the black sheet, crossing through the valves. (b) orientation for the figures at constant height z .

3.4.2 Results and discussions

In this section the results from the simulations are presented and discussed. The main features of the flow are illustrated in figure 3.11. Figure 3.11a illustrates the origin and location of two large-scale jet-like structures. When following these structures downwards along the cylinder walls a clear mean rotational flow is observed, referred to as a swirling motion. The right picture (figure 3.11b) shows the streamlines of the mean velocity field on a cross-section in the domain. Two recirculation areas can be identified, which illustrate the second effect characteristic for engine geometries: tumble. The size of the tumbling motion scales to the size of the valves.

By averaging the data over the performed simulation time mean and turbulent flow field data have been evaluated, which will be presented in the next subsections. First the mean flow properties are considered, focussing on the tumble and the swirling motion. Then the turbulent flow properties will be considered. All data is compared on several planes in the domain. A vertical plane is extracted such that it crosses the two valves, see figure 3.12a. Moreover at three locations, $z = 0.25D$, $z = 1.25D$ and $z = 1.75D$ below the cylinder head, with D being the cylinder diameter, horizontal cross sections are extracted. At the lower two levels PIV data of the flowfield in spanwise direction is available.

Tumble

Figure 3.13 shows the contour levels of the mean vertical velocity fields for the five different cases. It is observed that in all simulations, except for the URANS simulation *Kiva A*, the flow is directed towards the right valve. This can be explained by the inflow geometry, figure 3.12. The runners induce a strong jet directed to the wall of the cylinder. The angle and strength of this jet will determine the strength of the swirling motion in the cylinder. The jet in *Kiva C* is more inclined towards the wall than in *Kiva B* and *FASTEST A,B*. This indicates the impact of the mass balancing in the two runners.

The resemblance of the two FASTEST simulations indicates that these simu-

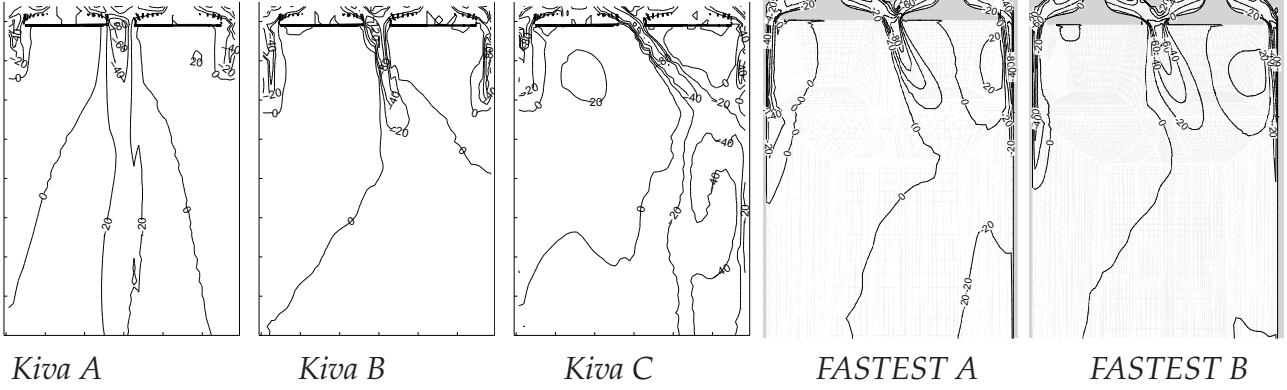


Figure 3.13 : $\langle \tilde{w} \rangle$ -component velocity fields in the plane indicated in figure 3.12. Contour levels are shown in steps of 20 m/s.

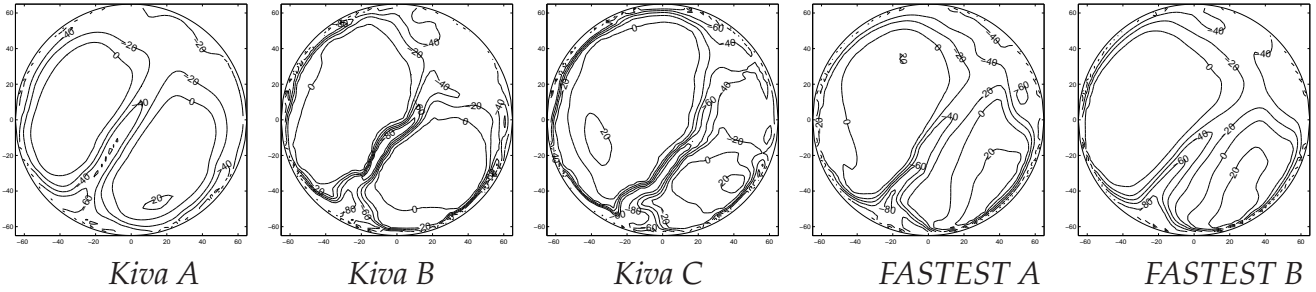


Figure 3.14 : $\langle \tilde{w} \rangle$ -velocity fields at $z = 0.25D$ below the cylinder head.

lations can be considered relatively grid-independent. The two jets emerging between the valve and the cylinder walls do not penetrate deeply into the cylinder as the shear at the walls is relatively large. These jets will be mainly responsible for the tumbling effects.

The tumble is best observed in figure 3.14. In case *Kiva A* the two tumbling regions are equally large, consistent with the $\langle \tilde{w} \rangle$ -contour plot from figure 3.13. In the other simulations the tumbling region at the right side of the cylinder is slightly smaller than the left side, which is in correspondence with the centered jet in the previous figure. The *Kiva C* simulation predicts a relatively large deviation between the two tumbling regions.

Swirl

When looking at the mean spanwise velocity fields in figures 3.15 and 3.16, it is found that the large-scale vortices are relatively weak for the URANS simulation *Kiva A*. The Large-Eddy simulations show a stronger contribution to the vortical motions. In all cases two large-scale vortical structures are found at $z/D = 1.25$, in correspondence with the PIV experimental data. In case *Kiva B* the vortical structures are not equal in strength, just like the FASTEST results and experiments.

The mean spanwise velocity vector field from simulation *FASTEST B* changes from a complex flow structure near the valves to two counterrotating vortices, figure 3.15. Lower in the cylinder the stronger counter-clockwise vortex still survives, figure 3.16. This is in contrast to the experiments and the simulations from *Kiva-3V*.

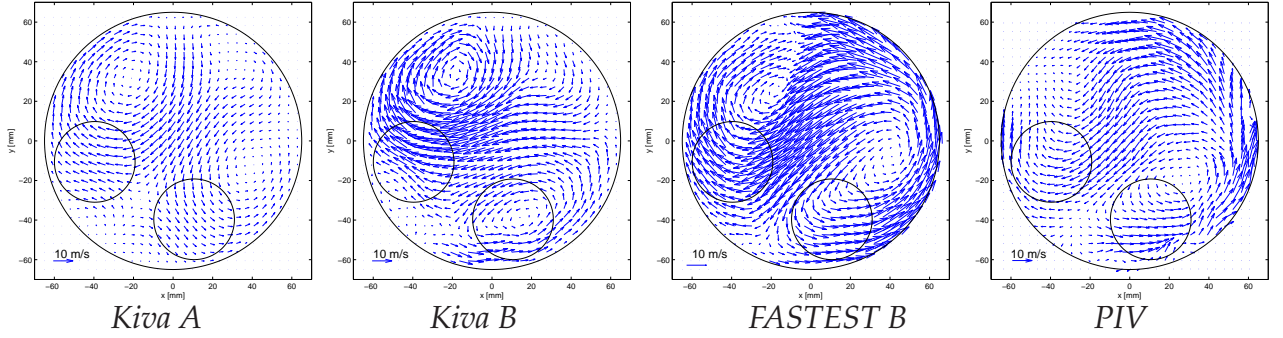


Figure 3.15 :mean spanwise velocity fields at $z = 1.25D$ below the cylinder head.

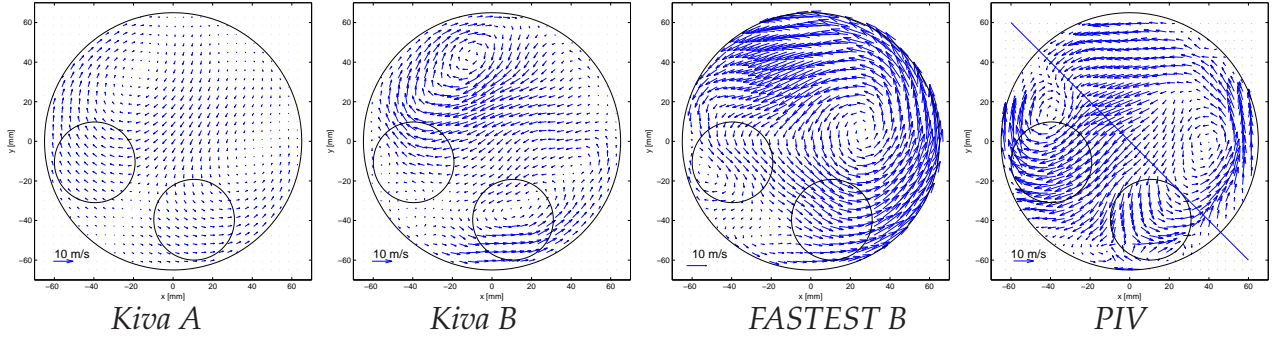


Figure 3.16 :mean spanwise velocity fields at $z = 1.75D$ below the cylinder head.

Resolved turbulence intensities

Figure 3.17 shows a qualitative figure of the turbulence intensities at $z = 1.25D$ compared to the experimental data. The two main hotspots can be found opposite to each other, similar to observations from figure 3.14. This indicates that a large correspondence between the jet flow and the turbulence levels can be expected.

In simulation *Kiva A* the turbulence level remains fairly low and constant over the complete range. The URANS model is apparently far more diffusive and reduces the extrema. There is a considerable difference between the simulations and also compared to experiments. Figure 3.18 shows the resolved turbulence intensity in the same vertical plane as for figure 3.13. The highest levels of turbulence intensities are found in the center of the cylinder where the two runners meet. But the Kiva-LES simulations *Kiva B* and *Kiva C* show only an increase in turbulence intensity below the valves, whereas the URANS simulation *Kiva A* and the FASTEST simulation already show increased turbulence intensities in between of, and even above the valves. Finally, similar observations can be made from these figures as for figure 3.13: whereas the URANS simulation *Kiva A* shows a symmetric solution, simulation *Kiva B* and *FASTEST B* lead to an increase of turbulence intensity to the right hand side.

3.4.3 Discussion

Due to the under-resolved wall as well as the numerical inaccuracies the results differed substantially from one another. In some of the simulation cases the global features could be captured.

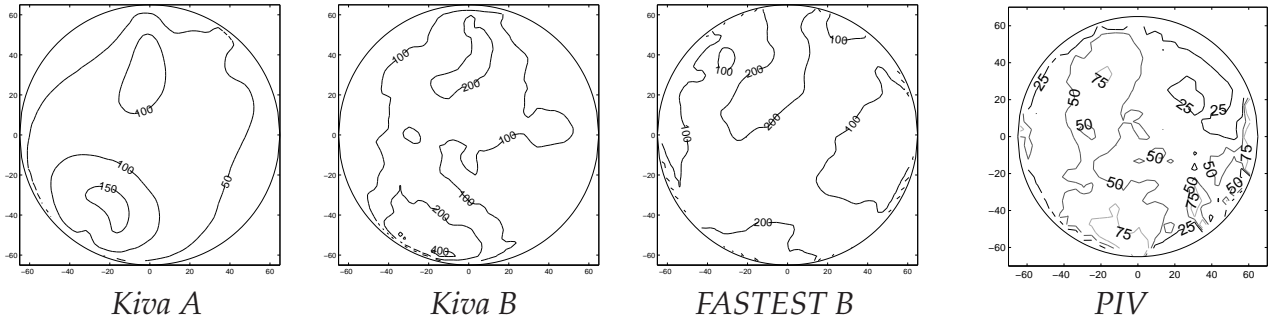


Figure 3.17 :Turbulence intensities k in m^2/s^2 at $z = 1.25D$ below the cylinder head.

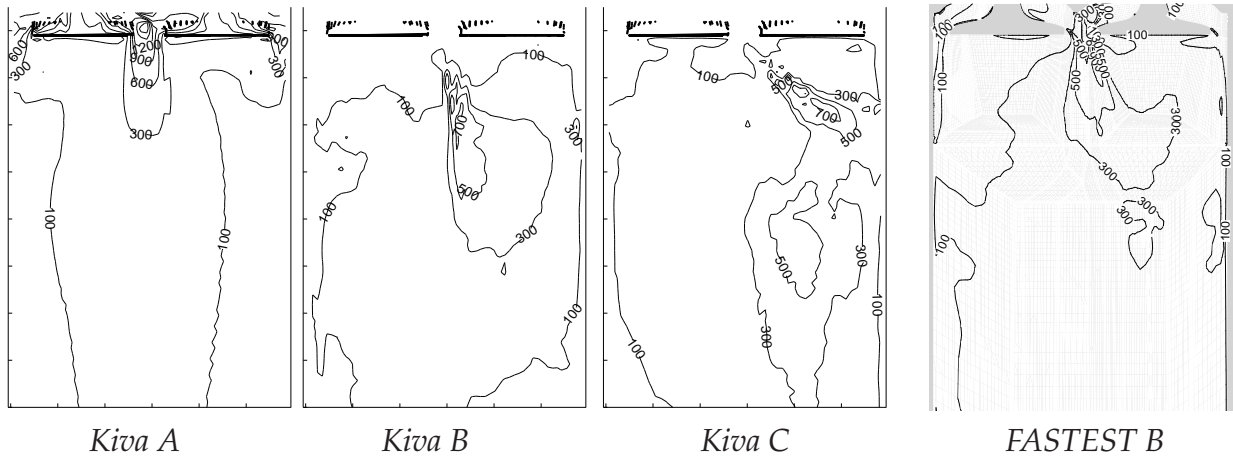


Figure 3.18 :Turbulence intensities k in m^2/s^2 at the plane indicated in figure 3.12.

From the performed simulations it turns out that the URANS $k-\varepsilon$ simulation with Kiva-3V is able to recover some of the complex flow effects as occurring in the cylinder. However, all mean flow structures are very weak as the $k-\varepsilon$ model is very dissipative. The predicted turbulence intensities themselves are therefore relatively low in the complete domain. Yet the computational expenses are only a fraction of the Large-Eddy simulations as a steady situation is reached in a short time.

Near the valves where the geometry is very curved the computational cells are severely skewed. This compels the introduction of upwinding in the convective schemes that obviously leads to numerical diffusion. The FASTEST simulations show correspondence to experimental data in the upper region of the cylinder. Down the cylinder some flow features, such as the two counterrotating vortical structures disappear. The Kiva-3V simulation with equal inflow velocity at the two runners shows results comparable to the FASTEST simulations for the mean flow and turbulent quantities in the cylinder. The flow field from the Kiva-code with modified inflow boundary conditions does give a discernible difference in flow structure.

This illustrates that the distribution of mass through the two runners will have an important effect on the flow field downstream in the cylinder. Circumventing this problem by applying the steady boundary conditions from a more detailed simulation does not guarantee success. This illustrates the issue of the inflow conditions for LES in complex configurations. Therefore it can be suitable to include a larger part of the upstream domain into the computational domain, as done in the FASTEST simulations.

3.5 Conclusions

In this chapter the numerical procedure as applied in Kiva-3V has been sketched. The convective scheme of the Kiva-3V code has been adapted with a less dissipative TVD scheme, in order to increase accuracy but at the same time keeping stability.

A number of subgrid scale models has been implemented in the Kiva-3V code. These were tested on the turbulent flow in a square duct geometry. Additionally, results are compared to a *no model* variant, where the SGS contribution is switched off. A general conclusion from the performed simulations is that global flow features are recovered, but if the wall region is not well resolved it is hard to quantitatively predict the shear, as well as all other flow properties.

In the latter part of this chapter a more realistic engine geometry has been investigated: a complex turbulent, swirling and tumbling flow in an engine cylinder that is induced by the inlet manifold. A number of Large-Eddy simulations have been performed with the FASTEST and Kiva-3V code, and additionally one URANS simulation. The effect of the poor wall resolution and the numerical scheme in the Large-Eddy simulations on the flow field statistics was relatively large. Again, only global flow features could be captured appropriately. A detailed data analysis and comparison of the different simulations with each other and with experiments is problematic as small differences in the complex flow result in large differences of specific flow quantities at specific locations.

LES gives an indication of the unsteady, turbulent processes that take place in an engine. However, this study shows that for a quantitative predictive quality the numerical scheme as well as the computational resolution have to be improved.

Recommendations

In this subsection some remarks will be presented to give an indication on future modeling approaches for complex (engine) setups. To gain more confidence in the unsteady flow behaviour, an Large-Eddy simulation can be more preferable to an URANS based calculation, on the condition that available computational power is not a restriction. For the near wall regions, however, a hybrid approach would definitely be more suitable, see, e.g., Tessicini *et al.* [154].

It appears that reasonable in-cylinder flow results can be achieved when only modeling a relatively small part of the upstream region, basically because the flow around the valves will create the main flow structures. As pointed out above, the best approach is to include a larger part of the upstream region into the computational domain.

By showing the sensitivity of the inflow conditions on the flow pattern in a steady geometry it can be concluded that this will be very sensitive on any changes in inflow conditions as encountered in moving piston geometries: any erroneous valve-motion modeling and grid-handling will lead to relatively large deviations in the flow patterns. This is especially true for detailed flow information that, for example, can be extracted from experimental LDA methods. It can be expected that it remains very hard to make such a detailed prediction with any CFD method on this level. But interesting information from the simulations can be extracted on the level

of global flow fields, as well as turbulence intensities. Best practice today concerning realistic engine geometries is to compare data from simulations to experimental techniques like PIV. In future more accurate, detailed measurements can serve as a validating tool. Then, with increasing computational power sensitivity studies can more easily be performed using LES.

In the introduction it has been remarked that the flow in an engine at real operating conditions is strongly influenced by the squish at the end of the combustion phase. Concerning future work it is a challenging, and important question to investigate its impact on the turbulent cylinder flow, induced by the inflow manifold, to study cycle-to-cycle variations.

Modeling the turbulent mixing of a gas jet

In this chapter the properties of a gaseous fuel jet have been studied using the LES method, for three different fuel to ambient gas density ratios. The impact of the injected gas density on the resulting flow field is considered. The penetration depth and the cone angle are analyzed, and it is shown that the gaseous fuel jets follow well the similarity theory. By applying a virtual Schlieren postprocessing method to the simulation data problems related to this experimental technique could be enlightened. Also the correspondence of the gas jet flow dynamics compared to those of a liquid spray is analyzed. When corrected for the cone angle, the gas jet dynamics follows well the scaling laws proposed for the liquid fuel sprays.

4.1 Introduction

In the previous chapter the modeling of non-reacting fluid flow for engine applications has been considered. The combustion process is of main concern in engine modeling, and is governed by the chemical reactions that take place in a combustible mixture. In Diesel engines, fuel is injected into the air near the end of the compression stroke. The ensuing mixing process does influence the combustion parameters, such as ignition delay, location of ignition, heat production, reaction products formation and soot formation. Modeling of the mixing process in an engine is of key importance for the prediction of combustion in engines. Especially for future engine types, applying Homogeneous Charge Compression Ignition (HCCI) combustion concepts, the mixing of the fuel and oxidizer is an important controlling variable of the combustion, Cook *et al.* [33].

Previous studies on Diesel injection have enabled a general understanding of the effect of high pressure direct injection systems on fuel-air mixing, Naber and Siebers [99]. Classical mixing models based on a RANS approach can be reasonably accurate for the use as a modeling tool; all physical effects that have been observed experimentally can be represented, Abraham and Magi [2]. Only average, global flow information had been available from experiments, which are the quantities that are accounted for in the RANS modeling environment. Gas injection systems

are generally studied based on RANS type methods, e.g. Ouellette and Hill [107] and references therein.

However, it has been argued in chapter 1 that for pollutants modeling like NO_x and soot it is very hard to predict concentration fields if only average flow quantities are available. Therefore a more accurate and detailed description of the processes that govern this formation is required. This concerns both detailed experimental data as well as numerical studies on the mixing process in fuel gas jets and sprays. The LES approach is chosen, as it yields a more detailed, instantaneous flow and mixing information compared to RANS. Along with modeling the turbulent flow field the transport of any representative scalar field can be evaluated. In principle this scalar field can be used to define the chemical state of the fluid. For non-homogeneous mixtures like in Diesel engines, this scalar field is chosen such that it represents the fuel-to-air mixing ratio, given by the mixture fraction Z .

When the fuel is injected in the gas phase the modeling can be performed using a single phase flow solver. The evolution of a gaseous mixture can be modelled by solving scalar transport equations for the different species separately. In Diesel engines, fuel is injected in the liquid phase and not in the gas phase. Therefore, droplet breakup, collisions and evaporation in a turbulent environment should in principle be accounted for. However, the quantitative optical diagnostics on droplet statistics (size, speed, amount, location) is a tedious task, as has been discussed by Bruneaux [24]. At the same time the simulation of two-phase flows in this field remains a challenge, and has -until now- been limited to very simple geometries, needing very specialized solvers. Moreover in most studies of two-phase flows only low droplet densities can be considered. Thus the modeling of dense sprays, as can be found in Diesel engine injection systems, remains a major challenge, Jay *et al.* [70]. Most solvers that apply particle/droplet models are nowadays based on a RANS turbulence description, because for LES methods the computational demands are much larger. These limitations lead to the decision to study a gaseous fuel jet instead. This modeling simplification needs justification. Liquid jets can obviously not in all regions be simplified to gas jets. On the other hand, when all fuel droplets are vaporized, finally the fuel spray flow resembles a gas jet structure.

An additional topic can be formulated regarding the data treatment. From experimental techniques difficulties remain in gathering and interpreting accurate measurement data, Klein-Douwel *et al.* [75]. Therefore a Large-Eddy simulation can help: a three-dimensional time-resolved dataset of all relevant flow parameters is provided. Whereas in the experiments uncertainties with respect to measurement and visualization techniques are present, in simulations numerical inaccuracies and model limitations restrict the global predictability. Yet, the simulations can help to serve as a tool for validating experimental visualization techniques, and give information on problems concerning numerical and experimental data treatment. A standard practice in experimental methods is to use a Schlieren method, where light rays are deflected due to density gradients in the gaseous jet. This can in principle be simulated and applied to the numerical results.

Objective of current research

For the above given reasons the leading questions for this work can be formulated: how does a gaseous jet behave in its development region, and how in its steady state behavior? To what extent is it possible to represent a *liquid* fuel jet by a *gaseous* fuel jet? And additionally, how does the virtual Schlieren method relate to the numerical data from the simulations? Therefore this chapter has the following structure. In the next section the gaseous and liquid jet dynamics are described phenomenologically. Obviously, the modeling of a gas jet flow will greatly simplify the modeling efforts. However, it is necessary to keep the essential parameters with respect to the mass and momentum transfer, in order to provide proper initial conditions for the combustion phase. Arguments are given how to compare those jets.

In section 4.3 the governing equations for the mixing model are presented. Then the numerical setup, along with an assessment of the differences with the experimental gas-jet setup are described. In section 4.4 results on the turbulent mixing of a gas jet will be presented and discussed. Also the application of a virtual Schlieren method is discussed. The final section will provide some conclusions.

4.2 Phenomenology of liquid and gaseous fuel jets

In this section the phenomenology of liquid (subsection 4.2.1) and gaseous (subsection 4.2.2) jets is presented, based on a literature review of these subjects. This considers both information from experimental studies, theoretical/phenomenological considerations and numerical investigations. The dynamics of both jets is compared in the last subsection.

4.2.1 Liquid fuel jets

Fuel sprays in Diesel engine conditions are essentially characterized as two-phase flows. A liquid fuel jet is schematically presented in figure 4.1a. Fuel is injected as a liquid, which will break up into smaller droplets, vaporize and form a combustible mixture. These processes and the standard modeling approaches have been described in Stiesch [149], and are summarized below.

Liquid core

The region just above the nozzle exit is referred to as the liquid core region. The kinetic energy of the spray represents one of the main sources for turbulence production in the combustion chamber, Reitz and Rutland [132]. Due to the high density of the fuel compared to the gas phase, the contribution of the liquid phase to the gas phase dynamics is relatively large. The volume fraction of the liquid fuel occupies locally more than 50%. This means that the liquid cannot be considered as dispersed within a continuous gas phase.

Therefore, for the modeling of this region of the spray, a flow solver is needed that is adapted for the modeling of two phase flow and the surface tracking of the liquid core. These are Volume of Fluid (VOF) methods. However, as the liquid core

region is normally very small and exists only close to the nozzle exit, this is usually neglected in typical spray simulation solvers, e.g. Amsden *et al.* [5], Naud [100].

Breakup region

In the next region separate fuel droplets can be identified in a continuous gas phase. The liquid core has now broken up into first ligaments and droplets. Three effects drive this primary breakup process: the turbulence within the liquid phase, the implosion of cavitation bubbles and aerodynamic forces acting on the liquid jet [149]. Depending on injection parameters such as the relative velocity v_{rel} between the liquid and the gas, the liquid density and gas density ρ_a , the droplet radius r_d and surface tension σ , the relative contribution of the different mechanisms to the spray breakup varies, resulting in different breakup lengths and different droplet sizes. This is described by the characteristic Weber number:

$$We = \frac{\rho_a r_d v_{rel}^2}{\sigma}. \quad (4.1)$$

This describes the strength of the aerodynamic forces, relative to the surface tension of the droplets. For instance, with increasing relative velocity between liquid and gas phase, the aerodynamic forces acting on the liquid surface are intensified and the wavelength of the disturbances become shorter, resulting in smaller average droplet diameters.

With the large-scale liquid fuel being transformed into droplets after the primary breakup, the secondary breakup region is driven by aerodynamic forces acting on the droplets by the surrounding gas phase. Droplets are distorted from their initially spherical shape, and broken up into two (vibrational breakup) or many small droplets (catastrophic breakup) depending on the Weber number.

Particle interactions and evaporation

Another process that complicates the spray dynamics concerns the particle-particle interactions. Collisions between particles have a strong impact on the mean droplet size and its spatial distribution. The different regimes can be defined based on a collision Weber number. After collision the particles can bounce elastically, coalesce permanently or shatter into tiny droplets, depending on their relative velocity.

Finally, the evaporation takes place, which will provide a combustible mixture, when mixed with fresh air. Heat is transported into the droplet, while fuel vapor mass is transferred from the boundary layer at the drop surface into the gas. The penetration depth of the spray is influenced by the evaporation rate. Naber and Siebers [99] show that for high ambient gas densities vaporizing sprays can be represented by non-vaporizing liquid fuel sprays. Only with decreasing ambient air density, at a fuel-to-air density ratio of about 20 (for instance, using n-heptane at 684 kg/m³ injecting in compressed air of about 35 kg/m³), the non-vaporizing fuel jets show an enhanced penetration depth up to 20% more, compared to the vaporizing jet. This is because the fuel droplets do not transfer momentum instantaneously from the injected fluid to entrained gas. Thus, depending on the rate of vaporization, a velocity difference may exist for some time, leading to a delayed entrainment

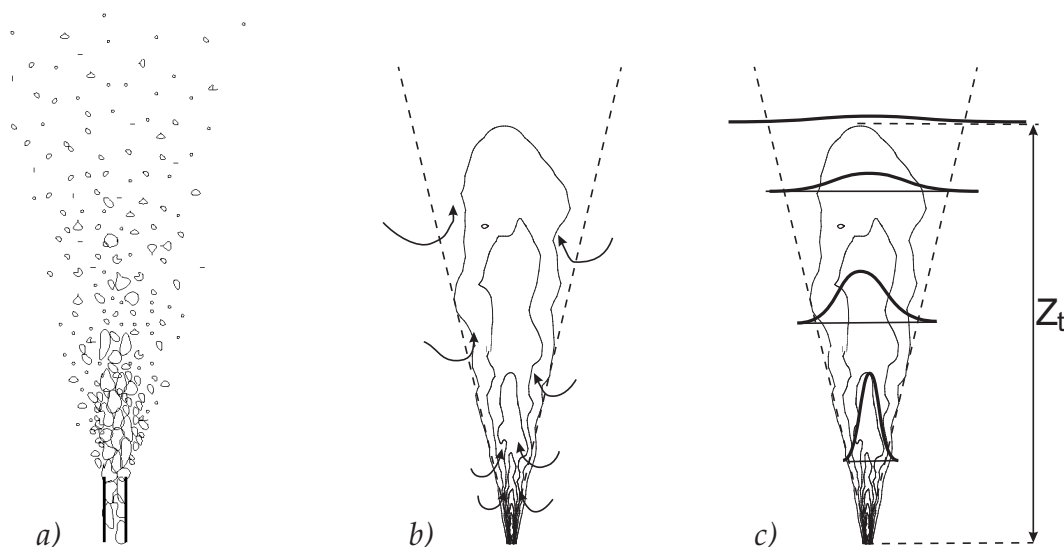


Figure 4.1 : (a) Conceptual representation of a liquid fuel jet. (b) Concentration field and entrainment pattern of a round turbulent jet. (c) Schematics of the self-similar concentration profiles.

and enhanced penetration. Typically, poor evaporation will result in poor mixing, that will increase the soot production. Very rapid evaporation on the other hand will cause an increase in nitrogen oxides, due to a relatively large, hot premixed combustion phase.

4.2.2 Gaseous fuel jets

For steady, round turbulent gas jets at moderate to high Reynolds number a wide range of experimental data exists. This type of jets is a standard test case when developing turbulence models for practical applications. Olsson and Fuchs [106] have shown LES results on a circular jet for three different Reynolds numbers ranging from $1 \cdot 10^4$ up to $50 \cdot 10^4$. Here the region close to the nozzle exit has been simulated. The main difference between a gas jet at engine operating conditions and standard experimental turbulent jets as generally reported in the literature [41, 67, 109] are the physical dimensions (tens of millimeters instead of centimeters / meters) and the density ratio. For fuel jets the density ratio of fuel to ambient air can be up to 100, whereas in most gas jet experiments only small variable density has been studied, with density ratios ranging from 0.5 to 5. The turbulent jet consists phenomenologically by the core, the shear layer and the jet tip regions. In the remainder of this section these aspects are described.

Potential core region

In the first region above the injector the gaseous fuel is not yet diluted with ambient air. This region is denoted as the potential core, and is comparable to the liquid core for liquid jets. Lubbers *et al.* [91] note that the injection geometry does have an impact on the resulting jet dynamics. This will be discussed below.

Shear layer

The injected jet momentum generates a high shear, which produces a wide range of turbulent structures, from small to large scale. Within this shear layer a large entrainment of ambient gases can be expected.

The main mechanism of entrainment is by engulfment of ambient fluid along the edges of the large-scale turbulent jet structures, as depicted in figure 4.1*b*. Subsequently mixing takes place by stretching of the interface that is formed between the entrained fluid and the jet fluid. Both jet and entrained fluid come into contact at ever smaller scales, until, at the Kolmogorov scale, the fluid from the two streams becomes fully mixed. This is well documented by Schefer *et al.* [140].

Jet Tip

The jet tip can be described as the top region of the visible, developing jet. In section 4.4.2 a more detailed definition will be provided. Bruneaux [24] showed experimentally the existence of very steep gradients in the mean profiles near the jet tip. Compared to the mixing in the shear layer this indicates a lower turbulent mixing rate, which apparently is only involving the large scales. Due to this low mixing rate the formation of uniformly distributed fuel pockets with steep gradients at the edge is enhanced. Therefore large differences exist between independent instantaneous flow profiles. By averaging these profiles, an erroneous figure on the mixing may appear, described by a gradually increasing level of fuel concentration. Bruneaux showed that the fuel mass distribution function at the spray tip is represented by a double-peak function, which illustrates these unmixed, uniformly distributed fuel / air pockets with steep gradients in between.

Also the analysis by Schefer *et al.* [140] of instantaneous profiles in a turbulent jet has shown a close relationship between the fuel profile characteristics and the structure of the turbulent velocity field. This can be characterized in terms of large-scale, quasi-periodic, and organized structures. There are significant departures of the instantaneous profiles from conventional time-averaged profiles. This shows that a proper description of the mixing process at the trailing edge of the jet is not possible when using a RANS-type model for the flow field. Here it is favorable to account for instantaneous flow field phenomena.

Additionally, as described by Pope [126], the standard $k - \varepsilon$ model is not adequate to model jets: the mass entrainment rates are under-predicted. A solution is to include a second moment closure. Another modeling approach, keeping a two-equation RANS approach, is to adapt the turbulent modeling coefficients $C_{\varepsilon 1}$ and $C_{\varepsilon 2}$ in equation 2.24 to better reproduce the mass entrainment rate in steady-state jets. However, this means giving up the idea that these established coefficients are universal, which leads to ad hoc assumptions for any changing geometrical case.

Self-similarity theory

The gaseous jet dynamics can be described phenomenologically using self-similarity theory. This is very helpful for understanding the governing physics of a gaseous fuel jet. An important scaling parameter for injection systems is the momentum

injection rate at the nozzle exit M_0 . This parameter is evaluated from

$$M_0 = \int_A \rho_0 u_0^2 dA, \quad (4.2)$$

with u_0 the local injection velocity, ρ_0 the density of the injected mass and A the injection area. It has been generally accepted that a self-similarity solution does exist for this type of problems, Dowling and Dimotakis [41]. For a discussion see, e.g., Lubbers *et al.* [91]. A similarity equation can be derived for a well developed turbulent jet, which is at Reynolds numbers larger than 3×10^3 and distances larger than $20 d_0$ (i.e., out of the potential core region). Then the mass entrainment rate correlation of Ricou and Spalding [136] is used. This relates the penetration depth z_t of turbulent jets to a typical diameter d_{eff} :

$$\frac{z_t}{d_{\text{eff}}} = \Gamma \left(\frac{\pi}{4} \right)^{1/4} \left(\frac{t u_0}{d_{\text{eff}}} \right)^{1/2}, \quad (4.3)$$

with d_{eff} the equivalent, or effective diameter, defined as $d_{\text{eff}} = d_0(\rho_0/\rho_a)^{1/2}$ and d_0 being the nozzle diameter. In this equation ρ_a is the ambient air density. Furthermore, Γ is a constant with a value of about 3.0 for turbulent jets with round nozzles. This equation can also be written in terms of the momentum injection rate:

$$z_t = \Gamma (M_0/\rho_a)^{1/4} t^{1/2}. \quad (4.4)$$

Also the decrease of the mean velocity and mixture fraction along the central axis can be described using similarity theory. Generally, due to the conservation of momentum flux at each cross-section of the jet, the velocity decay rate will decrease for increasing gas jet density. The impact of the ambient air entrainment on the jet decay are written in decay correlations:

$$\frac{u_0}{u} = K_u \frac{z}{d_{\text{eff}}}, \quad \frac{Z_0}{Z} = K_z \frac{z}{d_{\text{eff}}}, \quad (4.5)$$

with K_u and K_z the entrainment rates for velocity and mixture fraction respectively and Z_0 the mixture fraction at the nozzle exit. Thus, through the use of the effective diameter the density effect is taken into account.

There is an ongoing debate whether self similarity theory is really valid, as the decay-rate and other aspects depend considerably on the inlet conditions, e.g., Lubbers *et al.* [91]. Carazzo *et al.* [26] discusses that complete self-similarity can only be found at very large distances from the nozzle exit. At intermediate distances only self-similarity can be found at increasing heights, for identical setups. This self-similarity is different for different setups. Also Ruffin *et al.* [137] write that for variable density jets no exact self-similarity can be found, due to varying relative influences of the inertial, gravitational and viscous forces as present in the jet dynamics. On the other hand, the self-similarity model has proven its usability and global accuracy. Therefore it will be used in the discussion and analysis of the results below.

4.2.3 Modeling Diesel sprays using a gas jet

Due to the complications as given in subsection 4.2.1, it is tried to mimic the mixing process of a liquid fuel jet and the final state of the jet prior to ignition and combustion using a gas jet. One of the leading questions is how accurate such a jet simulation can represent typical liquid Diesel sprays. Obviously, some important physics will be missing, especially at the regions of large liquid void fraction close to the nozzle exit. On the other hand, further downstream where only a very dilute spray is present, it can be argued that the jet dynamics originating from a liquid spray follows the gas jet dynamics, Desantes [38].

For certain applications it has been argued that gaseous jets and Diesel sprays with small droplet size (of the order of a few microns) mix at about the same rate, when injected into air of typical Diesel chamber density and with an equivalent momentum injection rate, Ouellette and Hill [107]. Also Abraham and Magi [1] have investigated two RANS $k - \varepsilon$ based models for gas jets to mimic Diesel sprays. There it was concluded that the numerical accuracy and resolution was far more decisive than the applied modeling approach.

The question here is, which working point of a gas jet should be chosen such that the liquid fuel jet is well reproduced at the important regions where first ignition and consequently combustion will take place. Typical working point variables for liquid Diesel jets are as follows (see, e.g. Naber and Siebers [99]). With respect to the fuel: Diesel fuel density is $\rho_0 = 835 \text{ kg/m}^3$; injection pressures range between $\Delta p_{inj} = 100 - 200 \text{ MPa}$ and injection velocity $v_0 \approx 350 \text{ m/s}$. The injector nozzle radius is usually $d_0 = 0.1\text{-}0.24 \text{ mm}$. The ambient density in the cylinder at injection ranges between $\rho_a = 20\text{-}40 \text{ kg/m}^3$.

For the simulations the injection velocity is subsonic; in this work an incompressible solver is used. For the ambient density a constant value of $\rho_a = 25 \text{ kg/m}^3$ is applied. The conservation equation for energy is not solved, therefore no heat release is accounted for. The jet density ρ_0 ranged from 25 to 250 kg/m^3 , with an injection velocity of about 180 m/s . However, by correcting for the applied momentum injection rate and using the effective diameter it is assumed that the main parameters (spreading rate; turbulence intensity; jet penetration depth) can be corrected for typical engine conditions, and compared to liquid jet data.

4.3 The mixing model

For the current investigation the FASTEST-3D code has been used. This code is a incompressible finite volume, code, validated for Large-Eddy simulations on cold flow engine setups. For a more detailed description of the code, see appendix A, or e.g. Wegner [163]. The standard LES equations on the mass and momentum conservation are solved. Additionally a mixing model is applied. This will be described in the following. Then some details on the numerical setup will be provided.

4.3.1 The mixture fraction

In non-premixed combustion systems the mixture fraction Z can be used to define the chemical composition of the fluid. This scalar field for this type of problems can be written in the following way, Peters [114]:

$$Z = \frac{\nu_{st} Y_F - Y_{Ox} + Y_{Ox,2}}{\nu_{st} Y_{F,1} + Y_{Ox,2}}, \quad (4.6)$$

where the subscripts 1, 2 denote the fuel stream and air stream respectively, and Y_F and Y_{Ox} the local mass fractions of fuel and oxidizer respectively. In this equation ν_{st} refers to the stoichiometric oxidizer-to-fuel mass ratio, which can be written as (using subscript u to refer to the initial conditions in the unburnt mixture):

$$\nu_{st} = \left. \frac{Y_{Ox,u}}{Y_{F,u}} \right|_{st}. \quad (4.7)$$

Yet, for pure mixing problems, as presented in this chapter, Z simply corresponds to the injected fuel mass fraction. In the LES approach a transport equation for the filtered mixture fraction field \tilde{Z} is solved:

$$\bar{\rho} \frac{\partial \tilde{Z}}{\partial t} + \bar{\rho} \tilde{u}_j \frac{\partial \tilde{Z}}{\partial x_j} = \frac{\partial}{\partial x_j} \left(\bar{\rho} (\tilde{D}_Z + D_t) \frac{\partial \tilde{Z}}{\partial x_j} \right). \quad (4.8)$$

The mixture fraction is bounded between zero and unity: Z equals 0 in the air stream, whereas $Z = 1$ in the injected fuel stream. The LES filtered molecular and turbulent diffusion of mixture fraction is correlated to the viscosity using a constant molecular and turbulent Schmidt number:

$$\tilde{D}_z = \tilde{\nu}/Sc, \quad D_t = \nu_t/Sc_t, \quad (4.9)$$

where ν_t is modeled dynamically, using equation 2.50. In this work both Schmidt numbers are set to 0.9. Similarly, for completeness we can write a transport equation for the subgrid scale mixture fraction variance $\widetilde{Z''^2}$ as [114]

$$\bar{\rho} \frac{\partial \widetilde{Z''^2}}{\partial t} + \bar{\rho} \tilde{u}_j \frac{\partial \widetilde{Z''^2}}{\partial x_j} = \underbrace{\frac{\partial}{\partial x_j} \left(\bar{\rho} D_t \frac{\partial \widetilde{Z''^2}}{\partial x_j} \right)}_I + \underbrace{2\bar{\rho} D_t \left(\frac{\partial \tilde{Z}}{\partial x_j} \right)^2}_{II} - \underbrace{2\rho D_Z \left(\frac{\partial \tilde{Z}}{\partial x_j} \right)^2}_{III}. \quad (4.10)$$

The three terms in above equation denote I the turbulent transport, II the $\widetilde{Z''^2}$ production and III the filtered scalar dissipation rate, given by

$$\tilde{\chi} = 2D_Z \left(\frac{\partial \tilde{Z}}{\partial x_j} \right)^2. \quad (4.11)$$

Notice that in the LES approach the mixture fraction variance transport equation is usually not solved. Instead an analytical model is used to describe the unresolved part. Then, to find an estimate of the mixture fraction variance, a similar procedure

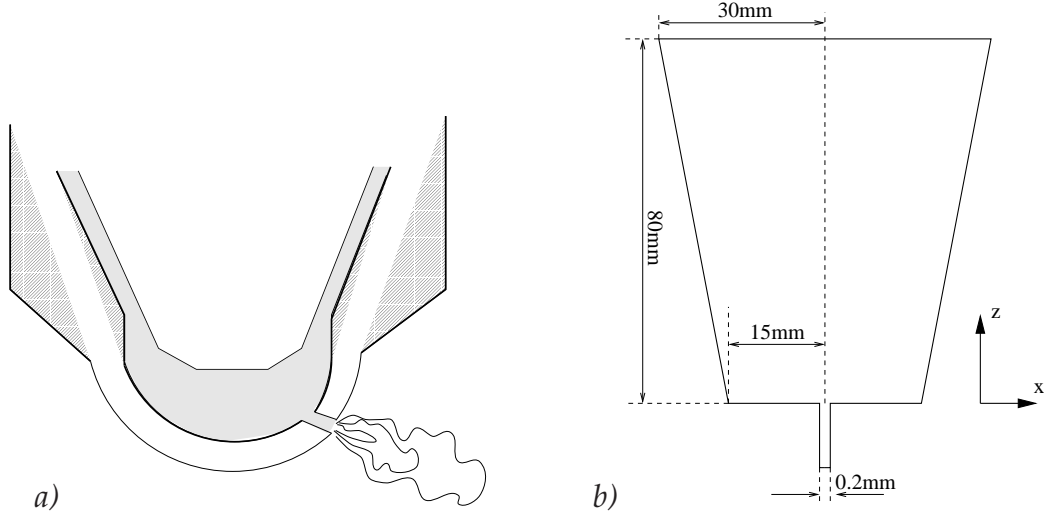


Figure 4.2 : (a) Schematics of the gas injection system. (b) Applied geometry for the performed simulations

Table 4.1 : List of performed simulations. Subscript 0 denotes the values at the nozzle exit and ρ_a denotes the ambient density that is set to 25 kg/m³.

Simulation	number of cells	ρ_0/ρ_a	ρ_0 kg/m ³	ν_0 m ² /s	M_0 (kgm/s ²)	Re ₀
Jet 1A	50,000	1	25	2.68×10^{-5}	19.6×10^{-3}	1300
Jet 1B	50,000	2	50	1.2×10^{-5}	39.3×10^{-3}	3000
Jet 2A	400,000	1	25	2.68×10^{-5}	21.3×10^{-3}	1300
Jet 2B	400,000	2	50	1.2×10^{-5}	42.3×10^{-3}	3000
Jet 2C	400,000	10	250	1.05×10^{-5}	209×10^{-3}	3400

as for the sgs turbulence intensity q_{sgs}^2 can be followed, see section 2.3.1. By assuming local equilibrium, the production balances the scalar dissipation rate. Then, by scaling analysis this leads to a model for $\widetilde{Z''^2}$ of the form (Branley [22])

$$C_Z \left(\frac{\partial \tilde{Z}}{\partial x_j} \right)^2 = \frac{\widetilde{Z''^2}}{\Delta^2}. \quad (4.12)$$

In this equation, for C_Z the value of 0.15 is assumed, Wegner [163].

4.3.2 The numerical setup

A typical gas-injection system is characterized by a small nozzle ($\sim 0.1 - 0.4$ mm), that injects fuel at high speeds into a pressurized combustion chamber, as is schematically shown in figure 4.2a. The gas enters the chamber perpendicular to the surrounding exit plane. The numerical setup is designed as shown in figure 4.2b. The diameter of the injector orifice is $d_0 = 0.2$ mm. Mass is injected with a maximum velocity speed of $U_0 = 180$ m/s; the average jet velocity at the nozzle exit was about 140 m/s. Then, a time scale can be defined: $\tau^* = d_0/U_0 = 4.5\mu s$. For the jet correlated inflow data has been generated with turbulent statistics corresponding to a turbulent pipe flow, Eggels [43]. In total five independent simulations have been

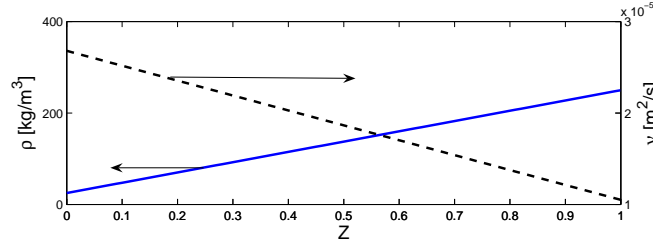


Figure 4.3 : Viscosity ν and density ρ as function of the mixture fraction Z , shown for *Jet 2C*.

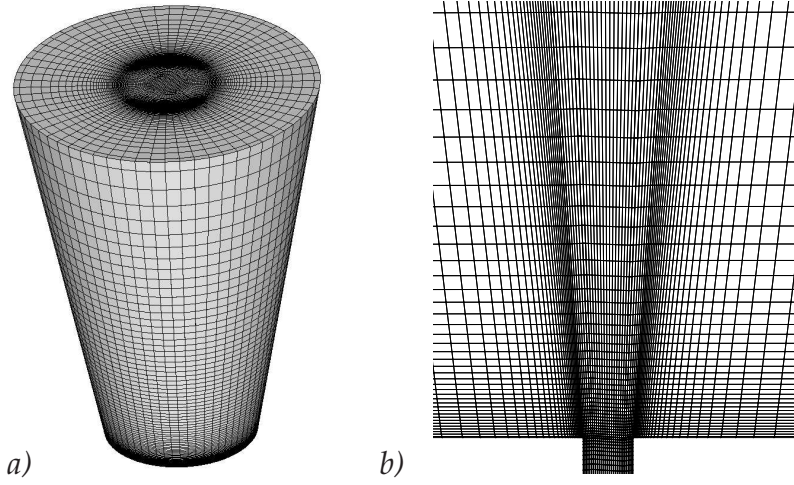


Figure 4.4 : (a) Sketch of the applied mesh. (b) Cross section around the nozzle for the fine grid simulations.

performed, on two different meshes and applying three different density ratios, see table 4.1.

The ambient density ρ_a in all simulations was set to 25 kg/m^3 , which is typical for the ambient air density in an engine around top dead center, and comparable to the gasjet study performed by Desantes [38]. Three density ratios have been studied: one where the fuel injection density ρ_0 was equal to the ambient gas density ρ_a , and an additional simulation with a density ratio $\rho_0/\rho_a = 2$, which corresponds to a type of fuel with twice the density of air, e.g., ethane. The third density ratio reached a level of $\rho_0/\rho_a = 10$, i.e., the injected fuel had a density of 250 kg/m^3 , which corresponds to a more practical engine fuel.

The viscosity has been computed from correlations provided by Evlampiev [44]. Here, data from the ethane fuel for the specific conditions lead to values ranging from $2.68 \times 10^{-5} \text{ m}^2/\text{s}$ for the ambient gas viscosity and $1.05 \times 10^{-5} \text{ m}^2/\text{s}$ for the fuel viscosity at 250 kg/m^3 . A linear dependence is applied for the laminar mixing of the fuel and ambient gas densities and viscosities, as is described in Evlampiev [44]. Then the applied mixing rules $\tilde{\nu} = \nu(\tilde{Z})$, $\tilde{\rho} = \rho(\tilde{Z})$ for simulation *Jet 2C* is presented in figure 4.3. The Reynolds number based on the nozzle diameter, the maximum velocity and the fuel viscosity at the nozzle exit ranged between 1.3×10^3 and 3.5×10^3 .

The applied mesh is shown in figure 4.4. The height of the computational domain was set to 8 cm , which corresponds to a scaled height of $H = 400d_0$. For the

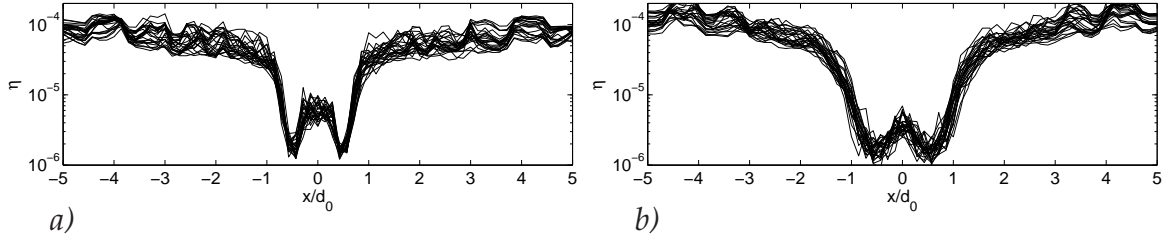


Figure 4.5 : (a) Instantaneous recordings of the Kolmogorov length scale η [m] for simulation *Jet 2A* at $z/d_0=0.5$ above the nozzle exit. (b) η at $z/d_0 = 2.5$

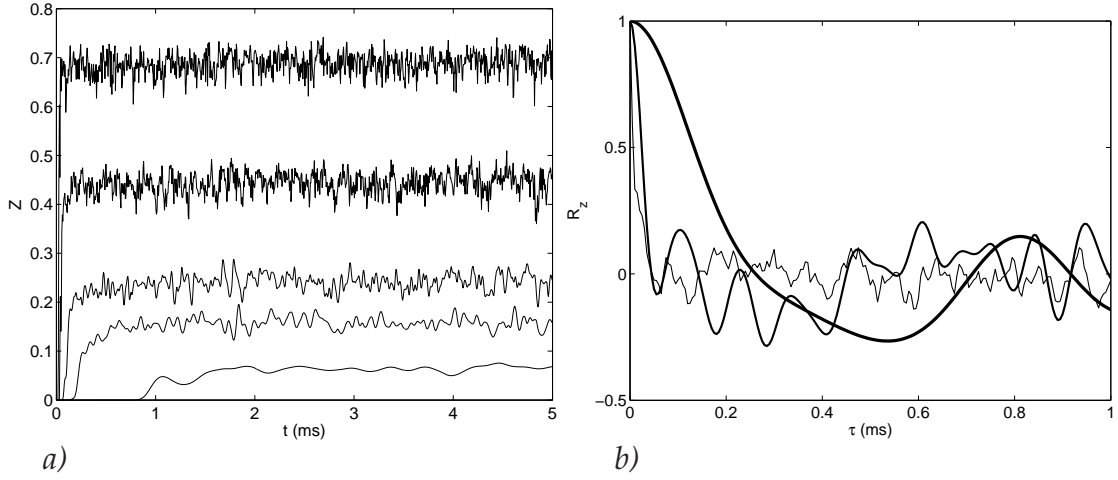


Figure 4.6 : (a) Evolution of mixture fraction field for simulation *Jet 2A*, at five different heights above the nozzle exit: $z/d_0 = 15, 20, 30, 40$ and 80 from top to bottom. (b) Correlation functions R_z for the mixture fraction at three different heights at the central axis, $z/d_0 = 20, 40$ and 80 , marked with increasing line thickness.

fine grid the number of grid cells in every direction has been doubled, compared to the coarse grid. In simulations *Jet 1A* and *Jet 1B* the cell size at the nozzle exit is of the order of $13 \mu\text{m}$, while for the fine grid this is $6.7 \mu\text{m}$, see figure 4.4b. The minimal Kolmogorov scale, evaluated using equation 2.8, and equation 2.33 for the dissipation term, was about $1.5 \mu\text{m}$ for simulation *Jet 2A* (figure 4.5) to $1 \mu\text{m}$ for *Jet 2B* and $0.8 \mu\text{m}$ for *Jet 2C*. Thus, with the applied grid spacing the ratio Δ/η is approximately 4 to 7 and 8 for simulation *Jet 2A*, *Jet 2B* and *Jet 2C* respectively. A dynamic Smagorinsky model has been applied to model the subgrid-scale turbulence.

4.4 Results

The steady state behaviour of the turbulent jet can be analyzed if the jet flow is well developed. This depends on the location of the jet, see figure 4.6a. Close to the nozzle exit the averaging procedure can start relatively early, whereas higher up in the domain it takes longer before steady state is reached. Also sufficient statistical information should be present to perform a proper analysis. In figure 4.6 the temporal correlation length is plotted for three different locations, for simulation *Jet 2A*. A turbulent time scale can be defined based on the first crossing of the line $R_z = 0$. Close to the nozzle exit, at $z/d_0 = 20$, the fields remain strongly correlated for about

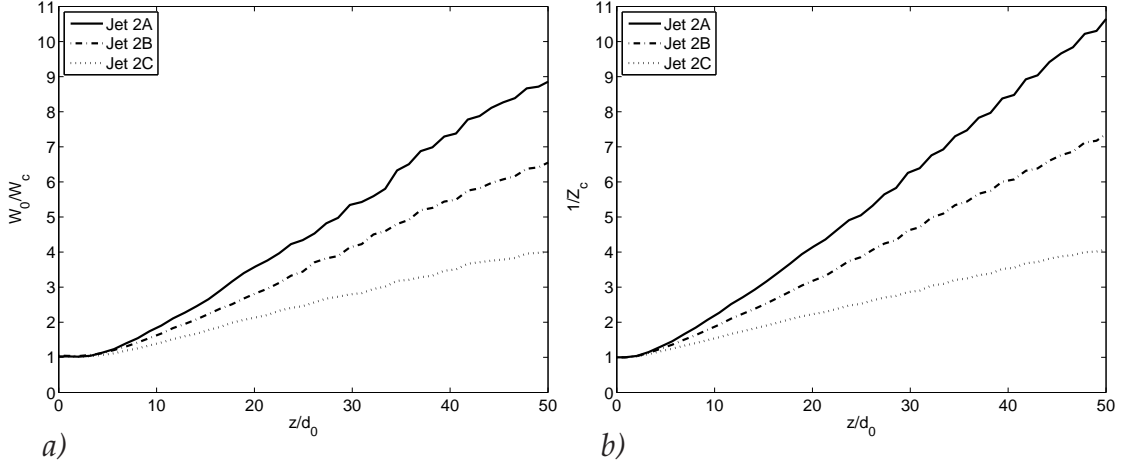


Figure 4.7 : (a) Inverse velocity decay and (b) inverse mixture fraction decay at the centerline, as a function of z/d_0 , for the two different density jets.

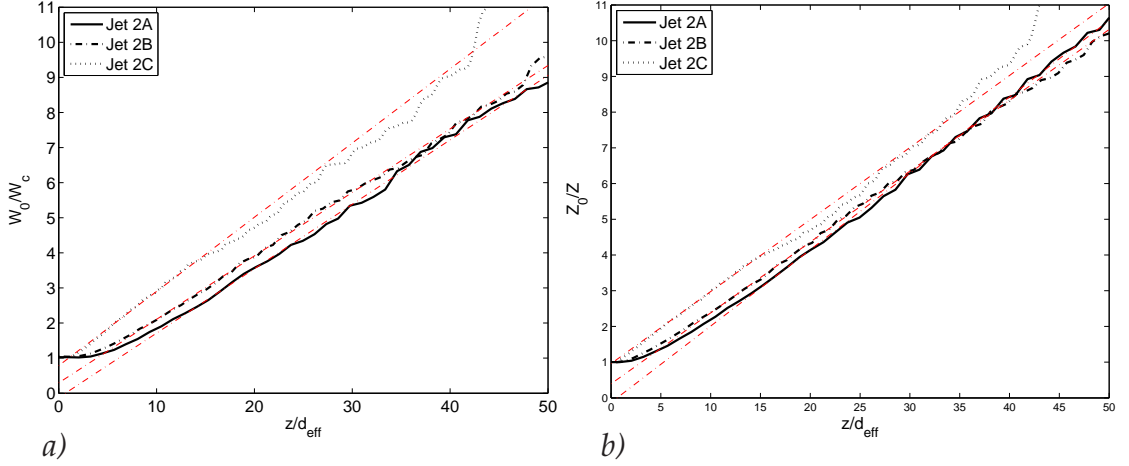


Figure 4.8 : (a) Inverse velocity decay and (b) inverse mixture fraction decay at the centerline, as a function of z/d_{eff} , for the two different density jets

0.05 ms. This is similar at $z/d_0 = 40$ and increases for $z/d_0 = 80$ up to about 0.3 ms. The total simulation time was always 5 ms, which means that up to $z/d_0 = 40$ about 100 statistically independent realizations could be used. Therefore, up to this height the steady state behaviour will be examined, as presented in the first subsection. In the next subsection, results on the unsteady, developing behaviour is presented.

4.4.1 Steady state behaviour

The decay of the averaged inverse centerline velocity and mixture fraction is shown in figure 4.7. Here on the horizontal axis the depth is scaled to the nozzle diameter d_0 . Then, for both figures it can be seen that the velocity decay is reduced with increasing jet density. The unscaled core length remains constant for all three density cases, as is visible from figure 4.7. This is in correspondence with numerical observations from RANS calculations, Sanders *et al.* [138]. Here it was remarked that in the far field, where the density across the jet is almost uniform, the similarity theory applies well. A more universal decay rate is found when scaling the depth with the

Table 4.2 : Predicted velocity and scalar decay rates K_u and K_z and predicted spreading rates S_u and S_z , compared to data from literature. The reference data is at ρ_0/ρ_a is unity.

Simulation	K_u	K_z	S_u	S_z
<i>Jet 1A</i>	0.113	0.146	-	-
<i>Jet 1B</i>	0.095	0.117	-	-
<i>Jet 2A</i>	0.184	0.214	0.091	0.108
<i>Jet 2B</i>	0.181	0.198	0.094	0.108
<i>Jet 2C</i>	0.211	0.202	0.095	0.101
experimental	0.165 [109] - 0.169 [67]	0.21 [133]	.096 [109]	.113 [133]
RANS SMC	0.218 [138]-0.20 [137]	0.247 [138]-0.25 [137]	0.128 [138]	0.144 [138]
DNS [91]	0.164	0.182	.092	0.108

effective nozzle diameter d_{eff} , see figure 4.8. Then, the decay rate constants K_u and K_z for all three jets show similar values. The only visible difference concerns the length of the core region. This is shorter for increasing density gradient and can be explained from the applied scaling. These near-field effects cannot be described by the similarity theory given in section 4.2.2.

The constants K_u and K_z as defined in equation 4.5, are listed in table 4.2 for the performed simulations. These rate constants have been defined using a least squares method, based on data ranging from $z/d_{\text{eff}} = 10 - 50$. The most important observation is that the coarse mesh simulations strongly under-predict the decay rates compared to the other simulations and reference data. This is probably due to an under-resolved level of turbulence, thereby laminarizing the jet flow and thus reducing the decay rates. Therefore these simulations are discarded for the remainder of this analysis.

The decay rates K_u as reported in experiments range between 0.165 [109] to 0.169 [67], depending on the exact inlet conditions. Thus, the computed decay rates from simulations *Jet 2A* and *Jet 2B* are slightly over-predicted. However, an improvement is reached compared to reported RANS simulations, [138] and [137]. At the same time, the DNS simulation as performed by Lubbers [91] reports a smaller value, both compared to reported experiments and to the current simulations. This shows a trend of decreasing modelled decay rates, with decreasing amount of modeled subscale energy, when comparing RANS, LES and DNS data. The same holds for the decay rates for the mixture fraction. Again, an exact comparison between the different setups is not possible, as the definition of the exact inlet conditions will play an important role for these decay rate details. Another observation is that the decay rate of mixture fraction is larger than that of momentum, i.e. the concentration field spreads faster than the velocity field. This is in agreement with observations from Sanders [138] and Lubbers [91]. A preferential transport of scalar over momentum is observed in correspondence to the applied the Schmidt numbers.

The mean axial velocity and mixture fraction at two different heights in the jet are plotted in figure 4.9 and 4.10 respectively. This shows a clear indication of the self-similarity of the flow, using the scaling of the spanwise coordinate

$$r_s = r/(z - z_0) \quad (4.13)$$

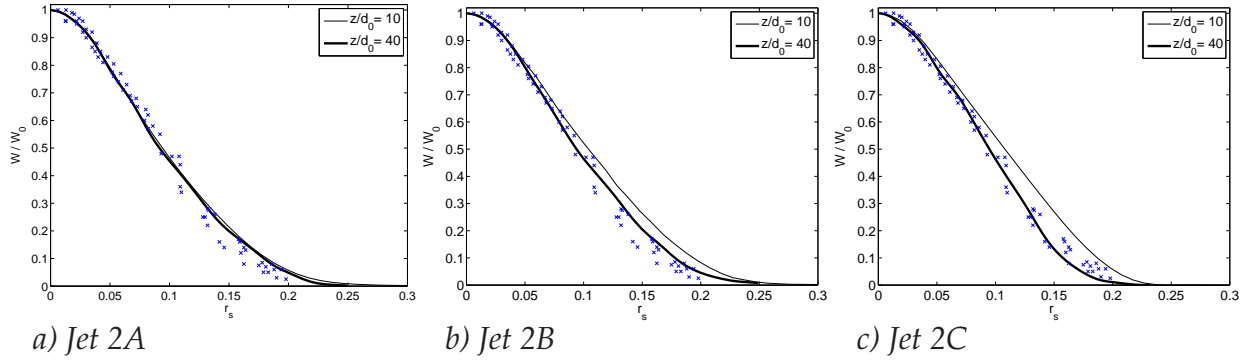


Figure 4.9 : Mean axial velocity as a function of the self-similarity coordinate r_s for simulation *Jet 2A*, *Jet 2B* and *Jet 2C*, at two different heights above the nozzle exit. \times : experiments by Panchapakesan [109].

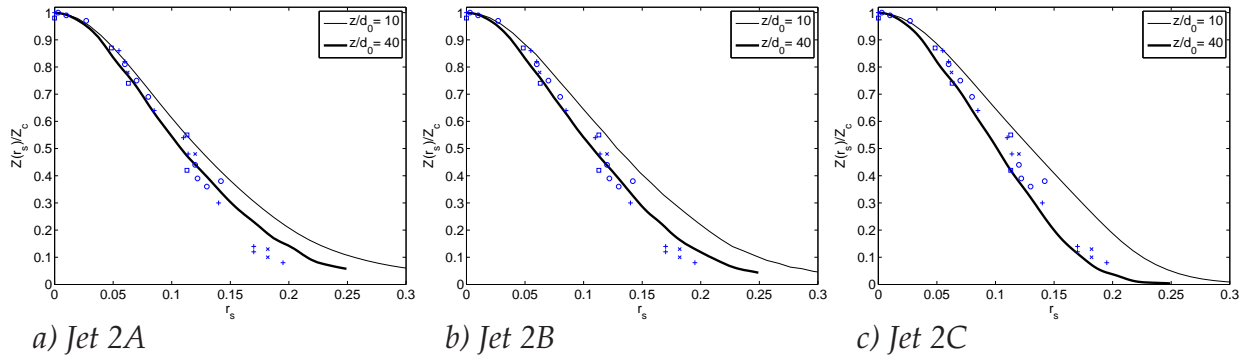


Figure 4.10 : Mean mixture fraction as a function of the self-similarity coordinate r_s for simulation *Jet 2A*, *Jet 2B* and *Jet 2C*, at two different heights above the nozzle exit. Symbols: experiments by Dowling [41].

with z_0 the virtual origin of the jet. Still, there exists some difference between the solution at the different heights. A better correspondence is found at $z/d_0 = 40$. This can be due to the applied inlet conditions for this simulation, which are tuned to match engine conditions. The spreading rates S_u and S_z , are given in table 4.2. These values are defined as the half-width values of r_s , i.e. the scaled radial coordinate where the velocity and mixture fraction are half the centerline values: $\langle \tilde{w} \rangle = \langle \tilde{w}_c \rangle / 2$, $\langle \tilde{Z} \rangle = \langle \tilde{Z}_c \rangle / 2$ respectively. These values have been defined at the location $z = 40d_0$ above the nozzle, where the self-similar solution is well established. Compared to the experimental values and the DNS data, the spreading rates are very well predicted. It is found that the spreading rate S_z is constantly larger than S_u , in line with experiments and other simulations, and in line with the larger decay-rate K_z , compared to K_u , indicating the more progressive transport of the scalar field.

Turbulence statistics

The Reynolds shear stress as a function of r_s is presented in figure 4.11. The thin lines represent the resolved shear, $\langle \tilde{u}'' \tilde{w}'' \rangle$, while the thick lines in the figures are

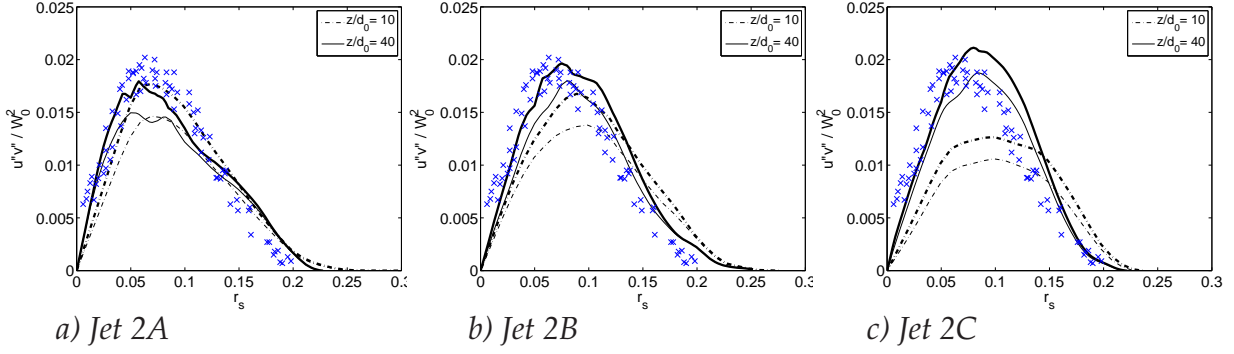


Figure 4.11 : Reynolds shear stress as a function of the self-similarity coordinate r_s at two heights above the nozzle exit, for simulation *Jet 2A*, *Jet 2B* and *Jet 2C*. \times : Panchapakesan [109]. Thin lines represent the resolved part, thick lines the total shear stress.

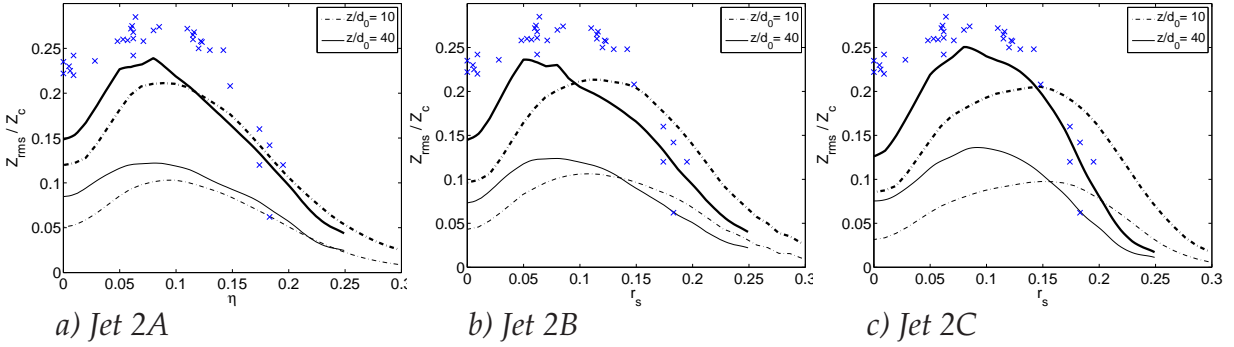


Figure 4.12 : rms of the mixture fraction, scaled with mean axial mixture fraction, as a function of the self-similarity coordinate r_s , for simulation *Jet 2A*, *Jet 2B* and *Jet 2C*. Thin lines: Resolved RMS of mixture fraction variance, thick lines: total rms of mixture fraction. \times : Experiments by Dowling [41].

related to the total shear, including the subgrid-scale part. This is evaluated by

$$\tau_{ij} = \langle \tilde{u}'' \tilde{w}'' \rangle + \langle \nu_t \left(\frac{\partial \tilde{u}}{\partial z} + \frac{\partial \tilde{w}}{\partial x} \right) \rangle, \quad (4.14)$$

with $\langle . \rangle$ denoting averaging over time. The simulation data is compared to experimental data from Panchapakesan and Lumley [109], where no density gradient was present. Then, it is observed that the profiles of the shear stress at $z/d_0 = 10$ and 40 start to differ more with increasing density ratio. This can be explained by the applied absolute scaling of the vertical coordinate with d_0 . For the higher density ratios the jet is still more in its early development period. Then the shear stress is not well reproduced at $z/d_0 = 10$, see figure 4.11c. At $z/d_0 = 40$ the magnitude and shape is generally well captured in all simulations, when taking into account the unresolved part. A slight trend is visible comparing the three simulations: an increase of maximum shear stress with increasing density ratio.

Figure 4.12 shows the radial distribution of the mixture fraction variance, which is usually called the unmixedness, Z_{rms}/Z_c . The thin lines are referring to the resolved part $\langle \tilde{Z}'' \tilde{Z}'' \rangle$, and the thick lines to the total variance, including the subgrid scale part. Here the averaged subgrid mixture fraction variance $\langle \tilde{Z}''^2 \rangle$ is evaluated

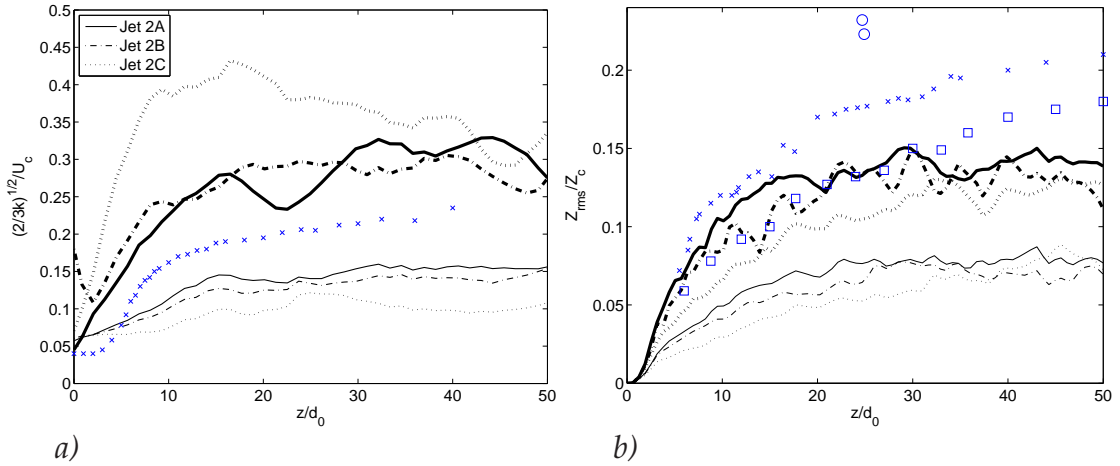


Figure 4.13 : (a) Scaled turbulent kinetic energy along the jet axis. Thin lines: resolved part of turbulent kinetic energy k ; thick lines: total k ; \times : experiments [4]. (b) Mean axial mixture fraction variance along the jet axis. Thin lines: Resolved RMS of mixture fraction variance, thick lines: total Z_{rms} . Experiments from Birch [18]: \times , Dahm [34]: \square and Dowling [41]: \circ .

using the equilibrium model, equation 4.12. The simulation data is compared to experimental data from Dowling and Dimotakis [41]. In the present simulations a substantial part of the total mixture fraction variance is in the subgrid scales: these magnitudes are approximately equal in size as the resolved scales. Still the total mixture fraction is relatively well predicted. This shows that the mixture fraction field can be modelled adequately at this resolution. However, if the mixture fraction will have a more drastic effect on the flow field than in these simulations it is advised to increase the resolution, until about 80% of the turbulence intensity is resolved, Pope [129]. No large difference can be observed between the three simulations. As was also observed in the results of τ_{ij} in figure 4.11, the profiles close to the nozzle exit, at $z/d_0 = 10$, are spreading out more in radial direction. This effect increases with increasing density ratio.

Similarly as looking to the fluctuations in the mixture fraction field the turbulent kinetic energy k can be considered. Again, the contribution of the resolved part $q_{res} = 0.5 \langle \tilde{u}_i'' \tilde{u}_i'' \rangle$ and a subgrid scale part q_{sgs}^2 can be considered. The latter is estimated using the formulation proposed by Lilly [88]:

$$q_{sgs}^2 = \frac{\nu_t^2}{(C_\mu \Delta)^2}, \quad (4.15)$$

with C_μ equal to 0.094. With this expression the q_{sgs}^2 can be evaluated directly from the local filtersize and turbulent viscosity. However, this model is known for its overprediction of the subgrid scale energy, Klein [74]. Also information on the dynamic coefficient C in equation 2.53 has not been included. Figure 4.13a shows the turbulent kinetic energy along the central axis, scaled using the local centerline velocity. The results are compared to the air-air jet experiments from Amielh [4]. It shows that the resolved turbulence intensities are lower than the experimental ones, suggesting that the subgrid-scale contribution should be included. However, with this inclusion the total kinetic energy is over-estimated, specially in case *Jet 2C*. This

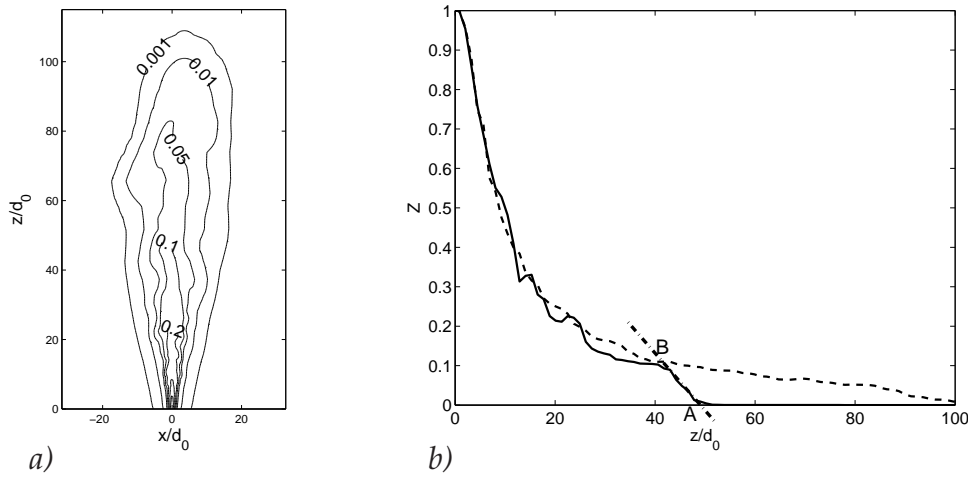


Figure 4.14 : (a) Instantaneous contour plot of the mixture fraction field at a single sheet, $y = 0$, $t = 2$ ms, simulation *Jet 2A* (b) instantaneous mixture fraction profiles for two time steps, (—) $t = 0.5$ ms and (- - -) $t = 2$ ms. Point A denotes the jet forefront and B the backside of the front jet.

leads to the conclusion that the estimation of the sgs energy by equation 4.15 still is too large. However, for a better estimation of the turbulence intensity it will be necessary to increase the resolution close to the nozzle exit.

Figure 4.13b shows the axial mixture fraction variance, scaled to the average local mixture fraction Z_{rms}/Z_c . In this figure experimental data from three independent sources are plotted. These simulations agree relatively well with the experimental data from Birch [18] and Dahm [34]. On the other hand, the agreement with the measurements from Dowling is rather poor, similar as was found previously for Z_{rms}/Z_c at the central axis in figure 4.12.

4.4.2 The unsteady behaviour of the turbulent gas jet

Important parameters regarding the unsteady behaviour of a gas jet are the penetration depth, the change in cone angle and the development of coherent structures. To study these unsteady phenomena in fuel jets experimentally, often visual methods are used, where light rays traverse through the experimental setup: so-called line-of-sight methods, thereby integrating information over the light ray path. It is helpful to apply such methods to the numerical data, in order to study the specific measurement setup behaviour numerically. In this section, first some experimental methods are introduced and applied to the numerical data. Next, using some of these techniques, the numerical data are compared to gas jet models, and also to liquid jet models, with respect to the penetration depth and the cone angle.

The definition of the penetration depth

It is generally not clear how to compare the numerical data from the simulations to the experimental data. One of the difficulties is related to the definition of the jet tip. The jet tip is the upper point of the jet, which defines the penetration depth, and is found at the location where the mixture fraction drops to zero.

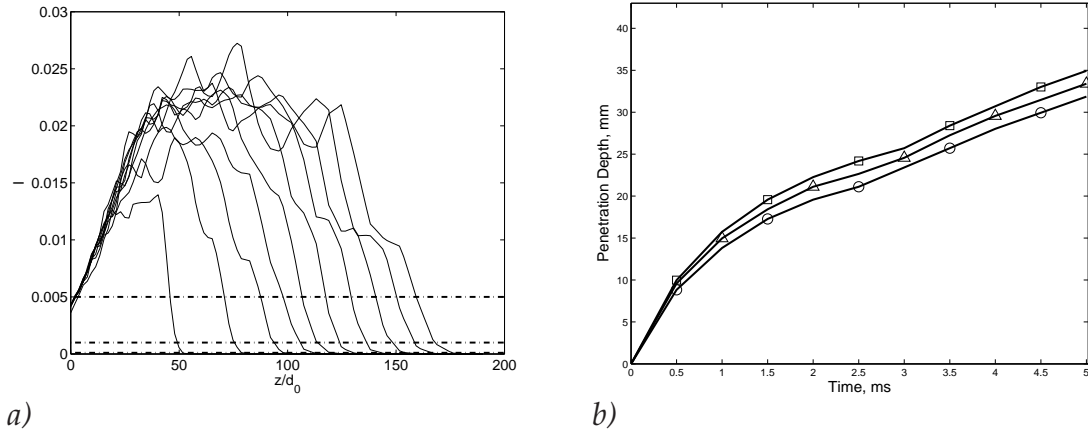


Figure 4.15 : (a) Integrated mixture fraction profiles I for simulation *Jet 2A*, as a function of time. (b) Penetration depth for different mixture fraction limits. \circ : $I = 0.005$, \triangle : $I = 0.001$, \square : $I = 0.0001$.

However, from simulations this location is not completely well defined. This can be illustrated from figure 4.14a, where the instantaneous mixture fraction field at the plane $y = 0$ is shown, which is the central plane through the nozzle jet. Then the mixture fraction field reduces with increasing height. But a zero value cannot easily be defined. One method, as shown by Ouellette [107], is to define the penetration depth by the location where the tangent to the steepest part of the forefront intersects with the axis, point A in figure 4.14b. This method is well applicable for limited penetration depths. However, with increasing time the plateau levels off, making it difficult to extrapolate the forefront position. Also the change of the slope that identifies the beginning of the jet head, denoted as point B, becomes less visible, see figure 4.14b.

A simple method though is to define a cutoff level of the mixture fraction at the center axis. This can easily be realized and can give a proper indication. However, in this case the cutoff level itself is a matter of discussion. A standard practise from experimental methods (e.g. Klein-Douwel [75]) is to integrate the total mixture fraction field as a function of the height, figure 4.15a. Here, the total integral $I(z)$ is defined as

$$I(z) = \int_V \tilde{Z} dV^*(z), \quad (4.16)$$

where $dV^*(z)$ denotes a volume slice at a height z , and thickness dz . Notice that the absolute value of this integral does not have a meaning, it will only be used to define a (relative) cutoff height. In this method the jet tip does not necessarily have to lie at the center axis. Thus a cutoff level for I has to be defined, to relate a penetration depth to the integral. As shown in figure 4.15b, the observed quantities, such as penetration depth, can vary up to 10% in magnitude, depending on the chosen cutoff criterion.

The virtual Schlieren method

In engine-like environments fuel jets are typically studied experimentally using optical methods, e.g., Klein-Douwel [75]. In this work a reconstruction of a Schlieren

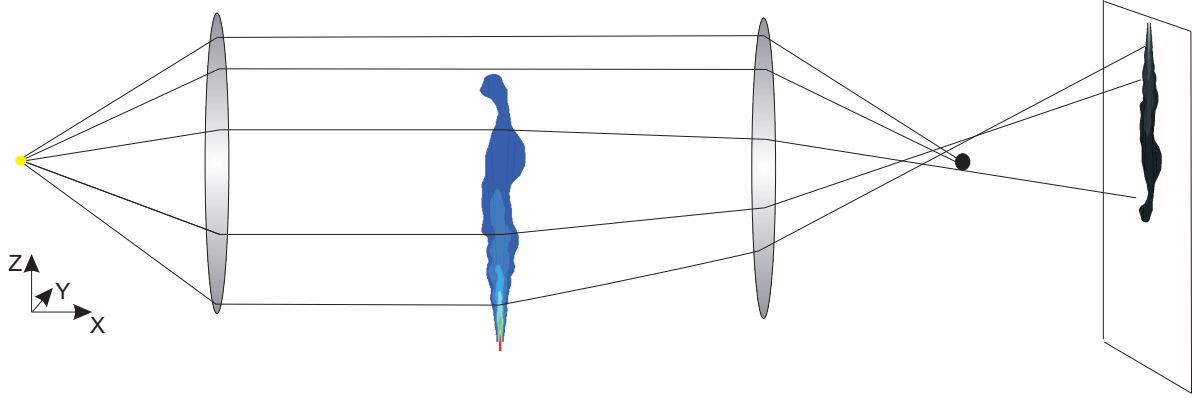


Figure 4.16 :Setup applied in Schlieren reconstruction method. The projected jet on the screen illustrates the area where the light rays are visible.

image is performed, based on the numerical dataset from our simulations. In this way the numerical data is treated similarly compared to an experimental Schlieren setup. Schlieren imaging is a visualization of the integrated density-gradient through the jet, as illustrated in figure 4.16, see, e.g., Settles [143]. To perform the Schlieren reconstruction a ray tracing technique is developed. This can be deduced from several methods, Hecht [61]. Here the derivation of Sutherland [151] is followed. Starting from Snell's Law, a path taken by a ray of light satisfies

$$n \cos \phi = \text{Const.} \quad (4.17)$$

Here $n(x, y, z)$ is the refractive index and $\phi(x, y, z)$ is the angle corresponding to the light ray and a surface of constant n . The next step is to introduce a ray coordinate $s(x, y, z)$ and decompose this into the coordinates perpendicular and parallel to surfaces of constant n , s_{\perp} and s_{\parallel} respectively, see figure 4.17. Using that the differentiation of these coordinate directions are written as

$$\frac{ds_{\perp}}{ds} = \sin \phi \quad , \quad \frac{ds_{\parallel}}{ds} = \cos \phi, \quad (4.18)$$

it can be derived, [151] that

$$\frac{d^2 s_{\perp}}{ds_{\parallel}^2} = \frac{1}{\cos^2 \phi} \frac{\partial \phi}{\partial s_{\parallel}} = \frac{1}{n \cos^2 \phi} \frac{\partial n}{\partial s_{\perp}}. \quad (4.19)$$

This equation relates the deflection of the light ray in perpendicular direction s_{\perp} to the gradient of the refractive index in this direction. The effects of the streamwise variation (the along-ray variation) can be ignored if $\partial n / \partial s_{\perp}$ remains finite while $|ds_{\perp} / ds_{\parallel}| \ll 1$, i.e., when the local deflection remains very small. Now, when s_{\parallel} is taken in the x -direction, see figure 4.16, relationship 4.19 can be simplified and linearized to light rays described with functionalities $y = \xi(x)$, $z = \zeta(x)$:

$$\frac{d^2 \xi}{dx^2} = \frac{1}{n \cos^2 \phi_y} \frac{\partial n}{\partial y} \quad (4.20)$$

$$\frac{d^2 \zeta}{dx^2} = \frac{1}{n \cos^2 \phi_z} \frac{\partial n}{\partial z} \quad (4.21)$$

$$(4.22)$$

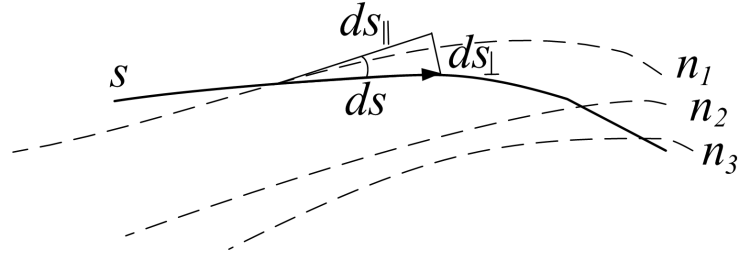


Figure 4.17 :Geometrical orientation of the deflection of the light rays.

where ϕ_y and ϕ_z represent the angles of the incident light ray related to the x -axis, in y - and z -directions respectively. For small angles, $\cos \phi \approx 1$, such that this set of equations can be simplified to

$$\frac{d^2 \xi}{dx^2} = \frac{1}{n} \frac{\partial n}{\partial y} \quad (4.23)$$

$$\frac{d^2 \zeta}{dx^2} = \frac{1}{n} \frac{\partial n}{\partial z} \quad (4.24)$$

$$(4.25)$$

The integration of this equation then can be written, initially assuming the light rays to be parallel to the x -axis:

$$\xi(x) = y(0) + \int_0^x \epsilon_y(x') dx' \quad (4.26)$$

$$\zeta(x) = z(0) + \int_0^x \epsilon_z(x') dx' \quad (4.27)$$

Here ϵ_y and ϵ_z denote the local light deflection, written as

$$\epsilon_y(x) = \int_0^x \frac{1}{n} \frac{\partial n}{\partial y} dx', \quad \epsilon_z(x) = \int_0^x \frac{1}{n} \frac{\partial n}{\partial z} dx'. \quad (4.28)$$

These equations model the ray deflection ϵ in both perpendicular directions y and z , when traversing in x -direction. The relationship between the refractive index and the density is assumed to be linear, Settles [143], which leads to

$$\frac{\partial n}{\partial y} = \frac{dn}{d\rho} \frac{\partial \rho}{\partial y} = \beta \frac{\partial \rho}{\partial y}, \quad (4.29)$$

where β is a constant. Additionally, in our computations the density field for this mixing problem is linearly related to the mixture fraction. Therefore the mixture fraction and density are directly exchangeable for analysis. By filtering out the non-deflected rays using a stop at the focal point, as illustrated in figure 4.16, an image of the integrated density gradient is recovered. This picture largely depends on the location of the rays at the focal point. The radial distance from the focal point E_r is defined as

$$E_r = \sqrt{\xi^2(x_{fp}) + \zeta^2(x_{fp})} \quad (4.30)$$

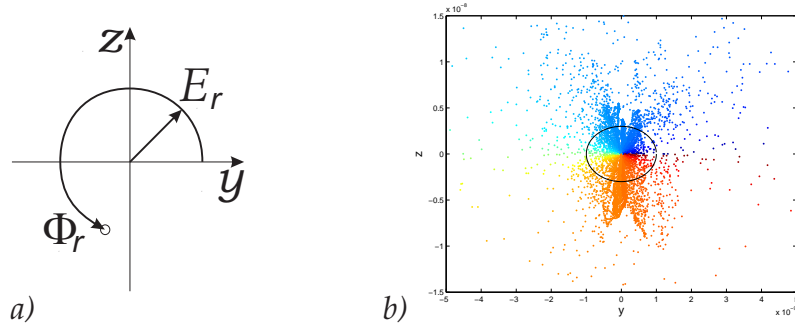


Figure 4.18 : (a) Classification of resulting Schlieren ray $r(y, z)$, evaluated at the focal point. This can be described with a total deflection angle Φ_r and deflection magnitude E_r . (b) Typical scatter plot of light rays at the focal point. The circle denotes the filtering level E_F .

and is compared to the focal point filter size E_F . Also a deflection angle Φ_r can be reconstructed from the (y, z) coordinates at the focal point, see figure 4.18a. This is a measure of the total integrated deflection angle. Both the magnitude and the angle give information of the flow field that has been traversed. Notice that also an inverse figure can be generated, by filtering away all the deflected light rays. Then instead of a stopper a pinhole should be used experimentally and numerically.

Equations 4.26, 4.27 are integrated numerically in the virtual Schlieren method. In order to get sufficient resolution a large number of rays is followed through the domain. In present analysis a number of $N_y \times N_z = 70 \times 100$ rays are tracked. A typical result of a scatter of the light rays at the focal is plotted in figure 4.18b. A simplification to the ray tracing method is possible if it is assumed that the deflection angle remains very small. Then the Schlieren image will directly scale to the integrated transverse density gradients, because as a first order estimation the rays remain at their original (y, z) coordinates. Then the total deflection magnitude E_i scales to

$$E_i = \int \left(\left| \frac{\partial \rho}{\partial y} \right|^2 + \left| \frac{\partial \rho}{\partial z} \right|^2 \right)^{1/2} dx. \quad (4.31)$$

For this numerical method also a measure for the deflection angle can be defined:

$$\Phi_i = \arctan \left(\frac{\int \left| \frac{\partial \rho}{\partial y} \right| dx}{\int \left| \frac{\partial \rho}{\partial z} \right| dx} \right). \quad (4.32)$$

Comparing visualisation methods

In the previous two subsections three visualization methods have been proposed. One is based on a single sheet mixture fraction field, using a cutoff mixture fraction level. This method is referred to as the *direct field* visualization. The next is based on the *virtual schlieren* visualization technique, following the path of the light rays. The last method is a simplified variant of the previous method, referred to as the *integrated gradient* visualization. The different integration methods are qualitatively compared to each other in figure 4.19 for simulation *Jet 2A*, after 1 ms.

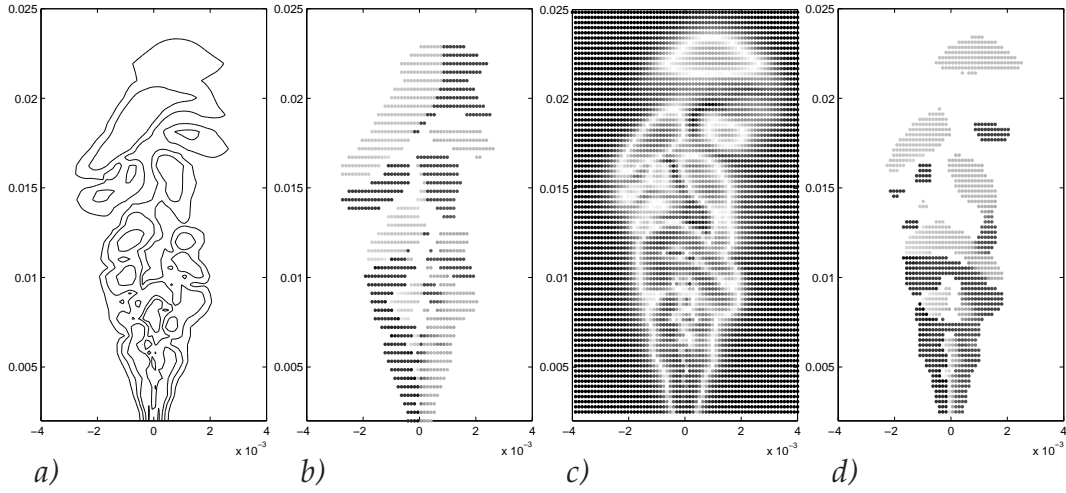


Figure 4.19 :Qualitative comparison of different line of sight imaging procedures for it Jet 2A. (a) *integrated gradient* (b) *integrated gradient* colored by the deflection angle Φ_i (c) *Virtual Schlieren* colored using a *distance from focal point measure* (d) *Virtual Schlieren* colored by the deflection angle Φ_S .

Previously, in figure 4.14a, the *direct field* method has been shown for the symmetry intersection plane $y = 0$. This figure shows a broad range of contours, and only few turbulent structures. Compared to this figure, more turbulent structures are visible when using any of the two line-of-sight methods as shown in figure 4.19. With increasing heights the turbulent structures become larger as well. In figure 4.19b additional information on the direction of the transverse gradient is included by coloring (using gray-scales) the contours of E_i using information of the deflection angle Φ_i . This includes information of the orientation of the vortical turbulent structures. The *Virtual Schlieren* method, as presented in figures 4.19c and d exhibit largely similar structures as the previous two figures. Figure 4.19c presents a (gray-scale) color plot of the distance to the focal point. This is a measure of the ray deflection, which is closely related to the integrated magnitude of density gradient.

The last figure 4.19d includes again information on the angle of deflection. This is largely comparable with figure 4.19b. Therefore it is shown that for the performed simulations a detailed ray-tracing method is not necessary, as the ray deflection remains very small, and therefore the ray remains mainly normal to the plane of measurement. The density gradients can simply be integrated in the direction of the incident rays, to get a qualitative visualization that can be compared to an experimental Schlieren imaging.

Coherent structures

Figure 4.20 shows the development of the turbulent jet, simulation *Jet 2C*, as obtained from the *virtual schlieren* procedure. Here the movement of the turbulent structures can be identified. The top of the jet is moving upward whereas the total magnitude of deflection is weakening. As time progresses, coherent turbulent structures are released and moving upward. Already from this figure the jet penetration depth development can qualitatively be observed, as well as information on the cone angle. These items will be discussed in the following two subsections.

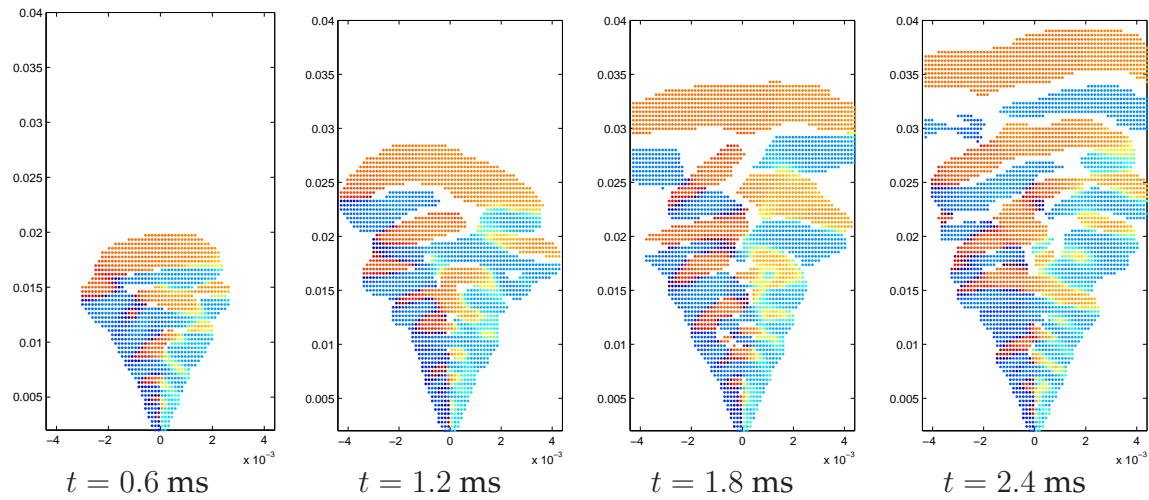


Figure 4.20 :Development of *Jet 2C* for subsequent times separated by 0.6 ms, visualized with the virtual Schlieren method. The different color scales in the plots are related to the deflection angle Φ_r .

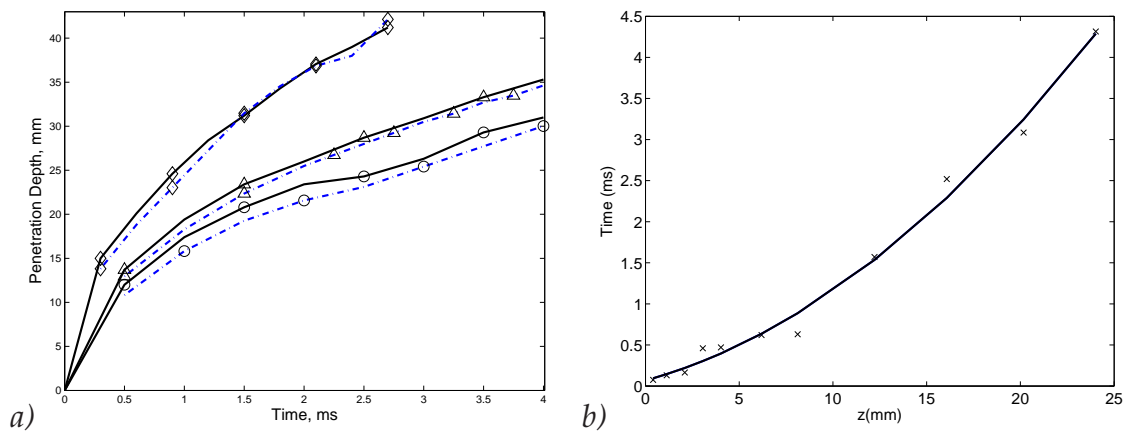


Figure 4.21 : (a) Penetration depths based on a Schlieren intensity (Solid lines), and integrated mixture fraction intensity (dash-dotted lines) for simulations *Jet 2A* (\circ), *Jet 2B* (\triangle) and *Jet 2C* (\diamond) if a cutoff level of $I = 10^{-4}$ is used, see figure 4.15a. (b) Time when steady state is reached, for simulation *Jet 2A*, based on data as presented in figure 4.6a.

Penetration depth

For all three simulations the penetration depth is plotted in figure 4.21a. In this figure the definition of penetration depth is based on a *virtual schlieren* intensity as well as on an integrated intensity, where $I < 10^{-4}$. The general trend is that by increasing the density ratio the penetration depth is enhanced, simply due to the increased jet momentum. This figure shows at what time the mixture fraction departs from its initial value $Z = 0$ for the first time. Now a typical jet structure will start to develop. Globally the two methods lead to similar results, but the *virtual Schlieren* method mostly leads to a faster identification of the jet tip, notwithstanding the stringent measure of the integration method, see figure 4.15.

It is more difficult to find a time instant when the steady state situation has been reached at a specific location above the nozzle exit. Kuo [78] has shown an analysis

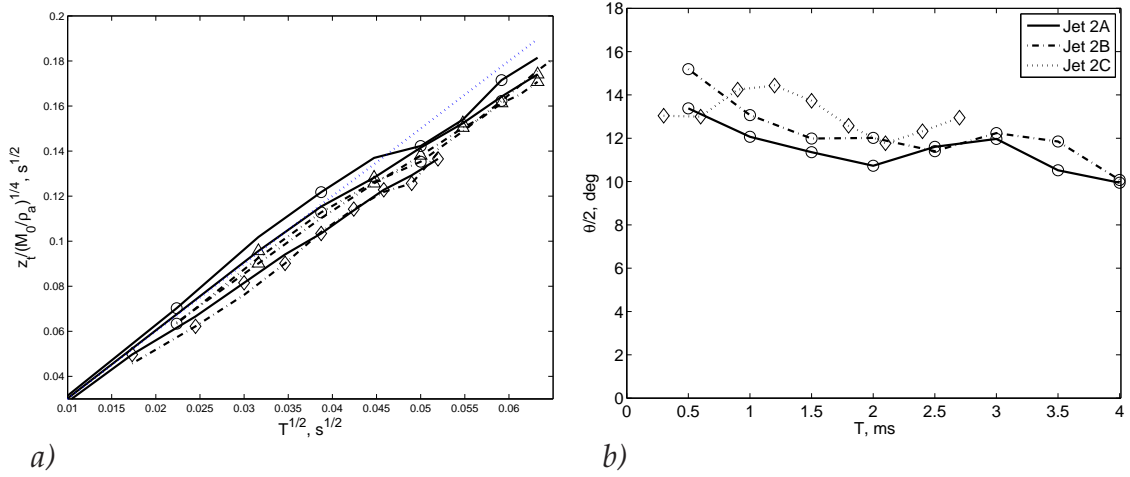


Figure 4.22 : Nondimensionalised penetration depths for all simulations. The solid lines denote the results based on a Schlieren intensity, the dash-dotted lines the integrated mixture fraction intensity. the symbols denote simulation *Jet 2A* (\circ); *Jet 2B* (\triangle) and *Jet 2C* (\diamond). The dotted line represents the theoretical value, $\Gamma = 3.0$, Ricou [136]. (b) evaluated instantaneous half cone angles.

for RANS simulations, evaluating the time when steady state is reached. However, this method is more difficult to apply in the current (LES) problem formulation, as only a single realization of the flow field is available. This is especially problematic when the fluctuations are of the order of magnitude of the absolute value for the mean mixture fraction. In figure 4.21b the moment of reaching steady state is based on the time-trace of the mixture fraction field along the central axis. The time-evolution data is shown in figure 4.6a. As only a single realization of the jet is used for gathering the data, there exists some scatter in the results, denoted by the symbols. The curve shows a least-squares fit of the results. As a general trend we can see that figures 4.21b is the inverse of figure 4.21a, which is a logical result.

Scale similarity is shown in many of the previous figures on the steady state behaviour. For the penetration depth as function of time the relationship 4.4, which states a square root dependency, is tested for the performed simulations, see figure 4.22a. In this figure the data as presented in figure 4.21a is used, also adopting the two visualisation methods. Good agreement is observed independent of models, for all simulations. There is a small trend visible of a decreasing value for Γ with an increasing density ratio: For simulations *Jet 2A*, *Jet 2B* and *Jet 2C* the constant Γ decreases from 2.9 to 2.8 and 2.7 respectively, indicating a reduced -scaled- penetration depth velocity with increasing density ratio.

Cone Angle

In this work the jet angle θ is defined at half the jet penetration depth (see figure 4.23):

$$\theta_{abs} = \tan^{-1} \left(\frac{D_{z_t/2}}{(z_t/2)} \right), \quad (4.33)$$

with $D_{z_t/2}$ the diameter of the jet at half the penetration depth z_t . This definition relates an angle to the outer boundary of the upstream portion of the jet, i.e. the

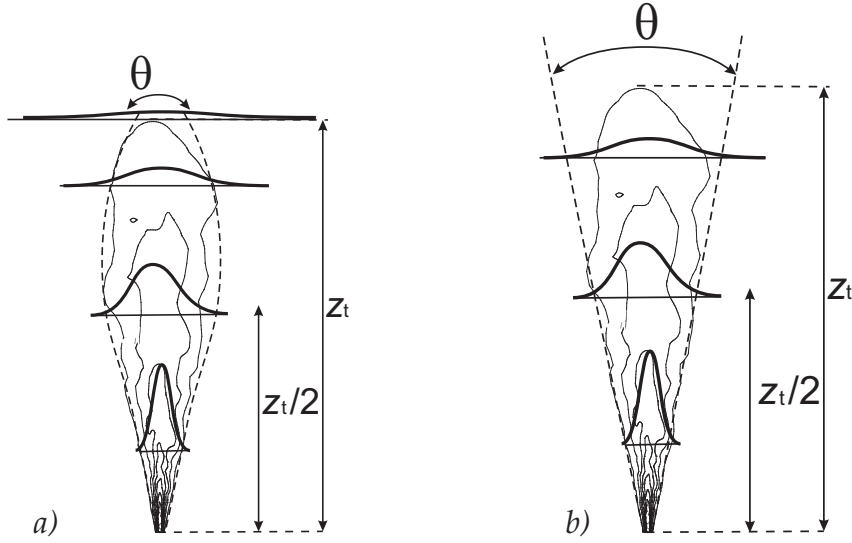


Figure 4.23 : (a) Schematics of an absolute value cone-angle definition, (b) Schematic representation of a self-similar cone angle and penetration depth.

unsteady head of the jet does not influence this cone angle. The diameter $D_{z_t/2}$ and spray penetration depth z_t are defined based on the *virtual Schlieren* line-of-sight approach, in order to follow the standard experimental method. Thus, an absolute cone angle definition is used, based on instantaneous, unscaled information from the mixture fraction field, as depicted in figure 4.23a.

Figure 4.22b shows the cone half angle for the three simulations as a function of time. Two trends are visible: The cone angle decreases as a function of time, which is the best visible for simulations *Jet 2A* and *Jet 2B*, and the absolute value increases with increasing density ratio. The cone angle for simulation *Jet 2A* is on average $\theta_{abs}/2 = 11.4$ deg, whereas for *Jet 2B* and *Jet 2C* it is 12.2 deg and 13.1 deg, respectively. Both observations need some clarification. First, note that the used definition, based on an experimental method, is not completely unambiguous. This can be explained as follows. The sketch given in figure 4.23b, shows a cone angle that is related to a constant value of the self-similarity mixture fraction $Z(r_s)/Z_c$. Using this definition the cone angle is independent of the height above the nozzle exit. Both definitions (based on the absolute mixture fraction and based on its relative value) are equal for steep gradients of the mixture fraction, as appearing close to the nozzle exit. Higher up in the domain an absolute cone angle definition will lead to deviating results. Therefore in experimental studies using absolute values it is wise to use the definition of the spray angle at about half the penetration depth. Close to the nozzle exit the jet is not yet well developed, whereas above half the jet penetration depth the cone angle cannot be well defined due to low levels of mixture fraction. This leads to different cone angles defined at different locations above the nozzle exit.

Notice also that the found cone angles can be related to figure 4.10, i.e. the cone angle $\theta/2$ can be given in terms of self-similarity coordinate $r_s = r/(z - z_0)$, given that $\theta_s/2 = \tan(r_s)$, where the subscript s denotes the similarity-theory cone angle. This means that, for instance, a typical cone angle of $\theta_s/2 = 10$ deg corresponds to $r_s = 0.17$.

Consequently r_s corresponds to a relative mixture fraction. For $r_s = 0.17$ it is

found $Z(r_s)/Z_c \approx 0.2$, see figure 4.10. However, a measure for the spreading rate has already been introduced, namely S_z , as presented in table 4.2. Note, that these spreading rates are defined at a constant height, $z/d_0 = 40$, whereas here the angles $\theta_{abs}/2$ are defined on instant-time basis, and thus at increasing heights. For instance, at 4 ms, half the penetration depth z_t/d_0 is at about 30.

This means that the cone angle data, as presented in figure 4.22b are evaluated at locations relatively close to the nozzle exit. For these early time instants the fully developed self-similar region has not been reached. A similar observation has already been made with respect to figure 4.10b,c: the spreading of the mixture fraction close to the nozzle ($z/d_0=10$) is much wider than at $z/d_0=40$. At the same time the spreading rates S_z at $z/d_0 = 40$ are almost identical for all three simulations, see again table 4.2. This indicates that with increasing density ratio the location of the self-similar region shifts in the down-stream direction. This is an additional problem in the definition of the cone angle based on this type of flow field data.

Moreover, notice that if an experimental jet visualization technique would be based on the absolute density levels, such as the Schlieren method, then an increasing jet density ratio will lead additionally to an increased value of the cone angle $\theta_{abs}/2$, while the relative cone angle θ_s will remain constant.

To conclude: a cone angle definition that is related to the absolute value of the mixture fraction depends on the operating conditions, and this definition itself does not show self-similar behaviour. This statement is similar to the discussion of the unscaled velocity and mixture fraction decay, figure 4.7. At the same time these observations concerning the cone angle show a similar difficulty as has been encountered when analyzing the jet penetration depth.

4.4.3 Comparison to a liquid jet model

The gas jets can also more directly be compared to the experiments and models for a liquid jet. The current simulations are compared to a study from Naber and Siebers [99]. A relationship for the penetration depth as function of time is derived, and validated on a set of vaporizing / non-vaporizing liquid fuel jet experiments. The proposed relationship reads

$$\tilde{t} = \frac{\tilde{z}}{2} + \frac{\tilde{z}}{4}\sqrt{1 + 16\tilde{z}^2} + \frac{1}{16} \ln \left(4\tilde{z} + \sqrt{1 + 16\tilde{z}^2} \right), \quad (4.34)$$

with $\tilde{t} = t/t^+$ and $\tilde{z} = z_t/z^+$ a scaled time and penetration depth, based on

$$t^+ = \frac{d_{\text{eff}}}{a \tan(\theta/2) u_0}, \quad z^+ = \frac{d_{\text{eff}}}{a \tan(\theta/2)}. \quad (4.35)$$

In the above equation a is a fitting parameter that defines the ratio of the model jet cone angle to the practically observed jet angle. This parameter is introduced to account for ambiguities in the cone angle definition, as discussed in the previous section. Naber proposes $a = 0.66$, which is also used in our scaling. In the relationship 4.34 two limits can be defined. For small \tilde{t} the penetration depth follows a linear behaviour. Close to the nozzle exit fluid dynamics is then governed by the injected fluid. For large \tilde{t} equation 4.34 follows a square root dependency. Here the

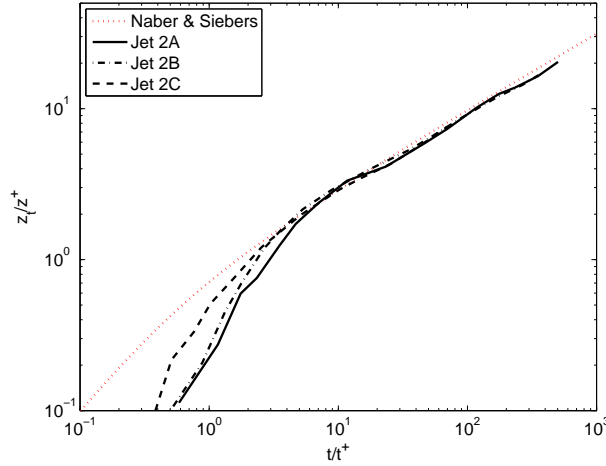


Figure 4.24 :A comparison of the simulation data to a correlation validated for liquid fuel sprays by Naber and Siebers [99]

entrainment of the surrounding gas plays an important role. The transition region is around $\tilde{t} = 1$. Naber and Siebers show that except for some small deviations in the transition region the non-vaporizing liquid spray experiments agree well with the given correlation, for density ratios over nearly two orders of magnitude. Notice that Naber shows vaporizing and non-vaporizing jet sprays over a range of density ratios from 250 to 10, while in this work the density ratios range from 10 to 1. This means that care needs to be taken when extrapolating the given relationship.

For our simulations the scaling parameters s^+ and t^+ are 1.5 mm, 2.0 mm and 4.0 mm and $8.5 \mu s$, $11 \mu s$ and $23 \mu s$ for simulations *Jet 2A*, *Jet 2B* and *Jet 2C* respectively. The penetration depths, as presented in figure 4.21a, are rescaled accordingly and shown in figure 4.24. All simulations give good agreement for $\tilde{z} > 2$. This is at about the location $z/d_0 = 20$, where the self-similarity models start to be appropriate, see also figures 4.8-4.12. This is reasonable, as further away from the nozzle exit all jets should behave similarly, according to similarity theory.

However, for short penetration times ($\tilde{t} < 3$) the penetration depth \tilde{z} is under-predicted. The correspondence gets worse with decreasing density ratio. A simple explanation is that in our simulations a gas jet is modeled, where the entrainment rate close to the nozzle exit is relatively large. On the other hand in the liquid fuel jets the entrainment rate close to the nozzle remains relatively low, because a large amount of liquid particles retain a strong momentum. Only at locations above $z_t > 2z^+$, where the droplets are sufficiently small, the penetration depth of liquid non-vaporizing fuel jets can be described by the similarity theory developed for gas jets.

Naber and Siebers [99] have observed a range of values for the spray cone angles. For the density ratio $\rho_0/\rho_a = 1$ their estimate for the half cone angle ranges between $\theta_{NS}/2 = 12 - 16 \text{ deg}$ while the cone angle is about $\theta_{NS}/2 = 11 - 14 \text{ deg}$ for a density ratio of $\rho_0/\rho_a = 10$. This range depends on the specific jet inlet geometry. Naber reports a decrease of cone angle with an increasing density ratio, in contrast to our observations, using the virtual Schlieren method. This difference in trend can be attributed to the difference in observation methods, and due to the different density

gradient range. The gaseous fuel as simulated in this study has a larger spreading rate with increasing density ratio, mainly due to the visualization method, as explained in the previous section. In our simulations the spreading rate based on a scaled mixture fraction field remains constant, though. On the other hand, liquid fuel jets will show a delayed entrainment rate with increasing density ratio. The liquid fuel particles do not feel any large impact from the surrounding gas, until they are sufficiently small that they start to behave as a gas with all mixing and spreading rate consequences.

It is remarkable that the spray model fits so well to the jet simulation, and therefore the similarity theory. To compare the similarity theory of the gas jet model to the liquid fuel spray model of Naber, we can look at the similarity region of the liquid spray. Then, for large times, equation 4.34 collapses to

$$\tilde{t} = \tilde{z}^2. \quad (4.36)$$

This equation can be compared to the similarity model, given by equation 4.3. Then, by rewriting equation 4.36 to physical coordinates, we get

$$\frac{z_t}{d_{\text{eff}}} = \frac{1}{\sqrt{a \tan(\theta/2)}} \left(\frac{tu_0}{d_{\text{eff}}} \right)^{1/2}. \quad (4.37)$$

Therefore, the quantity Γ in equation 4.3 can be related to the cone angle through

$$\Gamma_{NS} = \frac{1}{\sqrt{a \tan(\theta/2)}} \left(\frac{\pi}{4} \right)^{-1/4}. \quad (4.38)$$

This implies for the found cone angles that the constants Γ are 2.9, 2.8 and 2.7 for simulations *Jet 2A*, *Jet 2B* and *Jet 2C* respectively, see also figure 4.22.

This explains why the gas jet simulation data match so well to the liquid fuel jet model, considering that in the present simulations the penetration depth in the gas jet is corrected using the found cone angles. This effect is accounted for by the constant Γ , which is different for different (experimental) setups. For the typical spray conditions, performed by Naber, Γ ranges from 2.3 to 2.8 for density ratios $\rho_0/\rho_a = 10 - 100$. Therefore one should take this effect into account when using a gas jet for the modeling of a turbulent liquid fuel spray.

4.4.4 Global mixture composition

One important parameter for ignition/combustion problems is the change of chemical energy content of the mixture, as a function of time. This defines whether a mixture can be classified as highly reactive and explosive, or relatively un-mixed. Therefore it is interesting to study the distribution of gas as a function of equivalence ratio. This gives an indication on the global mixing of the total injected fuel, as a function of time. Depending on the total mass and mass-rate of the injected fuel, and the dynamics of the fuel jet, the composition of the mixture varies. By attributing an energy content to every equivalence ratio, a measure for the energy content can be given.

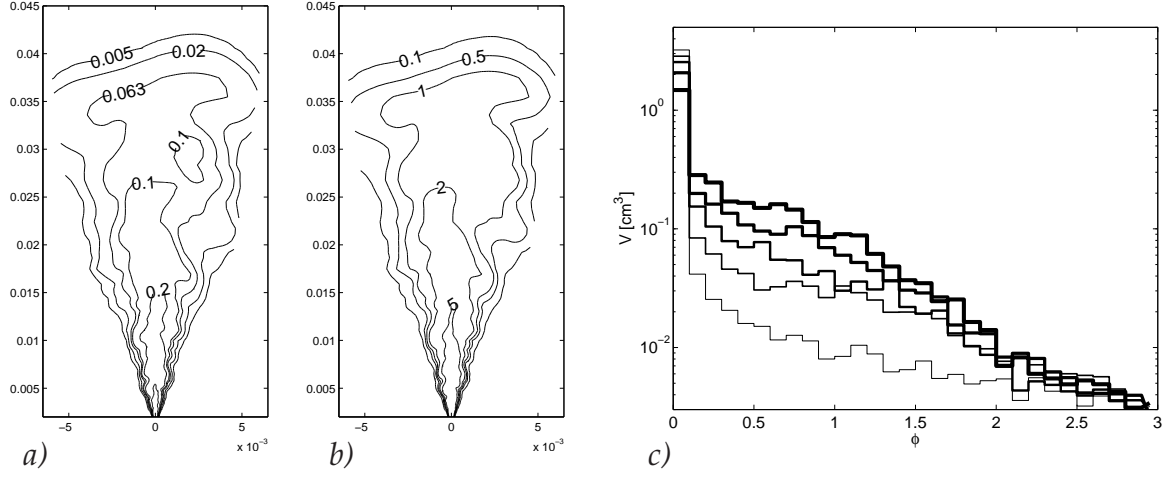


Figure 4.25 : (a) Typical result of mixture fraction and (b) equivalence ratio. Simulation *Jet 2C*, 2.7 ms after start of injection. (c) integrated volume bins for certain equivalence ratio, with increasing time. The time frame is from 0.3 ms to 2.7 ms after start of injection, visualised by five series of bins with increasing line width.

The equivalence ratio ϕ denotes the fuel-to-air ratio in the unburnt mixture compared to the stoichiometric ratio. This quantity is generally used in the combustion community to refer to fuel-rich or fuel-lean engine conditions. So, the equivalence ratio is given by

$$\phi = \frac{Y_{F,u}/Y_{O_2,u}}{(Y_{F,u}/Y_{O_2,u})_{st}} = \frac{\nu Y_{F,u}}{Y_{O_2,u}}, \quad (4.39)$$

where ν is the stoichiometric oxygen-to-fuel mass ratio. The equivalence ratio can be coupled to the mixture fraction, using equation 4.6:

$$\phi = \frac{Z}{(1-Z)} \frac{1-Z_{st}}{Z_{st}}. \quad (4.40)$$

Here, Z_{st} denotes the stoichiometric mixture fraction. For a typical fuel like n-heptane, $Z_{st} \approx 0.063$. This means that for small Z a linear dependence exists, whereas for $Z \rightarrow 1$ the equivalence ratio behaves as $\phi \propto 1/(1-Z)$. With this definition a typical mixture fraction field can be rewritten into an equivalence ratio field, as presented in figure 4.25b.

A number of bins of increasing equivalence ratio is defined from $\phi = 0 - 3$, and a bin width of $\Delta\phi = 0.1$. The total volume of gas is evaluated, that is found for every single bin. The total volume V_ϕ over which the integration is performed is defined such, that at time $t = 2.7$ ms, the global equivalence ratio equals 0.5, based on the total injected fuel and the total available oxygen. This integration domain V_ϕ , used for this analysis, is constructed as a relatively narrow cone around the injected fuel stream. Then, the amount of volume at a specific equivalence ratio can be written

$$V(\phi_i) = \int_{V_\phi} dV_{\phi_i}^*, \quad (4.41)$$

with dV_{ϕ_i} a discretized volume at a local equivalence ratio between $\phi_{i-1/2}$ and $\phi_{i+1/2}$. This is presented in figure 4.25c for five increasing time instances. Initially the

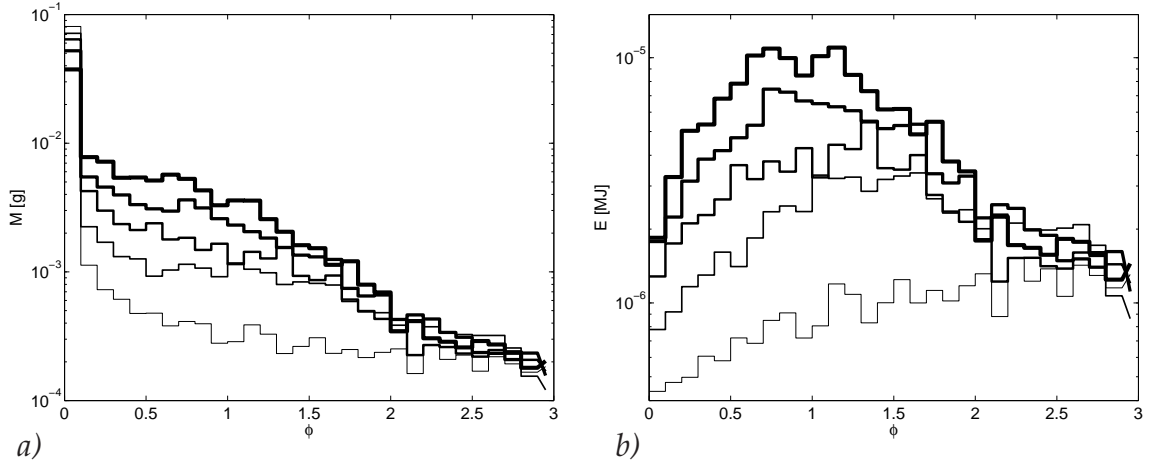


Figure 4.26 : Integrated volume bins for certain equivalence ratio, with increasing time. The time frame is from 0.3 ms to 2.7 ms after start of injection. (a) Integrated mass, (b) integrated energy.

largest volume is related to the lowest equivalence ratio ($\phi = 0 - 0.1$), whereas for increasing times the volume at larger ϕ starts to increase, and the volume at $\phi = 0 - 0.1$ decreases accordingly. By multiplying the volume with the local density $M(\phi_i) = \rho(\phi_i)V(\phi_i)$ the amount of mass in a specific range of equivalence ratios can be retrieved, see figure 4.26a. This figure has a similar shape as figure 4.25c, except that the slope $M(\phi)$ is less steep than in the previous figure. This is because the density follows a linear dependence to the mixture fraction, and thus, (for small Z) to ϕ .

By multiplying the mass with the energy content of the fuel the total energy in a bin can be calculated: $E(\phi_i) = \Delta H_F Y_F(\phi) M(\phi)$, with $\Delta H_F = 45$ MJ/kg the reaction enthalpy, figure 4.26b. Because Y_F is linearly related to Z the total energy is proportional to the volume $V(\phi_i)$ and the equivalence ratio squared:

$$E(\phi_i) \propto \phi_i^2 V(\phi_i). \quad (4.42)$$

For early injection times the total energy is small: the energy content for small ϕ is little due to the small local equivalence ratios, whereas for large ϕ the total amount of $V(\phi_i)$ is limited. For increasing times, the maximum energy content shifts from the rich side, $\phi > 1$, towards stoichiometry, $\phi = 1$, while the maximum value increases one order of magnitude. With increasing times, the maximum can be expected to be located more around $\phi = 0.5$, because of the ongoing mixing with the surrounding air.

4.5 Conclusions

In this chapter the turbulent mixing process in gaseous jets has been studied using the LES method, for three different fuel to ambient air density ratios. This study was focussed on three aspects. 1. The investigation of a turbulent jet for engine-relevant conditions, 2. To investigate an experimental visualization technique using the numerical simulation data 3. To compare the gaseous fuel jets to a phenomenological liquid spray model and experiments on liquid jets. Finally, a global measure

of the total mixture composition and its distribution of the energy content has been given, by expressing the mixture fraction field in terms of equivalence ratios. In future work such information can be used for injection-ignition studies of gaseous turbulent, burning fuel jets.

1. Concerning the steady state statistics of the fuel jet, it is shown that this follows well the similarity theory developed for turbulent gas jets. The fuel core length increases with increasing density ratio, which means that this region is shifted more downstream in the fuel jet.

In the performed simulations it is observed that a substantial part of the turbulent kinetic energy and mixture fraction fluctuations is present in the subgrid scales. Notwithstanding this observation, suitable results have been achieved, especially regarding the mixture fraction variance profiles. This gives confidence in the applied subgrid-scale model for the mixture fraction fluctuations.

Also the penetration depth as a function of time follows the self-similarity theory properly for a fuel-to-air density ratio of unity. With increasing density ratios, the scaled penetration depth decreases slightly.

2. A virtual Schlieren postprocessing method is developed in order to analyze the results similarly as is typically done experimentally. The development of separate turbulent structures could be tracked when considering the turbulent jet at different time instances. When defining the penetration depth similar problems are encountered as typically in experiments. These are related to the cutoff signal intensity of the post-processing method. Moreover, it is shown that the virtual Schlieren ray-tracing method, based on an integration of the density gradients, leads to similar results when an integrating all density gradients in one direction.
3. When comparing the evolution of the penetration depth of a gaseous jet with models for liquid fuel sprays, the phenomenological models for both jets are exchangeable for larger penetration depths. This is because the penetration rate from liquid sprays is governed by the entrainment rate, and therefore scales to \sqrt{t} , which is similar as for gaseous jets. Only for very short distances the simulation departs from the liquid jet experiment, due to the large liquid void fraction in liquid jets and accordingly the reduced entrainment rate. However, it remains questionable if gas jet models can simply be used to replace the model for fuel sprays. The cone angle for gas jets deviates from those observed in spray experiments. This corresponds to a different constant Γ in equation 4.3 for fuel sprays compared to gas jets. Whereas this quantity is universal for relatively simple round turbulent gas jets, hardly depending on Re , the ratio ρ_0/ρ_a or d_0 , for a fuel spray Γ strongly depends on the specific spray conditions.

Modeling finite-rate chemistry in turbulent diffusion flames

In this chapter, two non-premixed turbulent flames are considered, where finite-rate chemistry plays a role. In the first flame three flamelet-based methods are compared to account for finite-rate chemistry in a diffusion type of flame. These three methods are the classical steady laminar flamelet method and two methods based on a reaction progress variable. The test flame is a piloted methane/air flame (Sandia flame D). The second flame is a turbulent benzene diffusion flame. This flame is modeled using a modified flamelet method, where the PAH/soot source terms are extracted from a steady laminar flamelet database.

5.1 Introduction

Nowadays, the modeling of chemical processes that take place in Internal Combustion (IC) Engines is a major research topic, [44, 132]. As explained in the first chapter, legislation puts more and more stringent rules on pollutant formation and CO₂ emission. To keep up with the demands more detailed information about the physics and chemistry of the combustion process in IC engines is required. Based on such knowledge, efficient modeling tools need to be developed that can be applied for predictive studies on future engine concepts, Evlampiev [44].

In the previous chapters the LES method for non-reactive flows, its application to an engine geometry and a mixing model have been discussed. Here, we turn to an additional step related to LES modeling of IC engines concerns the modeling of turbulent combustion.

5.1.1 Combustion regimes encountered in engine flows

For typical combustion problems it is not feasible to solve the complete chemical system within the CFD solver, just by evaluating transport equations for all species. For turbulent flows the large range of length and time scales present in this prob-

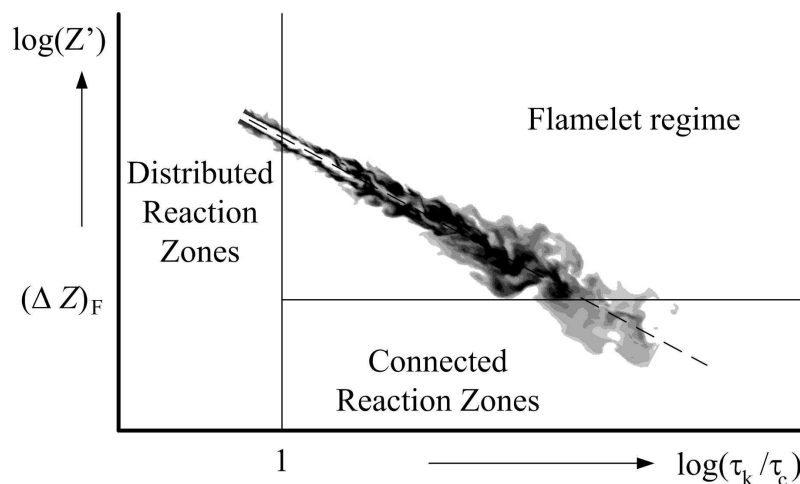


Figure 5.1 : Regimes in non-premixed turbulent combustion. The horizontal axis describes the turbulent time scale and the vertical axis the fluctuations in mixture fraction space. The typical regions encountered by a turbulent jet flame are illustrated, Bray and Peters [23].

lem, along with the number of chemical species that need to be tracked makes this problem unsolvable using a DNS approach, Poinso and Veynante [124]. This calls for a reduction method for the chemistry, and additionally a filtering (using LES) or averaging (in RANS) approach.

To identify an appropriate reduction method, the chemical system of a direct injection Diesel engine is classified. In a combustion cycle the fuel is typically injected near top dead center, see figure 2.4. At the time of ignition the fuel is not fully mixed with the surrounding air. Therefore the mixture in the combustion chamber of a Diesel engine can largely be regarded as non-homogeneous, and thus the ensuing combustion system is largely non-premixed. This means that the mixture fraction can be used as a primary marker of the local chemical composition, Peters [113].

In figure 5.1 the regimes that can be defined in such a reaction system are illustrated, Bray and Peters [23]. Also a typical fuel jet is indicated, showing the different combustion regimes that are encountered. A relatively large part of the flame is located in the flamelet regime. In this regime it appears that the reaction zone is closely attached to the stoichiometric value of the mixture fraction, and convected and diffused along with the mixture field. A typical fluctuation ΔZ in the mixture fraction space can be responsible for corrugations (like curvature) of the flame surface. For small variations of the mixture fraction field, due to intense mixing or premixing, the reaction zones are connected. This region corresponds more to (partially) premixed than to non-premixed combustion. The criterion introduced by Bray and Peters to distinguish between the two regimes depends on an appropriate flame thickness in mixture fraction space, $(\Delta Z)_F$, as encountered in the flame that is considered. The second criterion is a typical chemical time scale τ_c , related to the Kolmogorov time scale τ_k . In case that the Kolmogorov time scale, which is the smallest characteristic turbulent time scale, is larger than the largest chemical time scale the flame front can be considered in a quasi-steady state situation. Otherwise, if the turbulent mixing is very intense, and faster than the chemistry, the flamelet

regime breaks down and regions of intense mixing and reaction will appear. This is referred to as the distributed reaction zones regime. The main part of the combustion process in the engine, concerning the heat release, can be modeled within the flamelet regime. Therefore, methods to model turbulent combustion in this regime are primarily considered. On the other hand, chemical species as soot and NO_x cannot directly be described within this framework [6, 101].

Flamelet methods

The classical method to solve the problem of non-premixed chemistry in the flamelet regime is the steady laminar flamelet method (SLF). It is based on a one-dimensional laminar diffusion flame, Peters [113]. The application of the flamelet method to engine-related chemical problems has been investigated by Evlampiev [44]. In the current thesis its application to fluid-dynamical problems is considered. The application of the classical method is problematic for several reasons, as will be explained in section 5.2. Therefore there is a search for alternative approaches to the classical flamelet method. In this thesis the application of a so-called progress variable method is investigated, and compared to the classical method.

Soot formation processes are relatively slow chemical processes, depending on residence time, D'Anna *et al.* [6]. This is related to the connected reaction zones regime where all main combustion reactants, such as CO_2 and H_2O have approached their equilibrium values. It appears that also in this case a steady laminar flamelet approach will not be appropriate. A more suitable, time-dependent approach for the modeling of soot formation in turbulent diffusion flames is required.

5.1.2 Objectives

In this chapter two non-premixed turbulent flames are studied, with a focus on the modeling of finite-rate chemistry. On the first flame a relatively new method for non-premixed chemistry problems is investigated, where the appropriate flamelet is defined based on an additional transport equation for a characteristic reactive species C . This variable accounts for the reaction progress, and plays a role where finite-rate chemistry takes place. Such a progress variable is used in a number of premixed chemistry problems. Three different methods are compared to each other: the classical flamelet method, Peters [113], where the chemistry is parameterized using the mixture fraction Z and the scalar dissipation rate χ ; a progress variable method, where the same non-premixed flamelet database is parameterized with Z and a progress variable C , Pierce [116]; and finally the same progress variable method, but now based on a premixed chemical database, van Oijen [104]. These three methods are compared to each other on a well documented test flame, the Sandia flame D, [155]. The main concern in this flame is a correct prediction of the temperature and major species.

To test the flamelet method for soot formation problems, in the second flame a sooting turbulent diffusion flame is investigated. Soot formation and oxidation takes place mainly in the connected reaction zones regime, so the use of the classical flamelet method is in principle not allowed. In the latter part of this chapter the state

of the art methods are outlined, and a new method for modeling soot formation in turbulent diffusion flames will be presented, in which the reaction source terms for soot are extracted from a flamelet database. The method is applied to a benzene diffusion flame.

5.1.3 Chapter layout

This chapter is constructed as follows: In the next section the governing equations for flamelet combustion modeling are introduced, describing the classical flamelet method. Also the progress variable method is introduced. In section 5.3, the LES submodels for the combustion module are outlined. These methods have been implemented in the FASTEST-3D code. Its application to a turbulent jet flame is shown in section 5.4. In section 5.5, the application of a flamelet method to a sooting, turbulent, benzene diffusion flame is considered. Here, a method to account for soot formation processes in this diffusion flame is described, and the flow results are presented. Main conclusions are presented in section 5.6.

5.2 Non-premixed combustion modeling

As discussed in the introduction, the solution of the full chemical problem in a turbulent flame is not feasible. Therefore a reduction method is necessary, to simplify the problem. Flamelet methods, which will be discussed in this section, assume that the chemical time-scales are much shorter than the fluid-dynamical scales. In this case the local chemical solution can be modelled by a 1D stagnation flame. Then, based on a few (typically one or two) controlling variables, the chemical problem can be solved, by constructing a database where all relevant chemical parameters are stored as a function of the controlling parameters.

In this section first the classical method to describe non-premixed diffusion flames is outlined. Also a description of another method, based on a progress variable is discussed. This method can remedy some of the limitations of the classical method, subsection 5.2.2.

5.2.1 Diffusion flamelet modeling

In non-premixed combustion systems the mixture composition of fresh gases and the fuel largely defines the local chemical state. To express this composition quantitatively the mixture fraction variable Z is introduced, Peters [113]. This scalar is constructed such that it is conserved, i.e. change in Z can only take place due to diffusion and convection; chemical reactions do not change the mixture fraction. The mixture fraction represents the mass fraction of fuel in the unburnt mixture. If the mixture fraction is based on the Bilger definition [17], this reads

$$Z = \frac{Z^* - Z_{\text{ox}}^*}{Z_{\text{fu}}^* - Z_{\text{ox}}^*}, \quad (5.1)$$

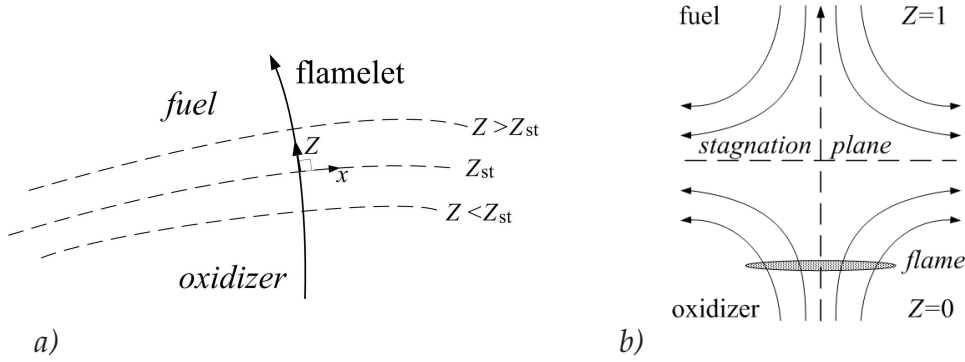


Figure 5.2 : (a) Coordinate system attached to the surface of the stoichiometric mixture Z_{st} of a flame. (b) Geometry of a counterflow diffusion flame.

with

$$Z^* = 2 \frac{Z_C}{M_C} + \frac{1}{2} \frac{Z_H}{M_C} - \frac{Z_O}{M_O}. \quad (5.2)$$

In this equation Z_C , Z_H and Z_O are the element mass fractions and M_C , M_H and M_O the element molar masses. The subscripts fu and ox denote the composition in the pure fuel and oxidizer stream respectively. Then, a transport equation for the mixture fraction can be constructed:

$$\rho \frac{\partial Z}{\partial t} + \rho u_j \frac{\partial Z}{\partial x_j} = \frac{\partial}{\partial x_j} \left(\rho D_Z \frac{\partial Z}{\partial x_j} \right). \quad (5.3)$$

A coordinate transformation can be performed around the vicinity of the surface of stoichiometric mixture, figure 5.2a, with the coordinates x_2 and x_3 the coordinates along the flame surface, x_1 is the coordinate normal to it. Now the mixture fraction Z can replace the original coordinate x_1 , while x_2 and x_3 are retained. This leads to a transformed species transport equation, which in the original coordinate system is given by equation 2.5, and now reads [113]

$$\frac{\partial \rho Y_i}{\partial t} + \sum_{j=2}^3 \frac{\partial \rho u_j Y_i}{\partial x_j} = \rho \frac{\chi}{2} \frac{\partial^2 Y_i}{\partial Z^2} + \sum_{j=2}^3 \frac{\partial}{\partial x_j} \left(\rho D_i \frac{\partial Y_i}{\partial x_j} \right) + 2 \rho D_i \sum_{j=2}^3 \frac{\partial Z}{\partial x_j} \frac{\partial^2 Y_i}{\partial Z \partial x_j} + \omega_i. \quad (5.4)$$

In this equation Y_i is the mass fraction of species i , and ω_i is the chemical source term. Here, the chemical source term is an Arrhenius-like expression, see, e.g., Warnatz *et al.* [162]. The scalar dissipation rate, χ , is defined as

$$\chi = 2 D_Z \frac{\partial Z}{\partial x_k} \frac{\partial Z}{\partial x_k}. \quad (5.5)$$

If the flame is thin in the Z -direction, asymptotic analysis shows that this equation can be reduced to a purely one-dimensional flamelet, [113]. Subsequently all terms including x_2 and x_3 can be neglected, and equation 5.4 for the flamelet can be written in a steady state formulation as

$$\rho \frac{\chi}{2} \frac{\partial^2 Y_i}{\partial Z^2} - \omega_i = 0. \quad (5.6)$$

In this equation, the diffusivities D_i of all chemical species are assumed to be identical. In this way we end up with a one-dimensional flame model. This problem formulation can be applied to a counterflow-diffusion flame, which is a well established numerical and experimental diffusion-flame setup, figure 5.2b. For this setup the scalar dissipation rate may be approximated by [113]

$$\chi(Z) = \frac{a}{\pi} \exp \left(-2 [\operatorname{erfc}^{-1}(2Z)]^2 \right). \quad (5.7)$$

In this equation erfc^{-1} denotes the inverse complementary error function and a is the so-called strain rate. This parameter is usually applied as a boundary condition in the one-dimensional diffusion flame setup, and is defined as the velocity gradient in the oxidizer stream. This means that the chemical problem is in principle closed, as $\chi(Z)$ can be extracted from the flow field, using equation 5.5.

For the application of this one-dimensional flame formulation in practical, multi-dimensional (turbulent) flame simulations a steady laminar flamelet database is constructed. This database is generated from the solutions of a number of flamelets at different strain rates. For every strain rate the scalar dissipation rate at stoichiometry χ_{st} is defined, which is the lookup parameter in the CFD simulation, using

$$\chi_{st} = \chi \frac{f(Z_{st})}{f(Z)}, \quad (5.8)$$

where

$$f(Z) = \exp \left(-2 [\operatorname{erfc}^{-1}(2Z)]^2 \right). \quad (5.9)$$

This framework is shown to be successful on a wide range of applications, see, e.g., Pitsch et al. [120].

5.2.2 A progress variable method for non-premixed systems

A relatively new approach to model finite-rate chemistry effects in non-premixed combustion problems is proposed by Pierce [116]. Instead of using χ , a new scalar field C is introduced additional to the mixture fraction. Key aspect here is that this variable is directly related to the reaction progress of a representative chemical species that is considered, instead of relating the reaction progress to a mixing time scale χ . Contrary to the mixture fraction field, the transport equation for this variable is not conserved, but contains a source term, that changes the variable concentration depending on the local chemical composition. Then the transport equation for this variable C reads

$$\rho \frac{\partial C}{\partial t} + \rho u_j \frac{\partial C}{\partial x_j} = \frac{\partial}{\partial x_j} \left(\rho D_C \frac{\partial C}{\partial x_j} \right) + \omega_C, \quad (5.10)$$

where D_C is the diffusion coefficient of C and ω_C is the reaction source term. When using this scalar field the chemical solution can be attributed to the combination of Z and C . The chemical source term for the progress variable ω_C can be extracted from a flamelet database. In contrast to the $Z - \chi$ method no direct assumption on the shape of the scalar dissipation rate in the flamelet is necessary. Therefore, the

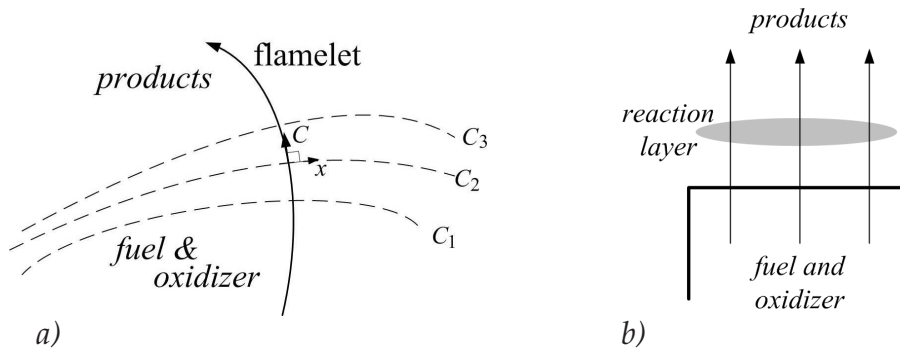


Figure 5.3 : (a) Coordinate system attached to the progress variable C of a premixed flame. (b) Geometry of a burner for a one-dimensional premixed flame.

progress variable method is by its nature a local method. The question remains, how this method then compares to the classical $Z - \chi$ parametrization, since in both methods the same chemical database generator is applied.

One main concern though is the choice of an appropriate progress variable. As pointed out in [116], the progress variable should be an important controlling quantity that contains the essential features of the process it is supposed to represent. Moreover, it should provide a unique mapping of all of the chemical states in the flamelet library. Pierce and Moin [117] have applied this method to Large Eddy simulations using a steady diffusion flamelet database. There $C = Y_{H_2O} + Y_{CO_2}$ has been used as a progress variable. Improved predictions for mixture fraction and product mass fractions have been observed, especially close to the nozzle exit. However, further away, and for other quantities, there is room for improvement, as the classical flamelet model casually outperforms the progress-variable approach.

The extra computational expenses in the Large-Eddy simulation are reasonable compared to the $Z - \chi$ parametrization: one additional transport equation needs to be solved. Notice that this approach is easily extendible with additional reactive scalar fields, e.g. to account for ignition or for pollutant formation problems.

Another advantage of the $Z - C$ method is that it is in principle independent from the flamelet generation method. The database can in principle also be based on a premixed chemistry, van Oijen [104], as will be discussed below. In this way the application of the progress variable method to non-premixed systems leads to a more general approach to turbulent combustion problems.

A premixed flamelet database for non-premixed systems

The flamelet methodology, assuming locally a one-dimensional flame structure, can in principle also be adopted for the modeling of a premixed flame, as shown by van Oijen [104]. Here, a reduction method for premixed flames has been developed. The main difference now is that a progress variable is used to define a local coordinate, figure 5.3a. Then, in a one-dimensional flame system a mixture, at constant mixture fraction Z , is simulated which is unburnt on the one side of the domain and burnt on the other side, figure 5.3b. By varying the initial mixture composition, a range of flamelets can then be evaluated, depending on the flammability limits of the studied flame. By extrapolating these flames to $Z = 0$ and $Z = 1$, mimicking a diffusion

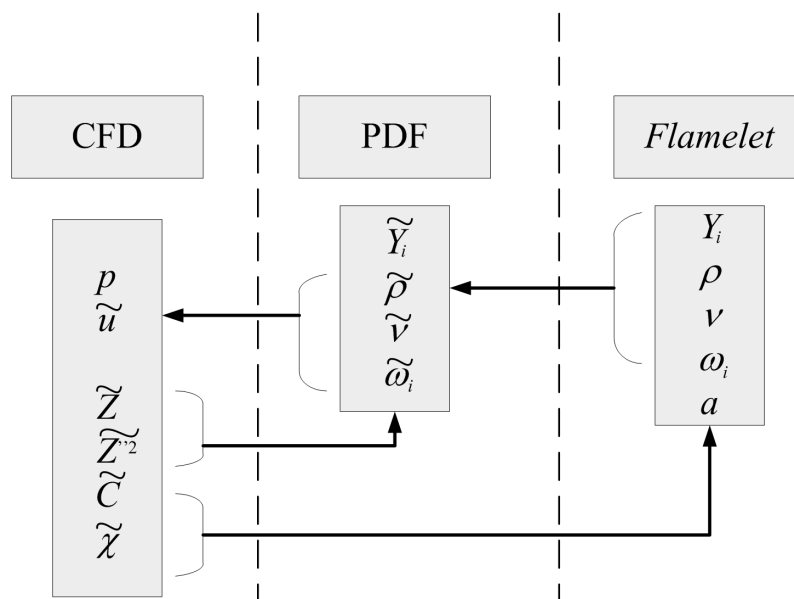


Figure 5.4 : Flow chart of the coupling between the turbulent CFD problem and the laminar Flamelet solutions, using probability density functions (PDF).

process, the complete range in non-premixed chemistry can be constructed from the premixed flame simulations. A (combination of) reactive species can be used to give an expression for the reaction progress.

However, a premixed flame simulation only accounts for diffusive transport processes in the direction of the progress variable. This is less appropriate in non-premixed diffusion flames where large gradients in Z are present. Only at locations in the flame where premixing takes place, or when the flame is well mixed, such that relatively small gradients in Z -direction are not present, this is fully appropriate, Bongers [19].

The Flamelet Generated Manifolds (FGM) method developed by van Oijen [104] is originally used for the modeling of premixed flame systems. But it has been applied successfully for the modeling of partially premixed laminar flames as well, van Oijen and de Goey [105]. It is also applicable in more practical combustion problems, for instance, for turbulent swirl combustors, Wegner [163].

5.3 Effects of turbulence

The previously described chemical models are developed for laminar flames, but are applied to turbulent combustion problems, in a LES environment. This means that the mixture fraction, scalar dissipation rate and progress variable need to be expressed in terms of filtered variables. Moreover, a coupling between the CFD and flamelet method needs to be provided using a probability density function (PDF) method, to reconstruct the filtered thermochemical data from the laminar flamelet solutions. This is illustrated in figure 5.4. In this section the governing filtered equations in the applied combustion Large-Eddy simulations are discussed. Also the subgrid-scale models and the PDF integration method are outlined.

5.3.1 The LES filtered governing equations

The classical flamelet method

For the classical flamelet method, the chemistry is controlled by the mixture fraction Z and the scalar dissipation rate χ . These equations are filtered in LES. For the mixture fraction field this generally leads to the filtered transport equation, as was presented in section 4.3.1:

$$\bar{\rho} \frac{\partial \tilde{Z}}{\partial t} + \bar{\rho} \tilde{u}_j \frac{\partial \tilde{Z}}{\partial x_j} = \frac{\partial}{\partial x_j} \left(\bar{\rho} (\tilde{D}_Z + D_t) \frac{\partial \tilde{Z}}{\partial x_j} \right). \quad (5.11)$$

The filtered diffusion coefficient \tilde{D}_Z is linked to the molecular viscosity using a Schmidt number relationship:

$$\tilde{D}_Z = \tilde{\nu} / \text{Sc}_Z, \quad D_t = \nu_t / \text{Sc}_t, \quad (5.12)$$

where both the laminar and turbulent Schmidt numbers are set to 0.7. It was found that when changing from a constant turbulent Schmidt number to a dynamically determined value this did not lead to very different results, Pitsch and Steiner [121]. Therefore, a constant value is adopted here, as this is computationally more efficient.

The filtered mixture fraction variance $\widetilde{Z''^2}$, is written as (Cook and Riley [32])

$$\widetilde{Z''^2} = \widetilde{Z^2} - \tilde{Z}^2 \quad (5.13)$$

and needs to be expressed based on the first moments. In literature several models for the mixture fraction variance $\widetilde{Z''^2}$ have been presented. In the equilibrium model, it is assumed that the dissipation equals the production in the unresolved scales, while the production is proportional to the mean gradient of the mixture fraction. This leads to the following expression, Branley and Jones [22]:

$$\widetilde{Z''^2} = C_Z \Delta^2 \left(\frac{\partial \tilde{Z}}{\partial x_k} \right)^2, \quad (5.14)$$

where C_Z is a model parameter which is set to $C_Z = 0.15$, Wegner [163]. Pierce [115] has proposed a dynamic procedure for the prediction of C_Z . A scale-similarity method has been proposed before by Cook and Riley [32]. This model assumes a scale similarity between the subgrid and the resolved distribution of the scalar:

$$\widetilde{Z''^2} = C_{sim} \left(\widehat{\left(\tilde{Z} \right)^2} - \left(\widehat{\tilde{Z}} \right)^2 \right), \quad (5.15)$$

where $\widehat{\cdot}$ denotes a filtering operation. It was remarked by Kempf [71] that the three models behave very similar in a practical CFD code. Therefore, the equilibrium model is used, because of its numerical efficiency and numerical stability.

For the classical flamelet approach a model for the filtered scalar dissipation rate needs to be provided. The unconditionally filtered scalar dissipation rate $\tilde{\chi}$ can be

modeled as (Girimaji and Zhou [55])

$$\tilde{\chi} = 2(D_m + D_t) \left(\frac{\partial \tilde{Z}}{\partial x} \right)^2. \quad (5.16)$$

The progress variable method

In case of the progress variable method a model description for the filtered values of Z and C is required. A discussion on the mixture fraction field is given above, the transport equation for \tilde{C} reads

$$\bar{\rho} \frac{\partial \tilde{C}}{\partial t} + \bar{\rho} \tilde{v}_j \frac{\partial (\tilde{C})}{\partial x_j} = \frac{\partial}{\partial x_j} \left(\rho (\tilde{D}_C + D_t) \frac{\partial \tilde{C}}{\partial x_j} \right) + \widetilde{\omega}_C. \quad (5.17)$$

Similarly to equation 5.11, the filtered diffusion coefficient \tilde{D}_C is linked to the molecular viscosity using a constant Schmidt number relationship, where Sc_C is assumed equal to Sc_Z .

5.3.2 The PDF Method

In the LES method the species concentrations, their source terms, the density, temperature and viscosity from the laminar flame solution cannot be used directly in the Large-Eddy simulation. Therefore these solutions need to be filtered. This is achieved by integrating these data over the joint PDF of the mixture fraction and the scalar dissipation rate in the classical $Z - \chi$ method, or the mixture fraction and the progress variable in the other method. For the two approaches a filtered scalar field can then be written as

$$\tilde{\phi} = \int_0^\infty \int_0^1 \phi(Z^*, \chi^*) P^*(Z, \chi) dZ^* d\chi^* \quad (5.18)$$

and

$$\tilde{\phi} = \int_0^1 \int_0^1 \phi(Z^*, C^*) P^*(Z, C) dZ^* dC^*, \quad (5.19)$$

where $P(Z, \chi)$ and $P(Z, c)$ denote the joint mass-averaged PDF. These functions are not known a priori. Here Z, χ and Z, C are assumed to be statistically independent. Then, we have

$$P(Z, \chi) = P(Z)P(\chi); \quad P(Z, C) = P(Z)P(C). \quad (5.20)$$

Here it is assumed that both $P(\chi)$ and $P(C)$ are Dirac delta functions. These assumptions are usually made in LES calculations, e.g., Kempf *et al.* [72], Pierce [116]. Ihme *et al.* [68] have studied the effects of the above given assumptions in cases of extinction and re-ignition, and conclude that assuming a β -pdf for the progress variable leads to improvements in case of RANS type of simulations. Yet, in LES the model contribution is relatively small, compared to RANS, therefore the impact of

the assumption is reduced. Moreover, only few cases of extinction will be encountered in the current study. Then, for the classical flamelet model the PDF reduces to

$$\tilde{\phi} = \int_0^1 \phi(Z^*, \chi^* = \tilde{\chi}) P^*(Z) dZ^* \quad (5.21)$$

$$\tilde{\phi} = \int_0^1 \phi(Z^*, C^* = \tilde{C}) P^*(Z) dZ^*. \quad (5.22)$$

In this work a presumed function for the PDF is used, namely the standard β -PDF function, Janicka and Kollman [69]. The PDF of a non-reactive scalar like the mixture fraction can reasonably be approximated by a β distribution function, Cook and Riley [32]. This functionality reads

$$P^*(Z) = P(Z^*, \tilde{Z}, \widetilde{Z''^2}) = \frac{Z^{*\alpha-1} (1 - Z^*)^{\beta-1}}{\int_0^1 Z^{*\alpha-1} (1 - Z^*)^{\beta-1} dZ^*} \quad (5.23)$$

with α and β related to the filtered mean and variance according to:

$$\alpha = \tilde{Z}\gamma, \quad \beta = (1 - \tilde{Z})\gamma, \quad \gamma = \frac{\tilde{Z}(1 - \tilde{Z})}{\widetilde{Z''^2}}. \quad (5.24)$$

5.3.3 The numerical methodology

As can be seen in figure 5.4 the impact of the chemistry on the fluid dynamics is only through the filtered viscosity and filtered density fields. In the previous chapter the mixing had a similar coupling with the fluid dynamics. However, in that case the dependency was only moderate. For typical combustion problems, however, the density is a strongly non-linear function of the mixture fraction, see also figure 5.8a. This poses more stringent requirements to the numerical code concerning mass and energy conservation as well as stability, Pierce [116]. Here the FASTEST-3D code is applied, as developed by Wegner [163]. Some details of the numerics are described in appendix A, with special emphasis on the implications of the variable density implementation. In this code, extensions for the progress variable method have been implemented.

5.4 LES of a piloted diffusion flame

In this section, simulations of a turbulent non-premixed flame are presented. Here, a piloted methane/air flame, the Sandia flame D is chosen. This is a diffusion flame. The choice for this flame is motivated by the availability of a comprehensive amount of experimental data [155] and [14, 15, 142]. For reference numerical studies the reader is referred to, e.g., [25, 98, 121]. Three different methods to account for finite-rate effects, which have been described in section 5.2 are compared to each other for this flame: the classical flamelet method and two progress variable methods, one based on the non-premixed flamelet solutions and a second one based on premixed flamelet solutions. In the following subsection the geometrical and chemical details for this flame are outlined. In subsection 5.4.2 the results are presented. A more detailed discussion of the global observations is given in section 5.4.3.

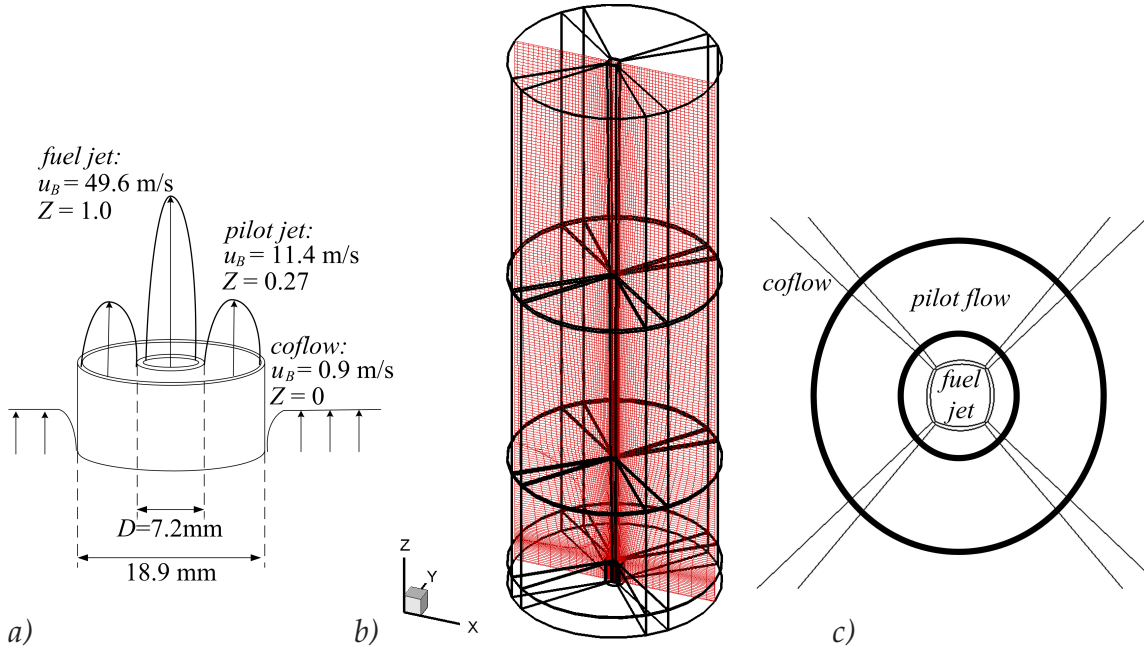


Figure 5.5 : (a) Inlet geometry and (b) illustration of the applied numerical mesh for Sandia flame D. The thick lines represent the block boundaries. (c) Blocking strategy of the inlet geometry, using a so-called O-grid inside the fuel jet. The thin lines denote the block boundaries, which have an overlap region.

5.4.1 The setup of the Sandia flame D

The Sandia flame D is a piloted methane-air flame. The dimension of the main jet inner diameter is $D = 7.2 \text{ mm}$, the outer diameter of the pilot is 18.9 mm , figure 5.5a. The wall thickness of the inner radius is 0.25 mm , at the outer radius this is 0.35 mm . The fuel jet bulk velocity is $u_B = 49.6 \text{ m/s}$, leading to a bulk Reynolds number of 22400. Its chemical composition is a mixture of 25% CH_4 and 75 % dry air by volume. The pilot jet is a lean premixed flame, at a mixture fraction $Z = 0.27$ and a bulk velocity of $u_B = 11.4 \text{ m/s}$. The stoichiometric mixture fraction is at $Z = 0.35$. The lean pilot flame is introduced to stabilize the flame. No effects of flame liftoff take place, whereas the reaction layer is thickened.

The height of the simulation domain was 50 cm , which corresponds to a height of $z/D = 70$, figure 5.5b. The diameter of the simulation domain was 20 cm , corresponding to a diameter of $28D$. For the mesh an O-grid structure was adopted, which guarantees an accurate geometrical description of the nozzle exit, while keeping a good grid quality, see figure 5.5c. The mesh which has been used for this flame consists of 28 separate blocks, whereas the total number of grid cells has been set to $N_{ax} = 420$, $N_{rad} = 70$, $N_{tan} = 60$, which leads to a total mesh size of about $1.5 \cdot 10^6$ points. The grid has been refined towards the walls of the nozzle to capture the boundary layer of the pipe flow. At the inlet a flow domain of 2.0 cm has been simulated upstream of the nozzle exit. For the fuel jet at the inlet turbulent pipe-flow data have been imposed, using the generator as described by Klein *et al* [73]. At the outlet a zero-gradient outflow boundary condition has been applied.

Table 5.1 : Definition of the three different parametrizations applied for the simulation of the Sandia flame D.

Case	Chemical flamelet setup	Parametrization
$Z\chi^D$	Diffusion	$a(\chi)$
ZC^D	Diffusion	H_2O
ZC^P	Premixed	H_2O

The chemical databases

The chemical databases that are used in this work are constructed from Steady Laminar Flamelet libraries. In case of the counterflow diffusion flame setup this library consists of a set of flames with the strain rate a as the defining flame parameter. Unity Lewis numbers are assumed, while the flame geometry is flat. The mixture fraction is based on the Bilger definition [17], expression 5.1. Both the non-premixed diffusion flames and the premixed flames are computed with the CHEM1D package [31]. The reaction mechanism GRI-3.0 [145] has been applied. For the non-premixed flamelet database the strain rate in the database starts from the lower limit $a = 10s^{-1}$, which is close to equilibrium and is increased with steps of about 10% up to quenching, which is at a strain rate of $a = 1250s^{-1}$.

In figure 5.6 the major species concentrations are plotted for this flame. The left figure shows the solution for $a = 10 s^{-1}$, whereas the right figure shows the solution near quenching. The OH concentration, here shown with a magnification factor of 50, shows its maximum at the location of the flame front. It can be seen that with decreasing strain rate the species mass fractions for the reaction products appear at the fuel-rich side ($Z > 0.35$), whereas the CH_4 and O_2 mass fractions decrease. Now at the quenching strain rate the oxygen concentration remains present and the methane concentration penetrates far more deeply into the flame zone, leading to a decrease of H_2O . The simulation that is based on this database, where the scalar dissipation rate χ is used to determine the flamelet with the corresponding strain rate a (using equation 5.8) is referred to as the $Z\chi^D$ method, see table 5.1.

For the progress variable method that is based on the non-premixed chemistry, the mass fraction of H_2O was chosen as the tracking variable. This variable showed the required behavior of monotonicity over the complete range of mixture fraction space: for every value of the mixture fraction the mass fraction of H_2O was increasing with decreasing strain rate. For this method the non-premixed flamelet database has been reconstructed, based on increasing H_2O mass fractions. This method is referred to as the ZC^D method.

For the premixed flamelet database a set of premixed flames with different chemical composition (different mixture fraction) has been generated, using the same mechanism and Lewis numbers. These flames are only evaluated between $Z = 0.15$ and $Z = 0.55$, as these are the flammability limits of this setup, as can be seen from the OH profiles, figure 5.7. The values lower than $Z = 0.15$ and higher than $Z = 0.55$ are constructed by interpolation with the boundary conditions at $Z = 0$ and 1. In fact this method represents a diffusion process in Z -space. In the premixed flamelet

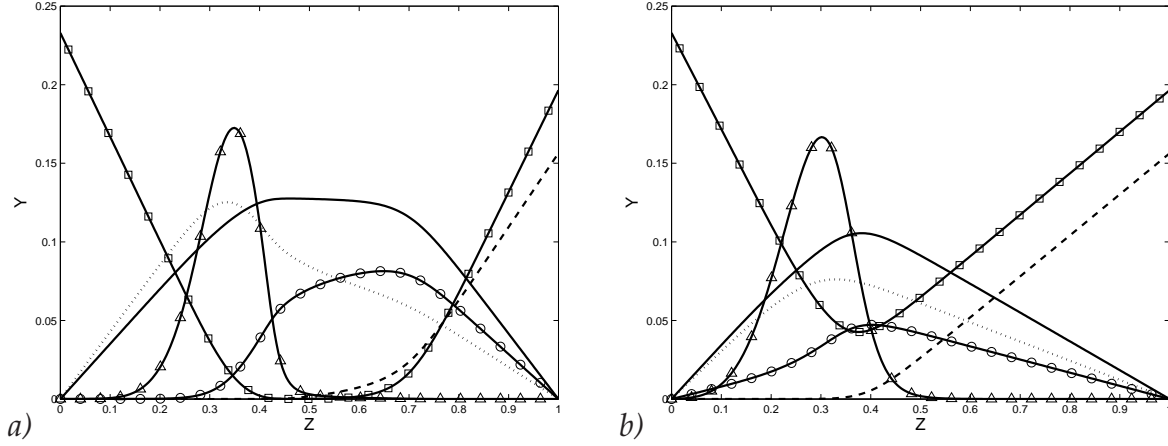


Figure 5.6 : Flamelet solutions for the non-premixed flame mass fractions of the major species for the Sandia flame D. (a) strain rate $a = 10 \text{ s}^{-1}$, (b) $a = 1250 \text{ s}^{-1}$. (—): H_2O , (---): CH_4 , (\cdots): CO_2 , \square : O_2 , \circ : CO , \triangle : OH , multiplied by a factor 50.

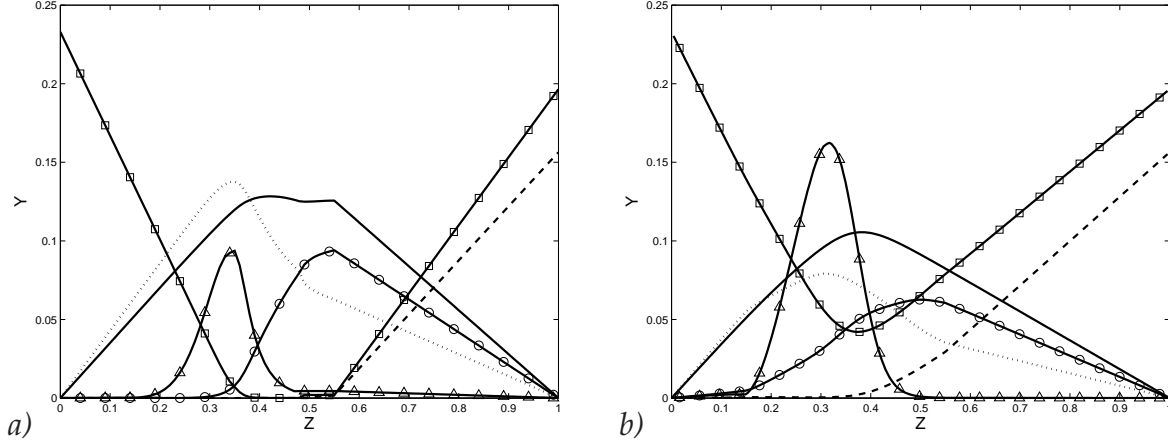


Figure 5.7 : Flamelet solutions for the premixed flame mass fractions of the major species for the Sandia flame D. (a) flame solution at maximum H_2O concentration, (b) flame solution based on the H_2O concentrations from the extinction flamelet in figure 5.6b. (—): H_2O , (---): CH_4 , (\cdots): CO_2 , \square : O_2 , \circ : CO , \triangle : OH , multiplied by a factor 50.

database the H_2O mass fraction does not show the required uniqueness outside these boundaries. Even at the rich premixed flames ($0.5 < Z < 0.55$) the mass fraction of H_2O did not show monotonicity. This non-uniqueness may call for the use of another progress variable. However, in order to remain consistent with the non-premixed approach, this option has not been chosen. Instead, the premixed flames have been cut off at the maximum H_2O mass fraction, as the remaining region in H_2O space is expected not be encountered in the practical simulations of the flame. This is a similar reasoning as for the non-premixed flamelet database, that has been cut off at a strain rate of 10 s^{-1} . Below this strain rate only diffusive effects at timescales larger than 0.1 s take place, which are expected not to be encountered in this flame. This assumption will also be discussed based on the results. The simulation that is performed with this database is referred to as ZC^P , see also table 5.1.

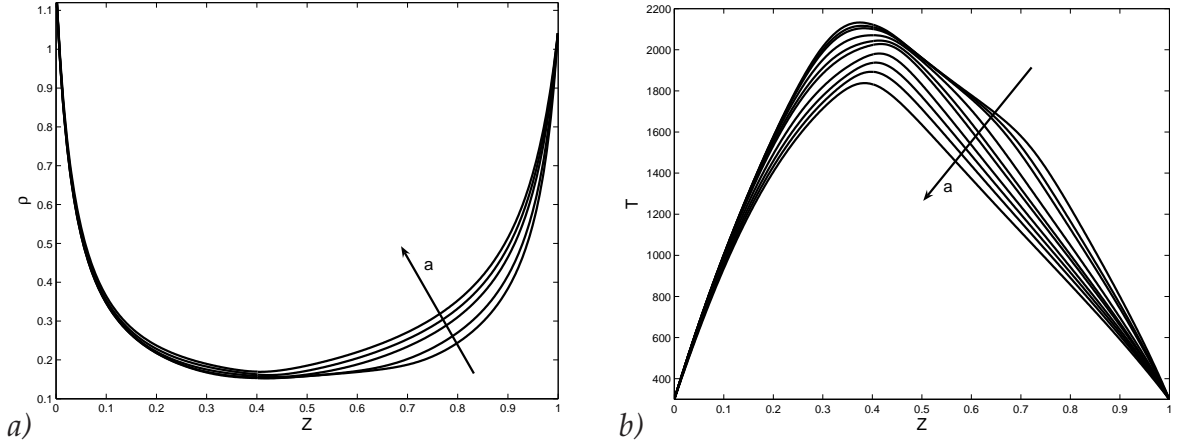


Figure 5.8 : Non-premixed flamelet solutions of the density and temperature for increasing strain rate a , for the Sandia flame D.

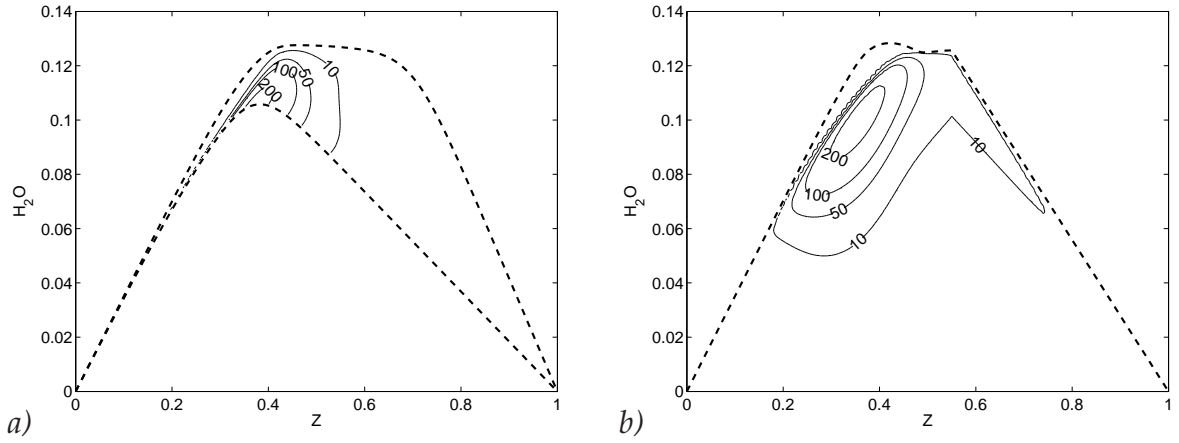


Figure 5.9 : Contour plots of the chemical source term for H_2O , in $\text{kg}/\text{m}^3\text{s}$ as a function of the H_2O mass fraction and the mixture fraction. (a) The non-premixed flamelet database, (- - -) denote the flamelet solutions for H_2O at strain rates 10 s^{-1} and 1250 s^{-1} . (b) Premixed flamelet database. (- - -) is the maximum H_2O concentration.

For the fluid dynamical problem the key parameter in the applied atmospheric flames is the local density. Its variation as a function of mixture fraction and strain rate is shown in figure 5.8a. Notice that this variation is very steep near the boundaries of the mixture fraction field, but very moderate over a large range of mixture fraction, near the middle. The corresponding temperature profile is at its maximum around stoichiometric mixture fraction, at $Z = 0.35$, figure 5.8b.

Figure 5.9 shows the flamelet solutions of the chemical source terms for the non-premixed and the premixed flames. In both cases the chemical source term decreases with increasing water concentration: with increasing H_2O concentration the near-equilibrium value is reached. One difference between the two databases is that the non-premixed flame database is defined only between the quenching flamelet and the flamelet related to $a = 10 \text{ s}^{-1}$, while in case of the premixed flame database the manifold reaches far beyond this level, down to a mass fraction of H_2O equal to zero. However, these locations of low concentration of H_2O at intermediate mixture fraction are hardly encountered in the flame, as only few instances of extinction can

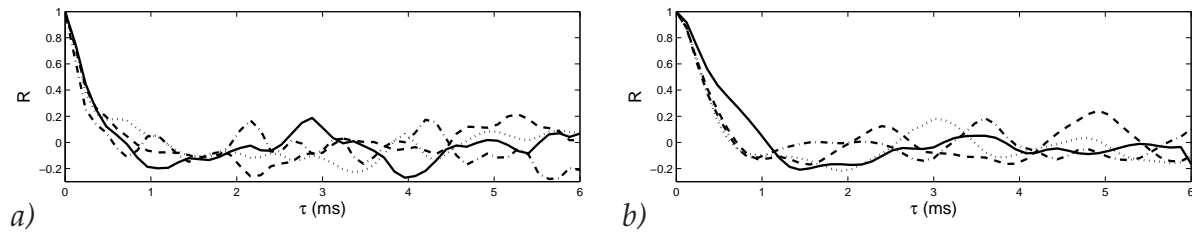


Figure 5.10 : Autocorrelation functions for simulation ZC^D , at two heights in the flame. (a) height $z/D = 30$; (b) height $z/D = 45$. (---) u velocity component, (- · - ·) v ; (—) w ; (···) Z .

be expected, Xu and Pope [165]. Therefore, this difference will not play a crucial role. On the other hand, the largest difference between the diffusion flame and the premixed flame is that in the latter case the chemical source term is active on a much wider range in Z -space. This is specially important at the rich side of the flame, $Z > 0.55$. This is an effect of the cut-off mixture fraction at $Z = 0.55$, after which the source term is interpolated. This leads to a wide "peak" where the chemistry remains artificially active. It can be expected to have an effect on the chemistry and flow dynamics in the Large-Eddy simulation at locations near the nozzle exit and therefore also further downwards.

Statistical analysis

Typically, a simulation run was performed over 30 msec, corresponding to 5000 time steps. The auto-correlation functions for the velocity field and the mixture fraction at the centerline are presented in figure 5.10. At height $z/D = 30$ the correlation time τ_c , here defined as the time where $R(\tau) = 0$, is about $\tau_c \approx 0.5$ msec. At the higher levels in the domain, $z/D = 45$, this increases up to $\tau_c \approx 0.8$ msec for all components except for the streamwise velocity: this gives a value of about 1.2 msec as an estimate for the turbulent time scale. Therefore, at a height of $z/D = 45$, thirty independent realizations could be captured at the central axis. For the radial profiles averaging in two planes has been performed leading to four statistically independent samples. Therefore only for the rms-values at heights at $z/D = 45$ and higher this can lead to inconclusive observations, but it is sufficient to distinguish the differences between the different models for the key variables, whose effects can be observed mainly at lower locations in the flame.

5.4.2 Results

Instantaneous flow fields of the turbulent flame are shown in figure 5.11, illustrating the complex behavior of the flame. The subgrid-scale mixture fraction variance, for instance, shows many small scale structures, illustrating regions of relatively high turbulence intensities. Yet the maximum value never exceeds the level of 0.04, indicating that only a relatively narrow pdf accounts for the subgrid fluctuations in the chemical fields. The scalar dissipation rate is generally well below the extinction rate, except near the nozzle exit (figure 5.11d). Here high levels near the

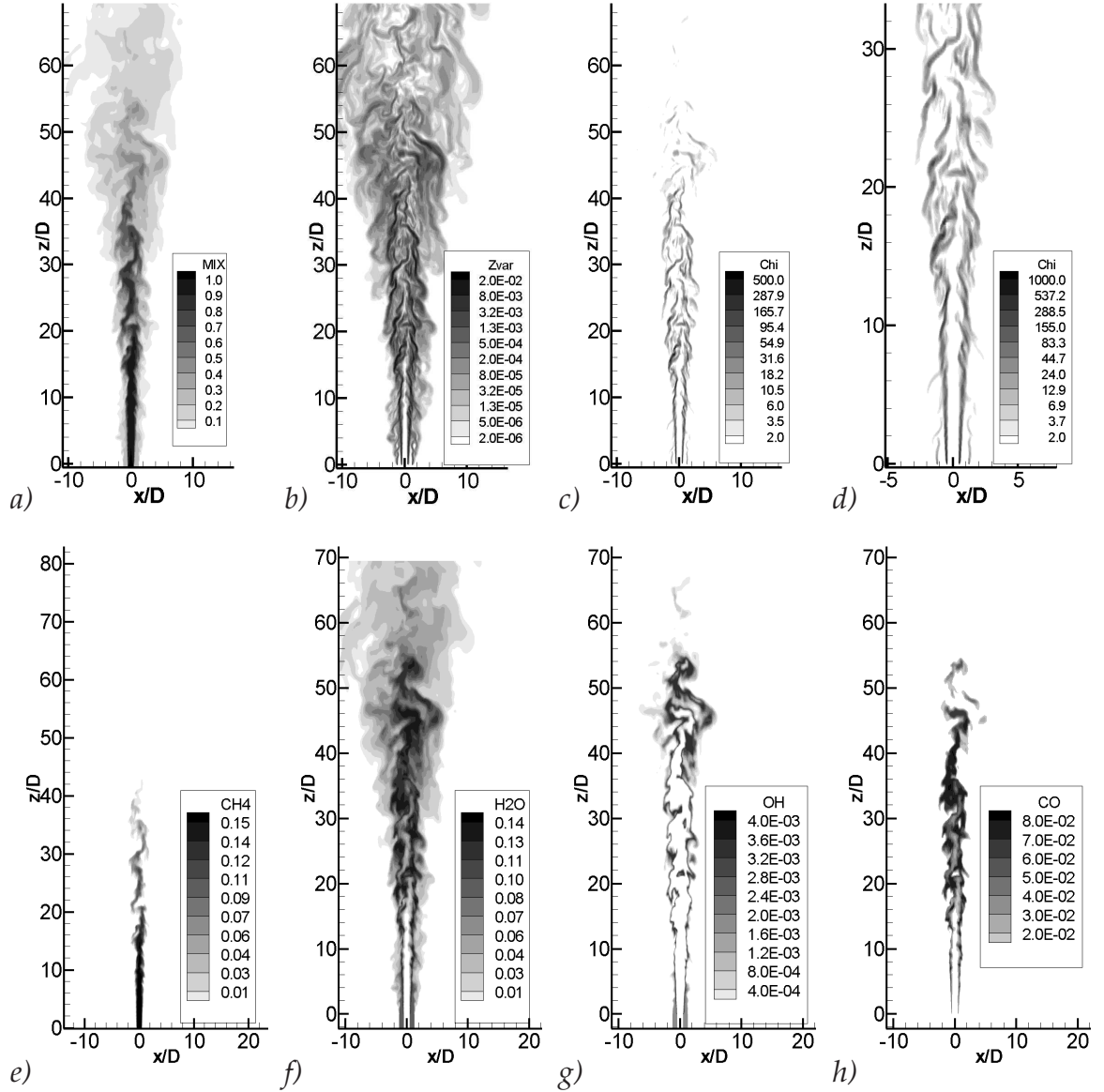


Figure 5.11 : Instantaneous flow profiles of (a) the mixture fraction, (b) the subgrid-scale mixture fraction variance $\widetilde{Z''^2}$, (c) the scalar dissipation rate and (d) a zoom plot of $\tilde{\chi}$ near the nozzle exit. Instantaneous mass fractions are shown for (e) CH_4 (f) H_2O , (g) OH and (h) CO .

extinction limit of the 1D counterflow geometry ($a \approx 1250 \text{ s}^{-1}$, corresponding to $\chi_{max} \approx 800$) are encountered, while more moderate levels of χ are found at the boundary between the pilot flame and the co-flow. However, these high levels cannot lead to extinction, because of the pilot jet, which is located at the lean side of the flame. Some snapshots of representative species mass fractions fields are presented in figure 5.11e-h. These species are recovered using the $Z\chi^D$ parametrization and indicate the different regions in the flame. The mass fraction of CH_4 is related to the non-burning core region where mainly convective/diffusive effects take place. The water mass fraction indicates the range in the flame where fuel products are present, while the OH concentration shows the location of the reaction front. CO is a representative species related to finite-rate chemistry effects.

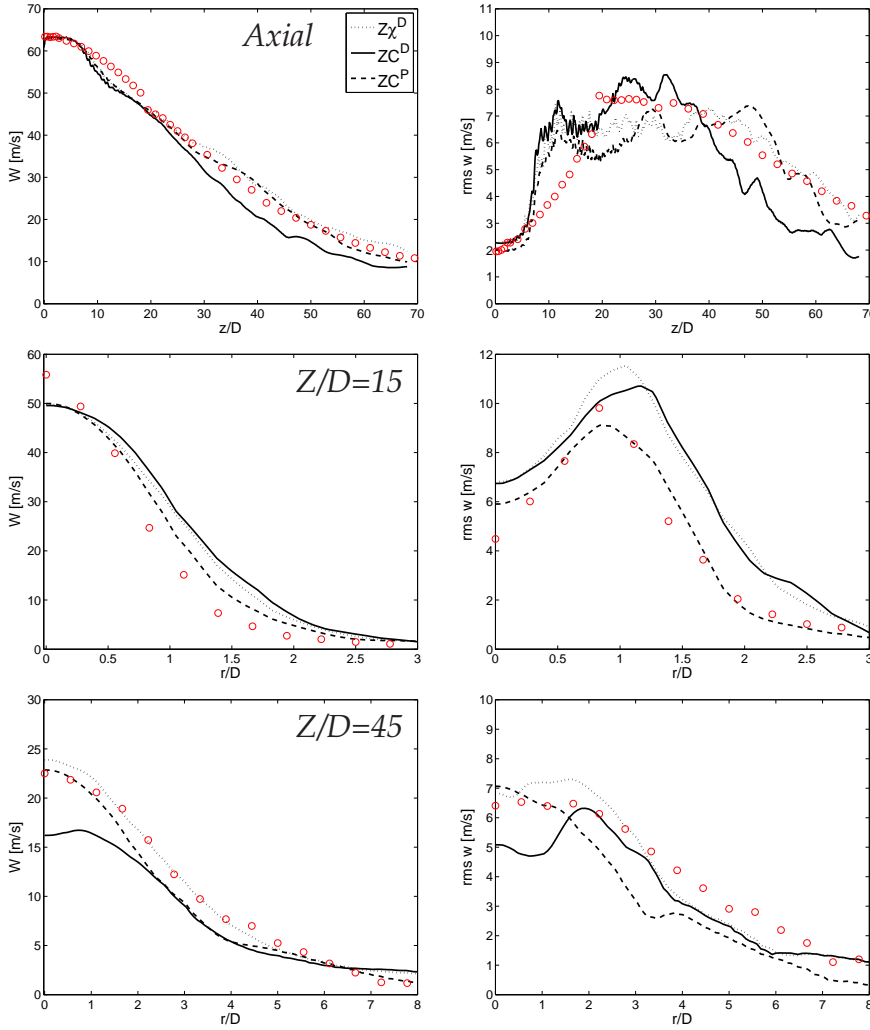


Figure 5.12 :mean and rms streamwise velocity Fields. (\cdots) $Z\chi^D$; ($—$) ZC^D ; ($- - -$): ZC^P ; \circ denote experiments.

The detailed results for the Sandia flame D are compared for three different models: the classical flamelet model ($Z\chi^D$), the progress variable method (ZC^D) based on the diffusion chemistry, and the progress variable method (ZC^P) based on premixed chemistry. In this section first the velocity fields are presented, as well as the turbulence statistics. This will mainly concern a description of the observations. Also the species mass fractions will be considered. In subsection 5.4.3 the differences will be discussed and an explanation of the observed differences will be provided.

The velocity field

The mean and rms streamwise velocity fields are presented in figure 5.12 and are compared to experiments from Schneider *et al.* [142]. At the centerline the streamwise velocity is generally well recovered. Only the ZC^D method shows a slight under-prediction at higher locations. The rms values $\langle \tilde{w}'' \tilde{w}'' \rangle^{1/2}$ are well reproduced at the nozzle, but at $z/D \approx 8$ they rise too strongly in all cases. This is a problem that is well known for this flame, and is related to the hardly resolvable thin mixing and boundary layer near the nozzle, Kempf *et al.* [72]. The maximum

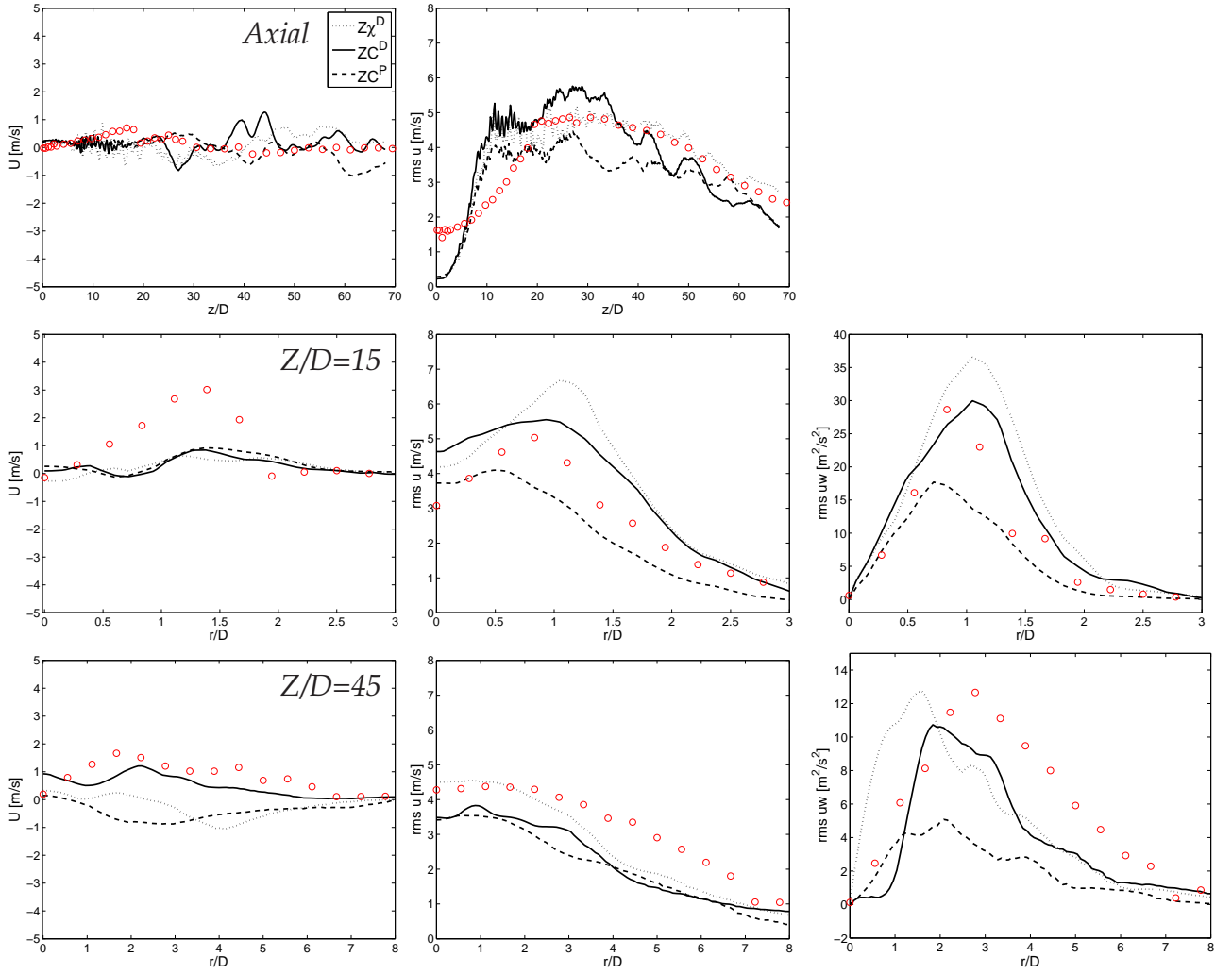


Figure 5.13 : mean and rms spanwise velocity fields and shear stresses $\langle \tilde{u}'' \tilde{w}'' \rangle^{1/2}$. (···) $Z\chi^D$; (—) ZC^D ; (---) ZC^P ; \circ denote experiments.

values are well recovered.

The spanwise profiles at $z/D = 3$ shows small differences on the mean velocity field as well as the rms values. When moving downstream in the flow, at $z/D = 15$, figure 5.12, the velocity profiles are slightly too wide, specially for the ZC^D and ZC^P method. The same holds for their rms intensities. The profiles at $z/D = 45$ show a decrease of the velocity magnitude for the ZC^D method at the centerline, which corresponds to the first figure of the streamwise velocity magnitude at the centerline. The other two methods show good correspondence to the velocity field measurements.

Figure 5.13 shows the spanwise velocity fields, as well as their rms values. Along the central axis, the mean spanwise velocity field should remain zero because of symmetry reasons. Just above the nozzle exit this is well recovered, showing that sufficiently many turbulent data-fields have been used. With increasing height mean spanwise velocity components depart from zero, up to velocity magnitudes of about 1 m/s. Different from the streamwise rms values, the boundary conditions for the rms values of the spanwise velocity field are zero at the nozzle exit. Still the rms

values of the u -velocity component at the centerline show a similar behavior as its streamwise counterparts. An abrupt increase is observed, followed by a steady level at about 4 - 5.5 m/s. The ZC^D method shows the largest values in the range up to height $z/D = 40$.

The mean velocity field in radial direction has not been recovered very well. On the other hand, the absolute magnitude is very small and well below the turbulent fluctuations. The fluctuations themselves are on average reasonably well recovered, which is the most important. The $\langle \tilde{u}''\tilde{w}'' \rangle^{1/2}$ components are recovered relatively well. Only the levels extracted from the ZC^P method give a significant underprediction at all heights.

Concluding it can be stated that the mean velocity field and turbulence intensities are well recovered in all simulations. There are minor differences visible, mainly at larger heights above the nozzle. Then the mean streamwise velocity at the centerline for the ZC^D method is lower than the other methods and the experiments. In the $Z\chi^D$ method the turbulence intensities just above the nozzle exit, near the pilot flame, are slightly over-estimated.

Species concentrations

Figure 5.14a shows the mixture fraction field along the central axis for the three different models. While the ZC^D model follows the experiments closely near the vicinity of the nozzle, it decreases relatively fast in magnitude at about $z/D = 20$. On the other hand in the ZC^P and $Z\chi^D$ methods the mixture fraction field corresponds accurately to the experiments, over the complete range. Yet the rms values are now slightly over-predicted, figure 5.14b. Close to the nozzle exit, below $z/D = 15$ the rms values from all models go to zero, while the fluctuations from the experiments remain present. The observed fluctuations in the experiments can either be due to errors in the experimental technique, such as previously suggested by Pitsch and Steiner [121] or due to preferential diffusion effects. In the latter case the average mixture fraction field, that is based on the Bilger definition, Bilger [17] can be unity, while instantaneous values can exceed this level, due to increased concentrations of hydrogen. When including preferential diffusion in the simulations in principle this effect can then be accounted for.

Because of the shift of mixture fraction field in the ZC^D method, all chemical species are shifted accordingly. This makes the analysis of the results, i.e. the impact of the parameterization unclear. To exclude the effect of the prediction of the chemistry as a function of the actual, spatial coordinates z/D and r/D , the species mass fractions will be presented as a function of the mixture fraction space. Then high values of Z correspond to low values of z/D , which is physically located close to the nozzle exit.

Figure 5.14c then shows the mass fraction of H_2O . This quantity is evaluated explicitly in the ZC^D and ZC^P method, as this is the chosen progress variable, but naturally reconstructed using the steady laminar flamelet database in the $Z\chi^D$ method. The ZC^D method predicts the concentration globally well, while it is underpredicted by the ZC^P method in the hot flame zone $0.3 < Z < 0.6$. Near the end of the physical domain, for small Z , the correct levels are recovered in the ZC^P

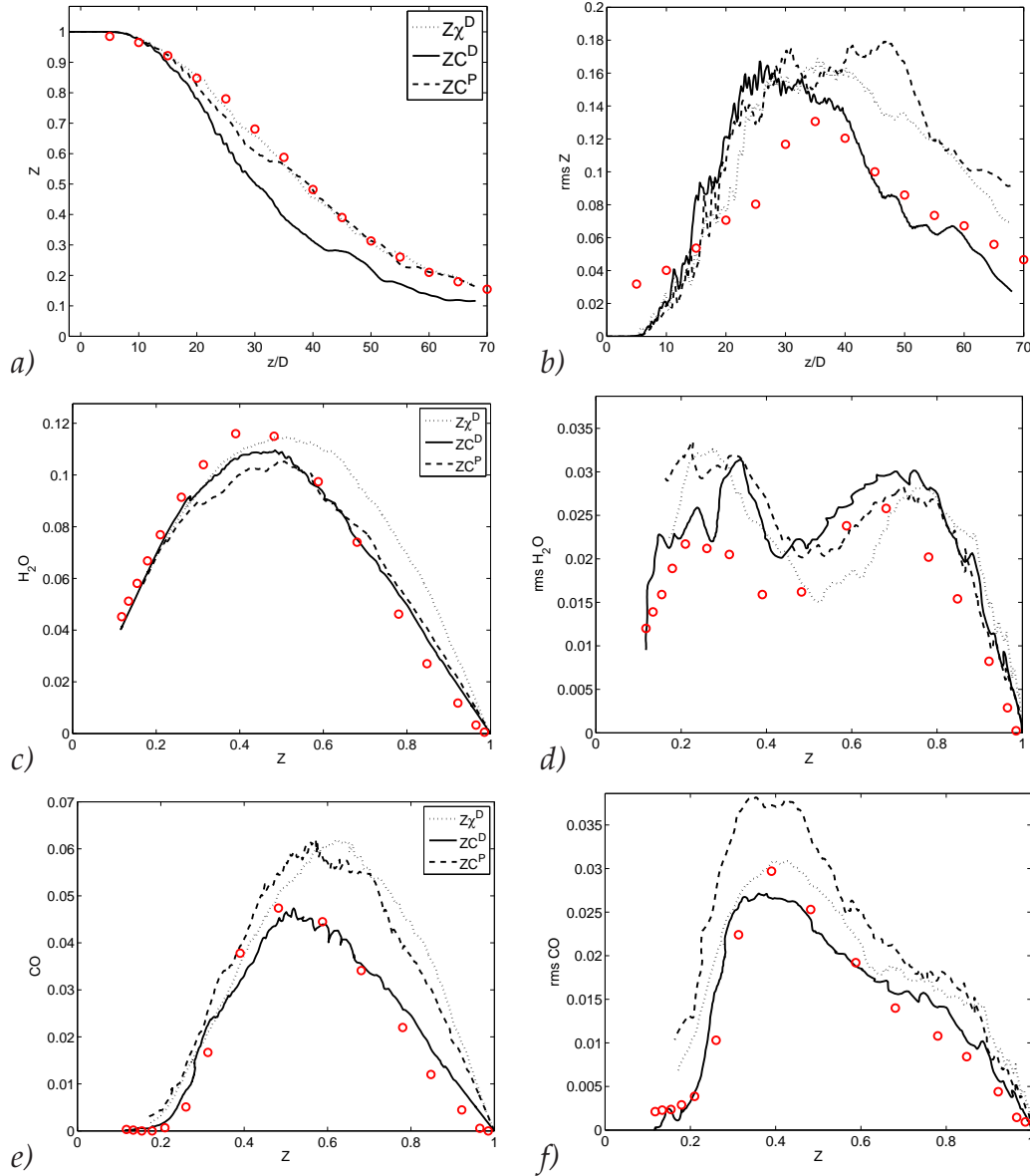


Figure 5.14 : Selected variables, and their rms values, along the center axis. (\cdots) $Z\chi^D$; (—) ZC^D ; (---) ZC^P ; \circ denote experiments. The mixture fraction is given as a function of the vertical coordinate z/D , the species mass fractions are given as a function of the mixture fraction Z .

method. The $Z\chi^D$ method shows an overprediction of the profiles at the rich side.

Concerning the variance, figure 5.14d, the first maximum is predicted too close to the nozzle exit ($z/D = 25$; $Z = 0.8$) for all cases. The second maximum as found in the experiments at $Z \sim 0.2$, is poorly recovered in all cases. The temperature fields exhibit a similar trend as the H_2O mass fractions, as these quantities are closely coupled. Finally the CO concentration fields are shown, representing the finite-rate chemistry. A remarkable correspondence is visible for the ZC^D method, which follows the experimental values closely. Both other methods give an overprediction at the rich side. Only at decreasing Z , i.e. higher up in the flame, the $Z\chi^D$ and ZC^P methods get in line with the experiments. The reason for this behavior will be discussed in more detail in the next subsection. The rms profiles show a correct

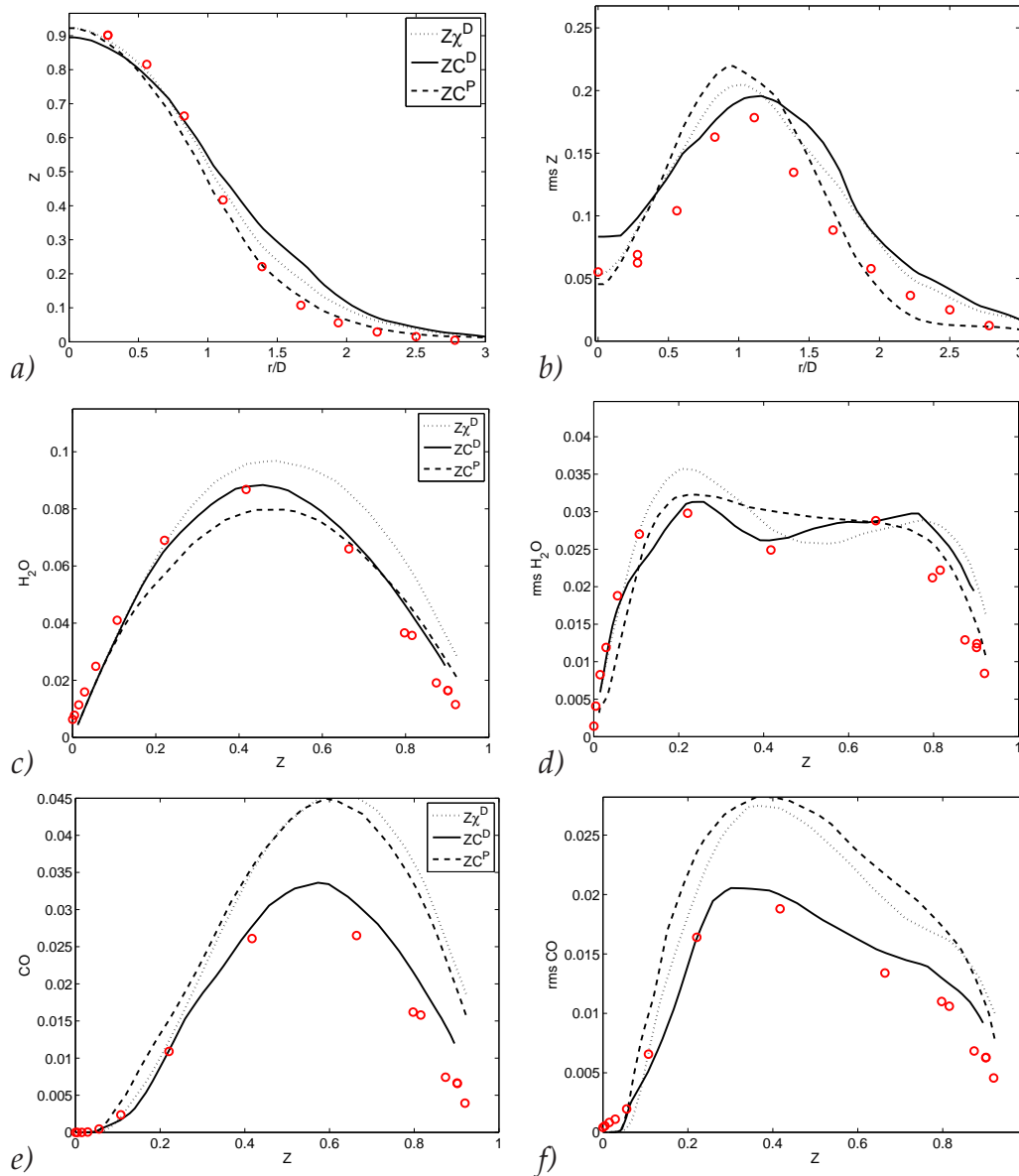


Figure 5.15 :Selected variables, and their rms values, at height $z/D = 15$. (\cdots) $Z\chi^D$; ($—$) ZC^D ; ($- - -$) ZC^P ; \circ denote experiments. The mixture fraction is given as a function of the radial coordinate r/D , the species mass fractions are given as a function of the mixture fraction Z .

profile for the ZC^D method as well as for $Z\chi^D$, while the ZC^P method over-predicts the variance.

In figure 5.15 the mixture fraction and species concentrations along the radial direction, at $z/D = 15$, are presented. The mixture fraction is best modelled by the ZC^P method. The rms profiles of the mixture fraction field is slightly predicted too wide, especially for the ZC^D and $Z\chi^D$ methods, figure 5.15b. The species concentrations and temperature field are again given as function of the mixture fraction coordinate. Then, for large Z , close to the central axis, the concentration of H_2O is constantly over-predicted for all models, figures 5.15c. Globally the concentration is best predicted using the ZC^D method. The progress variable method based on premixed chemistry gives an under-prediction of H_2O concentration, while the classical

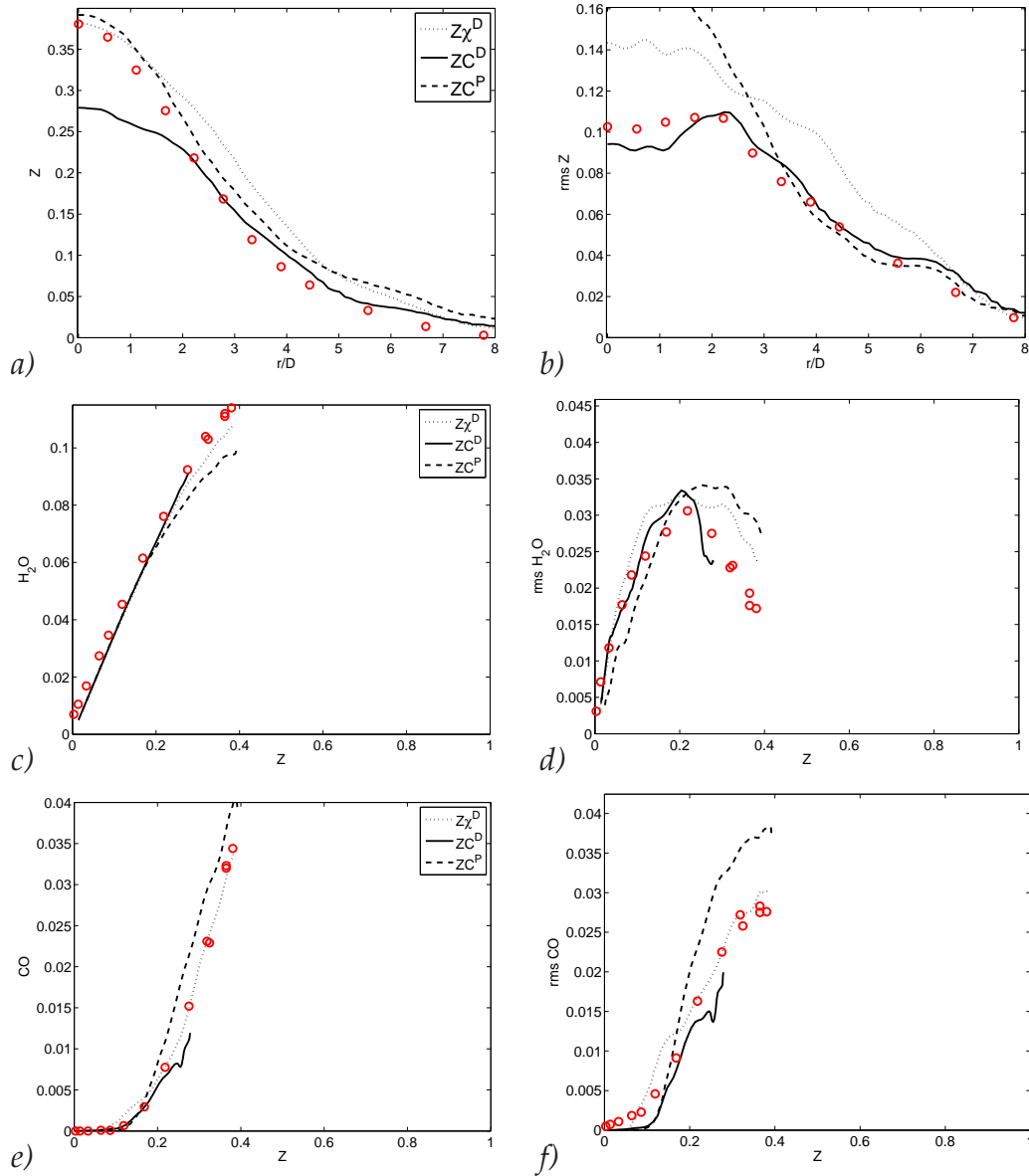


Figure 5.16 :Selected variables, and their rms values, at height $z/D = 45$. (\cdots) $Z\chi^D$; ($—$) ZC^D ; ($- -$): ZC^P ; \circ denote experiments. The mixture fraction is given as a function of the radial coordinate r/D , the species mass fractions are given as a function of the mixture fraction Z .

flamelet method leads to an over-prediction. For small Z the results from the different models collapse again. Also concerning the rms profile the ZC^D method is the best performing, figure 5.15d, showing the dip in the rms value of H_2O at the correct value of the mixture fraction. Concerning the CO mass fraction, the mean and rms values for the $Z\chi^D$ and ZC^P methods are overpredicted, figure 5.15g,h, while the ZC^D method shows a good correspondence to the experiments.

Higher up in the domain, at $z/D = 45$, figure 5.16, the ZC^P and $Z\chi^D$ methods predict the mixture fraction field correctly, but give a large overestimation of the fluctuating fields. At the same time the ZC^D simulation underpredicts the center-line value, but shows correct magnitudes of the variance. The mean mass fraction of H_2O are fairly equally predicted in all simulations, as are the rms values. The

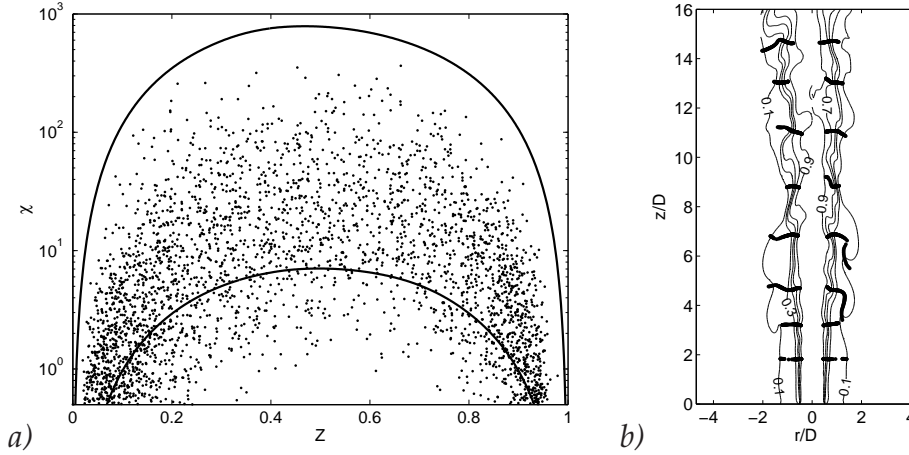


Figure 5.17 : (a) Scatter plot of the $Z\chi^D$ parametrization at $z/D = 15$. The two lines indicate the scalar dissipation rate corresponding to $a = 10$ and 1250 s^{-1} . (b) Reconstruction of the local flamelet structure, at one time instant. The contourplot shows the iso-lines of the mixture fraction field, the thick lines are the reconstructed flamelets.

ZC^P method underpredicts the maximum H_2O concentration, and overpredicts its variance at the larger values of Z . Concerning the CO profiles, figures 5.16e,f, the $Z\chi^D$ method now gives slightly better results compared to the other two methods, but the tendencies are similar.

To conclude, the global trend is that the ZC^P and $Z\chi^D$ methods predict the mixture fraction field better compared to the ZC^D method. The prediction of Z is crucial for the prediction of all remaining chemistry, therefore these methods show the best correspondence to experiments, when looking at spatial coordinates. On the other hand, to make a more fair comparison between the chemical models, the prediction of Z can be excluded. In that case on average a better correspondence between the experiments and the ZC^D method is achieved, especially for mixture fractions larger than 0.2. Higher up in the domain, for smaller values of Z , the differences between the models decrease. Thus, based on a chemical point of view, the ZC^D method performs the best, while when including the effect of the fluid dynamics, the other two methods are better.

5.4.3 Analysis of the chemistry models

The previous observations require an explanation. These cannot be extracted only from the presented observations alone, but are a result of a complex interplay of several processes. The focus is on the interaction of the chemistry and the fluid dynamics. First we will focus on the $Z\chi^D$ method. Then, the two progress variable methods will be discussed.

The classical flamelet method

In figure 5.11d the instantaneous scalar dissipation rate has been presented. This illustrates the presence of very high values of χ near the nozzle exit. When generating a scatter plot of the scalar dissipation rate at height $z/D = 15$ the appropriateness of

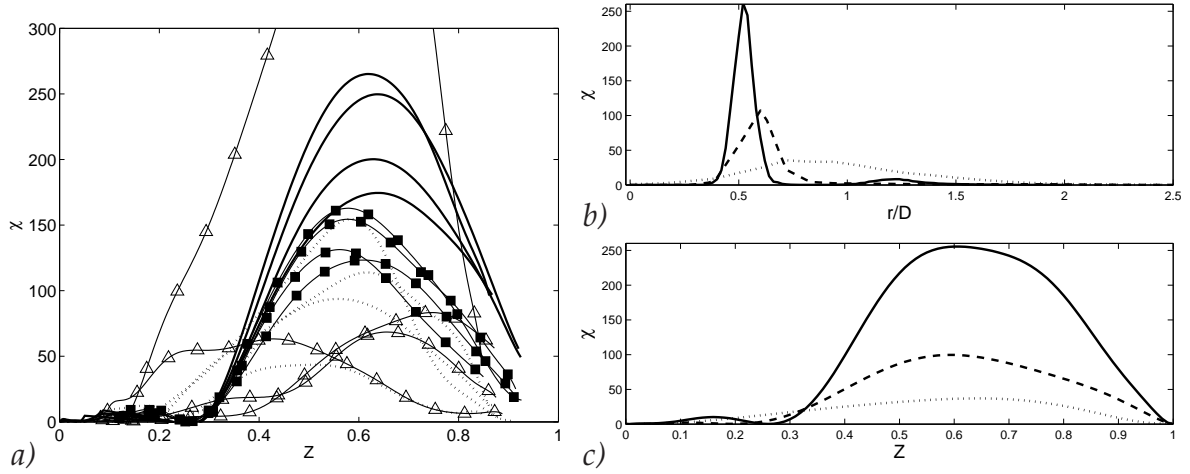


Figure 5.18 : (a) Examples of instantaneous $\tilde{\chi}(\tilde{Z})$ profiles reconstructed from flamelets in the $Z\chi^D$ simulation. Four flamelets at height $z/D = 1$, (—), $z/D = 3$, squares, $z/D = 7$, triangles, $z/D = 15$, (\cdots). (b): mean χ , as a function of radial coordinate, at three different heights. continuous line: $z/D = 1$, dashed: $z/D = 3$, dotted: $z/D = 15$. (c) conditional average of the mean scalar dissipation rate at the same heights.

the $Z\chi^D$ model can be checked in more general terms. This is shown in figure 5.17a. It is observed that a large amount of points are covered by the range of flamelets, from $a = 10 \text{ s}^{-1}$ to $a = 1250 \text{ s}^{-1}$. At these two strain rates the corresponding χ profiles are presented. A considerable amount of realizations can be found where the scalar dissipation rate is below its minimal value, mostly in the range close to stoichiometric conditions, $0.15 < Z < 0.5$.

Figure 5.17b shows an example of the instantaneous, filtered flamelets in a plane that intersects the central axis in radial direction. To evaluate the flamelets a coordinate transformation, as depicted in figure 5.2a, has been performed for this two-dimensional plane, using the instantaneous LES results. It shows that in this range $z/D < 15$ the flamelets are arranged mainly perpendicular to the vertical axis, i.e. at a constant height. The instantaneous $\tilde{\chi}(\tilde{Z})$ profiles, as reconstructed from these flamelets are presented in figure 5.18a. These profiles indicate that the assumption of a bell-shape profile, described by equation 5.7, does not hold on an instantaneous basis. Specially close to the nozzle exit this can lead to a wrong estimation of the strainrate.

Figure 5.18b shows the average profiles along the radial coordinate at three different heights above the nozzle exit. At $z/D = 3$ there are two peaks visible: a large one, between the fuel jet and the pilot flame, and a smaller one between the pilot and the co-flow. Also when plotting the time-averaged $\langle \tilde{\chi} \rangle$ as a function of the mixture fraction this functionality does not show a bell-shape profile, especially not close to the nozzle exit, figure 5.18c.

In the pilot flame, located at $0.5D < r < 1.3D$, where ($Z = 0.27$), the scalar dissipation rate is zero, as the pilot flame is in its chemical equilibrium. However, near the nozzle exit, close to the pilot, very high strain rates are encountered, that correspond to highly finite-rate chemistry. Therefore the diffusion flame chemistry should be described by a flamelet at high strain rate. But based on the applied para-

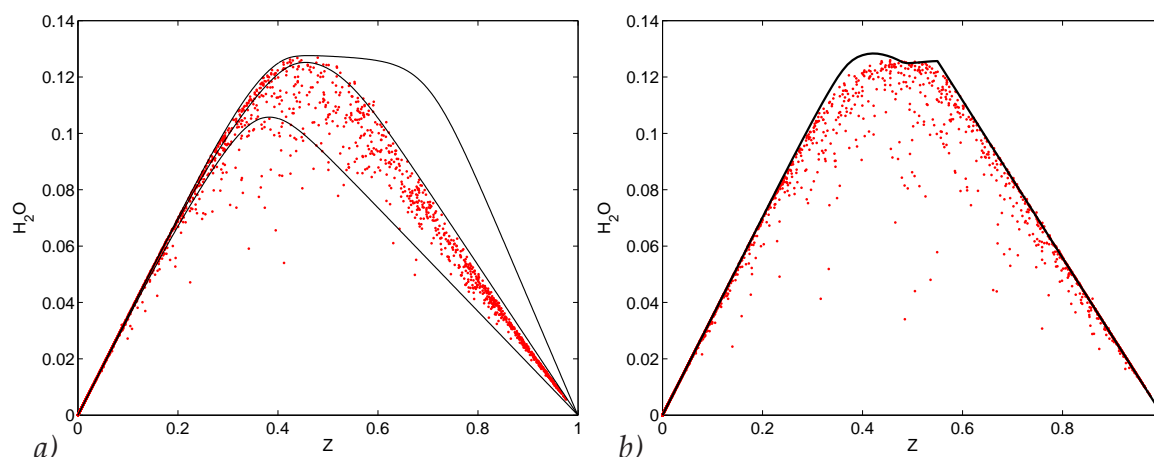


Figure 5.19 : (a) The scatter plot for the ZC^D flame, at $z/D = 15$, the lines indicating the flamelets at strain rates $a = 10, 100$ and 1250 s^{-1} (b) scatter plot for ZC^P flame at $z/D = 15$. The line indicates the maximum H_2O mass fraction in the FGM.

metrization, where a bell shape function for $\chi(Z)$ is assumed, a flamelet solution at low strain rate is used. The effect of this difference is rather large, because this takes place near stoichiometry. Here finite-rate chemistry effects on the density in the applied chemical database are clearly visible, see figure 5.8.

Pitsch and Steiner [122] have reported on this effect before. There the stabilizing effect of the pilot flame has been explained, by decreasing the scalar dissipation rate at stoichiometry. The difference on the chemical solution of a counterflow diffusion flame, between the scalar dissipation rate $\chi(Z)$, as found in this flame, and the presumed shape, equation 5.7, was evaluated. A considerable shift of the temperature profile towards the lean side had been observed.

All these considerations indicate that in the $Z\chi^D$ method flamelet solutions close to equilibrium, at low strain rates are used in the simulation. For the current simulations this leads to the results as presented in the previous section, showing reasonable prediction for the mixture fraction field, but less appropriate when considering the chemistry as a function of the mixture fraction coordinate.

The two progress variable methods

In the ZC^D and ZC^P methods the mass fraction of H_2O is evaluated independently from the mixture fraction. By plotting the instantaneous values of H_2O as a function of Z the applicability of the H_2O parametrization can be checked as well. This is shown in figure 5.19a for the ZC^D method, at height $z/D = 15$. Also three flamelets have been included in this figure: $a = 10 \text{ s}^{-1}$, $a = 100 \text{ s}^{-1}$ and $a = 1250 \text{ s}^{-1}$. Here it can be observed that for most points the instantaneous mass fraction of H_2O is covered by the domain defined by the non-premixed flamelets for strain rates smaller than $a = 100 \text{ s}^{-1}$. Still in some instances H_2O values are observed that are outside the range given by the flamelets, specially where lower concentrations of H_2O are encountered. In this case the flamelet solution at the highest strainrate is used to evaluate the species concentrations and transport variables.

The ZC^P model also parameterizes mixtures with low H_2O concentration, figure

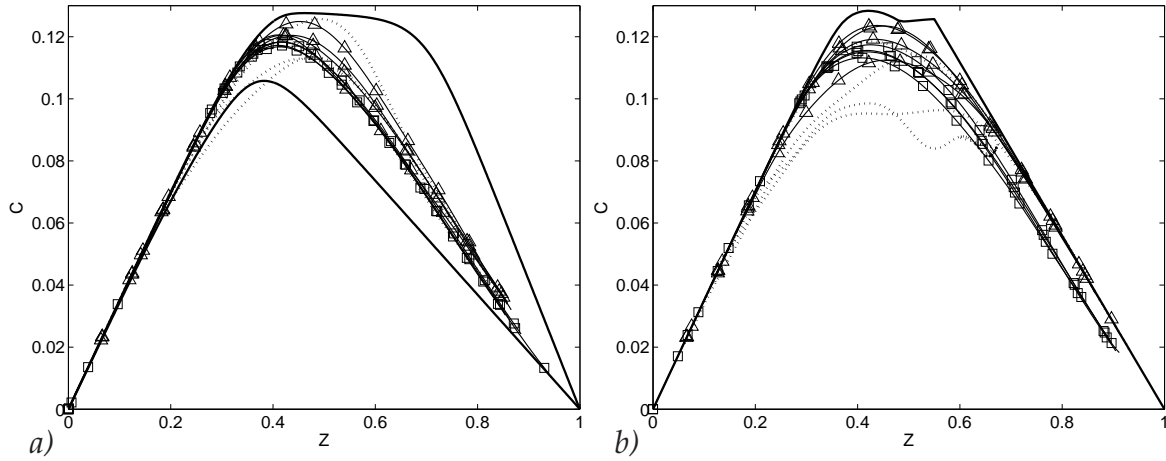


Figure 5.20 : (a) Examples of instantaneous $Z - C$ profiles reconstructed from flamelets in the ZC^D simulation. (—): minimum and maximum H_2O concentrations in non-premixed flamelet database. Four flamelets at height $z/D = 1$, squares, $z/D = 7$, triangles, $z/D = 15$, ($\cdot \cdot \cdot$). (b) The same, for the ZC^P method. (—): maximum H_2O concentration from premixed chemistry table.

5.19b. Here the black line denotes the maximum H_2O concentration. The minimum H_2O concentration in the premixed database is naturally at 0. In this case all instantaneous concentrations of H_2O are covered.

Figure 5.20a shows a few examples of reconstructed flamelets at three different heights close to the nozzle exit, for the ZC^D simulation. The reconstruction is performed in a similar way as was done in figure 5.18. Also two reference flamelets, from the 1D counterflow diffusion flame are plotted, for $a = 10 \text{ s}^{-1}$ and $a = 1250 \text{ s}^{-1}$. Then most flamelets are captured by the presumed shape, except for higher in the domain. At $z/D = 15$ examples can be found where the flamelet departs from the 1-D configuration.

Figure 5.20b shows the same for the ZC^P simulation. The maximum H_2O concentration is also shown. Compared to the ZC^D method, at $z/D = 1$ the H_2O concentration is lower. This can be explained as an effect of the parametrization. As in the premixed chemistry case, the H_2O concentrations up to 0 are covered, leading to low chemical source term. In case of the non-premixed chemistry, this source term is larger, as the quenching chemistry is used. This seems to be more appropriate, as in this flame no effects of lift off are present, i.e. the flame is directly burning. Again, higher in the domain, at $z/D = 15$ examples can be found where the flamelet shows structures that depart from a typical non-premixed flamelet-like structure.

Modeling the mass fraction of CO

The scatter plots given in figure 5.17a and figure 5.19 indicate that at $z/D = 15$ finite-rate chemistry effects are encountered, and will be taken into account when evaluating the chemical species. Its impact along the central axis is studied in some more detail in figure 5.21. Here the averaged H_2O mass fraction is plotted as a function of the mixture fraction field, along the axial coordinate. In figures 5.21a,b the dashed lines indicate the minimal (near-extinction) and maximal (near-equilibrium) values,

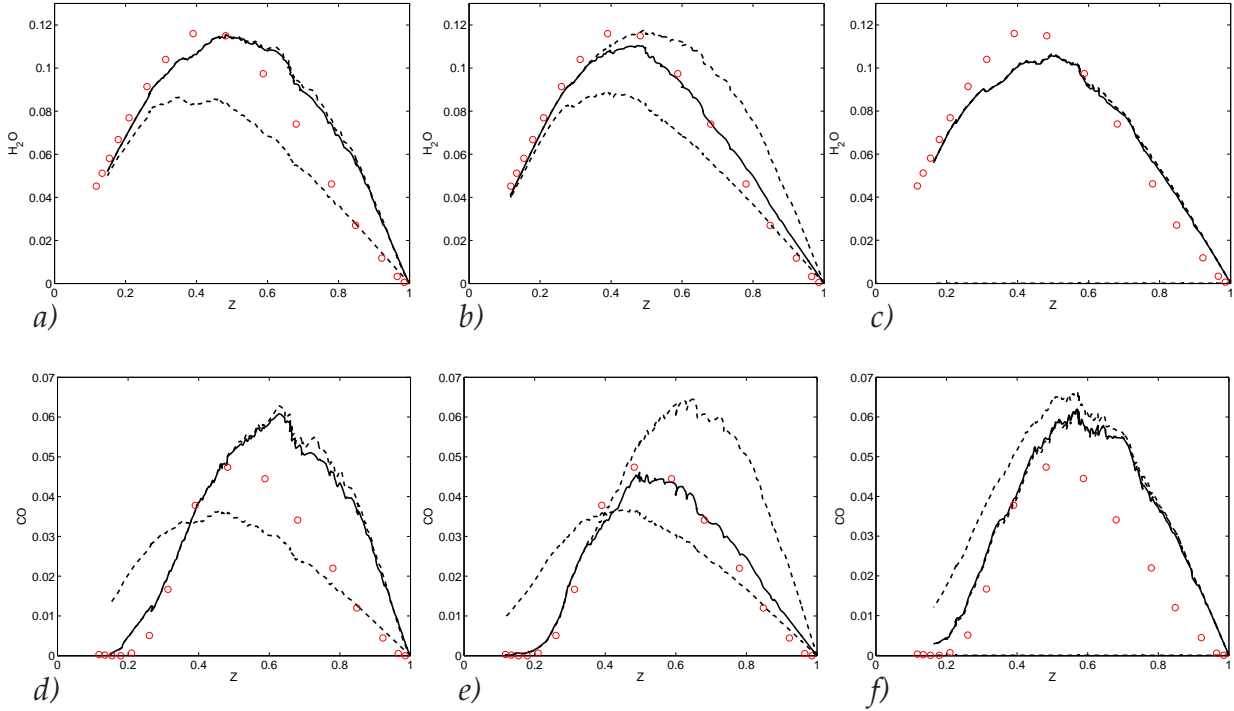


Figure 5.21 : Visualisation of impact of finite-rate chemistry on the solution along the central axis. In the figures (---) represent the minimum and maximum values in the chemistry database, between which the average solution (—) can move. The circles are the experimental values. (a,d) $Z\chi^D$ parametrization, (b,e) ZC^D parametrization, (c,f) ZC^P parametrization.

as found from the flamelet solutions for the maximal and minimal strain rate. Here, it is clearly observed that for the $Z\chi^D$ method, figure 5.21a, the chemistry is located along its near-equilibrium solution. This is different for the ZC^D parametrization, figure 5.21b. Then, for $0.4 < Z < 1$, which is at the axial coordinates $z/D \leq 40$, on average effects due to finite-rate chemistry exist. Therefore the H_2O concentration fields are reduced, compared to their equilibrium values, leading to a good prediction for the CO field. In figures 5.21c, f the ZC^P approach is presented. Here it is found that the H_2O mass fraction is always at its maximum value. Now finite rate chemistry effects in the diffusion region, as accounted for by the ZC^D method, are not recovered. This explains the similar observations for the ZC^P method and the $Z\chi^D$ method.

The reason why the ZC^P method does lead to values close to equilibrium whereas the ZC^D method shows finite-rate effects can be explained by differences in the source term, figure 5.9. Whereas the ZC^D method only shows chemical activity around stoichiometry, in the ZC^P method ω_C is also large at the rich side of the flame. This is an effect of the extrapolation procedure at $Z > 0.55$, as no flame solution exists for larger values of Z . Because of the large source term close to the nozzle exit the H_2O concentrations raise rapidly to their equilibrium values, leading to the over-prediction of the CO profiles in this region, figure 5.21f. In an additional test where the chemical source term was set inactive for $Z > 0.55$ this observation was confirmed. Now the ZC^P database based on the premixed chemistry behaved very

similar to the non-premixed chemistry for the mixture fraction field and the velocity field.

Therefore, based on a chemical analysis the ZC^D method leads to the best results, especially for large values of the mixture fraction, close to the nozzle exit. On the other hand, the mixture fraction field remains the crucial parameter, which is influenced largely by the fluid dynamics.

5.4.4 Concluding remarks

By comparing the three parameterization methods it has been observed that the classical flamelet method and the progress variable method based on premixed chemistry give the most suitable results, based on the prediction of the mixture fraction field. However, when showing the results as a function of the mixture fraction coordinate, the progress variable method based on non-premixed chemistry outperforms the two other methods. This leads to the conclusion that the parameterization of the chemistry, using this model, is better compared to the other two methods.

This indicates that the fluid dynamical part of the modeling problem needs improvement. Possible effects can be an adjustment of the initial turbulence level at the nozzle exit, as this has an important effect on breakup of the core region, Kempf [71]. Also an improved resolution of the shear layer close to the nozzle exit can lead to better results.

Improvements for the classical flamelet method can be achieved by applying a flamelet database that is better fitted to the current experimental setup. Especially the scalar dissipation rate as a function of the mixture fraction should be different from the one encountered in the counterflow flame geometry. With respect to the database of the premixed chemistry, a combination of species as progress variable should be used in order to prevent problems of non-monotonicity in the complete domain of the chemical manifold.

5.5 A sooting benzene diffusion flame

In the previous section the flame structure itself in the sense of the velocity field, the mixture fraction and their variances was of main concern. The impact of models for finite-rate chemistry was mainly shown through these quantities. Also most chemical species could well be described with the mixture fraction parameter solely, with an exception for the CO mass fraction. In this section we will focus on a turbulent flame where finite-rate chemistry has a large impact on the local chemical composition within the flame. Also a fuel type is chosen that is more of relevance for engine conditions than methane.

In internal combustion engines the fuels that are used consist of a mixture of large hydrocarbon molecules. This implies a reaction process that is rather complex. Detailed reaction mechanisms of primary reference fuels, such as n-heptane and iso-octane involve about 1000 species and 4000 elementary reactions, Ranzi *et al.* [130]. Also the total reaction path consists of a large number of steps. Apart from the combustion process, where the large fuel particles are broken up into the typical

reactants, such as CO, CO₂ and H₂O, the hydrocarbon molecules can interact with each other and form larger particles, known as polycyclic aromatic hydrocarbons (PAH's). These particles grow further in the case that there is not sufficient oxygen available. Then these PAH's can form soot particles that are highly mutagenic and carcinogenic, Harvey *et al.* [59], Avakian *et al.* [7]. The need to suppress the formation of these particles is a key driving force in current research activities.

In this work the soot formation process in a diffusion-type turbulent benzene flame is studied. Soot formation in a laminar flame is modeled using a detailed reaction mechanism, which is used to create a steady laminar flamelet database, Evlampiev [44]. From this database information is extracted that is used for the calculation of the soot formation processes in a turbulent diffusion flame. The proposed modeling procedures and their results are presented in this section.

But first the theory on soot formation processes is briefly introduced, with emphasis on diffusion flames, subsection 5.5.1. Then, in subsection 5.5.2 modeling approaches are discussed, and the currently applied method is proposed. In subsection 5.5.4 the results for the test flame are presented and discussed.

5.5.1 The process of soot formation

The processes that describe soot formation are highly complex, and consist of many sub-steps. It is not the focus of the current thesis to discuss the chemical problem, but rather to apply a given mechanism to a turbulent flame simulation. Therefore the chemical mechanism is only briefly described here. More details can be found in Richter and Howard [134] and Evlampiev [44]. The sub-steps that describe soot formation are usually classified as the formation of molecular precursors, particle nucleation, surface growth, particle coagulation and particle oxidation, see figure 5.22, Richter and Howard [134]. In all these sub-steps many types of particles play a role. The molecular precursors of soot are heavy polycyclic aromatic hydrocarbons (PAH's) with a molecular weight of 500 - 1000 amu. For the formation of these molecules a number of pathways have been proposed. Addition of C₂ and C₃ takes place, as well as other small units, such as acetylene. The specific type of reaction pathway depends much on the fuel type, see [134].

The soot particle inception phase links the gas-phase combustion to the particle dynamics. The production of nascent soot nanoparticles of the size of about 1.5 nm is governed by this step. This process is relatively poorly understood, also because experimental difficulties. Several inception pathways have been proposed, depending on the gaseous precursors that have been assumed: polyacetylenes, ionic species or PAH's. The growth of PAH's is believed to be governed by the so-called H-abstraction-C₂H₂-addition (HACA) mechanism: a hydrogen atom is removed from an aromatic molecule, which is then replaced by a gaseous acetylene group. With increasing size more of these blocks can be added via HACA.

In the next step, surface growth on the initial soot particles takes place by addition of gas phase species such as acetylene and PAH, and its radicals. In this process more than two particles at the same time can play a role, which will complicate the modeling of soot formation drastically. Soot particle coagulation finally increases the particle size, by the collisions of several particles with each other. In this process

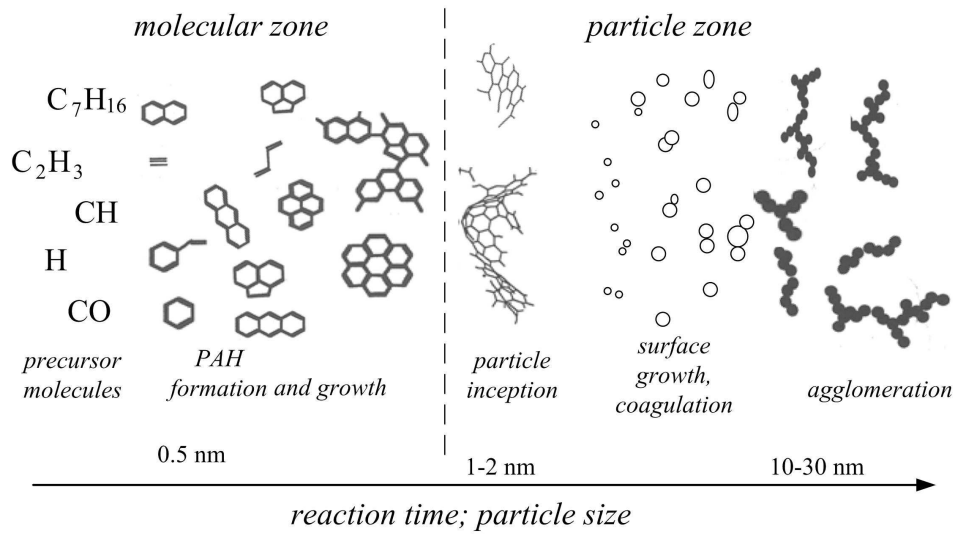


Figure 5.22 :Figure showing main mechanisms that describe soot formation, Richter and Howard [134]

aggregates of non-spherical morphology are formed.

The only mechanism that counteracts with the formation is the oxidation process of soot and PAH's. Then the PAH's are decomposed by the formation of CO and CO_2 .

Soot formation in turbulent diffusion flames

The global mechanisms of soot formation were described in the overview above. Compared to premixed flames, the soot formation process in non-premixed flames is generally more stimulated, as here the fuel and air are separated.

Yang and Koylu [168] recently presented an experimental study on a non-premixed turbulent lightly sooting ethylene/air flame. The inception region for soot precursor particles was observed in the range of $z/D = 10 - 30$, which is just above the nozzle exit of the burner. Above this height these early particles started to collide, leading to chainlike aggregates of nonspherical morphology. Growth in soot volume fraction f_v , which is a measure for the mass fraction, has been observed up to a flame height of $z/D = 100$. Here the soot volume fraction is defined as

$$f_v = \frac{\rho Y_s}{\rho_s}. \quad (5.25)$$

In this expression ρY_s is the total mass density of soot in the gas phase and ρ_s is the density of condensed soot, which is $\rho_s = 1800 \text{ kg/m}^3$. In [168] the rms values of the volume fraction were in the same order of magnitude as the volume fraction itself, which was about 1 ppm at $z/D = 100$. The initial increase of f_v is due to nucleation and coalescence growth processes. Higher up in the flame oxidation processes become more dominant, leading to a decrease in the number of particles. Yet, the particle size of the aggregates increased steadily, due to the aggregation processes, which depends strongly on the residence time.

For the modeling of diffusion flames a flamelet method is generally applied, Peters [114]. However, it is well known that the soot concentrations cannot be correlated to the mixture fraction field directly, Balthasar *et al.* [12], Moss [97]. The soot composition depends strongly on the residence time as well as on the local gas composition. However, recent observations show that this is mainly the case for the larger soot particles. D'Anna *et al.* [6] studied a turbulent ethylene/air flame, and observed two classes of particles. The first class are nanoparticles that consist of large poly-aromatic hydrocarbons, of the size of about 2 - 3 nm on average. These particles are mainly found in the fuel rich region of the flame, close to the nozzle. The second class, the larger particles, are formed with increasing residence times in the flame, as a result of the growth processes. These soot particles are dominant in the region of maximum flame temperature. D'Anna concludes that the concentration of the nanoparticles is not controlled by the chemical kinetics, but by the turbulent mixing, due to effects of inception and carbonization of precursor particles. It is shown that these nanoparticles correlate strongly to the major species concentration, and therefore the mixture fraction. A second flame with higher inlet velocity, that corresponds to a higher strain rate, shows lower concentrations of this type of nanoparticles. This indicates that these species are simply depending on the mixture fraction and the strain rate, but not directly on residence time. However, as mentioned, the larger soot particles cannot be correlated to the mixture fraction, but prevail in the regions close to the maximum flame temperature. The maximum concentrations of larger soot particles have been observed just after the maximum of the nanoparticle concentration.

5.5.2 Modeling soot in diffusion flames

As can be understood from the previous section the formation of soot is a highly complex phenomenon, depending on many parameters, such as the type of fuel, pressure, residence time, the availability of oxygen. Amongst others this defines the different paths of soot formation, and the final composition of the soot particles. The particle population can generally be defined by a particle size distribution function (PSDF): a continuous distribution of the number density N as a function of particle size diameter d .

A standard application of a flamelet method to model the soot composition in a turbulent flame is not appropriate, [12], as the soot is not correlated to the mixture fraction and scalar dissipation rate only. This calls for a dedicated methodology, where the laminar flamelet solutions can be applied. In this subsection first the two main approaches for the modeling of soot are discussed, that form the background of the applied methodology in the current LES calculations. These are the method of moments and the sectional method, which are the most popular in the application to turbulent sooting flames. Then the laminar flamelet solutions are presented, which are based on the sectional method. The analysis of the solutions will lead to the proposed flamelet method for the prediction of the total mass and number densities.

Method of Moments

In the method of moments (see Frenklach [48]) the soot particle distribution function is divided into a number of particle sizes, with a corresponding mass

$$m_i = i \cdot m_1, \quad (5.26)$$

where index i refers to soot particles with a mass that corresponds to i times the smallest mass unit, referred to as m_1 . Then the particle size distribution can be described by the moments of this distribution, where the moment M_r is written as

$$M_r = \sum_{i=1}^{\infty} m_i^r N_i. \quad (5.27)$$

In this expression N_i denotes the number density of particles of size i , and m_i the mass corresponding to this particle size. It can be seen that in expression 5.27 the first two moments, M_0 and M_1 denote the number density and the mass density of the soot, respectively. In the CFD method conservation equations for these moments are solved, using standard convection-diffusion transport equations:

$$\frac{\partial \widetilde{M}_r}{\partial t} + u_j \frac{\partial \widetilde{M}_r}{\partial x_j} = \frac{\partial}{\partial x_j} \left((D_t + D_r) \frac{\partial \widetilde{M}_r}{\partial x_j} \right) + \widetilde{S}_r, \quad (5.28)$$

with D_t the turbulent diffusion and D_r the diffusion coefficient corresponding to moment M_r . S_r is the source term corresponding to moment r , due to nucleation, surface growth and oxidation. The complete set of moments, ranging from $r = 0$ to $r = \infty$ defines the complete particle size distribution. In practical simulations only up to the second moment is being evaluated explicitly, e.g., Hong *et al.* [63]. This means that an assumption on the shape of the PSDF has to be made, which normally is the log-normal distribution function.

Sectional method

Another approach that can be followed is to divide the complete range of the soot particle size distribution into a number of sections, Pope and Howard [125], Hall *et al.* [56]. Then balance equations for every class of particles are composed which can be solved in a way analogous to all other gas phase species. Therefore no assumption on the shape of the PSDF has to be made: the PSDF is a result of the solution of the conservation equation for each section. Then the soot particle formation and oxidation processes can be expressed in terms of gas phase kinetics, using an appropriate reaction mechanism. This mechanism has to include aromatic growth, particle inception, surface reactions and coagulation.

Yet, this method is much more computationally demanding than the method of moments. In the sectional method a large reaction mechanism has to be used, incorporating all relevant reactions between soot particles and gas phase, and between soot particles themselves. The population balance equations are very stiff and highly non-linear, and therefore the problem cannot be solved by an explicit numerical method. Therefore a specialized numerical solver has been developed to tackle this problem, Evlampiev [44].

The flamelet database of a benzene flame

In this work a steady laminar flamelet library from a counterflow diffusion flame is adopted, to model soot formation in a turbulent benzene diffusion flame. The database is can be described by a $Z - \chi$ parametrization, where the strain rate a is coupled to the scalar dissipation rate χ using expression 5.7.

The reason to choose for this flame is that it is a highly sooting turbulent diffusion flame that resembles the situation in a conventional Diesel engine. Moreover, an extensive reaction mechanism exists for this fuel type, Richter *et al.* [135]. This mechanism consists of 295 species, 1102 conventional gas phase reactions and 5552 reactions describing particle growth and is based on the sectional method. On the other hand, no experimental data is available for this diffusion flame. The mechanism developed by Richter is constructed for the modeling of soot formation in premixed benzene/air combustion at low pressures, but it is here applied for the modeling of an atmospheric, turbulent non-premixed benzene flame, which is more relevant for engine conditions. In the mechanism the PAH/soot is distributed over 20 sections or bins, ranging from a particle size of 0.85 nm for bin 1 up to 67.8 nm for bin 20. The masses in the bins are increasing on a logarithmic scale from one bin to the next. The TROT-interpreter has been used to interpret and handle the mechanism, as well as all thermodynamic and transport property data, Evlampiev [44].

The steady laminar flamelet database for this flame has been constructed using the CFDF program, which is optimized for the treatment of this type of very large chemical problems, Evlampiev [44]. The temperature of the fuel stream was set to 600 K, just above the critical value of 562.1 K, such that the benzene is gaseous. The air stream was set to 300 K. The strain rates a have been varied from 10 to 192 s^{-1} , which was near the quenching strain rate for this flame. Despite this preheating the maximum temperature of the benzene flame (which was 2172 K) did not change much, compared to a reference ethylene flame, Evlampiev [44], where the fuel stream was set to 300 K. This is because the stoichiometric condition is at low mixture fraction, $Z = 0.1$, which means that the air stream contributes by 90% to the mass at stoichiometric conditions. Moreover, the activation energies for both flames are similar. The flamelet solutions for the major species are presented in figure 5.23 for two different strain rates. Notice that at the lowest strain rate, $a = 10 \text{ s}^{-1}$ there is no overlap between the oxygen and the C_2H_2 mass fractions. This indicates that the conditions for soot formation are very strong, as C_2H_2 is the major precursor for the HACA mechanism.

Also the PAH/soot bins in the laminar flames at different strain rates can be visualized, figure 5.24. This shows the relative contribution of the different particle sizes to the total amount of soot. For large strain rates the smallest particles are dominant, whereas for smaller strain rates the largest particle size gives the largest contribution to the total amount of soot mass. Notice also that the bins corresponding to the smallest particle size are relatively insensitive to the strain rate, corresponding to the observations of D'Anna [6].

In figure 5.25 the mass and mole fractions of the total PAH/soot, Y_S and X_S , which is the sum of all soot bins, are presented as a function of the mixture fraction, for increasing strain rates. It can be observed that these are very sensitive to

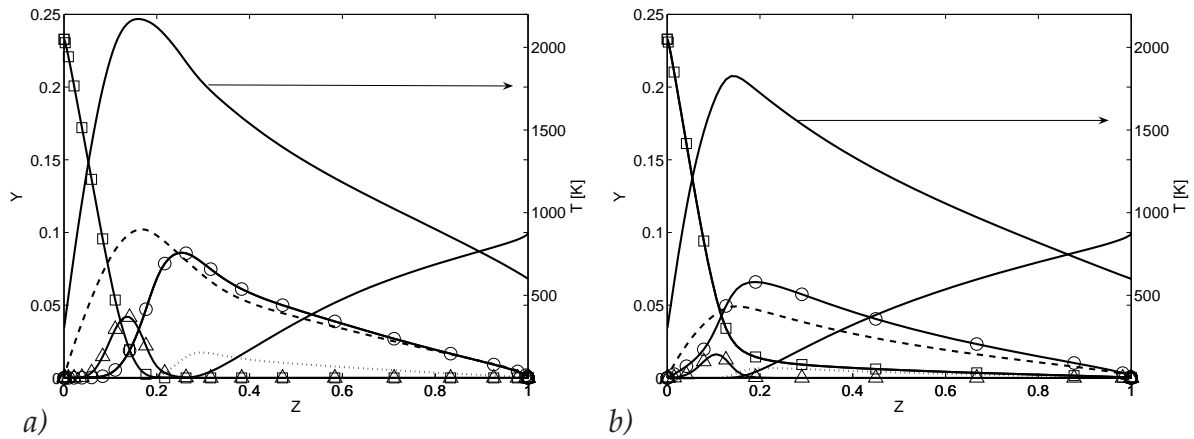


Figure 5.23 : (a) Flamelet solutions of the main species and temperature field at strain rate 10 s^{-1} (—) $\text{C}_6\text{H}_6/10$, (---) H_2O , (\cdots) C_2H_2 , \square O_2 , \circ CO , \triangle OH (b) The same at $a = 190 \text{ s}^{-1}$.

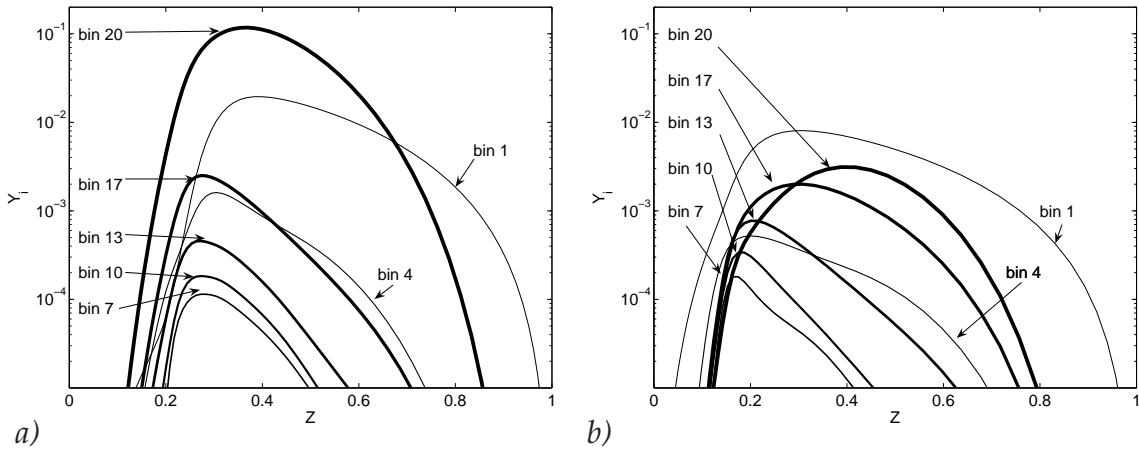


Figure 5.24 : Flamelet solutions of the mass fraction of the PAH/soot bins at two strain rates, (a) $a = 12 \text{ s}^{-1}$ and (b) $a = 120 \text{ s}^{-1}$. The bins with increasing line width correspond to particle sizes of about 0.85, 1.7, 3.4, 6.7, 14, 34, and 68 nm.

the applied strain rate. The total mass fraction changes one order in magnitude with decreasing strain rate by one order of magnitude. For the maximum PAH/soot mass fraction an exponential dependency on the strain rate was found [44], similarly as found by Decroix and Robert [36] for an experimental propane steady counterflow diffusion flame. This leads to two problems. First, as discussed in subsection 5.2.1, it can be hard to reconstruct the strain rate a from the scalar dissipation rate which is provided from the CFD calculations. A large sensitivity to the strain rate of the total PAH/soot makes the method inherently additionally sensitive if $a(\chi)$ is not well defined. Secondly, for low strain rates the flamelet assumption (i.e. a one-dimensional flame structure, where the chemical time scales are shorter than the turbulent time scales) does not hold anymore. This effect is visible from the flamelet database: the mass/mole fractions do not indicate the presence of an equilibrium value at the lowest strain rate, which does not change when the strain rate is decreased. This can be seen as in figure 5.25 the PAH/soot concentrations do not converge to such a single profile with decreasing strain rates, but remain constantly rising. Also the chemical

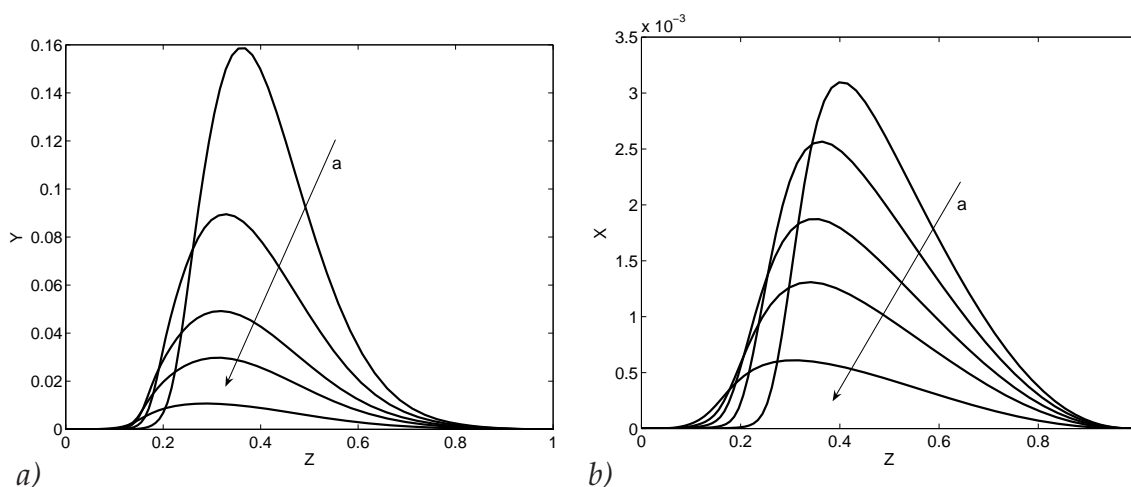


Figure 5.25 : (a) Flamelet solutions of the total PAH/soot mass fractions at different strain rates, $a = 12, 21, 45, 88, 190 \text{ s}^{-1}$. (b) Corresponding mole fractions.

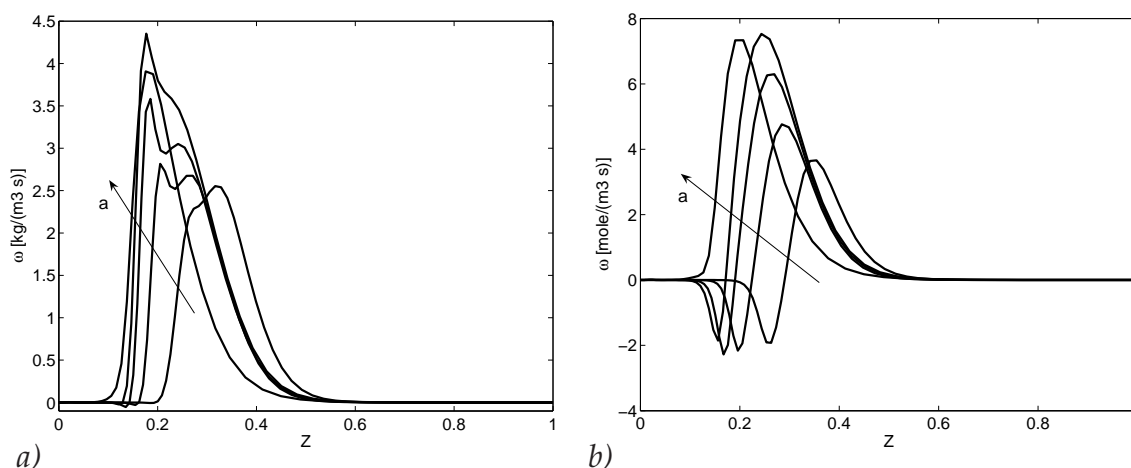


Figure 5.26 : Flamelet solutions of the total PAH/soot source terms at different strain rates, $a = 12, 21, 45, 88, 190 \text{ s}^{-1}$. (a) Mass source terms, (b) molar source terms.

source terms for the PAH/soot, figure 5.26, do not reach a zero level with decreasing strain rate.

On the other hand it has been observed that the chemical source terms for the soot particles show a different behaviour than the species or mass densities themselves, Evlampiev [44]: they are much less sensitive to the strain rate, see figure 5.26. With a decrease of a of one order of magnitude, the source terms for the mass and mole fractions only change less than a factor two. This means that the maximum reaction source term for the total mass of soot in the benzene flame is relatively insensitive to the strain rate. This is different from the behavior of the source term for H_2O , as presented in the previous section on the Sandia flame D, figure 5.9. But it is in line with the suggestions from D'Anna *et al.* [6] that the formation of the large soot particles is only depending on the residence time and takes place mainly at the hot flame zones, while the precursors can be described by the solutions from a steady laminar flamelet.

This means that we can use the information on the chemical source term for the production of PAH/soot from the database by the application of a $Z - \chi$ para-

metrization, while the mass fractions of the PAH's and the relatively small soot particles can be retrieved reasonably well directly, from the same $Z - \chi$ parametrization. This analysis in fact corresponds to an analysis of the effective timescales of the chemistry. With increasing chemical time scales the flamelet assumption becomes less appropriate, whereas the flame regime starts to be located in the connected reaction zones regime, figure 5.1. Then it is better to solve transport equations retrieving source terms from the steady laminar flamelet database.

A wide range of additional information is available from the flamelet solutions. Notice for instance, that for low strain rates the source term for the mole fraction becomes negative, whereas the mass fraction remains mostly positive. This indicates a shift of the soot particle size distribution from smaller, light particles to the larger ones. Also information concerning typical particle size distribution functions and on the presence and growth rate of typical toxic species, such as benzo[a]pyrene is available, [44], which can be of practical relevance in the turbulent flame simulations.

5.5.3 The setup for the Large-Eddy simulation

In the previous subsection a steady laminar flamelet database has been described where soot formation is modeled in a benzene flame, using the sectional method. Now a model needs to be provided in order to link the information of the SLF database to the turbulent flame simulations. Different from observations on all representative species in the Sandia flame D, in section 5.4, It has been shown in the previous section that even at the lowest strain rate, $a=10 \text{ s}^{-1}$ there is no evidence that soot is in its steady state value. This means that here it is certainly not appropriate to apply a progress variable method based on a typical soot concentration, and use this to lookup all remaining soot species using results from a flamelet solution.

Also the use of a typical progress variable such as H_2O is not expected to lead to improvements in the results. The chemical time scales of the soot formation process are in a completely different range as that of H_2O : while H_2O can be described by the solution given by the lowest strain rate, the soot will continue to change drastically. Moreover, in this flame no pilot flow is included. Therefore the $Z - \chi$ parametrization for major species, density and viscosity is reasonable in this case.

Recently Netzell *et al.* [102] reported a study where a sooting turbulent diffusion flame was evaluated based on the sectional method. The flow field had been evaluated based on a steady flamelet library incorporated into a standard RANS flame code, whereas the soot was reconstructed in a postprocessing step by using a time-dependent flamelet method. The representative flamelet was initialized by an extinguished flamelet at high strain rate. Then this flamelet traveled through the domain, while mixing is governed by following the maximum scalar dissipation rate at a specific height, leading to soot formation results in this flamelet. However, as soot was shown to be very sensitive on this scalar dissipation rate, the averaging procedure, where only a single representative flamelet is used that is subjected to a single χ -profile, can be an over-simplification, leading to unrealistic soot predictions.

A more natural method would be to transport separately a representative selection of soot bins. However, this method remains computationally rather expensive.

Additionally, the source terms for the separate PAH/soot particle sizes are not directly depending on the mixing rate, with only a mild sensitivity to the strain rate. The growth terms for separate PAH/soot particle sizes depend both on C_2H_2 content and temperature (the flamelet parameters), as well as on the concentration of the smaller soot particles (due to particle coagulation/growth) and the concentration of the larger soot particles (due to oxidation), Richter *et al.* [135]. The destruction term due to oxidation was shown to depend mainly on the OH-radical content and temperature, which are flamelet parameters.

Application of the SLF

With these considerations in mind we propose to base the soot chemistry on four parameters. First of all the mixture fraction field Z , to define the global mixing state of the turbulent diffusion flame. Secondly the scalar dissipation rate χ , to define the global mixing time scale, which is used to find the strain rate a . Based on these two parameters the temperature and the major species are retrieved, corresponding to the $Z\chi^D$ method, as described in the previous section on the simulation of the Sandia flame D. In a similar manner the chemical source terms for the total number density $\omega_{X_S}(Z, a)$ and mass density $\omega_{Y_S}(Z, a)$ are extracted from the steady laminar flamelet database. The third and fourth parameters are therefore two additional tracers that define the total number density of the soot X_S , i.e. the mole fraction, as well as the mass density Y_S . These total mole and mass fractions are the sum of the mass and mole fraction of all PAH/soot particles, defined by bin 1 up to bin 20. This methodology shows similarities to the work of Bai *et al.* [10]. There, an axi-symmetric, turbulent ethylene diffusion flame has been modeled using a RANS approach. The soot volume fraction was evaluated by extracting the source terms for the total volume fraction from a steady laminar flamelet calculation.

As has been argued in the previous section this method can be used for evaluating the total amount of PAH/soot, because these source terms are relatively insensitive to the strain rate, Balthasar *et al.* [12]. The method corresponds to a method of moments, in the sense that here the zeroth and first moment are evaluated explicitly in the Large-Eddy simulations. An important difference, though, is that the source terms are here based on the flamelet solutions from a detailed reaction mechanism for a benzene diffusion flame. Therefore no assumptions except for the rate constants and transport data in the chemical mechanism are necessary. Moreover, this method is naturally extendable, by introducing the transport of additional moments or bins in the LES calculation.

Having information on the total amount of mass and the total amount of particles is in general not sufficient to reconstruct all information on the separate soot particles. Therefore a particle size distribution function has to be assumed. Typically a log-normal shape is used, Hong *et al.* [63]. However, an increasing amount of evidence shows a bimodal size distribution of soot particles, with the first peak around 2 nm and the second peak at 20-50 nm, due to primary soot particles, D'Alessio *et al.* [3]. This functionality has also been observed from the steady laminar flamelet calculations, Evlampiev [44]. Such a particle size distribution can be recovered by evaluating the transport of the representative bins separately.

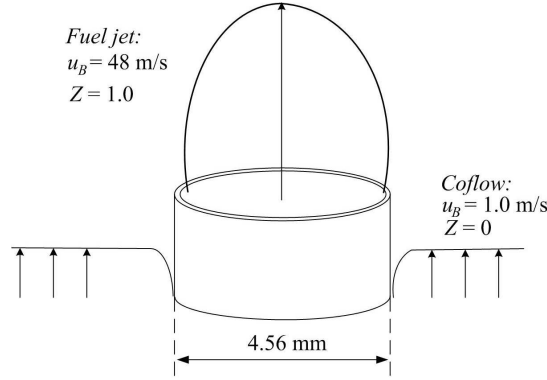


Figure 5.27 :Sketch of the numerical setup for the benzene flame.

Based on the first two moments an average particle size can be evaluated. Therefore an average particle mass m_p needs to be evaluated:

$$m_p = \frac{\tilde{Y}_s}{N_A \tilde{X}_s^*}, \quad (5.29)$$

where \tilde{X}_s^* is the number of moles of PAH/soot per kg gas, and N_A the Avogadro constant. Then, assuming a constant density of the PAH/soot, $\rho_s = 1800 \text{ kg/m}^3$, the average volume of the particle can be computed, and hence the average particle diameter d_p , assuming sphericity of the particles.

The computational setup for the Large-Eddy simulations

For the benzene test flame the following setup has been applied. A jet with a diameter $D = 4.56 \text{ mm}$ injects benzene, which is preheated to a temperature of 600 K . The gas enters the ambient air with an injection velocity of $u_B = 48 \text{ m/s}$, see also figure 5.27. The total domain that has been simulated has a diameter of 40 cm and a height of 80 cm . The applied grid consists of about 1.0 million grid nodes. Therefore a grid resolution of 280 cells in axial direction, 60 cells in radial direction and 60 in the tangential direction has been used. An O-grid arrangement was applied in order to mesh the nozzle pipe flow properly. Turbulent inflow boundary conditions have been used at the inlet, Klein *et al.* [73], while a pipe flow was allowed to develop in the initial region, before it was released in the ambient air. A coflow was included with a velocity magnitude of 1 m/s .

5.5.4 Results

In figures 5.28 - 5.30 the mass fraction of OH, the PAH/soot source term and the mass fraction of the total PAH/soot are shown for four time instances, 4 ms apart from each other. The OH concentrations represent the location of the thin reaction layer of the major combustion species. From this figure the flamelet structure is visible, specially near the vicinity of the nozzle. Higher up in the flame hot flame parcels appear from time to time. The chemical source term is active at the rich side of the flame surface, figure 5.29. This can be seen from the pockets that appear in time, which can be mapped just inside the OH profiles. Consequently local high

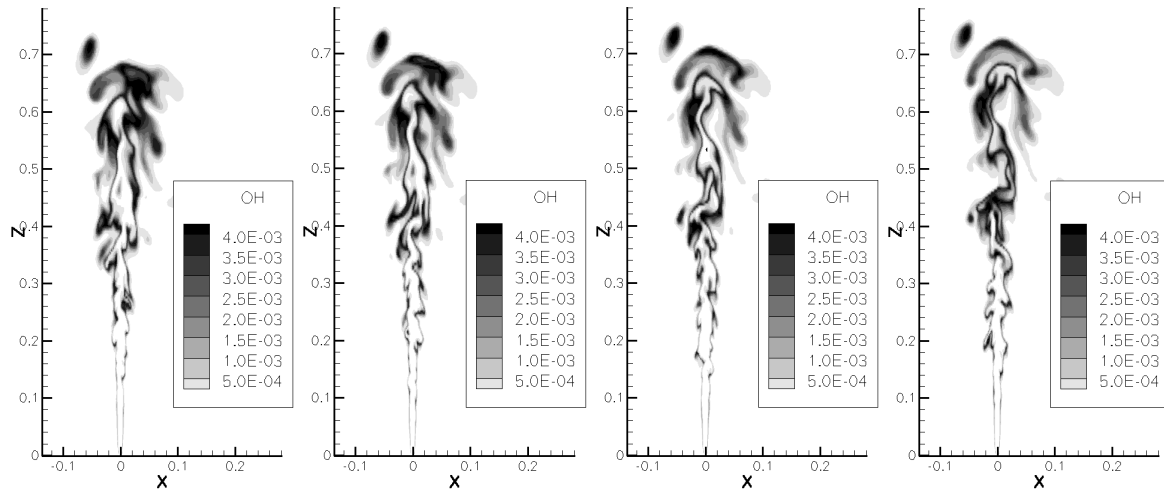


Figure 5.28 :Instantaneous OH mass fractions for the benzene flame, for four successive realizations, 4 ms apart.

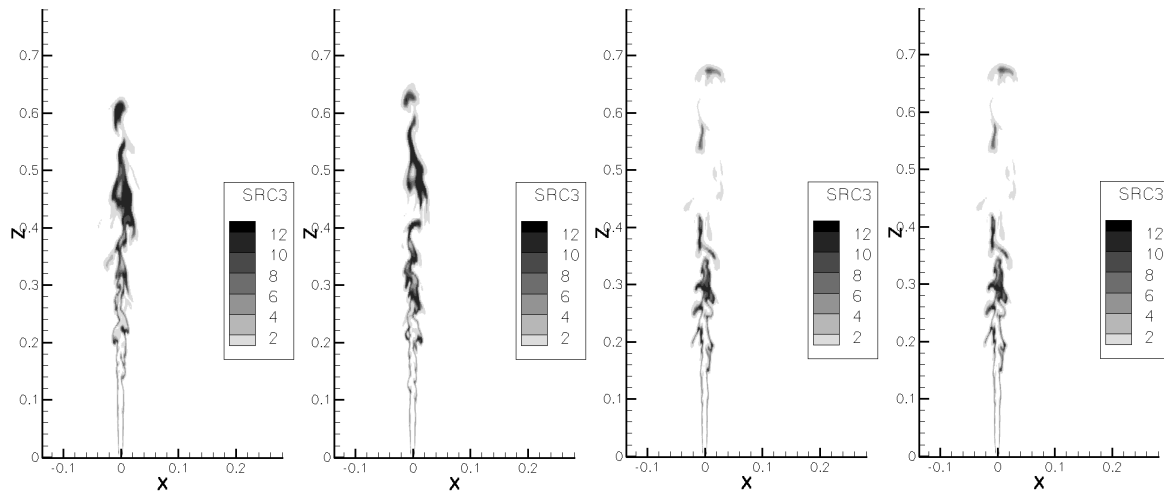


Figure 5.29 :Corresponding instantaneous (scaled) soot source terms (mass fractions) for the benzene flame.

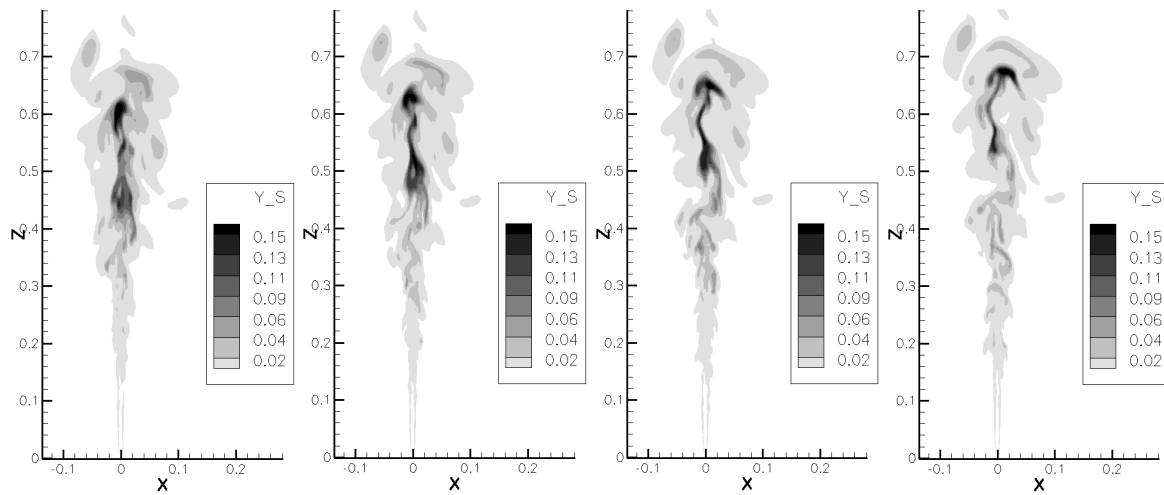


Figure 5.30 :corresponding instantaneous PAH/soot mass fractions for the benzene flame.

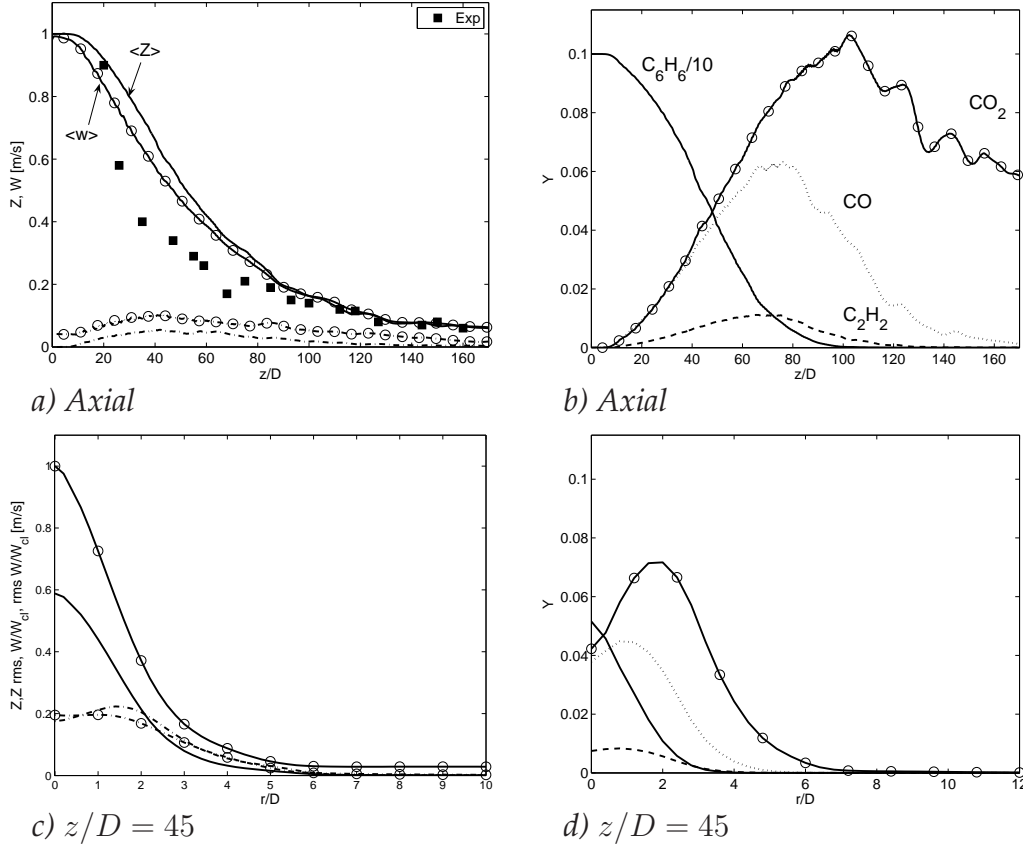


Figure 5.31 : (a,c) Profiles of the mixture fraction and streamwise velocity field of the benzene flame, along central axis and at $z/D = 45$, in radial direction. (—) denotes $\langle \tilde{Z} \rangle$, $(-\cdot-)$ $\langle \tilde{Z}''^2 \rangle^{1/2}$, $(-\circ-)$ $\langle \tilde{w} \rangle$ and $(-\circ\cdot-)$ $\langle \tilde{w}''^2 \rangle^{1/2}$. Squares: Experimental data for mixture fraction of ethylene flame, Moss [97]. (b,d) Main species mass fractions along the central axis and in radial direction. (—) $C_6H_6/10$, $(- - -)$ C_2H_2 , $(-\circ-)$ CO_2 and $(\cdot\cdot\cdot)$ CO .

intensities of PAH/soot are observed in figure 5.30 that show mild correspondence to the OH flamelet structure concerning its shape.

In figures 5.31a,c the global, averaged flow field results are presented for the mixture fraction, the streamwise velocity and their variances. In order to compare the simulations to experimental observations the data from Moss [97] are given by the black dots in figure 5.31a. There, measurements of the mixture fraction based on carbon mass fraction in a turbulent ethylene diffusion flame were reported. Whereas the flow conditions were similar in both cases, a noticeable difference between the current flame and the experiments is visible. This can partly be explained by the differences in fuel type of both flames (ethylene versus benzene), which means different fuel densities, and partly from the effects of the modeling. For instance, no quenching or lift-off due to high strain rates near the nozzle exit are accounted for in the numerical simulation.

Both the mixture fraction and the velocity field show the typical behavior, as was observed in the Sandia flame D results: a decreasing intensity along the central axis and accordingly a widening in spanwise direction, figure 5.31c. Notice that in this figure $\langle \tilde{w} \rangle$ and $\langle \tilde{w}''^2 \rangle^{1/2}$ are scaled to the average centerline velocity. From the

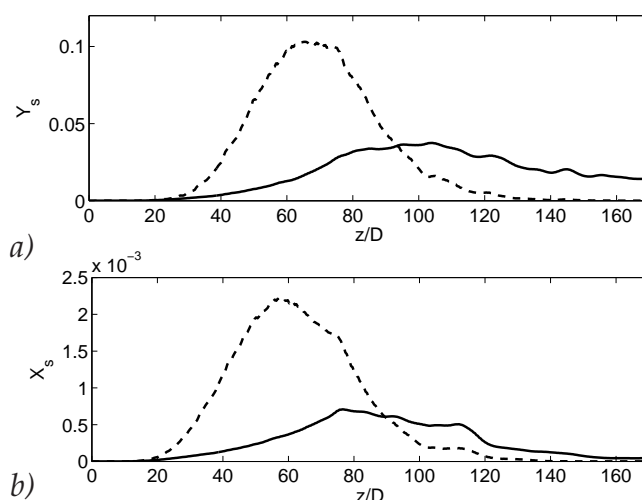


Figure 5.32 :Solutions from the averaged transported progress variables $\langle \tilde{Y}_s \rangle$ and $\langle \tilde{X}_s \rangle$ (—), compared to their steady laminar flamelet values (---).

mixture fraction fields and the corresponding scalar dissipation rates the concentrations of the major species have been retrieved. This is presented in figures 5.31b,d. The solid line represents the concentration of benzene. This is decreasing accordingly along the central axis, due to both (turbulent) diffusion and reaction. Typical species concentrations, such as CO_2 and CO are appearing instead. Also a precursor species like C_2H_2 is observed, which is an important precursor in the HACA mechanism, leading to the soot particle inception, Richter and Howard [134]. Thus, its presence indicates the region where large PAH's are formed.

Soot statistics

In figure 5.32 the axial evolution of the total mass fraction and the total number density has been tracked. At about $z/D = 30$ the PAH/soot mass fractions start to be visible, corresponding to observations of Yang and Koylu [168]. The number density starts slightly earlier to be visible, at about $z/D = 20$. This indicates a growth of small, young soot particles. The maximum PAH/soot mass fractions are recovered approximately at $z/D = 120$, which is close to the maximum reaction products concentrations, see figure 5.31b. This is also in correspondence with the observations of D'Anna *et al.* [6], where the maximum soot concentration is measured in the maximum flame temperature zone. The number density shows its maximum somewhat earlier in the flame, then it starts to decrease. This can be an effect of coagulation, followed by oxidation. Also the corresponding PAH/soot flamelet solutions are used to evaluate the soot concentrations directly based on the $Z\chi^D$ formulation, to compare to the method where PAH/soot source terms are extracted. This illustrates the difference between both methods. The PAH/soot concentrations based on the flamelet methods give an overestimation in magnitude, while their maxima are located relatively close to the nozzle exit, compared to the explicitly evaluated PAH/soot concentrations. Due to the time delay that is accounted for by tracking the development of PAH/soot directly, initially it takes more time for the soot to appear and grow. Also, higher in the flame, the oxidation process is delayed, com-

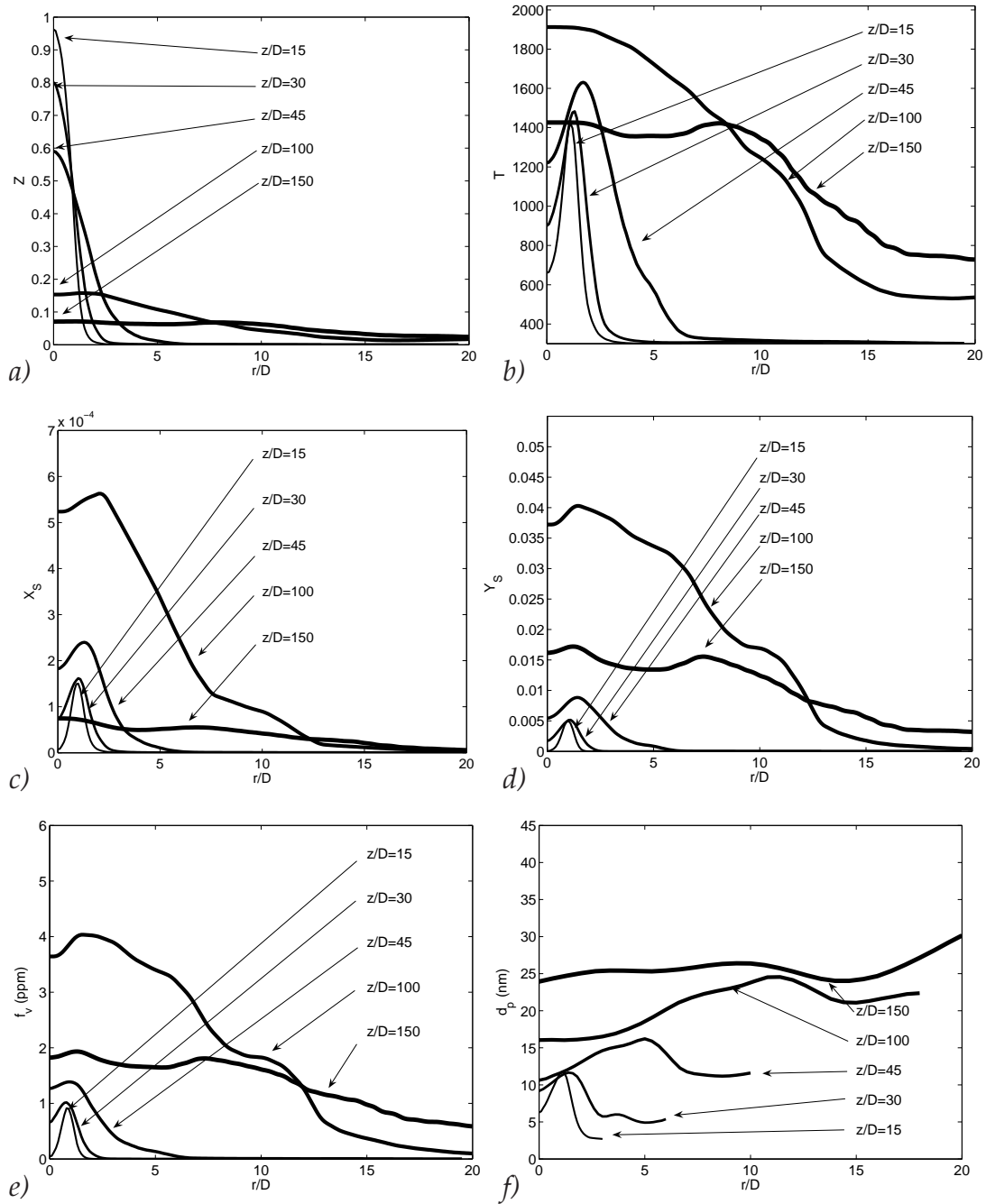


Figure 5.33 :Average profiles for the main variables in the benzene flame, at increasing heights. The lines indicate profiles at increasing heights, at $z/D = 15, 30, 45, 100, 150$, with increasing thickness (a) mixture fraction field, (b) temperature profiles, (c) mole fraction of total PAH/soot, (d) mass fraction of total PAH/soot, (e) volume fraction and (f) mean radius of soot particles.

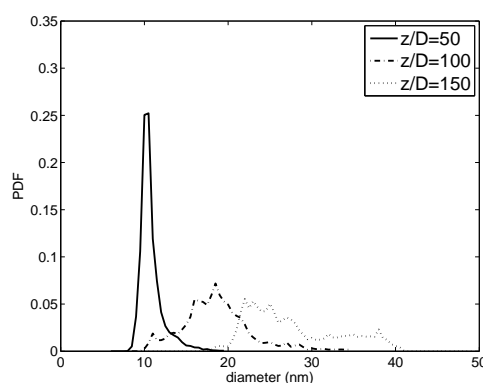


Figure 5.34 :Probability density function of the mean particle size of the PAH/soot, as a result of turbulent fluctuations, for three different heights along the central axis.

pared to results from the flamelet method.

Figure 5.33*a,b* shows the average evolution of the mixture fraction field and the corresponding temperature field. Especially the temperature field gives an indication on the range where soot formation processes becomes more active. This is at the rich side of the flame, $Z > 0.1$. Close to the nozzle exit, at $z/D = 15$, the mole and mass fractions of the total PAH/soot are only present at the flame zone, figure 5.33*c,d*. Higher up in the flame these profiles are widening, leading to a smoothly distributed averaged PAH/soot intensity. Despite the differences in magnitude, the shapes are very much comparable, showing an increase of total soot with increasing height. Notice that the PAH/soot mass fractions are constantly wider compared to the mole fraction. This is well visible at height $z/D = 100$, for $r/D > 10$. A reason for this is that the mole fraction has a negative source term at low strain rates. This leads to a reduced number of soot particles, whereas the mass fraction remains increasing. This indicates a shift of the particle size distribution to the larger particles. Higher up in the domain, $z/D = 150$ the intensities decrease again.

From these data the soot volume fraction has been reconstructed, using expression 5.25. This is a quantity that is typically used in experimental techniques. The volume fraction is largely related to the mass fraction, see figure 5.33*e*. The maximum volume fraction for the total PAH/soot that is reached for this benzene flame is about 5 ppm. Also a reconstruction of the average particle size diameter is performed, using both the information of the mass fractions and the mole fractions, expression 5.29. Here, it is assumed that the soot particles are spherical. The results are presented in figure 5.33*f*. Along the central axis, the average diameter increases up to 25 nm, while at the side of the flame the average size can increase up to 40 nm.

Figure 5.34 shows a probability density function of the flame of the mean particle sizes that are encountered at three locations along the central axis. These resulting PDF's are an effect of the turbulent fluctuations of the filtered mass fraction and mixture fraction of total PAH/soot only. Then, at $z/D = 50$ the mean particle size is about 11 nm in diameter, with a rms of 1.5 nm. With increasing height the mean and rms values of the PDF increase: at $z/D = 100$ these are 19 nm and 5 nm respectively, and at $z/D = 150$ these are 26 and 6 nm. Notice the wide tail at the larger particle sizes. This can indicate the occasional presence of flow parcels containing large (average) soot particle sizes, as identified by figure 5.30.

5.6 Conclusions

In this chapter two turbulent diffusion flames have been investigated. The focus was on modeling finite rate chemistry effects. Therefore, a progress variable approach has been implemented in the FASTEST-3D code and applied to a standard turbulent diffusion flame, the Sandia flame D. The relatively new method, where a progress variable is applied to non-premixed chemistry problems, is compared to the classical flamelet method where the non-premixed chemistry is parameterized using a mixture fraction and the scalar dissipation rate.

In the progress variable method two different databases have been used: one based on non-premixed flamelets and one based premixed flamelets. In both cases the mass fraction of H_2O is used as the progress variable. By comparing these three methods it is found that differences are most visible from a different prediction of Z , which is the crucial parameter for the prediction of the chemical parameters in Sandia flame D. Therefore, based on the prediction of Z the classical flamelet method and the progress variable method based on premixed chemistry give the most suitable results. However, when correcting for the wrong prediction of the mixture fraction field, the progress variable method based on non-premixed chemistry outperforms the two other methods. This leads to the conclusion that the parameterization of the chemistry, using this model, is better compared to the other two methods. At the same time effects from the fluid-dynamics are now disturbing these results. Improvements can be achieved by adapting the inflow turbulence, and/or by a better resolution of the shear layer. This should lead to a more appropriate (reduced) model prediction of the jet breakup in the progress variable method.

In the last section of this chapter a sooting turbulent benzene diffusion flame has been investigated. A steady laminar flamelet library has been used based on a very detailed reaction mechanism. In the Large-Eddy simulations the total soot mass and mole fractions have been computed explicitly, based on a $Z - \chi$ parametrization for the chemical source terms.

The regions of soot formation can be identified, showing distributed parcels where soot formation takes place. The results show a growth of soot volume fraction up to levels of about 4 ppm. The average particle sizes increase steadily in this flame, up to about 30 nm.

This study can be considered illustrative in giving a methodology for the application of a flamelet method for soot prediction in turbulent diffusion flames. In the current simulation one of the limitations is that up to today no chemical mechanisms exist for soot formation of more realistic fuel types, such as n-heptane. Nevertheless, it is believed that in future research this type of very large reaction mechanisms will be at the chemical basis for the modeling of soot in practical engine applications.

Recommendations

Apart from a better resolution of the shear layer and better inflow conditions, the simulation of the Sandia flame D can be improved by optimizing the flamelet database. Especially due to the pilot flame, the scalar dissipation rate is essentially different from the one in the counterflow flame geometry. With respect to the database of

the premixed chemistry, it is advised to use a combination of species as progress variable, such that problems of non-monotonicity can be prevented.

It would be interesting to study the impact of the inclusion of extinguished/re-ignition flamelets into the non-premixed flamelet database. This is specially relevant for the simulation of turbulent flames that depart more the chemical equilibrium solution than the Sandia flame D, such as the flames E and F. Then local extinction can have a more drastic effect on the fluid dynamics. These type of chemical problems are also more directly of interest for the modeling of turbulent combustion as takes place in Diesel engines. Here combustion is highly turbulent, ignition delay and lift-off are phenomena that need attention.

Concerning the modeling of soot in diffusion flame type problems, a first extension of the methodology as presented in this thesis, is to track an extra number of soot variables in the Large-Eddy simulations, related to the different PAH/soot particle sizes. Then less assumptions on the particle size distribution function has to be made. This requires a more deep analysis of the contribution from different chemical pathways to the growth/destruction rates for the different soot tracking variables. This methodology suits very well to the sectional approach, based on a very detailed reaction mechanism. Then, this type of information is in principle available.

Moreover, it is interesting to study a prediction method based on a zero - dimensional, stirred reaction model, applied to stream-tracers of fluid moving away from the reaction front. While the heat release is close to its chemical equilibrium state, the soot parcels can be tracked in time explicitly, as a function of temperature and oxygen content that are encountered by these parcels, due to transport and mixing.

Additionally, it can be necessary to include an equation for the energy of the system, as for sooting flames radiative effects can become important. In the case of the simulation of combustion in compressed cylinder, where additionally heat losses at the walls can take place, the explicit tracking of the energy is of even more importance.

General conclusions

In this thesis the application of the Large-Eddy Simulation technique is investigated as a tool for the modeling of turbulence and turbulent combustion problems that are relevant for engine conditions. It is found that its application to a complex engine geometry remains difficult, as the wall modeling and the accuracy of the numerical method can have a drastic impact on the flow statistics. On the other hand, a gaseous fuel jet and turbulent jet flames can well be modeled. Also the use of flamelet methods in turbulent diffusion flames and in models for soot formation in this type of flames has been discussed.

This thesis reports on a study where the Large-Eddy simulation technique is applied to model turbulent flow, mixing and combustion problems related to engines. Three subjects have been described: the turbulent flow in an engine-like geometry, the turbulent mixing of a gas jet system and the application of flamelet-based methods to Large-Eddy simulations of two turbulent diffusion flames. Because of our goal to study engine-related flow problems, two relatively practical, 'engineering-like' flow solvers have been selected for the simulations. This choice was motivated by their ability to cope with complex geometries as encountered in realistic, engine-like geometries. However, the modeling of these type of realistic geometries can lead to the sacrifice of two aspects in the formulation of the current simulations: the accuracy of the numerical schemes that can be applied and the grid resolution that can be achieved.

Modeling the turbulent flow in a confined engine-like geometry

In chapter three the impact of the numerical scheme of two flow solvers and the resolution has been investigated. It has been concluded from the performed simulations on a square duct flow that coherent structures can be detected and that global flow features are well recovered. On the other hand, as the boundary layer is not well resolved, the shear can not be predicted properly. Therefore the other flow properties, such as a typical secondary flow structure and the turbulence intensities, can only be captured qualitatively. Despite the improvements that have been implemented in the Kiva-3V code, by the less dissipative convective scheme, the numerical dissipation was shown to be obscuring most of the effects of the subgrid-scale models. This

is concluded by comparing the results from the simulations including the subgrid-scale models to two simulations where the subgrid-scale model was switched off.

The impact of an under-resolved shear layer and a dissipative numerical scheme have additionally been tested on a more realistic engine geometry: a complex turbulent, swirling and tumbling flow in an engine cylinder that is induced by the inlet manifold. For this geometry a number of LES simulations has been performed with the FASTEST-3D code as well as the Kiva-3V code. Additionally one URANS simulation has been performed with Kiva-3V. The flow field statistics from the LES simulations deviated substantially between one case and the next. Again, only global flow features could be captured appropriately, due to the previously mentioned shortcomings.

An additional sensitivity that has been observed, concerned the definition of the inflow conditions. Any uncertainty in the mass flow rates at the two runners, that are connected to the cylinder head, can greatly influence the remaining flow patterns. To circumvent this problem, it can be mandatory to include a larger part of the upstream flow geometry into the computational domain.

Nevertheless, LES gives an indication of the unsteady, turbulent processes that take place in an engine, whereas in the URANS simulations all mean flow structures are very weak and the turbulence intensities are predicted to be relatively low in the complete domain. But this study does show that, for a predictive quality of this type of LES on a quantitative level, the numerical scheme as well as the computational resolution have to be improved.

In the remainder of this thesis the geometry has been kept relatively simple and second-order numerical schemes were applied, and sufficient resolution could be reached to perform relatively accurate LES simulations.

Modeling a turbulent gas jet

In chapter four the turbulent mixing process in gaseous jets has been studied for three different fuel-to-air density ratios. This mimicked the injection of (heavy) fuel into a pressurized chamber. It is shown that the three jets follow well the similarity theory that was developed for turbulent gas jets. A main observation was that the fuel core length increases with increasing density ratio. Therefore the self-similarity region is shifted more downstream in the fuel jet for heavy fuel jets. Also the penetration depth as a function of time follows the self-similarity theory properly for a fuel-to-air density ratio of unity. In this case, an increase in density ratio leads to a slight decrease in the scaled penetration depth.

A virtual Schlieren postprocessing method has been developed, in order to analyze the results similarly as done experimentally, e.g., for the visualization of the development of turbulent structures. When defining the penetration depth based on this method, similar difficulties are encountered as in Schlieren experiments, related to the definition of the cutoff signal intensity.

By comparing the evolution of the penetration depth of a gaseous jet with models that have been developed for liquid fuel jets, it has been concluded that the phenomenological models for both jets are exchangeable for larger penetration depths. This is because the penetration rate from liquid sprays is governed by the entrain-

ment rate, which is similar as for gaseous jets. Only for very short distances the simulation departs from the liquid jet experiment, due to the large impact of the liquid particle dynamics on the entrainment rate, which is reduced accordingly. However, it remains questionable if gas jet models can simply be used to replace the model for fuel sprays. The cone angle for gas jets deviates strongly from those observed in spray experiments. Only when corrected for this effect, the penetration behavior was similar.

The application of flamelet-based chemistry to turbulent diffusion flames

In chapter five two turbulent diffusion flames have been investigated with a focus on the modeling of finite rate chemistry effects. For the first flame, the well known Sandia flame D, two methods have been compared to each other for the modeling of the main parameters of the turbulent flame, i.e. the main combustion products and heat release. The two methods are firstly the classical flamelet method where the non-premixed chemistry is parameterized using a mixture fraction and the scalar dissipation rate, and secondly a relatively new method, where a progress variable method is applied to non-premixed chemistry problems.

In the progress variable method two different databases have been compared: one based on non-premixed flamelets and one based premixed flamelets. It is found that the prediction of the mixture fraction field in the LES simulation of Sandia flame D is influenced by the different parameterizations. This is best predicted by both the classical flamelet method, and the progress variable method that is based on premixed chemistry, especially in the downstream region of the flow. In these cases the solution of the chemical species in the flame is mostly predicted close to their equilibrium values. When accounting for the shift of the mixture fraction field, the progress variable method based on non-premixed chemistry leads to the most appropriate results, especially at locations where finite-rate chemistry is important. It can be concluded that the fluid dynamical part of the modeling problem needs improvement.

In the last section of chapter five a sooting turbulent benzene diffusion flame has been investigated. A steady laminar flamelet library is applied which is based on a very detailed reaction mechanism for premixed benzene flames. In the LES simulations the total PAH/soot mass and mole fractions are computed explicitly, while the source terms for these variables are based on a classical flamelet parametrization. The current study of a benzene flame can be considered as illustrative in giving a methodology for the application of flamelet methods for the prediction of soot in turbulent flames. The regions of PAH/soot formation have been identified, showing distributed parcels where PAH/soot formation takes place. The results show a growth of PAH/soot volume fraction up to levels of about 4 ppm. The average particle size increases steadily in this flame, up to about 30 nm.

Recommendations

To gain more confidence in the unsteady flow behavior, in future modeling attempts of complex engine flows an LES simulation can be more preferable to URANS based calculations, on the condition that available computational power is not a restriction, and that stable and (second-order) accurate schemes are used. For the modeling of the near wall regions, however, a hybrid approach where RANS-like assumptions for the boundary layer are applied, would definitely be more suitable. This can lead to a correct prediction of the shear, which can result in a proper prediction of the instantaneous, mean and turbulent flow features in an engine.

Yet, the flow and consequently the combustion in an engine at real operating conditions is not only influenced by the inlet geometry, as was studied in this thesis, but also by the squish, that takes place at the end of the compression phase. Concerning future work it is a challenging question to investigate its impact on the turbulent in-cylinder flow field, using an LES approach, to study cycle-to-cycle variations.

In this thesis it is shown that for the modeling of a liquid fuel injection system, a gas jet system can be adopted. When accounting for the spreading rate of the jet, this can lead to a drastic simplification of the modeling efforts that are required for practical simulations of (burning) fuel sprays. On the other hand, in the end the inclusion of a droplet model is mandatory, as droplet breakup, collisions and evaporation can lead to different behavior of the burning fuel spray compared to the one of a gas jet.

When discussing the simulation of the turbulent diffusion flames, one can think of improvements in many aspects of the problem formulation. This can involve the turbulence and the chemical modeling, as well as with its interaction. Also the development of accurate, stable and efficient numerical discretization methods for all given models requires serious investigation.

Here we will confine ourselves to two examples of improvements that can be made related to chemical aspects of the problem. The inclusion of extinguished/re-ignition flamelets into the non-premixed flamelet formulation is one of the more challenging research questions, to study turbulent flames of practical relevance, for instance at engine conditions. Under these circumstances drastic departures from solutions close to chemical equilibrium can be expected. Local flame extinction can have a strong effect on the fluid dynamics.

Secondly, concerning the modeling of soot in diffusion flame type of problems, the introduction of an additional number of scalar fields can lead to better insight in the properties of the local PAH/soot in such a flame. In this way the contents of the different PAH/soot classes can be tracked in more detail. This will lead to an improved prediction of the soot particle size distribution.

The numerical scheme of FASTEST-3D

The numerical code FASTEST-3D is based on a boundary fitted, multi-block, finite volume method. The governing fluid-dynamical equations in the non-premixed combustion LES simulation consist of the conservation of mass, momentum, equations 2.26, 2.27. Additionally, in case of mixing problems and combustion LES, the filtered transport equations for the mixture fraction and the progress variable are solved, equations 5.11, 5.17, depending on the applied chemical model. The discretization of these transport equations is presented in this appendix.

A.1 Discretization

In the finite volume method the transport equations for the momentum and the scalar fields Φ are rewritten in the integral form:

$$\int_V \frac{\partial \rho \Phi}{\partial t} dV + \int_V \frac{\partial \rho u_i \Phi}{\partial x_i} dV = \int_V \frac{\partial}{\partial x_i} \left(\rho D \frac{\partial \Phi}{\partial x_i} \right) dV + \int_V \rho S_\Phi dV \quad (\text{A.1})$$

Here, integration is performed over all control volumes V . These volumes are arbitrary hexahedrons, see figure A.1 for a 2D representation. In above equation, and also in the remainder of this section the LES filtering operators have been omitted for simplicity. The different contributions to this equation are evaluated separately. These are the convective and diffusive fluxes and the source terms S_Φ . Their discretization will be presented in the following subsections.

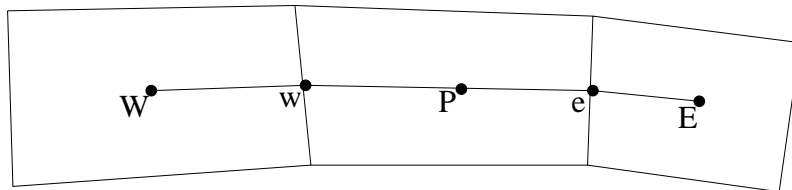


Figure A.1 : A sketch of the grid arrangement in the FASTEST-3D code.

Spatial discretization

The convective fluxes F_c are evaluated using the identity

$$F_c = \int_V \frac{\partial \rho u_i \Phi}{\partial x_i} dV = \int_S \frac{\partial \rho u_i n_i \Phi}{\partial x_i} dS = \sum_{nb} \int_{S_{nb}} \rho u_i n_i \Phi dS \quad (\text{A.2})$$

Here, the Gauss theorem is applied, converting the volume integral over the control volume V into a surface integral. Here, n_i denotes the normal vector on the control volume surface pointing outwards. This is then split up into a sum of the integrals over all neighbouring faces S_{nb} of the computational cell. Now, the face integral is estimated by the mean value $(\cdot)_m$, leaving

$$\sum_{nb} \int_{S_{nb}} \rho u_i n_i \Phi dS = \sum_{nb} (\rho u_i)_m n_i (\Phi)_m \delta S_{nb} \quad (\text{A.3})$$

Finally this can be rewritten, using the expression for the mass flux at the cell boundary $(\dot{m})_{nb} = (\rho u_i)_{nb} \delta S_{nb}$:

$$\sum_{nb} (\rho u_i)_m n_i (\Phi)_m \delta S_{nb} = \sum_{nb} (\dot{m})_{nb} \cdot (\Phi)_{nb} \quad (\text{A.4})$$

This means that both the mass flux and the value for Φ at the cell faces have to be defined, in terms of cell centered quantities. This can be achieved by several methods. A main concern is to keep the convective term stable, and at the same time accurate. One of the available schemes in the FASTEST-3D code which remains second order even on skewed grids is referred to as the multi-linear interpolation (MULI) procedure, Lehnhäuser and Schäfer [84]. This scheme is used for the evaluation of the momentum equations. On the other hand, for convection terms in the mixture fraction field a TVD scheme is adopted, to remedie strong oscillations in the density field, Wegner [163], Branley and Jones [21], Kempf [71]. In the current combustion simulations the CHARM scheme has been applied, which formalism has been presented in section 3.2.2. The CHARM limiter function has the advantage of being smooth, which aids to stabilize the code, Kempf [71].

Using a similar method as for the convective fluxes an expression for the diffusive fluxes F_d can be derived:

$$F_d = \int_V \frac{\partial}{\partial x_i} \left(\rho D \frac{\partial \Phi}{\partial x_i} \right) dV = \int_S \rho D \frac{\partial \Phi}{\partial x_i} dS = \sum_{nb} (\rho D)_{nb} \delta S_{nb} \frac{\partial \Phi}{\partial x_i} \Big|_{nb} \quad (\text{A.5})$$

Now the diffusion coefficient $(\rho D)_{nb}$ and the gradient of the variable $\frac{\partial \Phi}{\partial x_i} \Big|_{nb}$ need to be evaluated at the cell boundaries. This is performed using a scheme which is second order accurate, Lehnhäuser and Schäfer [84]. Finally, the source term is simply discretized as the multiplication of the cell volume with the cell center value $S_{\phi,P}$:

$$F_s = \int_V \rho S_{\phi} dV = \rho S_{\phi,P} \delta V_P \quad (\text{A.6})$$

For the momentum equation the source term is described by the gravity $S_u = g_x$ and for the progress variable it is the chemical source term $S_C = \dot{\omega}_C$.

Temporal Discretization

To discuss the temporal discretization, the convective and diffusive fluxes and the source term are now referred to as the sum of all fluxes $F(\Phi, t)$:

$$F(\Phi, t) = -F_c + F_d + F_s. \quad (\text{A.7})$$

This leads to the following form of the conservational equation:

$$\frac{\partial \rho \Phi}{\partial t} \delta V = F(\Phi, t). \quad (\text{A.8})$$

The solution is integrated to yield the value for the new timestep:

$$[(\rho \Phi)^{n+1} - (\rho \Phi)^n] \delta V = \int_{t_n}^{t_{n+1}} F(\Phi, t) dt. \quad (\text{A.9})$$

In the FASTEST-3D code the Crank Nicolson scheme is adopted. This is an implicit scheme, which is favourable for numerical stability. This leads to the expression

$$[(\rho \Phi)^{n+1} - (\rho \Phi)^n] \delta V = \Delta t \frac{1}{2} [F(\Phi^n, t) + F(\Phi^{n+1}, t)]. \quad (\text{A.10})$$

The solution procedure of this linear system is performed by a 7-diagonal version of the strongly implicit procedure (SIP), Stone [150] and is based on an incomplete LU decomposition that converges rapidly. Again, an exception is made for the transport of mixture fraction field and the progress variable. When solving the mixture fraction field using the Crank-Nicolson scheme the velocity field exhibits instabilities, probably due to the explicit contribution in the scheme, [163]. Oscillations in the mixture fraction field lead to oscillations in the density field, and hence in all other transported variables, such as momentum. Therefore it is chosen to use a fully implicit first order scheme. The reduction of the accuracy, both by introduction of the TVD scheme and by this first order time integration is argued to be allowed as the transport of the passive variables are mostly driven through convection. By treating the underlying velocity field to be second order accurate the mixture fraction field is remains well modelled, [116].

Pressure correction

The FASTEST-3D code adopts a Low Mach number approximation. The pressure correction takes place in order to fulfill the continuity constraint, using the so-called SIMPLE method, Patankar [110]. Here, the key steps are presented. With the use of the estimated velocity field u^* from the solution of the momentum equation the mass conservation equation leads to a virtual source b_m :

$$\frac{\partial \rho}{\partial t} + \frac{\partial(\rho u_i^*)}{\partial x_i} = b_m. \quad (\text{A.11})$$

Notice the extra $\frac{\partial \rho}{\partial t}$ -term which is absent in constant-density pressure correction schemes. The virtual source b_m can be related to the velocity correction $u'_i = u_i^{n+1} - u_i^*$ and the pressure correction $p' = p^{n+1} - p^*$ via

$$b_m = -\frac{\partial(\rho u'_i)}{\partial x_i} = \Delta t \frac{\partial^2 p'}{\partial x_i^2}. \quad (\text{A.12})$$

When this Poisson equation is solved to find the pressure correction p' , the velocity field can be corrected accordingly, using

$$\rho u_i^{n+1} - \rho u_i^* = -\Delta t \frac{\partial p'}{\partial x_i}. \quad (\text{A.13})$$

For the densities that appear in above formalism, the most recent values ρ^{n+1} are constantly used. The time derivative of the density field, which is needed in equation A.11, is here approximated by

$$\frac{\partial \rho}{\partial t} = \frac{\rho^{n+1} - \rho^n}{\Delta t}, \quad (\text{A.14})$$

which is second-order accurate in the framework of the Crank-Nicolson scheme. Whereas, amongst others, Pierce [116] applies a spatial filtering of the time derivative of the density field this appeared not necessary in the current formulation, due to the first-order implicit formulation of the mixture fraction field [163].

A.2 The solution algorithm

The numerical scheme as presented above leads to the solution procedure as shown in figure A.2. For every time step first the new combustion variables are evaluated, using a fully implicit scheme. Then the density is updated using the chemistry table:

$$\rho^{n+1} = \rho(Z^{n+1}, \dots). \quad (\text{A.15})$$

Also the other transport variables, such as the viscosity and diffusivities are updated here, as well as the density time derivative. Then the momentum equations are solved leading to the predicted velocity field u^* , using the Crank Nicolson scheme. The Poisson equation is solved based on the predicted velocity field. Finally, the velocity and pressure fields are corrected. Now, these steps are iterated, until a converged solution is achieved for the current time step. Then the algorithm proceeds to the next time step.

One inconsistency must be paid attention to [116]. The discretized transport of mixture fraction that leads to a new density field does not necessarily correspond to the discretized transport of mass, derived from the continuity equation. In other words, the constraint equation which is used in the pressure correction stage depends on the combustion progress variables implicitly. Therefore, the evaluation of

$$\frac{\partial \rho \Phi}{\partial t} \delta V = F(\Phi, t) \quad (\text{A.16})$$

followed by $\rho = \rho(\Phi)$, does not necessarily correspond to

$$\frac{\partial \rho}{\partial t} \delta V = F(\rho, t) \quad (\text{A.17})$$

Therefore it is of importance to use the same spatial discretization schemes in the Poisson equation as in the transport equation that drive the density via the scalar equations [163].

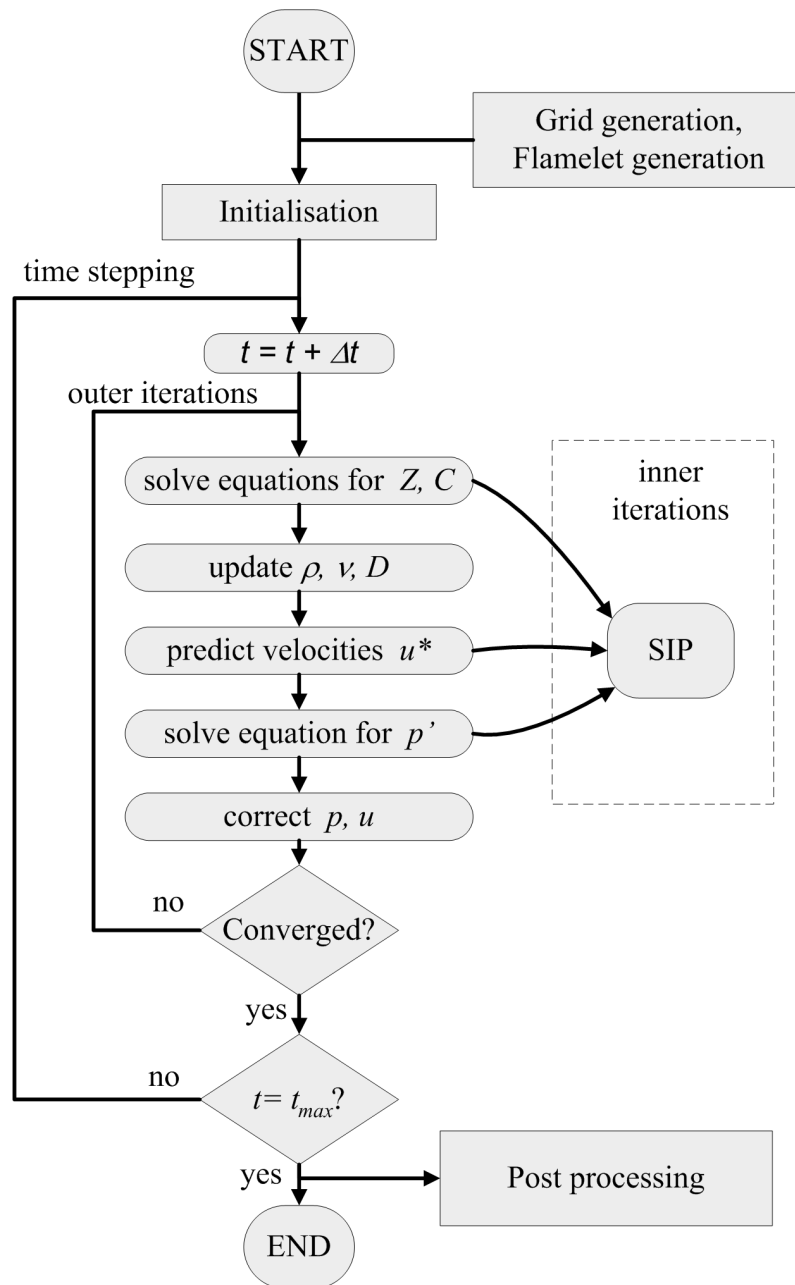


Figure A.2 : Flow chart of the applied solution procedure in FASTEST-3D.

Bibliography

- [1] J. Abraham, V. Magi, Computations of transient jets: RNG k-e model versus standard k-e model. *SAE Trans* 106 (1997) 1442-1452.
- [2] J. Abraham, V. Magi, A virtual liquid source (VLS) model for vaporizing diesel sprays. *SAE Trans* 108 (1999) 1363-1374.
- [3] A. D'Alessio, A.C. Barone, R. Cau, A. D'Anna P. Minutolo, Surface deposition and coagulation efficiency of combustion generated nanoparticles in the size range from 1 to 10 nm. *Proc. Comb. Inst.* 30 (2005) 2595-2603.
- [4] M. Amielh, T. Djeridane, F. Anselmet, L. Fulachier, Velocity near-field of variable density turbulent jets. *Int. J. Heat Mass Transfer* 39-10 (1996) 2149-2164.
- [5] A.A. Amsden, P.J. O'Rourke, T.D. Butler, KIVA-II: A Computer Program for Chemically Reactive Flows with Sprays. *Technical Report LA-11560-MS Los Alamos National Laboratory* (1989).
- [6] A. D'Anna, M. Commodo, S. Violi, C. Allouis, J. Kent, Nano organic carbon and soot in turbulent non-premixed ethylene flames. *Proc. Comb. Inst.* 31 (2007) 621-629.
- [7] M.D. Avakian, B. Dellinger, H. Fiedler, B. Gullet, C.Koshland, et al., The origin, fate, and health effects of combustion by-products: a research framework. *Environmental health perspectives* 110 (2002) 1155-1162.
- [8] <http://www.cerfacs.fr/cfd/> (2007).
- [9] J.S. Bagget, J. Jiménez, A.G. Kravchenko, Resolution requirements in large-eddy simulations of shear flows. *Annual Research Briefs, Center for Turbulence Research Stanford* (1998) 267-277.
- [10] X.S. Bai, M. Balthasar, F. Mauss, L. Fuchs, Detailed soot modeling in turbulent jet diffusion flames *Proc. Combust. Inst.* 27 (1998) 1623-1630.
- [11] E. Balaras, C. Benocci, U. Piomelli, Two-layer approximate boundary conditions for large-eddy simulations. *AIAA J.* vol. 34 (1996) 1111-1119.
- [12] M. Balthasar, A. Heyl, F. Mauss, F. Schmitt, H. Bockhorn, Flamelet modeling of soot formation in laminar ethylene/air diffusion flames. *Proc. Comb. Inst.* (1996) 2369-2377.

- [13] J. Bardina, J.H. Ferziger W.C. Reynolds, Improved turbulence models based on LES of homogeneous incompressible turbulent flows. *Rep. TF-19, Department of Mechanical engineering, Stanford* (1984).
- [14] R.S. Barlow, J.H. Frank, Effects of turbulence on species mass fractions on methane/air jet flames. *Proc. Combust. Inst.* 27 (1998) 1087-1095.
- [15] R.S. Barlow, J.H. Frank, and J.-Y. Chen, Scalar structure and transport effects in piloted methane/air jet flames. *Combustion and Flame* 143 (2005) 433-449.
- [16] H. Barths, C. Hasse, G. Bikas, N. Peters, Simulation of combustion in direct injection diesel engines using a eulerian particle flamelet model. *Proc. Comb. Inst.* 28 (2000) 1161-1168.
- [17] R.W. Bilger, The structure of nonpremixed turbulent flames. *Proc. Combust. Inst.* 22 (1988) 475-488.
- [18] A.D. Birch, D.R. Brown, M.D. Dodson, J.R. Thomas, The turbulent concentration field of a methane jet. *Journal of Fluid Mechanics* 88 (1978) 431-449.
- [19] H. Bongers, Analysis of flamelet-based methods to reduce chemical kinetics in flame computations. *Ph.D Thesis, TU Eindhoven* (2005).
- [20] M.J. Boussinesq, Essay sur la théorie des eaux courantes. *Mémoires Présentés par Divers Savants Étrangers à l'Académie des Sciences, Gauthier-Villars, Paris* (1877) 1.
- [21] N. Branley, W.P. Jones, Large Eddy simulation of a turbulent non-premixed flame. *Turbulent Shear Flows Conference II* 21 (1997) 1-6.
- [22] N. Branley, W.P. Jones, Large Eddy simulation of a turbulent non-premixed flame. *Combustion and Flame* 127 (2001) 1914-1934.
- [23] K.N.C. Bray, N. Peters, Turbulent Reacting Flows *Academic Press, London*, eds. P.A. Libby and F.A. Williams (1994).
- [24] G. Bruneaux, A study of mixture formation in direct injection diesel like conditions using quantitative fuel concentration visualizations in a gaseous fuel jet. *SAE Trans.* 2002-01-1632 (2002).
- [25] R.R. Cao, S.B. Pope, The influence of chemical mechanisms on PDF calculations of non-premixed piloted jet flames. *Combustion and Flame* 143 (2005) 450-470.
- [26] G. Carazzo, E. Kaminski, S. Tait, The route to self-similarity in turbulent jets and plumes. *Journal of Fluid Mechanics* 547 (2006) 137-148.
- [27] W. Cabot, P. Moin, Approximate wall boundary conditions in the large-eddy simulation of high Reynolds number flow. *Flow, Turbulence and Combustion* 63 (2000) 269-291.
- [28] I. Celik, I. Yavuz, A. Smirnov, J. Smith, E. Amin, A. Gel, Prediction of in-cylinder turbulence for IC engines. *Combustion Science and Technology* 153 (2000) 339-368.

-
- [29] I. Celik, I. Yavuz, A. Smirnov, Large eddy simulations of in-cylinder turbulence for internal combustion engines: a review. *Int. J. Engine Research* 2-2 (2001) 119-148.
 - [30] R. Cheesewright, G. McGrath, D.G. Petty, LDA measurements of turbulent flow in a duct of square cross section at low Reynolds number. *Technical Report Aeronautical Engineering Dept. Queen Mary Westfield College, University of London* ER 1011 (1990).
 - [31] CHEM1D. *a one-dimensional laminar flame code*. Eindhoven University of Technology (2007). <http://www.combustion.tue.nl>.
 - [32] A.W. Cook, J. Riley, A subgrid model for equilibrium chemistry in turbulent flows. *Physics of Fluids* 6 (1994) 2868-2870.
 - [33] D. J. Cook, H. Pitsch, J. H. Chen, E. R. Hawkes, Flamelet-based modeling of auto-ignition with thermal inhomogeneities for application to HCCI engines. *Proc. Comb. Inst.* 31 (2007) 2903-2911.
 - [34] W.J.A. Dahm, Experiments on entrainment, mixing and chemical reactions in turbulent jets at large Schmidt number. *Ph.D Thesis Caltech, Pasadena* (1987).
 - [35] J.W. Deardorff, A numerical study of three-dimensional turbulent channel flow at large Reynolds numbers. *Journal of Fluid Mechanics* 41 (1970) 453-465.
 - [36] M.E. Decroix, W.L. Roberts, Transient flow field effects on soot volume fraction in diffusion flames. *Combustion Science and Technology* 160 (2000) 165-189.
 - [37] J. Denev, T. Frank, K. Pachler, Large Eddy Simulation of Turbulent Square Channel Flow using a PC-cluster architecture. *Springer-Verlag Heidelberg, Lecture Notes in Computer Science* 2907 (2004) 363-370.
 - [38] J.M. Desantes, J. Arrègle, J.J. López, J.M. García, Turbulent gas jets and diesel-like sprays in a crossflow: A study on axis deflection and air entrainment. *Fuel* 85 (2006) 2120-2132.
 - [39] A. Devesa, J. Moreau, J. Hélie, V. Faivre, T. Poinso, Initial conditions for Large Eddy Simulations of piston engine flows. *Computers & Fluids* 36 (2007) 701-713.
 - [40] E. Doosje, R.J.M. Bastiaans, R.S.G. Baert, Application of PIV to characterize the flow-phenomena of a heavy-duty cylinder head on a stationary flow-bench. *Proceedings of the EUROPIV 2 workshop* (2004).
 - [41] D.R. Dowling, P.E. Dimotakis, Similarity of the concentration field of gas-phase turbulent jets. *Int. J. Fluid Mech.* 218, (1990) 109-141.
 - [42] F. Durst, M. Schäfer, A parallel blockstructured multigrid method for the prediction of incompressible flow. *Int. J. Numer. Meth. Fluids* 22, (1996) 549-565.

- [43] J.G.M. Eggels, F. Unger, M.H. Weiss, J. Westerweel, R.J. Adrian, F.T.M. Nieuwstadt, R. Friedrich, Fully developed pipe flow: A comparison between direct numerical simulation and experiment. *Journal of Fluid Mechanics* 268 (1994) 175-209.
- [44] A. Evlampiev, Numerical Combustion Modeling for Complex Reaction Systems, *Ph.D Thesis, TU Eindhoven* (2007).
- [45] J.H. Ferziger, Introduction to Turbulence Modeling. *Von Karman Institute for Fluid Dynamics lecture notes* (2004).
- [46] <http://www.avl.com/> (2007).
- [47] <http://www.fluent.com> (2007).
- [48] M. Frenklach, Method of moments with interpolative closure *Chemical Engineering Science* 57 (2002) 2229-2239.
- [49] C. Fureby, G. Tabor, H.G. Weller, A.D. Gosman, A comparative study of subgrid scale models in homogeneous isotropic turbulence. *Physics of Fluids* 9(5) (1997) 1416-1429.
- [50] E. Garnier, M. Mossi, P. Sagaut, P. Comte, M. Deville, On the use of Shock-capturing schemes for large-eddy simulation. *Journal of computational physics* 153 (1999) 273-311.
- [51] K. Horiuti, Large eddy simulation of turbulent channel flow by one-equation modeling. *J. Phys. Soc. Japan* 54 (8) (1985) 2855-2865.
- [52] S. Gavrilakis, Numerical simulation of low-Reynolds-number turbulent flow through a straight square duct. *Journal of Fluid Mechanics* 244 (1999) 101-129.
- [53] M. Germano, U. Piomelli, P. Moin, W.H. Cabot, A dynamic subgrid-scale eddy viscosity model. *Physics of Fluids A* 3 (7) (1991) 1760-1765.
- [54] B.J. Geurts, Database-analysis of interacting errors in large-eddy simulation. *Proceedings of the Quality Assessment of Unsteady Methods*. (2005)
- [55] S.S. Girimaji Y. Zhou, Analysis and modeling of subgrid scalar mixing using numerical data. *Physics of Fluids* 8 (1996) 1224-1236
- [56] R.J. Hall, M.D. Smooke, M.B. Colket, F.L. Dryer, R.F. Sawyer (Ed.), Physical and chemical aspects of combustion: a tribute to Irine Glasman. *Gordon & Breach* (1997).
- [57] F.E. Ham, F.S. Lien, A.B. Strong, Large-Eddy Simulation of the square duct flow using a parallel PC cluster. *Proceedings of the 8th Annual Conference of the CFD society of Canada* (2000).
- [58] K. Hanjalić, Advanced turbulence closure models: a view of current status and future prospects. *Int. J. Heat and Fluid Flow* 15-3 (1994) 178-203.

-
- [59] R.G. Harvey, Polycyclic aromatic hydrocarbons: chemistry and cancer, *Cambridge University Press*, Cambridge, UK (1991).
- [60] D.C. Haworth, K. Jansen, Large-eddy simulation on unstructured deforming meshes: towards reciprocating IC engines. *Computers & Fluids* 29 (2000) 493-524.
- [61] E. Hecht, Optics, 4th edition. , MA: *Addison-Wesley*, Amsterdam (2002)
- [62] C. Hirsch, Numerical computation of internal and external flows. *Wiley: Chichester* (1990).
- [63] S. Hong, M.S. Wooldridge, H.G. Im, D.N. Assanis, H. Pitsch, Development and application of a comprehensive soot model for 3D CFD reacting flow studies in a diesel engine *Combustion and Flame* 143 (2005) 11-26.
- [64] V. Huijnen, L.M.T. Somers, R.S.G. Baert, L.P.H. de Goey, Comparing different turbulence modelling approaches for square duct simulations using the kiva code. *Proc. ASME-PVP* 491-2 (2004) 335-362.
- [65] V. Huijnen, L.M.T. Somers, R.S.G. Baert, L.P.H. de Goey, Validation of the LES approach in Kiva-3V on a square duct geometry. *Int. J. Numer. Meth. Engineering* 64 (2005) 907-919.
- [66] A. Huser, S. Biringen, Direct numerical simulation of turbulent flow in a square duct. *Journal of Fluid Mechanics* 257 (1993) 65-95.
- [67] H. J. Hussein, S. P. Capp, W. K. George, Velocity measurements in a high-Reynolds number, momentum-conserving, axisymmetric, turbulent jet. *Journal of Fluid Mechanics* 246 (1993) 197-223.
- [68] M. Ihme, C.M. Cha, H. Pitsch, Prediction of local extinction and re-ignition effects in non-premixed turbulent combustion using a flamelet/progress variable approach. *Proc. Comb. Inst.* 30 (2005) 793-800.
- [69] J. Janicka, W. Kollmann, A two-variables formalism for the treatment of chemical reaction in turbulent H₂-air diffusion flames *Proc. Comb. Inst.* 17 (1978) 421-430.
- [70] S. Jay, F. Lacas, S. Candel, Combined surface density concepts for dense spray combustion. *Combustion and Flame* 144 (2006) 558-577.
- [71] A.M. Kempf, Large-Eddy Simulation of Non-Premixed Turbulent Flames. *PhD-thesis, TU-Darmstadt* (2003).
- [72] A. Kempf, F. Flemming, J. Janicka, Investigation of lengthscales, scalar dissipation, and flame orientation in a piloted diffusion flame by LES. *Proc. Combust. Inst.* 30 (2005) 557-565.
- [73] M. Klein, A. Sadiki J. Janicka, A digital filter based generation of inflow data for spatially developing direct numerical or large eddy simulations. *J. Comp. Physics* 186-2 (2003) 652-665.

- [74] M. Klein, An attempt to assess the quality of large eddy simulations in the context of implicit filtering. *Flow Turbulence and Combustion* 75 (2005) 131-147.
- [75] R.J.H. Klein-Douwle, P.J.M. Frijters, L.M.T. Somers, W.A. de Boer, R.S.G. Baert, Macroscopic diesel fuel spray shadowgraphy using high speed digital imaging in a high pressure cell. *Fuel* 87 (2007).
- [76] A.N. Kolmogorov, The local structure of turbulence in incompressible viscous fluids for very large Reynolds number. *Dokl Akad. Nauk SSSR* 30 (1941) 299-303.
- [77] R.H. Kraichnan, Eddy viscosity in two and three dimensions. *Journal of Atmospheric sciences* 33 (1976) 1521-1536.
- [78] T.-W. Kuo, On the scaling of impulsively started incompressible turbulent round jets. *Journal of Fluids Engineering* 104 (1982) 191-197.
- [79] C. de Langhe, B. Merci, E. Dick, Hybrid RANS/LES modelling with an approximate renormalization group. I: Model development. *Journal of Turbulence* 6 (13) (2005) 1-18.
- [80] C. de Langhe, B. Merci, K. Lodefier, E. Dick, Hybrid RANS/LES modelling with an approximate renormalization group. II: Applications. *Journal of Turbulence* 6 (14) (2005) 1-16.
- [81] B.E. Launder, D.B. Spalding, Mathematical models of turbulence. *Academic Press* (1972).
- [82] D. Laurence, Applications of Reynolds Averaged Navier Stokes Equations to industrial flows. *Von Karman Institute for Fluid Dynamics lecture notes* (2004).
- [83] R. de Leeuw, Comparison of PIV and LDA on a stationary flow-bench of a heavy-duty cylinder-head. *Master's thesis, TU/e, Eindhoven, The Netherlands* (2005).
- [84] T. Lehnhäuser and M. Schäfer, Improved linear interpolation practice for finite-volume schemes on complex grids. *Int. J. Numer. Meth. Fluids* 38 (2002) 625-645.
- [85] M. Lesieur, Turbulence in Fluids. *Kluwer Academic Publishers* (1997).
- [86] M. Lesieur, O. Metais, New trends in Large Eddy Simulations of turbulence. *Annual Review of Fluid Mechanics* 28 (1996) 45-82.
- [87] S. Liu, C. Meneveau, J. Katz, Experimental study of similarity subgrid-scale models as deduced from measurements in a turbulent jet. *Journal of Fluid Mechanics* 275 (1994) 83-119.
- [88] D. Lilly, The representation of small scale turbulence in numerical simulation experiments. *Proceedings of the IBM Scientific Computing Symposium on Environmental Sciences* (1996) 195-210.
- [89] D. Lilly, A proposed modification of the Germano subgrid-closure method. *Physics of Fluids* 4(3) (1992) 633-635.

-
- [90] T. S. Lund, X. Wu K. D. Squires, Generation of turbulent inflow data for spatially-developing boundary layer simulations. *Journal of Computational Physics* 140 (1998) 233-258.
- [91] C.L. Lubbers, G. Brethouwer, B.J. Boersma, Simulation of the mixing of a passive scalar in a round turbulent jet. *Fluid Dynamics Research* 28 (2001) 189-208.
- [92] R.K. Madabhushi, S.P. Vanka, Large eddy simulation of turbulence-driven secondary flow in a square duct. *Physics of Fluids A* 1 (1991) 2734-2745.
- [93] C. Mengler, Grobstruktursimulation der Strömungs- und Mischungsfelder komplexer anwendungsnaher Konfigurationen. *PhD-thesis, TU-Darmstadt* (2001).
- [94] J. Meyers, B. J. Geurts, M. Baelmans, Database analysis of errors in large-eddy simulation. *Physics of Fluids* 15 (2003) 2740-2755.
- [95] R. Mittal, P. Moin, Suitability of upwind-biased finite difference schemes for Large-Eddy simulation of turbulent flows. *AIAA Journal* 35 (8) (1997) 1415-1417.
- [96] P. Moin, K. Squires, W. Cabot, S. Lee, A dynamic subgrid-scale model for compressible turbulence and scalar transport, *Phys Fluids A* 3 (11) (1991) 2746-2757.
- [97] B. Moss, in: H. Bockhorn (Ed.), Soot formation in combustion - Mechanisms and models, Lecture notes in physics. *Springer New York* (1994) 561-569.
- [98] R. Mustata, L. Valiño, C. Jiménez, W.P. Jones, S. Bondi, A probability density function Eulerian Monte Carlo field method for large eddy simulations: application to a turbulent plotted methane/air diffusion flame (Sandia D). *Combustion and Flame* 145 (2006) 88-104.
- [99] J.D. Naber, D.L. Siebers, Effects of gas density and vaporization on penetration and dispersion of diesel sprays. *SAE Trans* 960034 (1996).
- [100] B. Naud, PDF Modeling of turbulent sprays and flames using a particle stochastic approach. *PhD-thesis, TU Delft* (2003).
- [101] S. Navarro-Martinez, A. Kronenburg, LES-CMC simulations of a turbulent bluff-body flame *Proc. Comb. Inst.* 31 (2007) 1721-1728.
- [102] K. Netzell, H. Lehtiniemi, F. Mauss, Calculating the soot particle size distribution function in turbulent diffusion flames using a sectional method. *Proc. Comb. Inst.* 31 (2007) 667-674.
- [103] F. Nicoud, F. Ducros, Subgrid-scale stress modelling based on the square of the velocity gradient tensor. *Flow, Turbulence and Combustion* 62 (1999) 183-200.
- [104] J.A. van Oijen, Flamelet-Generated Manifolds: development and application to premixed laminar flames. *Ph.D Thesis, TU Eindhoven* (2002).

- [105] J.A. van Oijen, L.P.H. de Goey, A numerical study of confined triple flames using a flamelet-generated manifold. *Combustion Theory and Modelling* 8 (2004) 141-163.
- [106] M. Olsson, L. Fuchs, Large eddy simulation of the proximal region of a spatially developing circular jet. *Physics of Fluids* 8 (8) (1996) 2125-2137.
- [107] P. Ouellette, P.G. Hill, Turbulent transient gas injections. *Journal of Fluids engineering* 122 (2000) 743-753.
- [108] J. Pallares, L. Davidson, Large-eddy simulations of turbulent flows in stationary and rotating channels and in a stationary square duct. *Technical Report Chalmers University of Technology* (2000).
- [109] N. R. Panchapakesan, J. L. Lumley, Turbulence measurements in axisymmetric jets of air and helium. Part 1. Air jet. *Journal of Fluid Mechanics* 246 (1993) 197-223.
- [110] S.V. Patankar, D. Spalding, A calculation procedure for heat, mass and momentum transfer in three dimensional parabolic flows. *Int. J. of Heat and Mass Transfer* 15 (1972) 1787-1806.
- [111] S.V. Patankar, Numerical Heat Transfer and Fluid Flow. *Hemisphere* Washington D.C., (1980).
- [112] F. Payri, J. Benaljes, X. Margo, A. Gil, CFD modeling of the in-cylinder flow in direct-injection Diesel engines. *Computers & Fluids* 33 (2004) 995-1021.
- [113] N. Peters, Laminar diffusion flamelet models in non-premixed combustion. *Progress in Energy and Combustion Science* 10 (1984) 319-339.
- [114] N. Peters, Turbulent Combustion. *Cambridge University Press* (2000).
- [115] C.D. Pierce, P. Moin, A dynamic model for subgrid-scale variance and dissipation rate of a conserved scalar. *Physics of Fluids* 10 (1998) 3041-3044.
- [116] C.D. Pierce, Progress-variable approach for large-eddy simulation of turbulent combustion. *Ph.D Thesis Stanford University* (2001).
- [117] C.D. Pierce, P. Moin, Progress-variable approach for large-eddy simulation of non-premixed turbulent combustion. *Journal of Fluid Mechanics* 504 (2003) 73-97.
- [118] U. Piomelli, High Reynolds number calculations using the dynamic subgrid-scale stress model. *Physics of Fluids* 5 (6) (1993) 1484-1490.
- [119] U. Piomelli, Large-eddy simulation: achievements and challenges. *Progress in Aerospace Sciences* 35 (1999) 335-362.
- [120] H. Pitsch, H. Barths, N. Peters, Three-dimensional modeling of NO_x and soot formation in DL-Diesel engines using detailed chemistry based on the interactive flamelet approach, *SAE Trans* 105 (1996) 2010-2024.

-
- [121] H. Pitsch, H. Steiner, Large-eddy simulation of a turbulent piloted methane/air diffusion flame (Sandia flame D). *Physics of Fluids* 12 (10) (2000) 2541-2554.
- [122] H. Pitsch, H. Steiner, Scalar mixing and dissipation rate in Large-Eddy Simulations of non-premixed turbulent combustion. *Proc. Comb. Inst.* 28 (2000) 41-49.
- [123] W.M. Pitts, Effects of global density ratio on the centerline mixing behavior of axisymmetric turbulent jets. *Experiments in Fluids* 11 (1991) 125-134.
- [124] T. Poinso, D. Veynante, Theoretical and numerical combustion. *Edwards Philadelphia* (2001).
- [125] C.J. Pope, J.B. Howard, Simultaneous particle and molecule modeling (spamm): an approach for combining sectional aerosol equations and elementary gas-phase reactions. *Aerosol Sci. Technol.* 27 (1997) 73-94.
- [126] S.B. Pope, An explanation of the turbulent round jet/plane-jet anomaly, *AIAA J.* 16-3 (1978) 279.
- [127] S.B. Pope, Computations of turbulent combustion: Progress and challenges, *Proc. Combust. Inst.* 23 (1990) 591-612.
- [128] S. B. Pope, Turbulent Flows. *Cambridge University Press* (2000)
- [129] S.B. Pope Ten questions concerning the large-eddy-simulation of turbulent flows. *New Journal of Physics* 6(35), (2004).
- [130] E. Ranzi, M. Dente, A. Goldaniga, G. Bozzano, T. Faravelli, Lumping procedures in detailed kinetic modeling of gasification, pyrolysis, partial oxidation and combustion of hydrocarbon mixtures, *Progress in Energy and Combustion Science* 27 (2000) 99-139.
- [131] J.D. Ramshaw and P.J. O'Rourke, L.R. Stein, Pressure gradient scaling method for fluid flow with nearly uniform pressure. *Journal of Computational Physics* 58 (1985) 361-376.
- [132] R.D. Reitz, C.J. Rutland, Development and testing of diesel engine CFD models, *Progress in Energy and Combustion Science* 21 (1995) 173-196.
- [133] C.D. Richards, W.M. Pitts, Global density effects on the self-preservation of turbulent free jets. *Journal of Fluid Mechanics* 254 (1993) 417-435.
- [134] H. Richter, J.B. Howard, Formation of polycyclic aromatic hydrocarbons and their growth to soot - a review of chemical reaction pathways. *Progress in Energy and Combustion Science* 26 (2000) 565-608.
- [135] H. Richter, S. Granata, W.H. Green, J.B. Howard, Detailed modeling of PAH and soot formation in a laminar premixed benzene/oxygen/argon low-pressure flame. *Proc. Comb. Inst.* 30 (2005) 1397-1405.

- [136] F.P. Ricou, D.B. Spading, Measurements of entrainment by axisymmetrical turbulent jets. *Journal of Fluid Mechanics* 11 (1961) 21-32.
- [137] E. Ruffin, R. Schiestel, F. Anselmet, M. Amielh, L. Fulachier, Investigation of characteristic scales in variable density turbulent jets using a second-order model. *Physics of Fluids* 6-8 (1994) 2785-2799.
- [138] J.P.H. Sanders, B. Sarh, I. Gökalp, Variable density effects in axisymmetric isothermal turbulent jets: a comparison between a first- and second-order turbulence model. *Int. J. Heat Mass Transfer* 40-4 (1997) 823-842.
- [139] P. Sagaut, Large eddy simulation for incompressible flows. *Springer* (2002)
- [140] R.W. Schefer, A. R. Kerstein, M. Namazian, J. Kelly, Role of large-scale structure in a nonreacting turbulent CH₄ jet. *Physics of Fluids* 6 (1994) 652-661.
- [141] R.C. Schmidt, A. R. Kerstein, S. Wunsch, V. Nilsen, Near-wall LES closure based on one-dimensional turbulence modeling. *Journal of computational physics* 186 (2003) 317-355.
- [142] C. Schneider, A. Dreizler, J. Janicka, Flow field measurements of stable and locally extinguishing hydrocarbon-fuelled jet flames. *Combustion and Flame* 135 (2003) 185-190.
- [143] G.S. Settles, Schlieren and Shadowgraph Techniques: Visualizing phenomena in transparent media. *Springer Verlag* (2001)
- [144] J. Smagorinsky, General circulation experiments with the primitive equations. *Monthly Weather Review* 91-3 (1963) 99-164.
- [145] G. Smith, D. Golden, M. Frenklach, N. Moriarty, B. Eiteneer, M. Goldenberg, C. Bowman, R. Hanson, S. Song, W. Gardiner, V. Lissianski, Z. Qin, GRI-Mech 3.0 - A Mechanism for the Combustion of Natural Gas, *The Gas Research Institute* (1999) http://www.me.berkeley.edu/gri_mech/.
- [146] J.J.M. Smits, Modeling of a fluid flow in an internal combustion engine. *Master's thesis, TU/e, Eindhoven, The Netherlands* (2006).
- [147] K. Sone, S. Menon, Effect of subgrid modeling on the in-cylinder unsteady mixing process in a direct injection engine. *ASME Journal of Engineering for Gas Turbines and Power* 125-4 (2003) 765-781.
- [148] <http://www.cd-adapco.com/> (2007)
- [149] G. Stiesch, Modeling Engine Spray and Combustion Processes. *Springer Verlag* (2003)
- [150] H. Stone, Iterative solution of implicit approximations of multidimensional partial differential equations. *SIAM Journal of Numerical Analysis* 5 (1968) 530-558.

-
- [151] B. R. Sutherland, S.B. Dalziel, G.O. Hughes, P.F. Linden, Visualization and measurement of internal waves by 'synthetic schlieren'. Part 1. Vertically oscillating cylinder. *Journal of Fluid Mechanics* 390 (1999) 93-126.
 - [152] F. Tao, D.E. Foster, R.D. Reitz, Characterization of soot particle distribution in conventional, non-premixed DI diesel flame using a multi-step phenomenological soot model. *Proc. Comb. Inst.* 31 (2007) 2991.
 - [153] L. Temmerman, M. Hadžiabdić, M.A. Leschziner and K. Hanjalić, A hybrid two-layer URANS-LES approach for large eddy simulation at high Reynolds numbers. *Int. J. Heat and Fluid Flow* 26 (2005) 173-190.
 - [154] F. Tessicini, L. Temmerman, M.A. Leschziner, Approximate near-wall treatments based on zonal and hybrid RANS-LES methods for LES at high Reynolds numbers. *Int. J. Heat and Fluid Flow* 27 (2006) 789-799.
 - [155] <http://www.ca.sandia.gov/TNF/DataArch/FlameD.html> (2007).
 - [156] M.S. Toledo, L. Le Penven, M. Buffat, A. Cadiou, J. Padilla, Large eddy simulation of the generation and breakdown of a tumbling flow. *Int. J. Heat and Fluid Flow* 28 (2007) 113-126.
 - [157] D. J. Torres, M. F. Trujillo, KIVA-4: An unstructured ALE code for compressible gas flow with sprays, *Journal of Computational Physics* 219 (2006) 943-975.
 - [158] S. Vedal, Ambient particles and health: lines that divide. *Journal of Air and Waste Management Association* 47 (1997) 551-581.
 - [159] B. Vreman, B. Geurts, H. Kuerten, Large-eddy simulation of the turbulent mixing layer. *Journal of Fluid Mechanics* 339 (1997) 357-390.
 - [160] A.W. Vreman, An eddy-viscosity subgrid-scale model for turbulent shear flow: Algebraic theory and applications. *Physics of Fluids* 16-10 (2004) 3670-3681.
 - [161] S. Wallin, A.V. Johansson, An explicit algebraic Reynolds stress model for incompressible and compressible turbulent flows. *Journal of Fluid Mechanics* 403 (2000) 89-132.
 - [162] J. Warnatz, U. Maas, R.W. Dibble, *Combustion* Springer Berlin Heidelberg, (1996).
 - [163] B. Wegner, A large-eddy simulation technique for the prediction of flow, mixing and combustion in gas turbine combustors. *PhD-thesis, TU-Darmstadt* (2006).
 - [164] World Energy, Technology and Climate Policy Outlook 2030. *European Commission, Directorate General for Research* (2003)
http://ec.europa.eu/research/energy/pdf/weto_final_report.pdf
 - [165] J. Xu, S.B. Pope, PDF calculations of turbulent nonpremixed flames with local extinction. *Combustion and Flame* 123 (2000) 281-307.

- [166] S.L. Yang, B.D. Peschke, K. Hanjalić, Second-Moment Closure Model for IC Engine Flow Simulation Using Kiva Code. *ASME Journal of Engineering for Gas Turbines and Power* 122 (2000) 355-363.
- [167] S.L. Yang, Y.K. Siow, C.Y. Teo, K. Hanjalić, A KIVA code with Reynolds-stress model for engine flow simulation, *Energy* 30 (2005) 427-445.
- [168] B. Yang, U.O. Koylu, Detailed soot field in a turbulent non-premixed ethylene/air flame from laser scattering and extinction experiments. *Combustion and Flame* 141 (2005) 55-65.

Abstract

On the Application of Large-Eddy Simulations in Engine-related Problems

In internal combustion engines the combustion process and the pollutants formation are strongly influenced by the fuel-air mixing process. The modeling of the mixing and the underlying turbulent flow field is classically tackled using the Reynolds Averaged Navier Stokes (RANS) modeling method. With the increase of computational power and the development of sophisticated numerical methods the Large Eddy Simulation (LES) method becomes within reach. In LES the turbulent flow is locally filtered in space, rather than fully averaged, as in RANS.

This thesis reports on a study where the LES technique is applied to model flow and combustion problems related to engines. Globally, three subjects have been described: the turbulent flow in an engine-like geometry, the turbulent mixing of a gas jet system and the application of flamelet-based methods to LES of two turbulent diffusion flames. Because of our goal to study engine-related flow problems, two relatively practical flow solvers have been selected for the simulations. This choice was motivated by their ability to cope with complex geometries as encountered in realistic, engine-like geometries.

A series of simulations of the complex turbulent, swirling and tumbling flow in an engine cylinder, that is induced by the inlet manifold, has been performed with two different LES codes. Additionally one Unsteady RANS simulation has been performed. The flow field statistics from the Large-Eddy simulations deviated substantially between one case and the next. Only global flow features could be captured appropriately. This is due to the impact of the under-resolved shear layer and the dissipative numerical scheme. Their effects have been examined on a square duct flow simulation.

An additional sensitivity that was observed concerned the definition of the in-flow conditions. Any uncertainty in the mass flow rates at the two runners, that are connected to the cylinder head, greatly influences the remaining flow patterns. To circumvent this problem, a larger part of the upstream flow geometry was included into the computational domain. Nevertheless, the Large-Eddy simulations do give an indication of the unsteady, turbulent processes that take place in an engine, whereas in the URANS simulations all mean flow structures are very weak and the turbulence intensities are predicted relatively low in the complete domain.

The turbulent mixing process in gaseous jets has been studied for three different fuel-to-air density ratios. This mimicked the injection of (heavy) fuel into a pressurized chamber. It is shown that the three jets follow well the similarity theory that

was developed for turbulent gas jets. A virtual Schlieren postprocessing method has been developed in order to analyze the results similarly as can be done experimentally. By defining the penetration depth based on this method, problems as typically in Schlieren experiments, related to the definition of the cutoff signal intensity have been studied. Additionally it was shown that gaseous jet models can be used to simulate liquid fuel jets, especially at larger penetration depths. This is because the penetration rate from liquid sprays is governed by the entrainment rate, which is similar as for gaseous jets. However, it remains questionable if gas jet models can in all cases replace the model for fuel sprays. The cone angle for gas jets can deviate strongly from those observed in spray experiments. Only when corrected for this effect, the penetration behavior was similar.

Two turbulent diffusion flames have been investigated with a focus on the modeling of finite rate chemistry effects. Concerning the first flame, the well known Sandia flame D, two methods are compared to each other for the modeling of the main combustion products and heat release. These methods are described by the classical flamelet method where the non-premixed chemistry is parameterized using a mixture fraction and the scalar dissipation rate, and a relatively new method, where a progress variable is used in non-premixed combustion problems. In the progress variable method two different databases have been compared: one based on non-premixed flamelets and one based premixed flamelets.

It is found that the mixture fraction field in the Large-Eddy simulation of Sandia flame D is best predicted by both the classical flamelet method and the progress variable method that is based on premixed chemistry. In these cases the flame solution was mostly located close to its equilibrium value. However, when correcting for the prediction of the mixture fraction in the spatial coordinates, it is shown that the progress variable method based on non-premixed chemistry is better, compared to experiments. Especially at locations where a flame solution near chemical equilibrium is not adequate this model is more appropriate.

Additionally a sooting turbulent benzene diffusion flame has been investigated. Therefore a steady laminar flamelet library has been applied which is based on a very detailed reaction mechanism for premixed benzene flames. In the Large-Eddy simulations the total PAH/soot mass and mole fractions have been computed explicitly, while the source terms for these variables are based on a classical flamelet parametrization. The regions of PAH/soot formation have been identified, showing distributed parcels where PAH/soot formation takes place. The results show a growth of PAH/soot volume fraction up to levels of about 4 ppm. The average particle size increases steadily in this flame, up to about 30 nm.

Samenvatting

In interne verbrandingsmotoren wordt het verbrandingsproces en de vorming van de uitlaatgassen sterk beïnvloed door het meng-proces van de brandstof en de lucht. Het modelleren van de turbulente stroming en menging is tot nu toe vooral gebaseerd op de zogenaamde Reynolds Averaged Navier Stokes (RANS) methode. Door de toename van de beschikbare rekenkracht en de verdere ontwikkeling van verfijnde numerieke methodes komt het gebruik van de zogenaamde Large-Eddy Simulatie (LES) methode binnen handbereik voor motor-toepassingen. In LES wordt de turbulente stroming lokaal gefilterd, in plaats van volledig gemiddeld, zoals in de RANS aanpak.

Dit proefschrift beschrijft een studie waarin de LES techniek is toegepast op het modelleren van stromings- en verbrandingsprocessen die gerelateerd zijn aan problemen in verbrandingsmotoren. Dit is opgesplitst in drie onderwerpen: de turbulente stroming in een motor-geometrie, het turbulente mengproces van een gas-jet systeem en de toepassing van zogenaamde flamelet-methodes in Large-Eddy simulaties van twee turbulente diffusie vlammen. Vanwege het doel om motor-gerelateerde stromingsproblemen te bestuderen zijn twee relatief praktische stromings-simulatie programma's geselecteerd. Deze keuze is gemotiveerd door het vermogen van deze programmatuur om de stroming in complexe (motor-)geometrieën te kunnen beschrijven.

Als eerste is een serie simulaties uitgevoerd van de complexe turbulente stroming in een cylinder van een verbrandingsmotor. Hier treden grootschalige wervelingen op, als gevolg van de vorm van het inlaat-spruitstuk. De voorspellingen van de turbulente stroming van de verschillende LES simulaties is behoorlijk verschillend. Alleen de globale aspecten van de stroming kunnen goed beschreven worden. Dit is te wijten aan de invloed van de niet-opgeloste schuiflaag aan de wanden, en aan het dissipatieve karakter van het numerieke schema. De effecten van deze invloeden zijn geanalyseerd op een simulatie van een relatief eenvoudige kanaal-stroming. Daarnaast is gebleken dat de stroming gevoelig is voor de opgelegde instroom-condities. Om dit probleem te omzeilen kan een groter deel van het stroom-opwaartse geometrie toegevoegd worden aan het rekendomein. Ondanks de gevonden onzekerheden geven Large-Eddy simulaties een indicatie van de stationaire turbulente processen die plaatsvinden in de verbrandingsmotor. Een RANS simulatie voorspelt hier alleen vrij zwakke stromings-profielen en turbulentie-intensiteiten.

Het turbulente mengproces van brandstof-gas-jets is bestudeerd voor drie verschillende brandstof/lucht dichtheids-verhoudingen. Dit kan gebruikt worden voor de modellering van de injectie van een (zware) brandstof in een hoge-druk kamer. In

deze simulaties is het aangetoond dat de drie verschillende jets de gelijkvormigheids-theorie, zoals die was ontwikkeld voor turbulente gas-jets, goed volgen. Een zogenaamde "virtuele Schlieren" methode is ontwikkeld om de simulatie-resultaten van de gas-jets vergelijkbaar te behandelen als in een experimentele opstelling. Door de meting van de indring-diepte te baseren op deze methode konden problemen zoals die kunnen optreden in Schlieren-experimenten, gerelateerd aan de definitie van de afsnijd-intensiteit, bestudeerd worden.

Ook is aangetoond dat gas-jet modellen gebruikt kunnen worden om de injectie van vloeibare brandstoffen te modelleren, vooral bij grotere indringdieptes. Toch blijft het te betwijfelen of een gas-jet model in alle gevallen gebruikt kan worden voor het modelleren van een vloeibare brandstofstraal. De hoek van de gas-straal kan sterk afwijken van die van een vloeistof-straal, zoals die gemeten is in experimenten. Alleen als hiervoor wordt gecorrigeerd zijn beide modellen uitwisselbaar.

Tot slot zijn twee turbulente diffusievlammen bestudeerd, met de nadruk op het modelleren van de relatief langzame chemie. Bij de eerste vlam, die bekend staat als de Sandia flame D, zijn twee methodes voor de modellering van de belangrijkste reactie-producten en warmte-productie met elkaar vergeleken. De eerste methode is de klassieke flamelet methode, waar de niet-voorgemengde chemie geparametriseerd is met de mengfractie en een diffusie-tijdschaal. In de tweede, relatief nieuwe methode wordt gebruik gemaakt van een reactie-voortgangsvariabele. In deze laatste methode zijn de toepassing van twee verschillende databases met elkaar vergeleken: een die gebaseerd is op flamelets van diffusie-vlammen en een gebaseerd op flamelets uit voorgemengde vlammen.

Uit de resultaten blijkt dat de mengfractie in de Large-Eddy simulatie van de Sandia flame D het best voorspeld wordt door zowel de klassieke flamelet-methode en de voortgangsvariabele-methode gebaseerd op de voorgemengde chemie. Bij deze simulaties was de voorspelling van de chemische compositie vooral dicht bij de evenwichts-situatie. Maar als wordt gecorrigeerd voor de voorspelling van de mengfractie in de ruimtelijke coördinaten dan kan aangetoond worden dat de voortgangsvariabele methode, gebaseerd op de diffusie-vlammen een beter resultaat geeft dan de andere twee, in vergelijking met de experimenten. Dit is vooral zichtbaar op plaatsen waar een vlamoplossing die dicht bij de evenwichts-concentratie zit niet terecht is.

Ook is een turbulente benzeen-diffusievlam gesimuleerd, met de nadruk op de modellering van de roetvorming. Hiervoor is gebruik gemaakt van stationaire laminaire flamelets (SLF), die berekend zijn met behulp van een zeer gedetailleerd reactie mechanisme. In de Large-Eddy simulatie is de totale massafractie en molfractie van grote poly-aromatische koolwaterstoffen (PAK) en roet expliciet berekend, door gebruik te maken van de brontermen voor deze variabelen, die gehaald zijn uit de SLF. De regio's waar PAK/roet gevormd wordt in de vlam konden geïdentificeerd worden, vaak in afzonderlijke, losstaande gebiedjes. Uit de resultaten volgt dat de PAK/roet volume-fractie groeit tot een niveau van 4 ppm. De gemiddelde deeltjes-grootte neemt langzaam toe in deze vlam, tot waarden van rond de 30 nanometer.

Curriculum Vitae

Vincent Huijnen

- | | |
|-----------------|--|
| 19 october 1978 | Born in Enschede, The Netherlands |
| 1992-1997 | Secondary school: VWO, Jacobus College, Enschede |
| 1997-2002 | Applied physics, Delft University of Technology |
| 2002 | Graduated at the Thermal and Fluids Sciences Section |
| 2003-2007 | Ph.D. research at the Section Combustion Technology,
Department of Mechanical Engineering,
Eindhoven University of Technology. |

Dankwoord

“Het komt allemaal goed.” Hoe vaak heb ik dat niet gehoord van de mensen om me heen. Soms wist ik niet zeker of ze nu een grapje maakten of het echt meenden. Maar wat blijkt: ze hadden gelijk. Voor u ligt het bewijs. Maar het had er nooit kunnen zijn zonder de hulp van velen. Niet in de laatste plaats bijvoorbeeld heb ik niks kunnen uitrichten zonder een goed werkend computer-systeem, waarvoor dank aan Jan Hasker, en het NCF. En wat was ik zonder Marjan Dijk, hulp biedend bij administratieve, maar ook vele andersoortige zaken?

Maar in de eerste plaats is het meer dan gepast om mijn copromotor Bart Somers te danken, die altijd een luisterend oor had voor mijn problemen. Nadat ik weer eens de weg kwijt was, wist hij me telkens weer motivatie op te wekken om er op een andere manier naar te kijken, om een doorgang te bieden. Dit geldt zeker ook voor Prof. Philip de Goey, die op belangrijke momenten zijn waardering voor mijn werk over heeft gebracht, waarvoor meer dan dank. Prof. Rik Baert dank ik voor zijn vertrouwen in mijn werk, en voor zijn prikkelende vragen die hij me telkens weer wist te stellen, die me hielpen scherp te blijven. Ook dank aan prof. Bernard Geurts, die mij, met zijn kritisch inzicht, heeft aangezet om het proefschrift aan te scherpen.

Special thanks go to Clemens Olbricht, who helped me a lot with realizing the first simulations using the FASTEST code, and for being very hospitable during my stays in Darmstadt. Thanks also go to Prof. Johannes Janicka and Prof. Amsini Sadiki, for being so kind to offer me a working facility at the TU Darmstadt. Bernhard Wegner, thank you for providing me the basis of the working simulation software.

Natuurlijk ben ik ook grote dank verschuldigd aan Alexey Evlampiev, die me veel wist te leren over chemie en software-ontwikkeling, en, tussendoor, over politiek en maatschappij, op grote en kleine schaal.

Dank aan mijn andere kamergenoten: Happy Bongers, die een bijzonder voorbeeld voor me is van iemand met een optimistische levensvisie. Voor het laatste jaar wil ik Liselotte Verhoeven en Giel Raemakers danken die het alledaagse werk leuk maakten. Stanley Delhaye en Jeroen van Oijen: dank voor de hulp bij het genereren en interpreteren van de flamelet data. En tot slot: Katrin, dank je voor al wat je me geeft. Er is zoveel waardevols in de wereld dat zich niet laat vangen door een wetenschappelijke benadering.

Vincent Huijnen, Eindhoven, juni 2007